# Multiscale Simulation of Transient Viscoelastic Free Surface Flows

by

Mohit Bajaj

Department of Chemical Engineering

Monash University

Clayton, Australia

April 21, 2006

This thesis, contains no material which has been accepted for the award of any other degree or diploma in any university or other institution. I affirm that, to the best of my knowledge, the thesis contains no material previously published or written by another person, except where due reference is made in the text of the thesis.

Mohit Bajaj

To my family

# Acknowledgements

At the outset, I would like to thank my parents and sister for always being there when I needed them the most, and for supporting me throughout.

The work presented in this thesis was carried out under the direct supervision of Dr. J. Ravi Prakash. I express my sincere gratitude to Ravi for his guidance and constant encouragement during the last four years. His enthusiasm and integral view on research with logical thinking, and aim for providing only high quality work and not less have made a deep impression on me. Ravi has helped a lot in developing independence and creativity in my thinking by giving ample freedom to implement my own ideas. I thank him further for his guidance in writing this thesis.

My research in this area of free surface flows would have been very difficult without the most invaluable inputs and the computational code from Dr. Matteo Pasquali at Rice University. I shall forever owe Matteo a debt of gratitude for sharing his deep knowledge and insight in the area of computational rheology. I further thank Matteo for his warm hospitality during my stay at Rice University.

I would like to thank all the former and current members of molecular rheology group, specially Prabhakar and Sunthar, for introducing me to the world of molecular rheology and for many stimulating technical discussions. It is a pleasure to thank Pradipto Bhattacharjee, Xiangnan Ye, Tri Pham, Satheesh Kumar, Duc At Nguyen and Jenny Ho for all the fun. Special thanks to Mohini Acharya and Nipen Shah for being the friends I can always count on. I would like to thank the complex fluids group at Rice University for their help and making my stay at Rice a life time experience. I thank particularly Pradeep P. Bhat, Oscar C. Mattuti (OCM), Xueying Xie and Dhruv Arora for their help in understanding the computational code. I really miss going to Valhalla every evening with Pradeep, Oscar and Prasad.

# Abstract

In this study, a computational method based on multiscale simulation is used to understand the role of viscoelasticity on transient free surface flows of dilute polymer solutions. Two different multiscale simulation strategies, namely, a conformation tensor based approach [M. Pasquali and L. E. Scriven, J. Non-Newtonian Fluid Mech., 108, 363-409, 2002] (which is a macroscopic description that yet provides averaged information on the stretch and orientation of polymer molecules) and a micro-macro approach based on combining the Brownian configuration fields (BCF) method [M. A. Hulsen, A. P. G. van Heel and B. H. A. A. van den Brule, J. Non-Newtonian Fluid Mech., 70, 79–101, 1997] with macroscopic conservation equations, have been developed and implemented for this purpose.

In the BCF method used in this work, polymer molecules are represented by a dumbbell model with both linear and non-linear springs, and hydrodynamic interactions between beads has been incorporated. An unconditionally stable fully implicit simulation algorithm for linear dumbbell models, and a novel semi-implicit predictor-corrector scheme for non-linear microscopic constitutive models is developed for time-integration of the non-linear stochastic differential equations governing the dynamics of dumbbells in complex flows. The computational method developed in this work is first validated by comparing with published results for Couette flow problem. The computational method is then applied to study a free surface flow, i.e., a slot coating flow.

Slot coating flow computations for linear dumbbell models i.e. infinitely extensible (Hookean) and pre-averaged finitely extensible (FENE-P) dumbbell models using the micro-macro approach, are in excellent agreement with their equivalent closed-form constitutive equations in the conformation tensor formulation. We observe that

the computations using the BCF approach are stable at much higher Weissenberg numbers. For non-linear dumbbells, we show that the semi-implicit time integration algorithm is fast and computationally efficient when compared to both an explicit scheme and a fully implicit scheme involving the solution of the non-linear equations with Newton's method for each configuration field. Moreover, we found significant differences between the stretch of polymers (a microscopic property) at the free surface for different microscopic constitutive models while the macroscopic properties (i.e. velocity and stress profile) are almost unaffected.

Besides micro-macro computations, macroscopic simulations based on the conformation tensor approach have been performed for a wide range of dimensionless parameters and for different constitutive models to compute slot coating flows. We show that the flow behavior of dilute polymer solutions is dramatically different from that of ultra-dilute solutions studied previously by Pasquali and Scriven [2002]. The results show that elastic stresses due to the viscoelastic nature of the fluid reduce the size of the recirculation zone under the die. The stagnation point moves from the free surface to the die wall as $Wi$ increase, and leads to a positive hoop stress when it reaches the static contact line. This is shown to be the mechanism by which viscoelasticity destabilizes the flow, in line with the stability analysis by Graham [Phys. Fluids, 15, 1702–1710, 2003]. Elimination of recirculation close to the static contact line exposes the geometric singularity that exists in slot coating flows to a relatively strong flow, and field variables such as the velocity gradient and the conformation tensor become singular.

With the micro-macro method developed in this work, it is possible to capture, at least qualitatively, the behavior of real polymer molecules in solution. Given adequate computational resources, this method can in principle be used for solving complex flow problems by incorporating most accurate models presently available, which are based on bead-rod and bead-spring models with non-linear interactions and many degrees of freedom.

# Contents

# List of Tables

# List of Figures

xi

xviii

# Chapter 1

# Introduction

Free surface flows occur when one or more layers of liquid meet a gas or interact with a deformable elastic solid at one or more interfaces. Such flows abound in coating technology (e.g. slot coating, roll coating, knife coating etc.), polymer processing, cell engineering (deformation of blood cells) and marine engineering. The majority of the free surface problems include various physical phenomena such as mass transfer through the interface, interfacial and capillary hydrodynamics, air entrainment as the liquid displaces air from the moving web, evaporation of volatile matters from the free surface, hydrodynamic instabilities caused by the presence of the free surface, instabilities due to the presence of the surfactant, and sensitivity of the flow due to the viscoelastic nature of the processed fluids. Hence, modeling free surface flows is a multi-disciplinary problem comprising fluid mechanics, mathematics, rheology, wetting, spreading, interfacial phenomenon etc. While the interaction of all these various physical phenomena and the competition between various forces associated with them decide the quality of the final product, a mathematical model accounting for all the phenomena can be too complex to deal with a analytically or even numerically. Alternatively, the effect of each physical phenomena can be investigated separately which can then be combined to draw a multi-dimensional diagram for various dimensionless parameters giving information on dominant forces in a particular process. In this work, the combined effect of rheology and capillary forces on coating flows has been investigated.

Due to the existence of a variety of industrial applications of coating flows e.g.

the paper industry, magnetic and optical storage media etc., numerous researchers have focused their attention on coating flow of Newtonian fluids in an effort to better understands and prevent interfacial instabilities [Carvalho and Kheshgi, 2000; Carvalho and Scriven, 1997a,b, 1999; Christodoulou and Scriven, 1992; Coyle et al., 1990; Gates, 1999; Greener et al., 1980; Mill and South, 1967; Musson, 2001; Pearson, 1960; Pitts and Greiller, 1961; Ruschak, 1976; Saito and Scriven, 1981; Sartor, 1990; Savage, 1984; Silliman and Scriven, 1980]. However, most of the coating fluids in commercial applications are polymeric liquids which show strong viscoelastic behavior i.e. they do not obey a simple linear relationship between the stress and the rate of strain and the fluid behaviour cannot be captured simply by Navier-Stokes equations. The polymer concentration in coating application ranges from a few parts per million to almost a pure polymer, as in a hot melt coating of low-molecular weight adhesives. The addition of a small amount of polymer to a Newtonian solvent can dramatically change the flow behaviour for example the shear viscosity of most polymer solutions falls with shear rate [Bird et al., 1987a]. The strange behaviour shown by viscoelastic liquids can be attributed to the finite time scale associated with these fluids which can be vastly different from that of the flow time scale. Experiments on various viscoelastic coating flows [Bauman et al., 1982; Dontula, 1999; Glass, 1978a,b,c; Grillet et al., 1999; Ning et al., 1996; Romero et al., 2004] reveal that coating flows are extremely sensitive to the viscoelastic nature of coating fluid. These experiments demonstrate that a minute amount of viscoelasticity leads to various instabilities, reduces the size of the stable coating window and can change the operating conditions of the process depending on the viscoelasticity of the processed fluid.

In spite of a variety of industrial applications, modeling viscoelastic free surface flows remains a scientific challenge largely due to the difficulties and computational cost associated with the large scale simulations of such flows. While computations of Newtonian coating flows abound in literature [Carvalho and Kheshgi, 2000; Carvalho and Scriven, 1997a,b, 1999; Christodoulou and Scriven, 1992; Gates, 1999; Mill and South, 1967; Musson, 2001; Pearson, 1960; Pitts and Greiller, 1961; Ruschak, 1976; Saito and Scriven, 1981; Sartor, 1990; Silliman and Scriven, 1980] etc., studies on viscoelastic coating flows are very recent and limited [Bhatara et al., 2004, 2005; Lee

et al., 2002; Pasquali and Scriven, 2002; Romero et al., 2004; Zevallos et al., 2005].
The pioneer work of Lee et al. [2002] and Pasquali and Scriven [2002] unarguably led
to an improved qualitative understanding of experiments on coating flows of dilute
polymer solutions. While Lee et al. [2002] investigated the effect of viscoelasticity
on the Hele-Shaw flow of dilute solutions, Pasquali and Scriven [2002] computed the
slot and knife coating flow of ultra-dilute solutions.

In general, viscoelastic flows are modeled by adding a closed-form constitutive
equation to the conservation laws of mass and momentum. The closed-form consti-
tutive equation relates the elastic stress to the rate of stain and thus, describes the
behaviour of polymer molecules in flow. The behaviour of polymer molecules have
been shown to be completely different in shear and extensional flows [Bird et al.,
1987a,b]. Coating flows, which are more complex than simple shear and extensional
flow, are almost always a combination of shear and extensional kinematics. For in-
stance in slot coating flows, in the vicinity of the web, the flow is dominated by shear
kinematics and close to the free surface, the flow is extensional in nature. The basic
properties of polymer such as length, molecular weight, stiffness and architecture sig-
nificantly affect the shear and extensional behaviour of polymer solutions. Hence, it
is appropriate to say that a theory that accurately predicts the shear and extensional
behaviour of polymer solutions is ideally the minimum requirement for simulating
complex flows where process flow kinematics departs substantially from both sim-
ple shear and extensional flows. The most accurate models presently available are
kinetic theory based bead-rod and bead-spring models with non-linear interactions,
such as the finite extensibility of polymer molecules and solvent polymer interac-
tions e.g. hydrodynamic and excluded volume interactions. Computations using
these models have been shown to be in excellent agreement with various predictions
of the rheological properties of dilute polymer solutions in homogeneous shear and
extensional flows [Cifre and De la Torre, 1999; DE Gennes, 1979; Hsieh et al., 2003;
Knudsen et al., 1996; Larson et al., 1999, 1997; Magda et al., 1988; Prabhakar, 2005;
Schroeder et al., 2003, 2004; Sunthar and Prakash, 2005]. It is found that the inclu-
sion of above mentioned non-linear interactions are extremely important in accurate
theoretical predictions.

At this point it is worth noting that typically, Brownian dynamics simulations

are used to solve the kinetic theory based constitutive models. The use of Brownian dynamics simulations avoids the need for closed-form constitutive equations. However, as it is well known that closed-form equations cannot be written for these accurate kinetic theory based models, which are essential for carrying out large scale simulations of viscoelastic or other complex fluids within a *macroscopic description* of a fluid. Closed-form constitutive equations can only be written when either all the non-linear effects are neglected or their linearized approximations are used.

While most approximate theories, obtained by approximating various non-linear interactions, are quantitatively inaccurate, they have been of vast interest in simulating industrial flows over the years. The reason for this continued interest in approximate theories is largely due to the fact that calculations with approximate models are much faster compared to calculations using accurate models. As a result, approximate models can be used to explore a much larger parameter space and hence provide invaluable insight into the various physical phenomena. An added advantage of these approximate closed-form equations over phenomenological equations derived from continuum mechanics is that they provide information on average stretch and orientation of polymer molecules. In this work, a conformation tensor based constitutive equation is used to investigate the effect of viscoelasticity of free surface flows [Beris and Edwards, 1994; Grmela and Carreau, 1987; Grmela and Öttinger, 1997; Jongschaap et al., 1994; Pasquali and Scriven, 2004]. The conformation tensor based constitutive equation can in principle be derived by approximating the most coarse-grained molecular model, namely, the dumbbell model. Simulations for two different constitutive models, namely, Oldroyd-B and FENE-P models are carried out for a wide range of parameters for both dilute and ultra-dilute solutions of slot coating flow. The most important result of these simulations is a clear distinction between the flow computations of dilute and ultra-dilute polymer solutions.

Although viscoelastic flow simulations using a closed-form constitutive model has been of great interest, failure of numerical computations at low to moderate fluid's viscoelasticity has been a long standing problem in computational rheology. It is found that various viscoelastic flow computations either fail to converge or give unphysical results beyond a certain Weissenberg number. The maximum Weissenberg number, $Wi = \lambda\dot{\gamma}$ (where $\lambda$ is the characteristic relaxation time of polymer, and $\dot{\gamma}$ is

the characteristic rate of strain) that can be obtained appears to depend upon the flow geometry and the constitutive equation. Until recently, it has not been clear whether the failure of computations at high $Wi$ is a numerical artifact or due to the use of a closed-form constitutive model. Only recently, Fattal and Kupferman [2004] have confirmed, by using a log-conformation approach, that the failure of numerical computations at high $Wi$ is purely a numerical artifact which can be avoided by a change of variable. However, it remains to be seen whether computations for equivalent microscopic models using Brownian dynamics simulations coupled with conservation equations remain numerically stable at high $Wi$.

The use of Brownian dynamics simulation to solve large scale viscoelastic flow problems was pioneered by Laso and Ottinger [1993]. The CONNFFESSIT method developed by Laso and Ottinger [1993] couples the solution of conservation equations with Brownian dynamics simulations to evaluate the polymer contribution to stress and hence avoids the need for a closed-form constitutive equation. As the CONNFFESSIT approach combines the idea of a description of the microstructure of polymer molecules with a macroscopic description of flow, this type of simulation technique is typically called as micro-macro approach. While the computation of large scale viscoelastic flows using bead-spring and bead-rod models are still beyond currently available computational resources, a coarser representation of polymer molecule, namely, a dumbbell model, can be be used to (i) compare the micro-macro results with macroscopic results when no non-linear interactions are incorporated, and (ii) to investigate qualitatively the effect of various non-linear effects when they are included. Micro-macro schemes can provide direct insight into the relationship between the flow and flow induced microstructure.

In this work, a more advanced micro-macro scheme, the Brownian configuration fields (BCF) method proposed by Hulsen et al. [1997] is used. While the BCF method is known from quite sometime, its application has been mostly limited to confined flows of linear dumbbell models. In this work, we have applied the BCF method to solve viscoelastic free surface flows. A dumbbell model with both linear and non-linear forces has been used to represent polymer molecules. Within the framework of large scale viscoelastic flow simulations, for the first time fluctuating hydrodynamic interactions between beads has been incorporated. A highlight of this

work is the demonstration of numerical stability of viscoelastic flow computations at high $Wi$ using the micro-macro approach for both linear and non-linear dumbbell models.

The present thesis is organized as follows. A detailed description of conformation tensor based constitutive models and the finite element formulation of the governing equations has been discussed in Chapter 2. The microscopic constitutive equations and the micro-macro scheme used here are discussed in Chapter 3. Chapter 4 presents the validation of micro-macro approach developed in this work by solving a Couette flow problem. In Chapter 5, results for macroscopic simulation of slot coating flow has been presented. Chapter 6 compares the micro-macro computations with macroscopic results for linear dumbbell models. Results for non-linear dumbbell models and for transient free surface flows are also discussed in Chapter 6. The major conclusions of this work are finally summarized in Chapter 7.

# Chapter 2

# Viscoelastic Free Surface Flow Modeling Using the Macroscopic Approach

This chapter summarizes the governing equations, boundary conditions, and computational method for solving two dimensional (2-D) free surface flows of viscoelastic liquids within the framework of the macroscopic description of fluid. The finite element method used to discretize the governing equations is discussed, and the corresponding weighted residuals and Jacobian matrices are presented in this chapter. The problem formulation presented in this chapter can in general be applied to solve any viscoelastic flow (i.e., confined or free boundary flow problems) using a closed-form constitutive equation.

Viscoelastic flows are usually modeled by adding an extra closed-form constitutive equation for the elastic stress. Hence, simulations of such flows require solving simultaneously the hyperbolic transport equation of elastic stress together with the momentum and mass conservation equations. Most of the constitutive equations used in modeling complex flows can be classified in to two classes. (i) Macroscopic models such as conformation tensor based models, rate-type models [Bird et al., 1987a,b]. (ii) Mesoscopic models based on bead-spring or bead-rod models of polymer solutions, where the microstructure is represented by micromechanical objects governed by stochastic differential equations [Bird et al., 1987a,b].

While, the mesoscopic models incorporate a richer degree of molecular detail, they are still limited to fairly simple flows because of computational cost [Bird et al., 1987a,b; Feigl et al., 1995; Halin et al., 1998; Hulsen et al., 1997; Laso and Ottinger, 1993; Laso et al., 1997]. Currently macroscopic models are considered the most appropriate for large-scale simulation of complex flows of complex fluids.

Within the framework of the macroscopic models, the rate-type equations used in computational rheology are mainly differential constitutive equations. Differential constitutive equations have a distinct advantage over integral constitutive equations in that they require a knowledge of current velocity and stress fields rather than the entire deformation history [Bird et al., 1987a]. In conformation tensor based approach the microstructure is modeled by means of one or more continuum variables representing the expectation value of microscopic features [Beris and Edwards, 1994; Grmela and Carreau, 1987; Grmela and Öttinger, 1997; Jongschaap et al., 1994; Pasquali and Scriven, 2004]. These rate-type and conformation tensor based constitutive equations for elastic stress e.g. Oldroyd-B, FENE-P etc. are obtained typically by approximating kinetic theory based constitutive equations with the help of *closure approximations*. For instance, the FENE-P model is obtained by pre-averaging the fluctuating non-linear FENE model.

Computational models based on the conformation tensor approach are no more expensive than models based on rate-type equations for viscoelastic stress, yet are much cheaper than models based on more detailed microstructural representations of the liquid based on bead-spring-rod models (e.g., stochastic methods such as CONFFESSIT, Adaptive Lagrangian Particle, and Brownian Configuration Fields) [Bird et al., 1987a,b; Feigl et al., 1995; Halin et al., 1998; Hulsen et al., 1997; Laso and Ottinger, 1993; Laso et al., 1997]. However, compared to the rate-type equations, conformation tensor models allow a much richer description of liquid microstructure and also ensure that microscopic models have thermodynamic consistency [Beris and Edwards, 1994; Grmela and Carreau, 1987; Grmela and Öttinger, 1997; Jongschaap et al., 1994; Pasquali and Scriven, 2004]. Recently viscoelastic flows have been successfully computed with conformation tensor models [Bhat et al., 2005; Pasquali and Scriven, 2002; Xie and Pasquali, 2004].

We have carried out viscoelastic flow computations using both macroscopic and

mesoscopic approaches. The problem formulation based on mesoscopic approach is discussed in detail in next chapter. In the framework of macroscopic approach, we have used the conformation tensor based constitutive models for modeling viscoelastic flows as it provides information on the microstructure of the flowing fluid (averaged configuration of flowing polymer molecules) in addition to the information on macroscopic properties of fluid.

The addition of constitutive equations for elastic stress to conservation equations considerably complicates the analytical and numerical tractability of the viscoelastic flow problem. While the analytical tractability of viscoelastic flow problems is out-of-question due to the severe non-linearities associated with it, the numerical solution of non-linear governing equations using the finite element method is still an open area of research and a major challenge specially for highly elastic liquids.

In this section, we have briefly summarized of various developments in the field of viscoelastic free surface flow modeling. Various state-of-art methods for solving the set of equations, governing viscoelastic flows, have been proposed in literature. Baaijens [1998] provides an extensive review on various developments of finite element techniques used to solve viscoelastic flows. The interesting feature of viscoelastic problems is that they involve a mixed elliptic-hyperbolic system which considerably complicates the mathematical analysis. The traditional Galerkin method is well suited for elliptic equations but produces inaccurate approximations in the solution of hyperbolic equations. Thus, a loss of convergence at quite modest value of $Wi$ has been observed when the Galekin method is applied to mixed problems. Attempts to maintain the elliptic character of the set of governing equations and obtaining a numerically stable and converged solution at high $Wi$ have been the major driving force in developing various solution strategies to solve viscoelastic flow problems.

Most of the advances in the use of finite element method to solve viscoelastic flows are based on several paradigms. These include,

1. Splitting the problem formulation into; (i) solution of the momentum and continuity equations for the calculation of the velocity and pressure fields, and (ii) the calculation of the extra stress field from the hyperbolic constitutive equation.

2. Reformulating the momentum and constitutive equation to make explicit the

elliptic character of this equation with respect to the velocity field.

3. Introducing accurate and smooth interpolation of velocity gradients for additional numerical stability in the solution of the constitutive equation.

4. Introducing a concept of adaptive viscosity to retain the elliptic character of the momentum equation even at high Weissenberg numbers ($Wi = \lambda\dot{\gamma}$, where $\lambda$ is the characteristic relaxation time of polymer, and $\dot{\gamma}$ is the characteristic rate of strain).

5. Applying numerically stable and accurate methods for the solution of the hyperbolic equations in order to obtain an accurate representation of the complex boundary layer structure that seems inherent in the solution of such flows.

Various methods proposed in literature, based on the above paradigms, have originated from the EVSS (Elastic Viscous Split Stress) formulation of Rajagopalan et al. [1990]. The EVSS and its successive variants DEVSS (Discrete Elastic Viscous Stress Split) [Guénette et al., 1992], DEVSS-G (Discrete Elastic Viscous Stress Split with interpolated velocity gradient) [Guénette and Fortin, 1995], DAVSS-G (Discrete Adaptive Elastic Viscous Stress Split with interpolated velocity gradient) [Sun et al., 1999] and DEVSS-TG (Discrete Elastic Viscous Stress Split with Traceless velocity gradient) [Pasquali and Scriven, 2002] give a converged and accurate solution at low and moderate values of $Wi$. However, at present, it is not clear whether the failure of these methods at higher $Wi$ is due to the constitutive model used to represent the behavior of polymers solutions, or due to the imposition of an incorrect boundary condition at geometric singularities or due, to the lack of mesh refinement. Another shortcoming of EVSS based formulations is that the selection of the interpolating functions for the various unknowns are restricted by compatibility conditions (e.g., the Babuska-Brezzi condition in flows of incompressible Newtonian fluids and the compatibility condition between velocity gradient and viscoelastic stress for viscoelastic liquids) [Babuska, 1971; Brezzi, 1974; Szady et al., 1995]. A Galerkin/Least-Square (GLS) based finite element method can be shown to overcome these compatibility conditions. Various forms of the GLS method have been successfully used to solve viscoelastic flows [Behr et al., 1993; Fan et al., 1999b;

Oscar et al., 2004]. Like EVSS based methods, the GLS method is also not numerically stable at high $Wi$. Fattal and Kupferman [2004, 2005] and Hulsen et al. [2005] have recently addressed the mystery of the high $Wi$ problem and have developed a so-called Log-Conformation method. Although the stability of numerical solutions at high $Wi$ can be obtained by using the Log-Conformation method of Fattal and Kupferman [2004], obtaining mesh convergence of results at high $Wi$ is still an open challenge. In this work, viscoelastic flow is computed by the DEVSS-TG finite element method proposed by Pasquali and Scriven [2002] primarily because it has been successfully used to solve a larger variety of viscoelastic flows when compared to the GLS or the Log-Conformation methods.

Modeling viscoelastic *free surface flows* adds another challenge to an already complicated problem, as the free surface location is unknown *a priori* and describing its evolution is a part of the solution of the problem. The computational method used to analyze such flows is required not only to explain the effect of viscoelasticity but also to accurately compute the free surface shape. Different ways of handling free surface flows using domain mapping methods (e.g., elliptic mesh generation and domain deformation) are discussed in more detail by Benjamin [1994]; Christodoulou and Scriven [1992]; DE Almeida [1995, 1999]; Kistler and Schweizer [1997]; Kistler and Scriven [1984]; Sackinger et al. [1996] and DE Santos [1991]. Apart from domain mapping methods, boundary mapping methods such as volume of fluid (VOF) [Hirt and Nichols, 1981; Maronnier et al., 2003], marker-and-cell (MAC) [Harlow and Welch, 1965], and spine technique [Ruschak, 1980] have also been used in literature. Although boundary mapping methods are computationally cheap compared to domain mapping techniques, they are not appropriate for flows where capillary forces are dominant and the free surface is significantly distorted. Domain mapping methods have been used successfully to solve various 2-D Newtonian and viscoelastic free boundary flow problems [Bhat et al., 2005; Bhatara et al., 2004, 2005; Carvalho and Kheshgi, 2000; Carvalho and Scriven, 1997a,b, 1999; Christodoulou and Scriven, 1992; Lee et al., 2002; Pasquali and Scriven, 2002; Romero et al., 2004; Xie, 2005; Zevallos et al., 2005]. In the domain mapping technique, the problem can be easily solved in a fully coupled way to give the boundary location and the value of the field variables simultaneously and hence reduce convergence problems for capillary

dominant flows. An elliptic mesh generation method proposed by DE Santos [1991] is used in this work to compute viscoelastic free surface flows. More details on the elliptic mesh generation method will be discussed in a subsequent section.

The equations governing viscoelastic free surface flows are well known. However, they are briefly reviewed here primarily to introduce the notation that will be used in the rest of the thesis.

## 2.1 Governing Equations

In this section we review the set of governing equations required to describe the viscoelastic free surface flow problem.

### 2.1.1 Transport Equation

The transport equations for mass and momentum in an unsteady, isothermal and incompressible flow of a dilute polymer solution, in the absence of any external forces, are :

$$0 \quad = \quad \boldsymbol{\nabla} \cdot \mathbf{v} \tag{2.1}$$

$$\mathbf{0} \quad = \quad \rho \left( \frac{\partial \mathbf{v}}{\partial t} + \mathbf{v} \cdot \boldsymbol{\nabla} \mathbf{v} \right) - \boldsymbol{\nabla} \cdot \mathbf{T} \tag{2.2}$$

where $\mathbf{v}$ is the liquid velocity, and $\rho$ is the liquid density. $\mathbf{T}$ is the total stress tensor, which is expanded as: $\mathbf{T} = -p\boldsymbol{\delta} + \boldsymbol{\tau}_{\mathrm{s}} + \boldsymbol{\sigma}$ where $p$ is the pressure, $\boldsymbol{\delta}$ is the identity tensor, $\boldsymbol{\tau}_{\mathrm{s}}$ is the viscous stress tensor and $\boldsymbol{\sigma}$ is the polymer contribution to the total stress tensor. The viscous stress is given by Newton's law of viscosity: $\boldsymbol{\tau}_{\mathrm{s}} = 2\eta_{\mathrm{s}}\mathbf{D}$ where $\mathbf{D}$ is the rate of strain tensor, given by $\mathbf{D} = \frac{1}{2}(\nabla\mathbf{v} + \nabla\mathbf{v}^{\mathrm{T}})$ and $\eta_{\mathrm{s}}$ is the Newtonian viscosity.

### 2.1.2 Macroscopic Constitutive Equation

In conformation tensor based models an independent variable, the conformation tensor $\mathbf{M}$, which carries information on local average stretch and orientation of a polymer molecule is related to the polymer contribution to stress through an

algebraic constitutive equation. Mathematically the conformation tensor can be written as the second moment of the end to end distance of polymer molecule as:

$$\mathbf{M} = \int_{\mathbf{Q}\epsilon R^3} \mathbf{Q}\mathbf{Q}P(\mathbf{Q},t)d\mathbf{Q} \tag{2.3}$$

Where $\mathbf{Q}$ is the end to end distance, and $P(\mathbf{Q},t)$ is the configurational distribution function which gives the number of polymer molecules whose end to end distance lies between $\mathbf{Q}$ and $\mathbf{Q}+d\mathbf{Q}$ at any given instant. Conformation tensor based models have been shown to be thermodynamically consistent [Beris and Edwards, 1994; Grmela and Carreau, 1987; Grmela and Öttinger, 1997; Jongschaap et al., 1994; Pasquali and Scriven, 2004] and invariants of the conformation tensor provide useful information on the microstructural state of polymer in various flow regions. The eigenvectors of the conformation tensor represent the principal direction along which polymer chains are stretched, contracted or oriented and its eigenvalues represent the square of principal stretch ratio. The time evolution of the dimensionless conformation tensor is [Pasquali and Scriven, 2002]:

$$\begin{aligned}
\mathbf{0} &= \frac{\partial \mathbf{M}}{\partial t} + \mathbf{v} \cdot \nabla \mathbf{M} - 2\xi \frac{\mathbf{D} : \mathbf{M}}{\mathbf{I} : \mathbf{M}}\mathbf{M} - \chi(\mathbf{M} \cdot \mathbf{D} + \mathbf{D} \cdot \mathbf{M} - 2\frac{\mathbf{D} : \mathbf{M}}{\mathbf{I} : \mathbf{M}}\mathbf{M}) \\
&\quad - \mathbf{M} \cdot \boldsymbol{\varpi} - \boldsymbol{\varpi}^{\mathrm{T}} \cdot \mathbf{M} + \frac{1}{\lambda}(g_0\mathbf{I} + g_1\mathbf{M} + g_2\mathbf{M}^2)
\end{aligned} \tag{2.4}$$

where $\boldsymbol{\varpi}$ is the vorticity tensor, and $\lambda$ is the characteristic relaxation time of polymer. The constitutive function $\xi(\mathbf{M})$ represents the polymer resistance to stretching along their backbone, $\chi(\mathbf{M})$ represents the polymer resistance to rotation with respect to neighbors and $g_0(\mathbf{M})$, $g_1(\mathbf{M})$, and $g_2(\mathbf{M})$ define the rate of relaxation of polymer segments. We use $R_{\mathrm{e}}^2/3$ as the length scale to normalize the conformation tensor where $R_{\mathrm{e}}$ is end to end distance of the polymer segment.

The elastic stress, $\boldsymbol{\sigma}$, is related to the conformation tensor as [Pasquali and Scriven, 2002]:

$$\boldsymbol{\sigma} = 2(\xi - \zeta)\frac{\mathbf{M}}{\mathbf{I} : \mathbf{M}}\mathbf{M} : \frac{\partial a}{\partial \mathbf{M}} + 2\zeta \mathbf{M} \cdot \frac{\partial a}{\partial \mathbf{M}} \tag{2.5}$$

where $a(\mathbf{M})$, is the Helmholtz free energy per unit mass of the polymeric liquid.

Although the computational algorithm is independent of the choice of constitutive functions $(\xi(\mathbf{M}), \chi(\mathbf{M}), g_0(\mathbf{M}), g_1(\mathbf{M}), g_2(\mathbf{M}),$ and $a(T,\mathbf{M}))$, particular forms

of these functions are chosen to represent a particular constitutive model for the liquid. Pasquali and Scriven [2002, 2004] have discussed conformation tensor based constitutive equations in detail. Two different conformation tensor based constitutive models used in this work are describe below.

- **Infinitely extensible molecules (Oldroyed-B model)** The constitutive function for the Oldroyd-B model are $\xi = 1, \chi = 1, g_0 = -1, g_1 = 1, g_2 = 0$. With these model parameters, the evolution equation of the dimensionless conformation tensor becomes

$$\frac{\partial \mathbf{M}}{\partial t} + \mathbf{v} \cdot \nabla \mathbf{M} = \nabla v^{\mathrm{T}} \cdot \mathbf{M} + \mathbf{M} \cdot \nabla \mathbf{v} - \frac{1}{\lambda}(\mathbf{M} - \mathbf{I}) \qquad (2.6)$$

  and the constitutive equation for stress reduces to

$$\boldsymbol{\sigma} = \frac{G}{2\rho} \mathbf{M} \qquad (2.7)$$

  where $G$ is the elastic modulus of polymer liquid and is related to the polymer relaxation time, $\lambda$, and polymer viscosity, $\eta_{\mathrm{p}}$, as $G \equiv \eta_{\mathrm{p}}/\lambda$.

- **Finitely extensible molecules** (FENE-P model) The constitutive function for the FENE-P model are $\xi = 1, \chi = 1, g_0 = -1, g_1 = (b_{\mathbf{M}} - 1)/(b_{\mathbf{M}} - \mathrm{Tr}\mathbf{M}/3), g_2 = 0$.

  The parameter $b_{\mathbf{M}}$ controls the molecular extensibility, and is defined as the ratio of the maximum length square of polymer molecules to their average length square at equilibrium. Note that the parameter $b_{\mathbf{M}}$ used in conformation tensor based models is different from the finite extensibility parameter $b$ commonly used in FENE-P formulations [Bird et al., 1987b] as elaborated in the next chapter. The evolution equation of the dimensionless conformation tensor for the FENE-P model can be written as:

$$\frac{\partial \mathbf{M}}{\partial t} + \mathbf{v} \cdot \nabla \mathbf{M} = \nabla v^{\mathrm{T}} \cdot \mathbf{M} + \mathbf{M} \cdot \nabla v - \frac{1}{\lambda} \left( \frac{b_{\mathbf{M}} - 1}{b_{\mathbf{M}} - \mathrm{Tr}\mathbf{M}/3} \mathbf{M} - \mathbf{I} \right) \qquad (2.8)$$

and the constitutive equation for polymer stress is given by:

$$\boldsymbol{\sigma} = \frac{G}{2\rho} \left( \frac{b_{\mathbf{M}} - 1}{b_{\mathbf{M}} - \mathrm{Tr}\mathbf{M}/3} \, \mathbf{M} - \mathbf{I} \right) \tag{2.9}$$

The constitutive parameters are the polymer elastic moduls ($G$), the relaxation time ($\lambda$), and the ratio of maximum length square of the polymer to their average length square at the equilibrium ($b_{\mathbf{M}}$) in the FENE-P model.

### 2.1.3 Mesh Generation

In order to solve free boundary problems by means of standard techniques, the set of differential equations posed in the unknown domain has to be transformed to an equivalent set defined in a known reference domain. This transformation is made by a mapping $\mathbf{x} = \mathbf{x}(\boldsymbol{\xi})$ which connects the known and the unknown domains. Here the unknown physical domain is parametrized by the position vector $\mathbf{x}$ and the reference domain by $\boldsymbol{\xi}$. A common approach is to use a simple quadrangular domain tessellated into unit squares. In many situations, however, the physical domain cannot be mapped into a simple quadrangular reference domain. In these situations the physical domain can be subdivided into subdomains (also called regions), each of which can be mapped to quadrangular reference regions. The mapping is arbitrary, except that boundaries of the reference domain have to be continuously mapped onto the boundaries of the physical domain and the mapping has to be invertible.

Theoretical research on mesh generation have addressed issues of existence and uniqueness of such mappings. The key idea in developing such a mapping technique is either to parameterize the free boundary as a mathematical curve or surface in space so that boundary conditions may be applied precisely at interfaces with well represented location, orientation and curvature, or to solve a system of equations for generating boundary fitted finite elements which are characterized by dimensional homogeneity, orthogonality and smoothness. A boundary fitted elliptic mesh generation method proposed by DE Santos [1991] and Benjamin [1994] is used here to construct the mapping between the physical domain and the reference computational domain. It relies on elliptic partial differential equations to relate points of

the physical domain to points of the reference domain. The mapping obeys:

$$\boldsymbol{\nabla} \cdot \tilde{\mathbf{D}} \cdot \boldsymbol{\nabla}\boldsymbol{\xi} = 0 \tag{2.10}$$

where $\boldsymbol{\xi}$ is the position in the computational domain and the dyadic $\tilde{\mathbf{D}}$, the diffusion coefficient, is a symmetric positive definite tensor which controls the spacing of the coordinate lines [Benjamin, 1994; Pasquali and Scriven, 2002]. Boundary conditions are needed in order to solve the second-order partial differential equation that describes the mapping from the reference domain to the physical domain. Boundary conditions used here will be discussed shortly.

In the area of time dependent free surface flow calculations, the Lagrangian and Eulerian based continuum mechanics approaches exist in literature. In purely Lagrangian calculations, a fluid region is subdivided into a finite-element grid which is then convected by the fluid motion. Therefore, the computational domain and the fluid region move identically at all times. The governing equation of flow have no non-linear advection term as there is no relative motion between mesh and the fluid. This method, however, produces large distortion of the mesh and hence, a automatic grid generator is required to correct mesh distortion. In Eulerian approach, the grid remains fixed and there is a net relative motion between the movement of the grid and that of the fluid. In this case no expensive remeshing is required but the equation of motion contains advection terms. There also exist mixed methods, so called arbitrary Lagrangian Eulerian (ALE) methods, between the two extremes represented by the Eulerian and the Lagrangian approaches. In ALE methods the grid is modified by the fluid flow. Grid nodal points move, although with a velocity different from that of the fluid. In order to ensure consistency, the equation of motion is modified by introducing a velocity of the grid while using the ALE approach.

The time dependent free surface flow problem is solved in this work by the ALE algorithm [Huerta and Liu, 1988; Lewis et al., 1997; Masud and Hughes, 1997; Ramaswamy, 1990] in which the time derivatives of any scalar, vector or a tensor quantity $\Phi$ are transformed to time derivatives at fixed iso-parametric coordinates (denoted by $\overset{\circ}{\Phi}$) as

$$\frac{\partial \Phi}{\partial t} = \overset{\circ}{\Phi} - \overset{\circ}{\mathbf{x}} \cdot \nabla \Phi \tag{2.11}$$

where $\overset{\circ}{\mathbf{x}}$ is the mesh velocity. Hence, $(\partial\mathbf{v}/\partial t)$ in Eq. 2.2 and $(\partial\mathbf{M}/\partial t)$ in Eq. 2.4 are replaced with $\left(\partial\mathbf{v}/\partial t - \overset{\circ}{\mathbf{x}} \cdot \boldsymbol{\nabla}\mathbf{v}\right)$ and $\left(\partial\mathbf{M}/\partial t - \overset{\circ}{\mathbf{x}} \cdot \boldsymbol{\nabla}\mathbf{M}\right)$ respectively.

### 2.1.4   Velocity Gradient Interpolation Equation

The interpolated velocity gradient variable $\mathbf{L}$ is introduced to improve the stability and convergence of the computational method. Szady et al. [1995] have suggested that close to stagnation regions and solid surfaces, the conformation transport equation relating the conformation tensor and velocity gradient reduces to an algebraic equation. Therefore, an additional variable called the interpolated velocity gradient should be used in the conformation transport equation in place of the raw velocity gradient and both the conformation dyadic and the interpolated velocity gradient should be represented by the same basis functions. Hence, the rate of strain tensor $\mathbf{D}$ and the vorticity tensor $\boldsymbol{\varpi}$ should be expressed in terms of $\mathbf{L}$.

$$\mathbf{D} = \frac{\mathbf{L} + \mathbf{L}^{\mathrm{T}}}{2}; \qquad \boldsymbol{\varpi} = \frac{\mathbf{L} - \mathbf{L}^{\mathrm{T}}}{2} \tag{2.12}$$

In incompressible flows, the velocity gradient should be traceless i.e. $\boldsymbol{\nabla} \cdot \mathbf{v} = \mathrm{tr}(\boldsymbol{\nabla}\mathbf{v}) = 0$, but the approximated velocity field computed with the finite element method is not exactly divergence free. Pasquali and Scriven [2002] suggested that inaccurate computations of $(\boldsymbol{\nabla} \cdot \mathbf{v})$ and hence, $\mathrm{tr}\mathbf{L}$ can lead to a larger error in the computations of conformation tensor and thus, the following equation should be used for the interpolated velocity gradient,

$$\mathbf{0} = \mathbf{L} - \boldsymbol{\nabla}\mathbf{v} + \frac{1}{\mathrm{tr}\mathbf{I}} \left(\boldsymbol{\nabla}\mathbf{v}\right)\mathbf{I} \tag{2.13}$$

This equation ensures that $\mathrm{tr}\mathbf{L}$ remains zero everywhere in the flow regardless of the value of $(\boldsymbol{\nabla} \cdot \mathbf{v})$. For two dimensional flow computations carried out in this work $\mathrm{tr}\,\mathbf{I} = 2$.

## 2.2 Finite Element Formulation of The Problem

The finite element method is used for spatial discretization of the system of equations. The DEVSS-TG (Discrete Elastic Viscous Stress Split) finite element formulation [Pasquali and Scriven, 2002] which is based upon the successive variations of EVSS (Elastic Viscous Stress Split) [Rajagopalan et al., 1990] DEVSS (Discrete Elastic Viscous Stress Split) [Guénette et al., 1992] and DEVSS-G (Discrete Elastic Viscous Stress Split with interpolated velocity gradient) [Guénette and Fortin, 1995] is used. The conformation tensor equation is solved using the SUPG (Streamline Upwind Patrov-Galerkin) finite element formulation. In DEVSS-TG formulation an additional equation for the traceless velocity gradient $\mathbf{L}$ is added to the set of equations and also a stabilization term is added to the momentum equation [Pasquali and Scriven, 2002]. The viscous stress term in equation 2.17 is rewritten as:

$$\boldsymbol{\sigma} = \eta_{\mathrm{s}} \left( \mathbf{L} + \mathbf{L}^{\mathrm{T}} \right) + \eta_{\mathrm{a}} \left( \nabla \mathbf{v} + \nabla \mathbf{v}^{\mathrm{T}} - \mathbf{L} - \mathbf{L}^{\mathrm{T}} \right) \tag{2.14}$$

where $\eta_{\mathrm{a}}$ is a numerical parameter. Pasquali and Scriven [2002] have shown that changing the value of $\eta_{\mathrm{a}}$ has no effect on the solution of the problem as long as $\eta_{\mathrm{a}} \equiv \eta_{\mathrm{s}} + \eta_{\mathrm{p,0}}$ where $\eta_{\mathrm{p,0}}$ is the polymer contribution to the zero shear rate viscosity. The finite element formulation of the governing equations is discussed below.

## 2.2.1 Weighted Residual Form of Governing Equations

The coupled set of transport equations for mass, momentum, interpolated velocity gradient and conformation tensor along with the mesh equations is:

$$\mathbf{0} = \boldsymbol{\nabla} \cdot \tilde{\mathbf{D}} \cdot \boldsymbol{\nabla} \boldsymbol{\xi} \tag{2.15}$$

$$0 = \boldsymbol{\nabla} \cdot \mathbf{v} \tag{2.16}$$

$$\mathbf{0} = \rho \left( \frac{\partial \mathbf{v}}{\partial t} + \mathbf{v} \cdot \boldsymbol{\nabla} \mathbf{v} \right) - \boldsymbol{\nabla} \cdot \mathbf{T} - \boldsymbol{\Theta} \tag{2.17}$$

$$\mathbf{0} = \mathbf{L} - \boldsymbol{\nabla} \mathbf{v} + \frac{1}{\mathbf{TrI}} \left( \boldsymbol{\nabla} \mathbf{v} \right) \mathbf{I} \tag{2.18}$$

$$\mathbf{0} = \frac{\partial \mathbf{M}}{\partial t} + \mathbf{v} \cdot \nabla \mathbf{M} - 2\xi \frac{\mathbf{D} : \mathbf{M}}{\mathbf{I} : \mathbf{M}} \mathbf{M} - \chi(\mathbf{M} \cdot \mathbf{D} + \mathbf{D} \cdot \mathbf{M} - 2\frac{\mathbf{D} : \mathbf{M}}{\mathbf{I} : \mathbf{M}} \mathbf{M})$$
$$- \mathbf{M} \cdot \boldsymbol{\varpi} - \boldsymbol{\varpi}^{\mathrm{T}} \cdot \mathbf{M} + \frac{1}{\lambda} (g_0 \mathbf{I} + g_1 \mathbf{M} + g_2 \mathbf{M}^2) \tag{2.19}$$

The weighted residual form of above set of equations is obtained by multiplying the governing equations with appropriate weighting functions and then integrating over the flow domain, as follows:

$$\mathbf{R}^{\mathbf{x},\alpha} = \int_{\Omega} \psi_{\mathbf{x}}^{\alpha} (\boldsymbol{\nabla} \cdot \tilde{\mathbf{D}} \boldsymbol{\nabla} \xi) \, d\Omega \tag{2.20}$$

$$\mathbf{R}^{c,\alpha} = \int_{\Omega} \psi_{c}^{\alpha} (\boldsymbol{\nabla} \cdot \mathbf{v}) \, d\Omega \tag{2.21}$$

$$\mathbf{R}^{\mathbf{m},\alpha} = \int_{\Omega} \psi_{\mathbf{m}}^{\alpha} \left[ \rho \left( \frac{\partial \mathbf{v}}{\partial t} + \mathbf{v} \cdot \boldsymbol{\nabla} \mathbf{v} \right) - \boldsymbol{\nabla} \cdot \mathbf{T} - \boldsymbol{\Theta} \right] d\Omega \tag{2.22}$$

$$\mathbf{R}^{\mathbf{L},\alpha} = \int_{\Omega} \psi_{\mathbf{L}}^{\alpha} \left[ \mathbf{L} - \boldsymbol{\nabla} \mathbf{v} + \frac{1}{\mathbf{TrI}} \left( \boldsymbol{\nabla} \mathbf{v} \right) \mathbf{I} \right] d\Omega \tag{2.23}$$

$$\mathbf{R}^{\mathbf{M},\alpha} = \int_{\Omega} \psi_{\mathbf{M}}^{\alpha} \left[ \frac{\partial \mathbf{M}}{\partial t} + \mathbf{v} \cdot \nabla \mathbf{M} - 2\xi \frac{\mathbf{D} : \mathbf{M}}{\mathbf{I} : \mathbf{M}} \mathbf{M} - \chi \left( \mathbf{M} \cdot \mathbf{D} + \mathbf{D} \cdot \mathbf{M} - 2\frac{\mathbf{D} : \mathbf{M}}{\mathbf{I} : \mathbf{M}} \mathbf{M} \right) \right] d\Omega$$
$$- \int_{\Omega} \psi_{\mathbf{M}}^{\alpha} \left[ \mathbf{M} \cdot \boldsymbol{\varpi} + \boldsymbol{\varpi}^{\mathrm{T}} \cdot \mathbf{M} - \frac{1}{\lambda} (g_0 \mathbf{I} + g_1 \mathbf{M} + g_2 \mathbf{M}^2) \right] d\Omega \tag{2.24}$$

where $\Omega$ is the unknown physical domain, $\psi_{\mathbf{x}}^{\alpha} .... \psi_{\mathbf{M}}^{\alpha}$ are the weighting functions with subscript denoting the relevant independent variable and superscript $\alpha$ varies from 1 to the number of independent weighting functions to be chosen for a particular equation.

The higher order derivatives in Eqs. (2.20) and (2.22) can be lowered by one

Table 2.1: Basis functions and weighting functions used for various field variables and governing equations

| Field Variables | Basis Functions | Weighting Functions |
|:---:|:---:|:---:|
| $\mathbf{x}$ | $\psi_{\mathbf{x}}$: Quadratic | $\phi_{\mathbf{x}} = \psi_{\mathbf{x}}$ (Mesh Equation) |
| $\mathbf{v}$ | $\psi_{\mathbf{v}}$: Quadratic | $\phi_{\mathbf{m}} = \psi_{\mathbf{v}}$ (Momentum Equation) |
| $p$ | $\psi_p$: Linear Discontinuous | $\phi_c = \psi_p$ (Continuity Equation) |
| $\mathbf{L}$ | $\psi_{\mathbf{L}}$: Linear Continuous | $\phi_{\mathbf{L}} = \psi_{\mathbf{L}}$ (Velocity Gradient Equation) |
| $\mathbf{M}$ | $\psi_{\mathbf{M}}$: Linear Continuous | $\phi_{\mathbf{M}} = \psi_{\mathbf{M}}$ (Conformation Tensor Equation) |

order using the divergence theorem as below

$$\mathbf{R}^{\mathbf{x},\alpha} = \int_{\Gamma} (\mathbf{n} \cdot \tilde{\mathbf{D}} \cdot \boldsymbol{\nabla}\boldsymbol{\xi})\psi_{\mathbf{x}}^{\alpha}\, d\Gamma - \int_{\Omega} (\boldsymbol{\nabla}\psi_{\mathbf{x}}^{\alpha} \cdot \tilde{\mathbf{D}} \cdot \boldsymbol{\nabla}\boldsymbol{\xi})\, d\Omega \tag{2.25}$$

$$\mathbf{R}^{\mathbf{m},\alpha} = \int_{\Omega} \psi_{\mathbf{m}}^{\alpha}\rho \left( \frac{\partial \mathbf{v}}{\partial t} + \mathbf{v} \cdot \boldsymbol{\nabla}\mathbf{v} \right) d\Omega + \int_{\Omega} \boldsymbol{\nabla}\psi_{\mathbf{m}}^{\alpha} \cdot \mathbf{T}\, d\Omega \quad - \int_{\Gamma} \psi_{\mathbf{m}}^{\alpha}(\mathbf{n} \cdot \mathbf{T})\, d\Gamma \tag{2.26}$$

where $\Gamma$ is the boundary of the physical domain and $\mathbf{n}$ is the outward pointing normal to the boundary.

Each independent variable in Eqs. (2.20)-(2.24) is represented by finite element basis functions as: $\boldsymbol{\Phi} = \sum_{\beta} \Phi^{\beta}\varphi^{\beta}$, where $\boldsymbol{\Phi}$ is a vector, dyad or scalar [$\mathbf{v}$, $p$, $\mathbf{x}$, $\mathbf{L}$, $\mathbf{M}$], $\varphi^{\beta}$ are the basis functions $\left[ \varphi_{\mathbf{v}}^{\beta}, \varphi_{p}^{\beta}, \varphi_{\mathbf{x}}^{\beta}, \varphi_{\mathbf{L}}^{\beta}, \varphi_{\mathbf{M}}^{\beta} \right]$ and $\Phi^{\beta}$ are the unknown coefficients $\left[ \mathbf{v}^{\beta}, p^{\beta}, \mathbf{x}^{\beta}, \mathbf{L}^{\beta}, \mathbf{M}^{\beta} \right]$. $\beta$ is a dummy index ranging from 1 to the number of basis functions for various variables.

The basis functions used to represent the variables and the weighting functions used in the residual equations are listed in Table 2.1. The particular choice of the basis functions for the velocity, velocity gradient and conformation tensor listed in Table 2.1 have been widely used in the finite element literature and have been shown to satisfy compatibility conditions [Babuska, 1971; Brezzi, 1974; Szady et al., 1995].

## 2.3  Boundary Conditions

In order to complete the mathematical formulation of viscoelastic free surface flows, appropriate boundary conditions must be specified. Here, we discuss the general boundary conditions for free surface flows. For the two dimensional free surface flow considered in this work, Eqs. (2.1), (2.2), (2.4), and (2.10) form a set of 9 scalar equations in 9 unknowns. Boundary conditions on momentum and mesh equations [Eqs. (2.2),(2.10)] are specified on all boundaries due to the elliptic nature of these equations. However, as the conformation tensor equation is hyperbolic in nature; it is required that the boundary condition is applied only at the inflow boundary where $\mathbf{n} \cdot \mathbf{v} < 0$. The boundary conditions on transport and mesh equations are discussed below.

### 2.3.1  Boundary Conditions on Transport Equations:

In the finite element method, boundary conditions are classified in two different ways as essential boundary conditions or as natural boundary conditions. The essential boundary condition is imposed by replacing the governing equation at the boundary with the boundary condition. The essential boundary condition can be applied either in a strong sense (field variables are replaced with the prescribed value of the field variable at the boundary) or in a weak sense (the boundary condition is applied in the weighted residual form). Natural boundary conditions are imposed on the additional boundary terms of the governing equations in its integral form. In the present work,

1. A no slip boundary condition is applied at the solid walls: $\mathbf{v} = \mathbf{v}_w$. This condition is applied by replacing the momentum residual (i.e., as an essential boundary condition).

2. The force balance at the free surface is imposed as a boundary condition on the momentum equation through the following traction boundary condition:

$$\mathbf{n} \cdot \mathbf{T} = -p_a \, \mathbf{n} + \varsigma \, \mathbf{n} \left( \boldsymbol{\nabla}_{\shortparallel} \cdot \mathbf{n} \right) \qquad (2.27)$$

where $\boldsymbol{\nabla}_{\shortparallel}$ denotes the surface divergence operator and is defined as $\boldsymbol{\nabla}_{\shortparallel} =$

$(\mathbf{I} - \mathbf{nn}) \cdot \boldsymbol{\nabla}$ [Slattery, 1990]. This boundary condition is discussed and derived in Appendix A. $p_a$ is the ambient pressure in the gas phase and $\varsigma$ is the surface tension. $\mathbf{n}$ is the unit vector normal to the free surface. The tangential component of Eq. (2.27) is the vanishing shear stress, at the free surface $\mathbf{t}\,\mathbf{n}$ : $\mathbf{T} = 0$ because the shear stress exerted by gas on the liquid is negligible; and the normal component of Eq. (2.27) is the traction inside the liquid which must balance the sum of the pressure in the gas and the capillary pressure induced by the curvature of the free surface. This boundary condition is applied naturally through the boundary integration of the traction term $(\mathbf{n} \cdot \mathbf{T})$ in the momentum equation.

As the normal vector $\mathbf{n}$ is discontinuous on the free surface, Eq. (2.27) can not be inserted directly in its present form into the traction term of the momentum equation. Ruschak [1985] proposed that the term $\mathbf{n}\,(\boldsymbol{\nabla}_{\shortparallel} \cdot \mathbf{n})$, which is measure of the inverse of the radius of curvature, can be replaced by $d\mathbf{t}/ds$, where $d\mathbf{t}/ds$ is the surface derivative of the local tangent vector with $s$ as the arc length along the boundary. Hence, the boundary condition in Eq. (2.27) can be rewritten as

$$\mathbf{n} \cdot \mathbf{T} = -p_a\,\mathbf{n} + \varsigma \frac{d\mathbf{t}}{ds} \tag{2.28}$$

As a result, the traction boundary condition imposed through the weighted residual integral of the traction $\mathbf{n} \cdot \mathbf{T}$ at a boundary $\Gamma$ is as follows:

$$\begin{aligned}
\int_\Gamma \psi_{\mathbf{m}}^\alpha \,(\mathbf{n} \cdot \mathbf{T})\, d\Gamma &= \int_\Gamma \psi_{\mathbf{m}}^\alpha (-p_a\,\mathbf{n} + \varsigma \frac{d\mathbf{t}}{ds}) d\Gamma \\
&= -\int_\Gamma (p_a \psi_{\mathbf{m}}^\alpha \mathbf{n} + \varsigma \frac{d\psi_{\mathbf{m}}^\alpha}{ds}) d\Gamma + \varsigma \psi_{\mathbf{m}}^\alpha \mathbf{t}|_{s_1}^{s_2}
\end{aligned} \tag{2.29}$$

where $s_1$ and $s_2$ are the start and the end point of boundary, and $\psi_{\mathbf{m}}^\alpha$ is the weighting functions of the momentum equation.

3. The flow rate at the inflow boundary is imposed by specifying a velocity profile $\mathbf{v} = f(\mathbf{x})$. This boundary condition is imposed by replacing components of the momentum equation with the prescribed velocity field.

4. The fully developed flow condition $\mathbf{n} \cdot \boldsymbol{\nabla}\mathbf{v} = \mathbf{0}$ at the outflow boundary is

imposed naturally as:

$$\int_\Gamma (\mathbf{n} \cdot \boldsymbol{\nabla} \mathbf{v}) \, \psi_\mathbf{v} \, d\Gamma = \mathbf{0} \tag{2.30}$$

5. The conformation transport equation [Eq. (2.4)] is a hyperbolic equation and the boundary condition on this equation is imposed weakly only at the inflow boundary. In fully developed flow, the polymer conformation does not change along a streamline [Pasquali and Scriven, 2002; Xie and Pasquali, 2004] and thus,

$$\mathbf{v} \cdot \boldsymbol{\nabla} \mathbf{M} = \mathbf{0} \tag{2.31}$$

holds at the inflow boundary. More detailed discussion on the boundary condition for conformation tensor based models can be found in [Pasquali and Scriven, 2002; Xie and Pasquali, 2004].

For steady state flow computations in this work, Eq. (2.33) is substituted in Eq. (2.4) and hence, the following algebraic equation holds at the inflow boundary

$$
\begin{aligned}
\mathbf{0} \;=\; & -2\xi \frac{\mathbf{D} : \mathbf{M}}{\mathbf{I} : \mathbf{M}} \mathbf{M} - \zeta (\mathbf{M} \cdot \mathbf{D} + \mathbf{D} \cdot \mathbf{M} - 2\frac{\mathbf{D} : \mathbf{M}}{\mathbf{I} : \mathbf{M}} \mathbf{M}) \\
& - \mathbf{M} \cdot \mathbf{W} - \mathbf{W}^\mathrm{T} \cdot \mathbf{M} + \frac{1}{\lambda}(g_0 \mathbf{I} + g_1 \mathbf{M} + g_2 \mathbf{M}^2)
\end{aligned}
\tag{2.32}
$$

Eq. (2.4) is replaced by Eq. (2.32) at the inflow boundary (i.e. applied essentially in strong sense). However, for unsteady state flow computations Eq. (2.33) is applied essentially in a weak sense:

$$\int_\Gamma (\mathbf{v} \cdot \boldsymbol{\nabla} \mathbf{M}) \, \psi_\mathbf{M} \, d\Gamma = \mathbf{0} \tag{2.33}$$

## 2.3.2 Boundary Conditions on Mesh Equations

The following boundary conditions are used to solve the mesh equation [Eq. (2.10)]:

1. At the fixed boundaries, positions are fixed at the initial values i.e., $\mathbf{x} = \mathbf{x_0}$. This boundary condition is applied essentially by replacing the mesh residual with fixed nodal positions. The location of nodes on the boundary is fixed at the inflow and on the two solid walls.

2. At the free surface, the kinematic boundary condition

$$\mathbf{n} \cdot \left( \mathbf{v} - \overset{\circ}{\mathbf{x}} \right) = 0 \tag{2.34}$$

   is applied essentially in the weak form as:

$$\int_{\Gamma} \mathbf{n} \cdot \left( \mathbf{v} - \overset{\circ}{\mathbf{x}} \right) \psi_{\mathbf{x}}^{\alpha} \, d\Gamma = \mathbf{0} \tag{2.35}$$

3. The nodes are distributed on the boundary of the physical domain according to a stretching function that controls the spacing of the nodes.

It is important to note that the same boundary conditions must be applied at the boundaries between subregions of the computational domain. Appropriate boundary conditions must be imposed at the contact line at which the free surface meets the solid wall. In this work we fixed the position of the static contact line. More details on mesh boundary conditions for elliptic mesh equations can be found in Pasquali [2000].

## 2.4   Dimensionless Numbers

Dimensional analysis of the system of equations suggests that it is convenient to introduce four dimensionless numbers, which are the combinations of the various macroscopic model parameters $\rho$, $\eta_{\mathrm{s}}$, $\varsigma$, $\eta_{\mathrm{p,0}}$, $\lambda$ etc. These dimensionless numbers are:

1. The Reynolds number $Re = \rho v L / (\eta_{\mathrm{s}} + \eta_{\mathrm{p,0}})$ where $v$ is the characteristic velocity, $L$ is the characteristic length of the problem and $\eta_{\mathrm{p,0}}$ is the zero shear rate solvent viscosity. The Reynolds numbers represents the ratio between inertial and viscous forces.

2. The Capillary number $Ca = (\eta_{\mathrm{s}} + \eta_{\mathrm{p,0}}) v / \varsigma$. The Capillary numbers measures the relative importance of viscous to the surface forces.

3. The viscosity ratio $\beta = \eta_{\mathrm{s}} / (\eta_{\mathrm{s}} + \eta_{\mathrm{p,0}})$. $\beta$ is the ratio of the polymer contribution to the total viscosity of the solution.

4. The Weissenberg number $Wi = \lambda v/L$, where $\lambda$ is the characteristic relaxation time of polymer. $Wi$ is the ratio of characteristic time scale of polymer to the characteristic time scale of the flow. A more detailed discussion on $Wi$ defined in terms of the microscopic properties of the polymer molecules is presented in the next chapter.

5. The Elastocapillary number $Ec = Wi/Ca = \lambda\varsigma/(\eta_{\rm s}+\eta_{\rm p,0})L$. The Elastocapillary number is a ratio of elastic and surface forces.

All simulations are preformed at $Re = 0$, by choosing $\rho = 0$ and at a dimensionless flow rate less then 0.33, for which a recirculation region is always present in the flow domain [Pasquali and Scriven, 2002]. The dimensionless numbers that are varied in this work are $Ca$, $\beta$, $Wi$ and $Ec$.

## 2.5 Computational/Physical Domain Mapping

As the physical domain is unknown *a priori*, the weighted residual integrals, Eqs. (2.20)-(2.24) are first mapped from the unknown physical domain ($\Omega$) to the known computational domain ($\Omega_0$) as follows:

$$\mathbf{R}^{\mathbf{x},\alpha} = -\int_{\Omega_0} (\boldsymbol{\nabla}\psi_{\mathbf{x}}^{\alpha} \cdot \tilde{\mathbf{D}} \cdot \boldsymbol{\nabla}\boldsymbol{\xi}) f d\Omega_0 + \int_{\Gamma_0} (\mathbf{n} \cdot \tilde{\mathbf{D}} \cdot \boldsymbol{\nabla}\boldsymbol{\xi}) \psi_{\mathbf{x}}^{\alpha} l d\Gamma_0 \tag{2.36}$$

$$\mathbf{R}^{c,\alpha} = \int_{\Omega_0} \psi_c^{\alpha} (\boldsymbol{\nabla} \cdot \mathbf{v}) f d\Omega_0 \tag{2.37}$$

$$\mathbf{R}^{\mathbf{m},\alpha} = \int_{\Omega_0} \psi_{\mathbf{m}}^{\alpha} \rho \left(\frac{\partial \mathbf{v}}{\partial t} + \mathbf{v} \cdot \boldsymbol{\nabla}\mathbf{v}\right) f d\Omega_0 + \int_{\Omega} (\boldsymbol{\nabla}\psi_{\mathbf{m}}^{\alpha} \cdot \mathbf{T}) f d\Omega_0 - \int_{\Gamma_0} \psi_{\mathbf{m}}^{\alpha} (\mathbf{n} \cdot \mathbf{T}) l d\Gamma_0 \tag{2.38}$$

$$\mathbf{R}^{\mathbf{L},\alpha} = \int_{\Omega_0} \psi_{\mathbf{L}}^{\alpha} \left[\mathbf{L} - \boldsymbol{\nabla}\mathbf{v} + \frac{1}{\mathbf{TrI}}\ (\boldsymbol{\nabla}\mathbf{v})\,\mathbf{I}\right] f d\Omega_0 \tag{2.39}$$

$$\mathbf{R}^{\mathbf{M},\alpha} = \int_{\Omega_0} \psi_{\mathbf{M}}^{\alpha} \left[\frac{\partial \mathbf{M}}{\partial t} + \mathbf{v} \cdot \nabla \mathbf{M} - 2\xi\frac{\mathbf{D} : \mathbf{M}}{\mathbf{I} : \mathbf{M}}\mathbf{M} - \chi\left(\mathbf{M} \cdot \mathbf{D} + \mathbf{D} \cdot \mathbf{M} - 2\frac{\mathbf{D} : \mathbf{M}}{\mathbf{I} : \mathbf{M}}\mathbf{M}\right)\right] f d\Omega_0$$
$$- \int_{\Omega} \psi_{\mathbf{M}}^{\alpha} \left[\mathbf{M} \cdot \boldsymbol{\varpi} + \boldsymbol{\varpi}^{\mathrm{T}} \cdot \mathbf{M} - \frac{1}{\lambda}(g_0 \mathbf{I} + g_1 \mathbf{M} + g_2 \mathbf{M}^2)\right] f d\Omega_0 \tag{2.40}$$

where $f$ (the Jacobian of the mapping) and $l$ represent the change in area and length respectively.

$$f = \frac{d\Omega}{d\Omega_0} = \det \mathbf{F} \tag{2.41}$$

$$l = \frac{d\Gamma}{d\Gamma_0} = f\sqrt{\mathbf{n}^0 \cdot \mathbf{K}^{\mathrm{T}} \cdot \mathbf{K} \cdot \mathbf{n}^0} \tag{2.42}$$

Here, $\mathbf{F}$ is the mapping deformation gradient defined as,

$$\mathbf{F} \equiv \lhd \mathbf{x} \equiv \frac{\partial \mathbf{x}}{\partial \boldsymbol{\xi}} \tag{2.43}$$

$\lhd$ denotes a gradient in the computational domain. $\mathbf{K}$ is the inverse of the mapping deformation gradient, $\mathbf{K} = \mathbf{F}^{-1}$ and the relation between gradients in the physical and computational domain is,

$$\boldsymbol{\nabla}\boldsymbol{\Phi} = \mathbf{K} \cdot \lhd \boldsymbol{\Phi} \tag{2.44}$$

$\mathbf{n}^0$ in Eq. 2.42 is the unit normal pointing outwards from the computational domain. It can be shown that the unit normal ($\mathbf{n}$) and unit tangent vector ($\mathbf{t}$) in the physical domain are related to the unit normal ($\mathbf{n}^0$) and unit tangent vector ($\mathbf{t}^0$) in computational domain as,

$$\mathbf{n} = \frac{f}{l}(\mathbf{K} \cdot \mathbf{n}^0); \quad \mathbf{t} = \mathbf{t}^0 \cdot \mathbf{F} \tag{2.45}$$

For more details on the mapping from the physical to the computational domain, see Pasquali [2000].

## 2.6 Time Integration of Governing Equation

The DEVSS-TG/SUPG spatial discretization results in a large set of differential-algebraic equations, $\mathbf{f}(t, \boldsymbol{\Phi}, \dot{\boldsymbol{\Phi}}) = \mathbf{0}$, for the vector of time dependent unknowns $\boldsymbol{\Phi} = [\mathbf{v}, p, \mathbf{x}, \mathbf{L}, \mathbf{M}]$. A fully implicit predictor-corrector scheme is used for time integration [Gresho et al., 1979]. A first order forward Euler predictor with first order backward Euler corrector step is used for the first few time steps to ensure time

smoothing [Luskin and Rannacher, 1982]. Subsequently, a second order Adams -
Bashforth predictor with second order trapezoidal rule corrector is used [Gresho
et al., 1979]. The algorithm for the time dependent scheme is

    IF (TimeIter<NEXPLICIT)

- Predictor Step: Forward Euler Scheme

$$\mathbf{\Phi}_{n+1} = \mathbf{\Phi}_n + \dot{\mathbf{\Phi}}_n \, \Delta t \tag{2.46}$$

- Corrector Step: Backward Euler Scheme

$$\dot{\mathbf{\Phi}}_{n+1} = \frac{1}{\Delta t} \left( \mathbf{\Phi}_{n+1} - \mathbf{\Phi}_n \right) \tag{2.47}$$

    ELSE

- Predictor Step: Second Order Adam - Bashforth

$$\mathbf{\Phi}_{n+1} = \mathbf{\Phi}_n + \frac{\Delta t}{2} \left[ 3\dot{\mathbf{\Phi}}_n - \dot{\mathbf{\Phi}}_{n-1} \right] \tag{2.48}$$

- Corrector Step: Second Order Trapezodial

$$\dot{\mathbf{\Phi}}_{n+1} = \frac{2}{\Delta t} \left( \mathbf{\Phi}_{n+1} - \mathbf{\Phi}_n \right) - \dot{\mathbf{\Phi}}_n \tag{2.49}$$

The fully coupled algorithm to solve the time dependent flow problem is illus-
trated in Fig 3.1. The simulation starts with given initial conditions for the field
variables. The time derivatives of field variables are assumed to be zero initially. At
the predictor step of the simulation, only field variables are updated according to
the numerical integration schemes listed above. However, the time derivatives are
not updated at the predictor step. At the corrector step, first the time derivatives
are updated using the predicted values of the field variables and then a fully implicit
scheme is used to solve the set of non-linear equations. The predicted values of field
variables and the corrected values of the time derivatives of field variables are used
as the initial guess for Newton's method. The set of coupled nonlinear equations are

solved using a frontal solver algorithm with Newton's method and analytical Jacobian at each time step [Pasquali and Scriven, 2002]. During the course of Newton's iteration, the time derivatives are also updated based on the updated field variables.

For steady state simulations the strategy to choose the initial guess for Newton's method will be discussed shortly.

## 2.7  Solution of Problem with Newton's Method

The system of non-linear Eqs. (2.36) - (2.40) is solved with the Newton's method at each time step. Thus, the weighted residual form ($\mathbf{R} = [\mathbf{R^{x,\alpha}}, \mathbf{R}^{c,\alpha}, \mathbf{R^{m,\alpha}}, \mathbf{R^{L,\alpha}}, \mathbf{R^{M,\alpha}}]$) of the equations and the Jacobian matrix ($\mathbf{J}$) are required for solving

$$\mathbf{J}\delta\mathbf{u} = -\mathbf{R} \tag{2.50}$$

where $\delta\mathbf{u} = \mathbf{u} - \mathbf{u}_0$ with $\mathbf{u}$ denoting the solution vector ($\mathbf{u} = [\mathbf{v}, p, \mathbf{x}, \mathbf{L}, \mathbf{M}]$) at the current Newton iteration and $\mathbf{u}_0$ denoting the solution vector at the previous Newton iteration. The Jacobian matrix ($\mathbf{J}$) is obtained by differentiating Eqs. (2.36) - (2.40) with respect to the various field variables, $\mathbf{J} = \dfrac{\partial \mathbf{R}}{\partial \mathbf{u}}$. The residual vector and Jacobian matrix is assembled and the linear system of equations is solved by a frontal solver [DE Almeida, 1995; Duff et al., 1989; Pasquali, 2000]. The tolerance on the 2 - norm of the Newton update and the residual were both set to $10^{-6}$ as the convergence criterion for Newton's method.

Pasquali [2000] has developed a general framework to analytically derive the Jacobian entries for viscoelastic flows. Pasquali [2000] provides the analytical Jacobian entries for steady free surface flows and hence it will not be discussed here. However, following the results of Pasquali [2000], derivatives of time dependent terms in Eqs. (2.22) and (2.24) with respect to the various fields variables are discussed in Appendix B. Note that the time dependent terms are in Eqs. (2.22) and (2.24) updated according to the Eq. (2.11).

Initialize the field variables
and time derivatives of field
Variables ($\mathbf{u}, \partial \mathbf{u} / \partial t$)

Predictor Step: Update $\mathbf{u}$

Corrector Step: Update $\partial \mathbf{u} / \partial t$

Initial guess for
Newton's method

Solve the set of governing
equations using the predicted
values of $\mathbf{u}$ and corrected
values of $\partial \mathbf{u} / \partial t$

$\mathbf{u}$ and $\partial \mathbf{u} / \partial t$ both are updated

Convergence criterion for
Newton's method satisfied

Time Integration Loop

Newton's Loop

NO

YES

Convergence criterion for
steady state satisfied

NO

YES

Exit

Figure 2.1: Time integration and Newton's algorithm to solve a set of non-linear differential-algebraic equations.

## 2.8 Initialization of Newton's Method for Steady State Flow Simulations

The Newton's method to solve a non-linear set of equations requires a good initial guess of the independent variables. The initial guess, i.e. the guessed values of the free surface location, velocity profile, pressure, velocity gradient and conformation tensor, should be close to the actual solution of the problem.

The strategy used here to generate a good initial guess for the Newton's method is the same as the strategy used by Pasquali [2000]. The initial shape of the free surface is approximated by a combination of straight lines and curves. The intertialess Newtonian flow (Eqs. 2.1 & 2.2 with $\boldsymbol{\sigma} = \mathbf{0}$) is first computed by treating the free surface as a perfectly slippery wall by imposing $\mathbf{n} \cdot \mathbf{v} = 0$ and $\mathbf{nt} : \mathbf{T} = 0$ on the free boundary. The initial guess for velocity and pressure is used as: $\mathbf{v}, p = 0$. The solution of this problem is used as the initial guess to solve the non-linear set of equations for Newtonian free surface flows.

The interpolated velocity gradient $\mathbf{L}$, Eq. 2.13, is then solved by fixing the position of the free surface, velocity and pressure. The Newton's method converges in two iterations as the equation for $\mathbf{L}$ is a linear equation.

The conformation tensor equation (Eq. 2.4) is then solved for a very small value of $Wi$ ($Wi \sim 0.01$) by fixing the position, velocity, pressure and the interpolated velocity gradient. The initial guess for conformation tensor is set to be $\mathbf{M} = \mathbf{I}$. The values of field variables computed so far are for an ultra-dilute polymer solution ($\beta = 1$) where there is no coupling between the momentum equation and the polymer conformation. The solution of the conformation tensor equation provides a very robust initial guess for a fully coupled free surface flow problem of dilute polymer solutions ($\beta < 1$).

The first order arc-length continuation method is used to compute the solution of the problem at different values of parameters [Pasquali and Scriven, 2002]. The step-size of the continuation algorithm depends upon the number of Newton's iterations required to get a convergent solution at the previous continuation step, failure of convergence, whether or not the mesh remained unfolded at the previous step, and whether or not the conformation tensor remained positive definite everywhere in the flow domain at the previous step.

## 2.9   Conclusion

In this chapter a computational method is described to solve 2-D viscoelastic time dependent free surface flows. A conformation tensor based formulation is presented to evaluate viscoelastic stresses. The governing equations and boundary conditions for both the flow field and mesh are presented and explained. The finite element method is applied and its corresponding formulations are presented. The Newton's method is applied to solve the non-linear equations. The residuals and analytical Jacobian matrix have also discussed in this chapter.

# Chapter 3

# Viscoelastic Free Surface Flow Modeling Using the Micro-Macro Approach

This chapter summarizes the micro-macro approach to solve viscoelastic free surface flows. The set of governing equations for a dumbbell model with a linear and non-linear spring force with hydrodynamic interactions is presented. A novel computational algorithm is discussed to compute complex flows with non-linear microscopic constitutive models.

In chapter 2, we discussed an approach to solve viscoelastic flows within the framework of a macroscopic description of the fluid. The macroscopic approach of modeling viscoelastic flows complements the set of governing equations (continuity and momentum equations) with a closed-form equation for the viscoelastic stress, relating either stress or the conformation tensor to the deformation history. In many flow situations, this approach provides a good qualitative understanding of various flow phenomena. However, a closed-form representation of the behavior of polymer molecules in solution is not sufficient to predict quantitative agreement with experiments even in simple homogeneous flows, such as shear and extensional flow. Therefore, it is necessary to use more sophisticated models capable of providing reliable predictions of various important flow phenomena such as, shear thinning, extensional hardening, universal properties and scaling laws [Bird et al., 1987a,b; Öttinger, 1996]

by understanding the interaction between flow and the flow induced microstructure. A recent review by Keunings [2001] on modeling of polymer solutions, described a number of levels, such as quantum mechanics, atomistic modeling, kinetic theory and continuum mechanics, that can be used for the description of fluid. However, the level of sophistication used is primarily governed by its analytical and computational tractability (numerical technique and computational resources). While the use of a quantum level description is out-of-question due to the requirements of excessive computational resources, atomistic modeling (molecular dynamics simulation) has been used to some extent to predict rheological properties in simple flows. However, the intense computational requirement makes such techniques, at least for another decade, inappropriate for complex flow simulations.

A kinetic theory based fluid description, although significantly more expensive than a macroscopic description of the fluid provides a good alternative to closed-form constitutive models for large scale simulation of viscoelastic flow. There are a number of ways in which a polymer can be represented within the framework of kinetic theory, providing a description of the polymer conformation (e.g., stretch and orientation) based on coarse-grained micro-mechanical molecular models. These micro-mechanical molecular models form a natural hierarchy in terms of the level of sophistication (e.g., bead-rod → bead-spring → dumbbell model) [Bird et al., 1987b; Öttinger, 1996]. Such models can incorporate important physics such as the finite extensibility of the polymer molecules and the presence of solvent mediated interactions such as hydrodynamic (HI) and excluded volume (EV) interactions between parts of the polymer chain. The incorporation of these effects is necessary to explain experimentally observed features such as shear thinning and bounded extensional viscosity in homogeneous flows of dilute polymer solutions [Bird et al., 1987a,b; Doyle and Shaqfeh, 1998; Hsieh et al., 2003; Kumar and Prakash, 2003; Öttinger, 1989; Prabhakar and Prakash, 2002, 2004; Prakash, 2002; Schäfer, 1999; Zylka and Öttinger, 1991]. In particular, inclusion of HI is shown to be extremely important in explaining various experimentally observed scaling laws, universal behavior of polymer solutions transport coefficients (e.g., diffusivity) [Cifre and De la Torre, 1999; DE Gennes, 1979; Hsieh et al., 2003; Knudsen et al., 1996; Larson et al., 1999, 1997; Magda et al., 1988; Öttinger, 1987; Prabhakar, 2005; Sunthar and Prakash, 2005].

Although the bead-rod and bead-spring models (for number of beads $\gtrsim 10$) are assumed to be accurate representations in capturing the behavior of real polymer molecules in solution, their application to solve complex flows is still beyond available computational resources. A dumbbell representation of a polymer molecule, although it does not accurately predict quantitative features, can be used to qualitatively investigate the effect of various non-linear phenomena for which no closed-form constitutive equation can be derived. A dumbbell consists of two Brownian beads with a friction coefficient $\zeta$. Kinetic theory allows one to write the so-called diffusion or Fokker-Plank equation, which is a partial differential equation in the probability density function describing the probability of finding a dumbbell with a given configuration. The solution of Fokker-Plank equation namely, the probability density function, can be used to evaluate macroscopic properties of interest such as the elastic stress. However, the Fokker-Plank equation is analytically intractable for non-linear dumbbells. An alternative technique called Brownian dynamics simulation or stochastic simulation is widely used to solve for the configuration of dumbbells without even solving for the probability density function which can then be subsequently used to evaluate elastic stress and other macroscopic properties.

Although the solution of kinetic theory based models via a so called Brownian dynamics simulation is known from quite sometime and has been explored successfully (specially in homogeneous flows) to predict various experimentally observed rheological properties, its application to solve complex viscoelastic flows has been somewhat limited. The idea of using stochastic simulations in solving complex viscoelastic flow was pioneered by Laso and Ottinger [1993]. The original work by Laso and Ottinger [1993], termed CONNFFESSIT (Calculation of Non-Newtonian Flow: Finite Elements and Stochastic Simulation Technique), combines the finite element solution of macroscopic flow equations with stochastic simulations to compute elastic stress. As the CONNFFESSIT approach combines the idea of description of microstructure of polymer molecule with the macroscopic description of flow, this type of simulation technique is called a micro-macro approach. This approach avoids the need for a closed-form constitutive model and hence, can be used for models for which no closed-form equation exist (e.g., FENE dumbbells, dumbbells with HI and

EV effects). CONNFFESSIT has been used extensively in literature to simulate viscoelastic flows [Cormenz et al., 2002; Feigl et al., 1995; Laso and Ottinger, 1993; Laso et al., 1997, 2004]. The major problem with CONNFFESSIT is that a large number of particles must be tracked as they move in the flow field which is CPU intensive and cumbersome. Apart from particle tracking, a feature of the CONNFFESSIT scheme (also of most other schemes involving stochastic simulation) is the presence of temporal and spatial fluctuations in computed velocity and stress fields. While the temporal fluctuations arises from the statistical error in calculating ensemble averages using a finite number of dumbbells, spatial fluctuations arise due to the divergence of the non-smooth stress field in the momentum equation. The temporal fluctuations can be controlled by increasing the number of dumbbells which in turn lead to an increase in the computational cost. Spatial fluctuations can be completely eliminated by using more advanced micro-macro schemes such as the Lagrangian particle method (LPM) by Halin et al. [1998] and Brownian Configuration Fields (BCF) method proposed by Hulsen et al. [1997].

While the LPM avoids the spatial fluctuations using correlated local ensembles, particle tracking still remains a problem. The problems of both particle tracking and spatial fluctuations are circumvented in the Brownian configuration fields method which also provides an efficient variance reduction in terms of temporal fluctuations. In the BCF approach, an ensemble of continuous configuration fields replaces the discrete particles. Each configuration field is subjected to the same Brownian force throughout the flow domain and hence, provides a smooth spatial representation of configuration fields. Another advantage of the BCF method over CONNFFESSIT and LPM is that the ensemble size is the same at each point of the flow domain even for locally very refined meshes. However, with CONNFFESSIT and LPM, it is difficult to work with locally refined meshes as smaller elements might end up without any dumbbell in them. The BCF method has been successfully applied to solve confined viscoelastic flows [Hu et al., 2005; Hulsen et al., 1997; Somasi and Khomami, 2000].

A micro-macro approach based on combining the BCF method with a Galerkin finite element method, using elliptic mesh generation equations coupled with time - dependent conservation equations, is used in this work to solve 2-D viscoelastic

free surface flows. Although, BCF based microscopic constitutive equations and Brownian dynamics simulations are well known and widely used in literature, they are briefly reviewed here.

## 3.1  Governing Equations

In this section we briefly review the basic equations required to describe the rheological behavior of dilute polymer solutions based on kinetic theory. Restricting ourself to the dumbbell representation of polymer molecules, a dumbbell has two Brownian beads connected with a massless spring. The massless spring takes into account entropic effects which describe the resistance of the polymer molecule to stretching. The bead friction coefficient, $\zeta$, is taken to be a constant and it is related to the Stokesian drag force as $\zeta = 6\pi\eta_{\text{s}}a$ for spherical beads with radius $a$ in a solvent with viscosity $\eta_{\text{s}}$. In kinetic theory based models, the solvent is considered to be Newtonian and treated as a continuum. The polymer solution consists of $n_p$ dumbbells per unit volume suspended in a sea of Newtonian solvent. In dilute polymer solutions, polymer molecules or dumbbells are assumed not to have any explicit interactions and therefore, all the intermolecular interactions are excluded from the model formulation.

In homogeneous flows (i.e., the velocity gradient is independent of spatial positions), the configurational state, stretch and orientation, of a dumbbell are specified by the dumbbell connector vector $\mathbf{Q}$ ($\mathbf{Q} = \mathbf{r}_2 - \mathbf{r}_1$) with $\mathbf{r}_1$ and $\mathbf{r}_2$ being the spatial position vectors of two beads. Using kinetic theory, it can be shown that the configurational probability distribution function, $P(\mathbf{Q}, t)$, of a dumbbell obeys the following Fokker-Planck or diffusion equation [Bird et al., 1987b]:

$$\frac{\partial P}{\partial t} = -\frac{\partial}{\partial \mathbf{Q}} \cdot \left\{ \boldsymbol{\nabla}\mathbf{v}^{\text{T}} \cdot \mathbf{Q} - \frac{2}{\zeta}\mathbf{A} \cdot \frac{\partial U}{\partial \mathbf{Q}} \right\} P + \frac{2k_{\text{B}}T}{\zeta}\frac{\partial}{\partial \mathbf{Q}} \cdot \mathbf{A} \cdot \frac{\partial P}{\partial \mathbf{Q}} \qquad (3.1)$$

where $T$ is the temperature of the solution and $k_B$ the Boltzmann's constant. Equation (3.1) describe the way in which the probability distribution function changes in time because of the change in the configuration of a polymer molecule by an imposed homogeneous flow field, the intramolecular potential and by the thermal

fluctuations in the solvent.

The dimensionless tensor $\mathbf{A}$ in the above equation is the diffusion tensor which is related to the hydrodynamic interaction tensor $\mathbf{\Omega}$ as

$$\mathbf{A} = \mathbf{I} - \zeta\mathbf{\Omega} \tag{3.2}$$

The hydrodynamic interaction tensor accounts for the change in the solvent flow field at one bead resulting from the movement of the other bead. The form of $\mathbf{\Omega}$ will be discussed in more detail shortly.

The intermolecular potential energy $U$ is the sum of the spring potential accounting for the polymer chain connectivity, and other local non-hydrodynamic intramolecular interactions such as excluded volume. In this work we have neglected excluded volume interactions and have only considered different spring potentials, which are related to the spring force $\mathbf{F}^s$ by

$$\mathbf{F}^s = -\frac{\partial U}{\partial \mathbf{Q}} \tag{3.3}$$

Three different spring force laws, all having the same following form, are used in this work.

$$\mathbf{F}^s = \Lambda\mathbf{Q} \tag{3.4}$$

For the Hookean dumbbell model, representing an infinitely extensible polymer molecule with the spring force varying linearly with molecular extension, $\Lambda = H$; for the FENE-P dumbbell model, representing a finitely extensible polymer molecule with the spring force varying linearly with molecular extension, $\Lambda = H/(1 - \langle Q^2 \rangle/Q_0^2)$; and for the non-linear FENE dumbbell model, representing a finitely extensible polymer molecule with the spring force varying non-linearly with molecular extension, $\Lambda = H/(1 - Q^2/Q_0^2)$. Where, H is the spring constant, $Q_0$ is the maximum extensibility (contour length) of the spring and $\langle Q^2 \rangle$ is the end-to-end distance of the dumbbell averaged over all the configurations of the dumbbell. The angular brackets denote an ensemble average with respect to the configurational probability distribution function, i.e.,

$$\langle \mathbf{g} \rangle = \int P\mathbf{g}\, d^3\mathbf{Q} \tag{3.5}$$

where **g** is any physical quantity.

The FENE spring force captures the essential features of the more accurate force law namely, the inverse Langevin expression [Bird et al., 1987b]. The singular behavior of the non-linearity of the FENE force as $Q = |\mathbf{Q}| \to Q_0$ causes the force to diverge which ensures that the spring is not stretched beyond its maximum contour length $Q_0$. It is well known that the parameters in force laws (H, $Q_0$) used in this work are related to the more fundamental properties of polymer molecules such as the number of Kuhn segments and the Kuhn length [Bird et al., 1987b; Prabhakar, 2005]. As $Q_0 \to \infty$, both the FENE and FENE-P spring force law expressions reduce to the Hookean force law.

In this work, a regularized form of the Oseen-Burgers tensor proposed by Zylka and Öttinger [1989] is used as the HI tensor. The original form of the Oseen-Burgers tensor [Bird et al., 1987a] has a singularity at $\mathbf{Q} = 0$. As a result of this singularity, the diffusion tensor **A** looses its positive definiteness for small values of **Q** [Öttinger, 1996]. Regularization of the Oseen-Burger tensor removes this singularity and ensures the positive definitiness of **A** for any value of **Q**. An important motivation in using this particular form of the Oseen-Burgers tensor is that the square root of **A** (which is used in Brownian dynamics simulations) can be obtained analytically.

The functional form of the regularized Oseen-Burgers tensor $\mathbf{\Omega}$ is given by:

$$\mathbf{\Omega}\left(\mathbf{Q}\right) = \frac{3\sqrt{3}\omega}{8\chi Q\left(Q^2 + \omega^2\right)^3} \left(M\,\mathbf{I} + N\,\frac{\mathbf{QQ}}{Q^2}\right) \tag{3.6}$$

where $\omega = 2h^*\sqrt{\pi kT/3H}$, and,

$$\begin{aligned} M &= Q^6 + \frac{7}{2}\omega^2 Q^4 + \frac{9}{2}\omega^4 Q^2 \\ N &= Q^6 + \frac{3}{2}\omega^2 Q^4 - \frac{3}{2}\omega^4 Q^2 \end{aligned} \tag{3.7}$$

Here, $h^*$ is the hydrodynamic interaction parameter defined as:

$$h^* = \frac{\zeta}{\eta_s}\sqrt{\frac{H}{36\pi^3 k_B T}} \tag{3.8}$$

To be consistent with the length scale used to normalize the conformation tensor,

$\sqrt{R_{\mathrm{e}}^2/3}$ is used here as the length scale for the dumbbell connector vector $\mathbf{Q}$, where $R_{\mathrm{e}}^2 = \langle Q^2 \rangle_{\mathrm{eqm}}/3$ with $\langle Q^2 \rangle_{\mathrm{eqm}}$ representing the ensemble average of the end-to-end distance of a polymer molecule at equilibrium. With the choice of $\sqrt{R_{\mathrm{e}}^2/3}$ as the length scale, the FENE parameter $b$ is $b = 3Q_0^2/R_{\mathrm{e}}^2$. In all our simulations we set $R_{\mathrm{e}}^2/3 = 1$ and hence $b = Q_0^2$.

Note that the definition of the FENE parameter used in this work is different from the one based on the length scale $\sqrt{k_B T/H}$ defined by Bird et al. [1987b]. The relation between three different $b$ parameters ($b, b_{\mathbf{M}}$ and $b_{\mathrm{bird}}$) is:

$$b = 3\, b_{\mathbf{M}}\,; \quad b = b_{\mathrm{bird}} + 5 \tag{3.9}$$

Once the configurational distribution function $P$ (the solution of the Fokker-Plank equation) is known, the polymer contribution to the stress $\sigma$, which is a macroscopic property, can be calculated using the Kramers expression [Bird et al., 1987b]:

$$\boldsymbol{\sigma} = -n_p k_{\mathrm{B}} T \mathbf{I} + n_p \langle \mathbf{Q}\, \mathbf{F}^{\mathrm{s}} \rangle \tag{3.10}$$

the angular brackets denote a ensemble average with respect to the configurational distribution function.

## 3.2 Brownian Dynamics Simulation and Micro-Macro Approach

The previous section has summarized the key features of the dumbbell model of dilute polymer simulations incorporating FENE and HI. It was shown in the previous section that the macroscopic properties of interest, such as the stress tensor, are related only to the expectations (averaged quantities) of the dumbbell configurations. Although, in principle the expectation values can be calculated once the probability distribution function is known, the use of a non-linear spring force and a configuration dependent hydrodynamic interaction tensor makes Eq. (3.1) analytically unsolvable and therefore, closed form equations for expectation values are unavailable. Equation (3.1) can be solved numerically to obtain the configurational distribution function but it is not practically viable to solve Eq. (3.1) because it

requires numerical integration over six dimensional space for a dumbbell model. In most of the cases, it is not actually required to solve Eq. (3.1) explicitly for $P$. Brownian dynamics simulation (BDS) provides an alternative approach to calculate the expectation values without actually evaluating the probability density function.

BDS is based on a formal procedure of writing a stochastic differential equation which is equivalent to the Fokker-Plank equation. Öttinger [1996] has extensively reviewed the relationship between a Fokker-Planck equation and its equivalent stochastic differential equation. The stochastic differential equation equivalent to Eq. (3.1) can be written as [Öttinger, 1996]:

$$dQ = \left[ \boldsymbol{\nabla} \mathbf{v}^{\mathrm{T}} \cdot \mathbf{Q} - \frac{2}{\zeta} \mathbf{A} \cdot \mathbf{F}^{\mathrm{s}} \right] dt + \sqrt{\frac{4k_{\mathrm{B}}T}{\zeta}} \left( \mathbf{B} \cdot d\mathbf{W} \right) \qquad (3.11)$$

where $\mathbf{W}$ is a time-uncorrelated Brownian force (Wiener process) which accounts for the random displacement of the beads due to thermal motion. $\mathbf{W}$ is a three dimensional vector whose components are three independent Wiener processes.

The components of the tensor $\mathbf{B}(\mathbf{Q})$, which corresponds to the diffusion term in Eq. (3.1), are chosen such that they satisfy

$$\mathbf{B} \cdot \mathbf{B}^{\mathrm{T}} = \mathbf{A} \qquad (3.12)$$

The equation above calculates the components $\mathbf{B}$ once the components of $\mathbf{A}$ are known. To obtain the components of $\mathbf{B}$, a scheme proposed by Öttinger [1996] is implemented. This scheme, which has been successfully used by Prabhakar and Prakash [2002] for simulating Hookean dumbbells with HI and EV, relies on a specific form of the HI tensor, and avoids matrix inversion and other matrix manipulations in order to evaluate the components of $\mathbf{B}$. It can be seen from Eqs. (3.2) and (3.6) that the tensor $\mathbf{A}$ has the form $g(\mathbf{Q}) \mathbf{I} + \tilde{g}(\mathbf{Q}) \, \mathbf{Q}\mathbf{Q}/Q^2$. Therefore, the tensor $\mathbf{B}$, assuming $\mathbf{B}$ is symmetric, can be chosen to be [Öttinger, 1996]

$$\mathbf{B}(\mathbf{Q}) = \sqrt{g(\mathbf{Q})} \, \mathbf{I} + \left( \sqrt{g(\mathbf{Q}) + \tilde{g}(\mathbf{Q})} - \sqrt{g(\mathbf{Q})} \right) \frac{\mathbf{Q}\mathbf{Q}}{Q^2} \qquad (3.13)$$

Evaluation of $\mathbf{B}$ completes Eq. (3.11) and BDS can be performed.

In BDS, Eq. (3.11) is integrated numerically (there exist no analytical solutions

of stochastic differential equations for non-linear models) to calculate the dumbbell configurations at discrete times. Because of the stochastic nature of Eq. (3.11), a large number of discrete dumbbells (also known as trajectories) are required to be convected in flow in order to reduce the error (stochastic variance) on averaged quantities. Once the configurations are known, the stress tensor is obtained by taking an ensemble average over all different trajectories. In the case of homogeneous flows, various trajectories are subjected to the same hydrodynamic force. However, they differ in terms of the random Brownian force acting on them.

The estimation of the ensemble average of any property, $f$, is accomplished by calculating the arithmetic mean of $f$ across all $N_\mathrm{T}$ trajectories:

$$\langle f \rangle = \frac{1}{N_\mathrm{T}} \sum_{j=1}^{N_\mathrm{T}} f_j \tag{3.14}$$

where $f_j$ is the property of interest for the $j$-th trajectory at any time $t$. The standard error in the estimate of the ensemble average of any property is calculated by $\sqrt{\mathrm{Var}(f)/N_T}$ where $\mathrm{Var}(f)$ is the variance of $f$ [Öttinger, 1996].

To solve complex viscoelastic flows using stochastic simulations, various micro-macro schemes have been developed in literature [Halin et al., 1998; Hulsen et al., 1997; Laso and Ottinger, 1993]. The first such micro-macro scheme, the CONNFFESSIT approach, combines the finite element solution of macroscopic flow equations with stochastic simulations to compute the elastic stress [Laso and Ottinger, 1993]. CONNFFESSIT uses Eqs. (3.10) and (3.11) to evaluate the polymer contribution to stress by convecting a large number of discrete particles with flow. However, as mentioned above, the BCF approach circumvents the problems associated with the CONNFFESSIT method. In the BCF method, instead of discrete particles an ensemble of continuous configuration fields is convected with the flow and the (Lagrangian) stochastic ordinary differential Eq. (3.11) is converted into the (Eulerian) stochastic partial differential equation [Hulsen et al., 1997] as:

$$d\mathbf{Q} = \left[ -\mathbf{v} \cdot \nabla \mathbf{Q}(\mathbf{x}, t) + \boldsymbol{\nabla} \mathbf{v}^\mathrm{T} \cdot \mathbf{Q} - \frac{2}{\zeta} \mathbf{A} \cdot \mathbf{F}^\mathrm{s} \right] dt + \sqrt{\frac{4 k_\mathrm{B} T}{\zeta}} (\mathbf{B} \cdot d\mathbf{W}) \tag{3.15}$$

Eq. (3.15) is very similar to the equation for the evolution of the connector vector

of a single dumbbell. The additional first term on the right-hand side of Eq. (3.15) accounts for the convection of the configuration field by flow. Here, $\mathbf{W}$ is a time-uncorrelated but *spatially homogeneous* Brownian force which makes the spatial gradients of configuration fields well defined throughout the flow domain. The expression for stress calculation remains as Eq. (3.10).

## 3.3   Boundary Condition

The stochastic differential equation used in the CONNFFESSIT algorithm is an ordinary differential equation and therefore, only an initial condition on dumbbell configuration is sufficient to solve Eq. (3.11). However, the configuration fields equation is hyperbolic in nature and hence, a boundary condition on configuration fields must be imposed at the inflow boundary where $\mathbf{n} \cdot \mathbf{v} < 0$. As the configurations of fields are not known in general, the inflow configuration profile depends upon the type of spring force and the presence or absence of hydrodynamic interactions for a given inflow velocity profile. In literature, most of the non-homogeneous viscoelastic flow calculations using the BCF method [Hu et al., 2005; Hulsen et al., 1997] are carried out either by imposing periodic boundary conditions or by calculating the configuration fields for a given velocity field (typically a linear or parabolic flow profile). Here, we propose a new way of imposing the inflow boundary condition on the BCF equation by assuming that the entry length is long enough to have a fully developed flow at the inlet boundary of the slot coater. Due to the fully developed flow between two parallel plates (Couette-Poiseuille flow in the slot coating die), the velocity and the velocity gradient do not change along streamlines. As a results, the evolution of configuration fields $\mathbf{Q}$ along the streamlines is independent of the flow field. The spatially correlated fields ensure that the gradient of $\mathbf{Q}$ remains zero i.e.,

$$\mathbf{v} \cdot \nabla \mathbf{Q} = \mathbf{0} \tag{3.16}$$

must hold at the inflow boundary. Equation (3.16) is independent of the microscopic constitutive model and initial condition on configuration fields. This boundary condition has the same form as the boundary condition on conformation tensor discussed

in chapter 2. This boundary condition is applied weakly as a vector boundary condition by replacing the configuration fields residual at the inflow boundary. Although the boundary condition itself is independent of spring force or other potentials such as EV, imposition of the boundary condition depends upon the numerical method used to solve the configuration field equation.

## 3.4  Dimensionless Numbers

The various dimensional numbers used in this work for micro-macro computations are identical to those for the macroscopic case defined in chapter 2. Except for $Wi$, all dimensionless numbers are functions of macroscopic properties. $Wi$ is a function of a microscopic property, namely, the relaxation time of the polymer ($\lambda_\eta$). The definition of $\lambda_\eta$ used in this work is based on the zero shear rate viscosity.

In micro-macro simulations $\lambda_\eta$ is related to microscopic parameters, such H, $\zeta$, $h^*$ etc, with a relationship that depends on the particular microscopic model. In order to compare results of different models at identical values of $Wi$, it becomes important, consequently, to choose appropriate values for these microscopic parameters. The scheme used here to determine these parameters is discussed in detail in Appendix C.

## 3.5  Computational Method

Most of the numerical methods used in literature, to solve viscoelastic flow problems using the micro-macro approach, decouple the solution of macroscopic flow equations from the solution of the stochastic differential equation to evaluate the polymer contribution to stress. The decoupled micro-macro algorithm proceeds as follows:

- Using the initial or given field's configurations (i.e. for a known elastic stress), a finite element solution of the macroscopic flow equations (mesh, continuity, momentum etc.) is computed using a standard finite element method by treating the elastic stress term as a fixed source term in the momentum equation.

- The computed field variables (velocity, pressure, mesh etc.) are then used to

compute updated configurations of Brownian fields as in BCF, or the configurations of dumbbells as in CONNFFESSIT by integrating the stochastic differential equation for fixed flow kinematics.

- The polymer stress is then evaluated using Kramer's expression in each element.

These 3 steps are carried out until a desired convergence is obtained. The decoupled scheme used in this work is shown schematically in Fig. (3.1). In the BCF based micro-macro approach, the Galerkin finite element method is used to spatially discretize the mesh, continuity and momentum equations together with the SUPG [Brooks and Hughes, 1982] formulation of the BCF equation [Somasi and Khomami, 2000]. The linear continuous basis functions ($\varphi_\mathbf{Q}$) for configuration fields and the SUPG finite element weighting function with $\psi_\mathbf{Q} \equiv \varphi_\mathbf{Q} + h^u \mathbf{v} \cdot \nabla \varphi_\mathbf{Q}$ are used to solve Eq. (3.24) where $h^u$ is the upwind parameter [Brooks and Hughes, 1982]. It is worth mentioning that the interpolated velocity gradient equation is not solved in the micro-macro formulation.

The set of governing equations in the micro-macro formulation is:

$$\mathbf{0} = \nabla \cdot \tilde{\mathbf{D}} \cdot \nabla \boldsymbol{\xi} \tag{3.17}$$

$$0 = \nabla \cdot \mathbf{v} \tag{3.18}$$

$$\mathbf{0} = \rho \left( \frac{\partial \mathbf{v}}{\partial t} + \mathbf{v} \cdot \nabla \mathbf{v} \right) - \nabla \cdot \mathbf{T} - \boldsymbol{\Theta} \tag{3.19}$$

$$\mathbf{0} = d\mathbf{Q} - \left[ -\mathbf{v} \cdot \nabla \mathbf{Q} + \nabla \mathbf{v}^\mathrm{T} \cdot \mathbf{Q} - \frac{2}{\zeta} \mathbf{A} \cdot \mathbf{F}^\mathrm{s} \right] dt - \sqrt{\frac{4k_\mathrm{B}T}{\zeta}} (\mathbf{B} \cdot d\mathbf{W}) \tag{3.20}$$

The numerical method used to solve the macroscopic flow equations have been discussed in chapter 2 and hence, will not be repeated here.

Two different time integration schemes, namely, a fully implicit time integration scheme for linear dumbbell models without hydrodynamic interactions and a semi-implicit time integration scheme for non-linear dumbbell models (FENE) or linear dumbbells with hydrodynamic interactions, are used to integrate the BCF equation. These two schemes are discussed below.
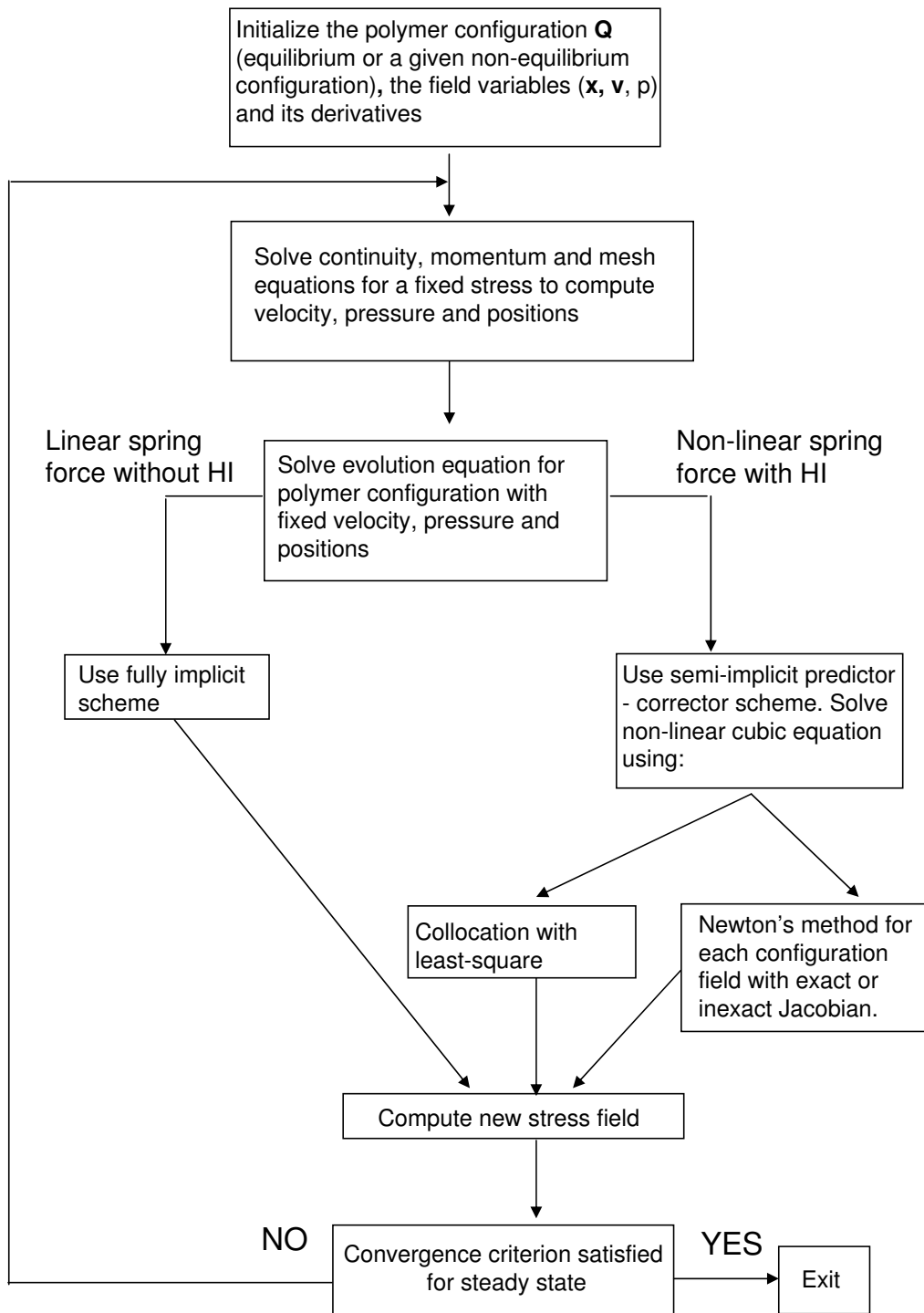
Figure 3.1: Algorithm of Micro-Macro Scheme.

### 3.5.1 Fully Implicit Scheme: Linear Spring Force Without Hydrodynamic Interactions

Micro-macro computations for various viscoelastic flow calculations using a fully explicit scheme to integrate the stochastic differential equation have been extensively used in literature [Cormenz et al., 2002; Feigl et al., 1995; Hu et al., 2005; Hulsen et al., 1997; Laso and Ottinger, 1993; Laso et al., 1997]. The exceptions are work the by Laso et al. [2004] within the CONNEFFSSIT framework and by Somasi et al. [2002] for homogeneous flows within the BCF framework. Both Laso et al. [2004] and Somasi et al. [2002] have used an implicit formulation. Use of an explicit scheme requires a small time step size in-order to have a stable numerical time integration algorithm making micro-macro schemes computationally inefficient. In this work, we use a fully implicit scheme by taking advantage of the fact that the BCF equation is linear in configuration fields for a linear spring force. The fully implicit scheme used here is as follows:

For the linear spring force without hydrodynamic interactions (i.e., with the diffusion tensor replaced with a unit tensor, $\mathbf{A} = \mathbf{B} = \boldsymbol{\delta}$) Eq. (3.15) can be rewritten as:

$$d\mathbf{Q} = \left( -\mathbf{v} \cdot \nabla \mathbf{Q} + \nabla \mathbf{v}^{\mathrm{T}} \cdot \mathbf{Q} - \frac{2\,\Lambda}{\zeta}\,\mathbf{Q} \right) dt + \sqrt{\frac{4k_{\mathrm{B}}T}{\zeta}} d\mathbf{W} \qquad (3.21)$$

where, as mentioned previously, $\Lambda = H$ for Hookean dumbbells and $\Lambda = H/(1 - \langle Q^2 \rangle / Q_0^2)$ for FENE-P dumbbells. Equation (3.21) can be discretized temporally using an implicit Euler scheme as:

$$\mathbf{Q}_{n+1} = \mathbf{Q}_n + \left( -\mathbf{v}_n \cdot \nabla \mathbf{Q}_{n+1} + \nabla \mathbf{v}_n^{\mathrm{T}} \cdot \mathbf{Q}_{n+1} - \frac{2\,\Lambda_n}{\zeta}\,\mathbf{Q}_{n+1} \right) \Delta t + \sqrt{\frac{4k_{\mathrm{B}}T}{\zeta}} \Delta \mathbf{W}_n$$

$$(3.22)$$

where $n$ is the previous time step and $(n + 1)$ is the current computational time step. By definition, the Wiener process $\mathbf{W}$ is a Gaussian random variable with mean $\langle \Delta \mathbf{W}_n \rangle = 0$ and variance $\langle \Delta \mathbf{W}_n^2 \rangle = \Delta t$ [Öttinger, 1996]. However, as the generation of Gaussian random variables is computationally expensive, non-Gaussian random variables are used to obtain approximate Gaussian random variables by equating the first two moments of the non-Gaussian random variables to those of the Wiener

process.

Eq. (3.22) can be rearranged as:

$$\mathbf{Q}_{n+1} + \left( \mathbf{v}_n \cdot \nabla \mathbf{Q}_{n+1} - \nabla \mathbf{v}_n^{\mathrm{T}} \cdot \mathbf{Q}_{n+1} + \frac{2 \Lambda_n}{\zeta} \mathbf{Q}_{n+1} \right) \Delta t = \mathbf{Q}_n + \sqrt{\frac{4k_{\mathrm{B}}T}{\zeta}} \Delta \mathbf{W}_n \quad (3.23)$$

The finite element method is used to solve Eq. (3.23). The weighted residual form of Eq. (3.23) is

$$\int_\Omega \left[ \mathbf{Q}_{n+1} + \left( \mathbf{v}_n \cdot \nabla \mathbf{Q}_{n+1} - \nabla \mathbf{v}_n^{\mathrm{T}} \cdot \mathbf{Q}_{n+1} + \frac{2 \Lambda_n}{\zeta} \mathbf{Q}_{n+1} \right) \Delta t \right] \psi_{\mathbf{Q}}^\alpha \, d\Omega$$
$$- \int_\Omega \left[ \mathbf{Q}_n + \sqrt{\frac{4k_{\mathrm{B}}T}{\zeta}} \Delta \mathbf{W}_n \right] \psi_{\mathbf{Q}}^\alpha \, d\Omega = \mathbf{0} \quad (3.24)$$

where, $\psi_{\mathbf{Q}}$ is the weighing function for the configuration fields equation. The configuration field $\mathbf{Q}$ can be expanded using finite element basis functions as $\mathbf{Q} = \sum_\beta \mathbf{Q}^\beta \varphi_{\mathbf{Q}}^\beta$ where $\mathbf{Q}^\beta$ represents the basis function coefficients and $\varphi_{\mathbf{Q}}^\beta$ are the basis functions for the configuration field.

Eq. (3.24) is a linear equation in $\mathbf{Q}_{n+1}$ and can be rearranged to obtain the following equation

$$\sum_\beta \mathbf{K}^{\alpha\beta} \mathbf{\Upsilon}_{n+1}^\beta = \mathbf{f}^\alpha \quad (3.25)$$

where the components of the matrix $\mathbf{K}^{\alpha\beta}$ for Hookean dumbbell are

$$\mathbf{K}_{ij}^{\alpha\beta} = \int_\Omega \left[ \varphi_{\mathbf{Q}}^\beta \delta_{ij} + \left\{ (\mathbf{v}_n \cdot \nabla \varphi_{\mathbf{Q}}^\beta) \delta_{ij} - \varphi_{\mathbf{Q}}^\beta (\nabla_j v_i{}^{\mathrm{T}})_n + \frac{2 \varphi_{\mathbf{Q}}^\beta H}{\zeta} \delta_{ij} \right\} \Delta t \right] \psi_{\mathbf{Q}}^\alpha \, d\Omega \quad (3.26)$$

and for FENE-P dumbbell are

$$\mathbf{K}_{ij}^{\alpha\beta} = \int_\Omega \left[ \varphi_{\mathbf{Q}}^\beta \delta_{ij} + \left\{ (\mathbf{v}_n \cdot \nabla \varphi_{\mathbf{Q}}^\beta) \delta_{ij} - \varphi_{\mathbf{Q}}^\beta (\nabla_j v_i{}^{\mathrm{T}})_n + \frac{2 \varphi_{\mathbf{Q}}^\beta H}{\zeta(1 - \langle Q_n^2 \rangle / b)} \delta_{ij} \right\} \Delta t \right] \psi_{\mathbf{Q}}^\alpha \, d\Omega \quad (3.27)$$

$\delta_{ij}$ representing the Kronecker delta. In Eq. (3.25) $\Upsilon^{\beta}_{j,\,\mathrm{n}+1}$ is a vector of the coefficients of configuration fields $\left(Q^{\beta}_{j,\,n+1}\right)$ and

$$\mathbf{f}^{\alpha}_i = \int_{\Omega} \left[ Q_{i,\mathrm{n}} + \sqrt{\frac{4k_{\mathrm{B}}T}{\zeta}} \Delta W_{i,\mathrm{n}} \right] \psi^{\alpha}_{\mathbf{Q}} \, d\Omega \qquad (3.28)$$

Equation (3.25) is assembled to obtain a global set of equations which in matrix vector form can be written as

$$\mathbf{K}\Upsilon_{\mathrm{n}+1} = \mathbf{f} \qquad (3.29)$$

where $\mathbf{K}$, $\Upsilon_{\mathrm{n}+1}$ and $\mathbf{f}$ are the assembled $\mathbf{K}^{\alpha\beta}$, $\Upsilon^{\beta}_{\mathrm{n}+1}$ and $\mathbf{f}^{\alpha}$ matrices respectively. The set of linear Eqs. (3.29) can be solved using LU decomposition of the matrix $\mathbf{K}$ followed by back substitution. It is clear from Eq. (3.26) that for Hookean dumbbells, the matrix $\mathbf{K}$ is independent of the configurations of the dumbbells. However, for FENE-P dumbbells, the matrix $\mathbf{K}$ is a function of the configurations of the dumbbells evaluated at the previous time step [see Eq. (3.27)]. It should be noted that the LU decomposition of the matrix $\mathbf{K}$ is performed at each time step because the mesh changes at each time step and $\mathbf{K}$ depends on the mesh. Equation (3.29) is the global equation set for a single configuration field. However, as the configuration fields are independent of each other, Eq. (3.29) holds for all the fields except that the Brownian force term and $Q_{i,\mathrm{n}}$ in Eq. (3.28) is different for each field.

For linear springs, the boundary condition is implemented by replacing the weighted residual of the configuration field equation, Eq. (3.24), with the weak form of Eq. (3.16).

## 3.5.2 Semi-Implicit Predictor-Corrector Scheme: Non-Linear Spring Force With Hydrodynamic Interactions

This scheme was originally developed by Öttinger [1996] for FENE dumbbells in homogeneous flows and has been recently extended to finitely extensible bead-spring chain models with and without hydrodynamic interactions in homogeneous flows [Hsieh et al., 2003; Prabhakar and Prakash, 2004; Somasi et al., 2002]. The semi-implicit formulation leads to greater stability of the numerical algorithm [Öttinger,

1996; Prabhakar and Prakash, 2004; Somasi et al., 2002] when compared to the explicit Euler scheme, and allows the use of larger time steps, which in turn leads to a reduction in the CPU time required for the microscopic computations. An explicit Euler scheme with a rejection algorithm [Hu et al., 2005; Öttinger, 1996] can also be used for non-linear dumbbell models. However, a large number of these rejections, occurring very frequently at high $Wi$, can significantly alter the true evolution of these dumbbells [Somasi et al., 2002]. Somasi et al. [2002] further demonstrated that for a given accuracy the semi implicit predictor-corrector scheme is three to four times faster than the explicit Euler scheme with a rejection algorithm. Somasi and Khomami [2000] have used the semi-implicit scheme for micro-macro simulations of FENE dumbbells in homogeneous flows. Here, we extend the same scheme to solve inhomogeneous flows of non-linear dumbbells with hydrodynamic interactions.

In the predictor step, the configuration fields are updated explicitly using a forward Euler time integration scheme as:

$$\mathbf{Q}_{n+1}^{*} = \mathbf{Q}_{n} + \left[ -\mathbf{v}_{n} \cdot \nabla \mathbf{Q}_{n} + \nabla \mathbf{v}_{n}^{T} \cdot \mathbf{Q}_{n} - \frac{2}{\zeta} \mathbf{A}_{n} \cdot \mathbf{F}_{n}^{s} \right] \Delta t + \sqrt{\frac{4 k_{B} T}{\zeta}} \left( \mathbf{B}_{n} \cdot \Delta \mathbf{W}_{n} \right)$$

$$(3.30)$$

where $\mathbf{Q}_{n+1}^{*}$ are the predicted configuration fields. Since $\mathbf{Q}_{n}$ is known from the previous time step, components of hydrodynamic interaction tensor $\mathbf{A}_{n}$, diffusion tensor $\mathbf{B}_{n}$, and the force vector $\mathbf{F}_{n}$ can be determined in the above equation. The finite element discretization of Eq. (3.30), by weighting Eq. (3.30) with a weighting function $\psi_{\mathbf{Q}}^{\alpha}$ and then integrating over the whole flow domain results in a set of linear equations. The set of linear equation in matrix vector form can be written as

$$\sum_{\beta} \mathbf{M}^{\alpha\beta} \mathbf{\Upsilon}_{n+1}^{\beta,*} = \mathbf{f}^{\alpha} \tag{3.31}$$

where $\mathbf{M}^{\alpha\beta}$ is the mass matrix

$$\mathbf{M}^{\alpha\beta} = \int_{\Omega} \psi_{\mathbf{Q}}^{\alpha} \, \varphi_{\mathbf{Q}}^{\beta} \boldsymbol{\delta} \, d\Omega \tag{3.32}$$

$\mathbf{\Upsilon}_{n+1}^{\beta,*}$ is a vector of the coefficients of configuration fields basis functions $\left( \mathbf{Q}_{n+1}^{\beta,*} \right)$

and $\mathbf{f}^\alpha$ is

$$
\begin{aligned}
\mathbf{f}^\alpha = &\int_\Omega \left[ \mathbf{Q}_n + \left( -\mathbf{v}_n \cdot \nabla \mathbf{Q}_n + \nabla \mathbf{v}_n^{\mathrm{T}} \cdot \mathbf{Q}_n - \frac{2}{\zeta} \mathbf{A}_n \cdot \mathbf{F}_n^{\mathrm{s}} \right) \Delta t \right] \psi_{\mathbf{Q}}^\alpha \, d\Omega \\
&+ \int_\Omega \sqrt{\frac{4k_{\mathrm{B}}T}{\zeta}} \left( \mathbf{B}_n \cdot \Delta \mathbf{W}_n \right) \psi_{\mathbf{Q}}^\alpha \, d\Omega
\end{aligned}
\tag{3.33}
$$

Equation (3.31) is assembled into a global set of linear equations which is solved using LU decomposition of the global mass matrix performed at each time step. The weighting function and the basis functions used for the configuration fields equation are the same as those used in the fully implicit scheme for linear dumbbell models.

The boundary condition on the configuration fields equation is not imposed while solving Eq. (3.31) because the term $(\mathbf{v} \cdot \nabla \mathbf{Q})$ is treated explicitly. However, a semi-implicit scheme, treating either $(\mathbf{v} \cdot \nabla \mathbf{Q})$ or both $(\mathbf{v} \cdot \nabla \mathbf{Q})$, and $(\nabla \mathbf{v}^{\mathrm{T}} \cdot \mathbf{Q})$ implicitly, can be developed to impose the boundary condition. It should be noted, however, that there is additional computational time required to factorize the mass matrix at the corrector step if the semi-implicit scheme is used. We have used the fully explicit scheme at the predictor step to reduce the computational cost. The slightly inaccurate predicted configuration fields have virtually no effect on the actual solution obtained using the corrected step.

Estimates of configuration fields generated at the predictor step $(\mathbf{Q}_{n+1}^*)$ are used in constructing the following corrector step:

$$
\begin{aligned}
\mathbf{Q}_{n+1} = &\mathbf{Q}_n - \frac{\Delta t}{2} \left( \mathbf{v}_n \cdot \nabla \mathbf{Q}_{n+1}^* + \mathbf{v}_n \cdot \nabla \mathbf{Q}_n \right) + \frac{\Delta t}{2} \left( \nabla \mathbf{v}_n^{\mathrm{T}} \cdot \mathbf{Q}_{n+1}^* + \nabla \mathbf{v}_n^{\mathrm{T}} \cdot \mathbf{Q}_n \right) \\
&- \frac{\Delta t}{\zeta} \mathbf{A}_n \cdot \left( \mathbf{F}_n^S + \mathbf{F}_{n+1}^S \right) + \sqrt{\frac{4k_{\mathrm{B}}T}{\zeta}} \left( \mathbf{B}_n \cdot \Delta \mathbf{W}_n \right)
\end{aligned}
\tag{3.34}
$$

In this equation, the values of the $\mathbf{A}_n$ and $\mathbf{B}_n$ tensors are the same as those used in Eq. (3.30) and hence, treated explicitly. As discussed previously by Öttinger [1996] and Prabhakar and Prakash [2004], the explicit treatment of the diffusion tensor is necessary in order to retain the Îto interpretation of the diffusion term $\mathbf{B} \cdot \Delta \mathbf{W}$. The force term, however, is treated *implicitly*, with the term $\mathbf{F}_{n+1}^{\mathrm{S}}$ being evaluated using the unknown $\mathbf{Q}_{n+1}$. Following the work by Prabhakar and Prakash [2004],

Eq. (3.34) can be simplified further

$$
\mathbf{Q}_{n+1} + \frac{\Delta t}{\zeta}\, \mathbf{F}^{\mathrm{S}}_{n+1} = \mathbf{Q}_n - \frac{\Delta t}{2}\left(\mathbf{v}_n \cdot \nabla \mathbf{Q}^*_{n+1} + \mathbf{v}_n \cdot \nabla \mathbf{Q}_n\right) + \frac{\Delta t}{2}\left(\nabla \mathbf{v}_n^{\mathrm{T}} \cdot \mathbf{Q}^*_{n+1} + \nabla \mathbf{v}_n^{\mathrm{T}} \cdot \mathbf{Q}_n\right)
$$

$$
- \frac{\Delta t}{\zeta}\left(\mathbf{A}_n \cdot \mathbf{F}^{\mathrm{S}}_n\right) + \Delta t\left(\mathbf{\Omega}_n \cdot \mathbf{F}^{\mathrm{S}}_n\right) + \sqrt{\frac{4 k_{\mathrm{B}} T}{\zeta}}(\mathbf{B}_n \cdot \Delta \mathbf{W}_n)
\tag{3.35}
$$

The term $\mathbf{A}_n \cdot \mathbf{F}^{S}_{n+1}$ in Eq. (3.34) has been expanded as

$$
\mathbf{A}_n \cdot \mathbf{F}^{\mathrm{S}}_{n+1} = (\mathbf{I} - \zeta \mathbf{\Omega}_n) \cdot \mathbf{F}^{\mathrm{S}}_{n+1}
\tag{3.36}
$$

$$
= \mathbf{F}^{\mathrm{S}}_{n+1} - \zeta(\mathbf{\Omega}_n \cdot \mathbf{F}^{\mathrm{S}}_{n+1})
\tag{3.37}
$$

to write Eq. (3.35). The first term on the R.H.S. of Eq. (3.37) is transformed to the L.H.S of Eq. (3.34) and treated implicitly. However, the second term in Eq. (3.37) is retained on the R.H.S of Eq. (3.34) and treated explicitly.

For FENE dumbbells, $\mathbf{F}^{\mathrm{S}} = H\mathbf{Q}/(1 - Q^2/Q_0^2)$ can be substituted into the equation above, which can then be rearranged into the following form

$$
\left[1 + \frac{H\,\Delta t}{\zeta\left(1 - Q^2_{n+1}/b\right)}\right]\mathbf{Q}_{n+1} = \mathbf{\Gamma}
\tag{3.38}
$$

where $\mathbf{\Gamma}$ is the R.H.S of Eq (3.35). $\mathbf{\Gamma}$ is a known function of the predicted values of the connector vector and of quantities whose values at the previous time step are known. However, the L.H.S is only a function of the unknown $\mathbf{Q}_{n+1}$. Equation (3.38) can be rearranged to get

$$
\left(1 - \frac{Q^2_{n+1}}{b} + \frac{H\,\Delta t}{\zeta}\right)\mathbf{Q}_{n+1} - \left(1 - \frac{Q^2_{n+1}}{b}\right)\mathbf{\Gamma} = 0
\tag{3.39}
$$

The equation above is a non-linear equation in $\mathbf{Q}_{n+1}$ for each configuration field. Within the frame work of the finite element method, Eq. (3.39) is solved in two distinct ways, as discussed below.

### 3.5.2.1  Newton's Method With a Rejection Algorithm

The finite element discretization of Eq. (3.39) results in a set of non-linear equations for each configuration field which can then be solved with Newton's method. Thus, for each configuration field:

$$\sum_{\beta} \mathbf{J}^{\alpha\beta} \, \Delta \mathbf{\Upsilon}^{\beta}_{n+1} = -\mathbf{R}^{\alpha}_{\mathbf{Q}} \tag{3.40}$$

where $\Delta \mathbf{\Upsilon}^{\beta}_{n+1} = \mathbf{\Upsilon}^{\beta}_{n+1} - \mathbf{\Upsilon}^{\beta}_{0, n+1}$ with $\mathbf{\Upsilon}^{\beta}_{n+1}$ denoting a vector of the coefficients of configuration fields $\left(\mathbf{Q}^{\beta}_{n+1}\right)$ at the current Newton iteration and $\mathbf{\Upsilon}^{\beta}_{0, n+1}$ is a vector of the coefficients of configuration fields $\left(\mathbf{Q}^{\beta}_{0, n+1}\right)$ at the previous Newton iteration. $\mathbf{R}^{\alpha}$ is the residual vector given by

$$\mathbf{R}^{\alpha}_{\mathbf{Q},i} = \int_{\Omega} \left[ \left( 1 - \frac{Q^2_{n+1}}{b} + \frac{H \, \Delta t}{\zeta} \right) Q_{i, n+1} - \left( 1 - \frac{Q^2_{n+1}}{b} \right) \Gamma_i \right] \psi^{\alpha}_{\mathbf{Q}} \, d\Omega \tag{3.41}$$

evaluated using the configuration fields at the previous Newton iteration. The previous time step values of configuration fields are used as the initial guess for Newton's method.

$\mathbf{J}^{\alpha\beta}$ is the Jacobian matrix obtained by differentiating Eq. (3.39) with respect to $\mathbf{Q}^{\beta}_{n+1}$ (see Appendix D for a derivation of the Jacobian matrix). The components of the $\mathbf{J}^{\alpha\beta}$ are

$$\mathbf{J}^{\alpha\beta}_{ij} = \int_{\Omega} \left[ \left( 1 - \frac{Q^2_{n+1}}{b} + \frac{H \, \Delta t}{\zeta} \right) \delta_{ij} - \frac{2}{b} Q_{i, n+1} Q_{j, n+1} + \frac{2}{b} \Gamma_i \, Q_{j, n+1} \right] \psi^{\alpha}_{\mathbf{Q}} \varphi^{\beta}_{\mathbf{Q}} \, d\Omega \tag{3.42}$$

evaluated using the configuration fields at the previous Newton iteration.

Equation (3.40) can be assembled to obtain a global matrix vector equation system. The solution of the resulting set of equations using Newton's method with the exact analytical Jacobian given by Eq. (3.42) can be very expensive for calculations with FENE dumbbells because of the large number of configuration fields and because the Jacobian matrix is a function of the field's configuration. However, an approximate analytical Jacobian can be derived by replacing the FENE force with

the Peterlin approximation (FENE-P), which has the following form:

$$\mathbf{J}_{ij}^{\alpha\beta} = \int_\Omega \left(1 - \frac{\langle Q_n^2 \rangle}{b} + \frac{H\,\Delta t}{\zeta}\right) \psi_{\mathbf{Q}}^\alpha \varphi_{\mathbf{Q}}^\beta \, \delta_{ij}\, d\Omega \tag{3.43}$$

Equation (3.43) can be derived by replacing $Q_{n+1}^2$ in Eq. (3.39) by $\langle Q_n^2 \rangle$ only in the derivation of the Jacobian matrix. Although Eq. (3.43) couples the configurations of all the fields through the term $\langle Q_n^2 \rangle$, note that $\langle Q_n^2 \rangle$ is evaluated at the previous time step; thus, Eq. (3.43) is independent of the configurations of the fields at the current time step and the LU factorization of the Jacobian matrix is done only once per time step for all the fields. Equation (3.43) was used as an approximate Jacobian except for those fields for which the desired convergence ($10^{-5}$) was not achieved in a given number of Newton iterations. For such cases, the exact Jacobian was used. During the course of Newton iterations any field whose magnitude stretched beyond its maximum length ($\sqrt{b}$) for FENE dumbbells, was reset to $0.98\sqrt{b}$.

An alternative Jacobian can also be derived which ensures a fast convergence and thus completely avoids the need for an exact Jacobian. In this work an approximate Jacobian based on an averaged exact Jacobian is used. The approximate Jacobian has the following form:

$$
\begin{aligned}
\mathbf{J}_{\text{approximate}} &\approx \langle \mathbf{J}_{\text{exact}} \rangle \\
&= \int P \mathbf{J}_{\text{exact}}\, d^3\mathbf{Q} \\
&= \int_\Omega \left[ \left( \mathbf{I} - \frac{\text{tr}\mathbf{M}_n}{b} + \frac{H\,\Delta t}{\zeta}\mathbf{I} \right) - \frac{2}{b}\mathbf{M}_n + \frac{2}{b}\langle \mathbf{\Gamma}_n\, \mathbf{Q}_n \rangle \right] \psi_{\mathbf{Q}}^\alpha \varphi_{\mathbf{Q}}^\beta\, d\Omega
\end{aligned} \tag{3.44}
$$

where $\mathbf{M}$ is the conformation tensor. $\mathbf{J}_{\text{approximate}}$ is independent of the unknown configuration of fields and hence required to be factorized only once per time step for all the configuration fields.

The boundary condition on the configuration field equation is imposed by replacing Eq. (3.41) with the week form of Eq. (3.16) at the inflow boundary.

### 3.5.2.2   Least-Squares Collocation method (LSC)

Using the implicit formulation in order to solve for $\mathbf{Q}_{n+1}$ leads to greater stability of the numerical algorithm [Öttinger, 1996], which in turn permits the use of larger times steps leading to a reduction in the CPU-time required for the simulation using the micro-macro approach. Iterative methods for the numerical solution of the nonlinear set of equations for the components of $\mathbf{Q}_{n+1}$, such as Newtons method described above, involve the calculation and inversion of large Jacobian matrices. Somasi et al. [2002] show that the computational overhead from Newton's method can outweigh the gains achieved by the increase in the time-step size. In addition, in the course of the iterations, it is possible that some springs have lengths greater than the maximum stretchable length of the spring, which could lead to unphysical results. Such effects are handled by replacing the unnatural spring lengths obtained during the course of a Newton iteration by values slightly less than maximum stretchable length [Öttinger, 1996]. However, Somasi et al. [2002] and Prabhakar and Prakash [2004] show that these problems are circumvented and considerable gains in computational efficiency over the Newton method can be achieved by using a novel cubic solution based scheme as described below.

Equation (3.38) can be rearranged into a cubic equation for the magnitude of $\mathbf{Q}_{n+1}$.

$$|Q|_{n+1}^3 - |\Gamma||Q|_{n+1}^2 - b\left(1 + \frac{H\,\Delta t}{\zeta}\right)|Q|_{n+1} + |\Gamma|b = 0 \qquad (3.45)$$

where $|Q|_{n+1}$ is the magnitude of $\mathbf{Q}_{n+1}$ and $|\Gamma|$ is the magnitude of $\mathbf{\Gamma}$. Given the values of H, $\zeta$, $b$ and $\Delta t$, the roots of this equation are functions of the parameter $|\Gamma|$. It can be shown that this equation has exactly one root in the domain $(0, \sqrt{b})$ when $0 < |\Gamma| < \infty$, and this root can be obtained analytically using standard formulae for solutions of cubic equations [Öttinger, 1996] or numerically.

In the LSC method, the cubic equation (3.45) is first solved at collocation points, which here coincide with the Gauss integration points. Eq. (3.45) can be solved at these collocation points in each element either analytically or numerically. The collocation point solution is then projected onto the computational nodes using a least-square projection. Details of this scheme are discussed below:

Let the solution of the cubic equation be $|Q|_{n+1} = y$. It can be seen from Eq. 3.38

that the direction of $\mathbf{Q}$ is same as the direction of $\boldsymbol{\Gamma}$, then, at each collocation (Gauss) point:

$$\tilde{\mathbf{Q}}_{n+1} = \left(\frac{\boldsymbol{\Gamma}}{|\boldsymbol{\Gamma}|}\right) y \tag{3.46}$$

The least square projection algorithm is used to evaluate the nodal values of $\mathbf{Q}_{n+1}$ by solving the following equations

$$\int_{\Omega} (\mathbf{Q}_{n+1} - \tilde{\mathbf{Q}}_{n+1}) \psi^{\alpha} d\Omega = 0 \tag{3.47}$$

The finite element discretization of Eq. (3.47) results in a set of linear equations which in matrix vector form can be written as:

$$\sum_{\beta} \mathbf{M}^{\alpha\beta} \boldsymbol{\Upsilon}^{\beta}_{n+1} = \mathbf{f}^{\alpha} \tag{3.48}$$

where $\mathbf{M}^{\alpha\beta}$ is the mass matrix given by (3.32), $\boldsymbol{\Upsilon}^{\beta}_{n+1}$ is the vector of coefficients of the configuration fields and

$$\mathbf{f}^{\alpha} = \int_{\Omega} \tilde{\mathbf{Q}}_{n+1} \psi^{\alpha}_{\mathbf{Q}} \, d\Omega \tag{3.49}$$

which can be evaluated trivially by Gauss quadrature because $\tilde{\mathbf{Q}}_{n+1}$ is known at all Gauss points. Equation (3.48) is assembled to obtain a global set of linear equations which is solved using LU decomposition of the global mass matrix followed by back substitution. The global mass matrix in Eq. (3.48) is the same as the mass matrix evaluated at the predictor step and hence there is no extra computational cost involved in computing and decomposing the mass matrix at the corrector step.

The boundary condition on the configuration field equation is imposed by replacing Eq. (3.47) with the weak form of Eq. (3.16) at the inflow boundary.

For linear dumbbells with hydrodynamic interactions (which is treated explicitly), Eq. (3.35) is linear in the connector vector $\mathbf{Q}_{n+1}$ and can be written as:

$$\mathbf{Q}_{n+1} = \frac{\boldsymbol{\Gamma}}{1 + (\Lambda \, \Delta t / \zeta)} \tag{3.50}$$

where $\boldsymbol{\Gamma}$ is the right hand side of Eq. (3.35) with a linear spring force. It can be

shown analytically that for linear dumbbell models both the Newton's method and the LSC method are identical (see Appendix E). As a result, the latter method can be used to evaluate the nodal values of $\mathbf{Q}_{n+1}$ from Eq. (3.50). The fully implicit scheme discussed earlier is not appropriate for linear dumbbells with hydrodynamic interactions because of the non-linear terms in the hydrodynamic interaction tensor $\boldsymbol{\Omega}$.

Equation 3.50 can be formulated in the form of Eq. (3.48), with

$$\mathbf{f}^{\alpha} = \int_{\Omega} \frac{\boldsymbol{\Gamma}}{1 + (\Lambda\,\Delta t/\zeta)}\,\psi_{\mathbf{Q}}^{\alpha}\,d\Omega \qquad (3.51)$$

The global mass matrix is the same as the mass matrix evaluated at the predictor step.

## 3.6   Conclusion

In this chapter a Brownian configuration fields based micro-macro approach has been formulated to solve viscoelastic free surface flows. A new way of the imposing boundary condition on the BCF equation has been discussed. Within the framework of micro-macro schemes present in literature, we show that it is now possible to include more appropriate molecular models (e.g., FENE and HI) in complex viscoelastic flow simulations although the computational time still remains a challenge. Two novel unconditionally stable time integration schemes to numerically integrate the BCF equation have been presented.

# Chapter 4

# Micro-Macro Code Validation

In this chapter, the micro-macro approach developed in chapter 3 is validated by carrying out simulations for the steady and start-up flow of polymer solutions confined between two parallel plates of infinite length (Couette Flow) and steady flow in a pipe (Poiseuille Flow). The results for various microscopic constitutive equations for both steady and start-up flows are compared with published results for a range of dimensionless parameters for the various cases listed in Table 4.1. In particular,

- the steady state results for homogeneous shear flow (Couette flow) using the micro-macro approach are compared for different $Wi$ with the analytical solution for Hookean dumbbells, the published results of Herrchen and Ottinger [1997] for FENE-P and FENE dumbbells and those of Prabhakar and Prakash [2002] for Hookean dumbbells with HI. Since the simulation results of Prabhakar and Prakash [2002] were reported for only a few shear rates, additional data were generated for the purpose of the present chapter with the same code used by Prabhakar and Prakash [2002]. The conformation tensor based approach has been successfully implemented to solve steady confined flows by Pasquali and Scriven [2002] and hence, results using the macroscopic approach are presented only for unsteady flows.

- the steady state results for Poiseuille flow are compared with results for homogeneous shear flow. In a Poiseuille flow, the shear rate varies with position. In this chapter material functions at various positions with Poiseuille flow, where the shear rates are different, are compared with simulations carried out in a

Table 4.1: The confined flow cases investigated for micro-macro code validation.

| Flow → Solution Method ↓ | Couette Flow | Poiseuille Flow |
|---|---|---|
| Micro-Macro Approach | Steady & Unsteady | Steady |
| Macroscopic Approach | Unsteady | - |
| Homogeneous BDS (Extension of data from Prabhakar and Prakash [2002]) | Steady (Hydrodynamic interactions for ultra-dilute solutions only) | - |

homogeneous Couette flow at the same shear rates. Thus, a single Poiseuille flow simulations corresponds to several Couette flow runs at different $Wi$.

- the results for start-up of Couette flow are presented and compared with the published results of Tomea et al. [2002] for Hookean dumbbells using the micro-macro approach and an Oldroyd-B fluid using the macroscopic approach. The transient results of Tomea et al. [2002] are also used to validate the time integration scheme developed for macroscopic flow equations in chapter 2. The results for FENE-P and non-linear dumbbells are compared with the published results for start-up of Couette flow by Laso and Ottinger [1993].

Homogeneous Couette flows for all the models considered here have been examined previously with BDS algorithms developed specifically for these flows. The algorithms developed here are more versatile since they are applicable to more complex flows. However in this chapter, for the purpose of validation, micro-macro and macroscopic results are presented for simple flows.

## 4.1 Flow Situations and Material Functions

In this section we review the flow situations, boundary conditions and material functions in simple shear flow.

Figs. 4.1 shows the flow geometry and boundary conditions for the Couette [Figs. 4.1(a)] and Poiseuille flow [Figs. 4.1(b)] computations. For steady flow of

$$v_x = U, v_y = 0$$

$$\boldsymbol{\nabla}\mathbf{v} = 0$$

$$\mathbf{v} \cdot \nabla\mathbf{M} = \mathbf{0}$$

$$\boldsymbol{\nabla}\mathbf{v} = 0$$

PSfrag replacements $\mathbf{v} \cdot \nabla\mathbf{Q} = \mathbf{0}$

$$v_x = 0, v_y = 0$$

(a) Couette Flow

$$v_x = 0, v_y = 0$$

$$p = p_0$$

$$\mathbf{v} \cdot \nabla\mathbf{M} = \mathbf{0}$$

$$p = 0$$

PSfrag replacements $\mathbf{v} \cdot \nabla\mathbf{Q} = \mathbf{0}$

$$\mathbf{nt} : \boldsymbol{T} = 0$$
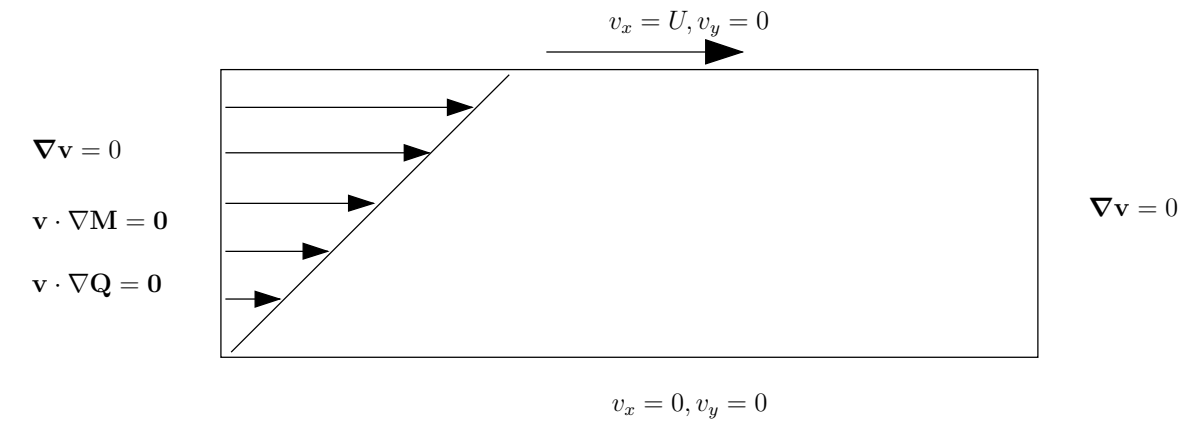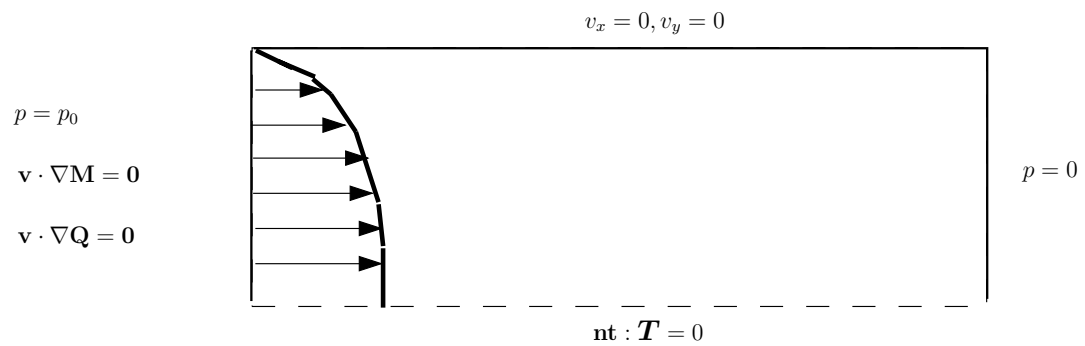
(b) Poiseuille Flow

Figure 4.1: Flow domain and boundary conditions for the Couette and Poiseuille Flow.

ultra-dilute solutions ($\beta = 1$), the conformation tensor and configuration fields equations are decoupled from the macroscopic conservation equations. The steady state velocity profile for a Newtonian liquid, $v_x = U(y/H)$, with $H$ being the distance between two plates, and $v_x = (-\boldsymbol{\nabla}p/2\eta_s L)(1 - y^2)$, with $L$ being the length domain, is used for Couette and Poiseuille flow computations of polymer liquids, respectively. The flow is generated by imposing a constant velocity, $U$, to the top plate in case of Couette flow and by imposing a constant pressure gradient per unit length of $(-\boldsymbol{\nabla}p/L)$ in case of Poiseuille flow.

For the start-up of Couette flow of dilute polymer solutions ($\beta < 1$), the fluid and both the plates are assumed to be at rest for time $t < 0$. In this case, the macroscopic conservation equations are coupled with the constitutive equations for polymer stress. At time $t = 0$, the upper plate starts moving in the x-direction with a constant velocity, $U$. A no-slip boundary condition, $\mathbf{n} \cdot \mathbf{v} = 0$, is imposed on both the plates. The fully developed flow boundary condition, $\mathbf{n} \cdot \boldsymbol{\nabla}\mathbf{v} = 0$, is imposed at inflow and outflow boundaries.

The velocity gradient for these flows has the following form:

$$\boldsymbol{\kappa} = \dot{\gamma}(\mathbf{x}, t) \begin{pmatrix} 0 & 1 & 0 \\ 0 & 0 & 0 \\ 0 & 0 & 0 \end{pmatrix} \tag{4.1}$$

where, $\dot{\gamma}(\mathbf{x}, t)$ is constant with $\dot{\gamma} = U/H$ for steady Couette flow, a function of spatial position, with $\dot{\gamma} = -(-\boldsymbol{\nabla}p/\eta_s L)y$ for Poiseuille flow, and a function of time for the start-up of Couette flow.

For these flows, the polymer contribution to the rheological properties, such as the viscosity, $\eta_{\mathrm{p}}$, and the first normal stress difference coefficient, $\Psi_1$, are given in dimensionless form by the following relations [Bird et al., 1987a]:

$$\eta_{\mathrm{p}}^* = \frac{\eta_{\mathrm{p}}}{nk_{\mathrm{B}}T\lambda_\eta} = -\frac{\sigma_{xy}}{nk_{\mathrm{B}}T\lambda_\eta\dot{\gamma}} \tag{4.2}$$

$$\Psi_1^* = \frac{\Psi_1}{nk_{\mathrm{B}}T\lambda_\eta^2} = -\frac{\sigma_{xx} - \sigma_{yy}}{nk_{\mathrm{B}}T\lambda_\eta^2\dot{\gamma}^2} \tag{4.3}$$

It should be noted that the relaxation time based on zero shear viscosity, $\lambda_\eta$, is

used here to non-dimensionalize various properties as opposed to the conventional use of $\lambda_H$. As the results for steady shear flow by Herrchen and Ottinger [1997] and Prabhakar and Prakash [2002] for FENE-P, FENE and Hookean dumbbells with HI are presented in terms of $\lambda_H$ as the characteristic time, their results are converted in terms of $\lambda_\eta$ using the relations between $\lambda_\eta$ and $\lambda_H$ given Table C.1. For Hookean dumbbells, $\lambda_\eta = \lambda_H$. For dumbbells with HI, the relation between $\lambda_\eta$ and $\lambda_H$ is a function of $h^*$ and cannot be written in a closed-form as in the case of dumbbells without HI. However, the Green-Kubo formula [Diaz et al., 1990; Doi and Edwards, 1986], discussed in Appendix C, is used here to convert results in terms of $\lambda_\eta$.

## 4.2 Steady Couette Flow

In this section, the steady state results for various microscopic constitutive equations are presented.

Fig. 4.2 shows the steady state values of shear viscosity and first normal stress difference coefficient for Hookean dumbbells. A mesh of 200 elements and a total of 4000 configuration fields is used for all the results presented in this chapter. For Hookean dumbbells, the analytical expression for both the shear viscosity and first normal stress are given by [Bird et al., 1987b]:

$$\eta_p^* = \frac{\eta_p}{nk_{\mathrm{B}}T\lambda_\eta} = 1 \tag{4.4}$$

$$\Psi_1^* = \frac{\Psi_1}{nk_{\mathrm{B}}T\lambda_\eta^2} = 2 \tag{4.5}$$

It is evident from Eqs. 4.4 and 4.5 that both the shear viscosity and the first normal stress difference coefficient are independent of shear rate. The micro-macro computations for Hookean dumbbells [see Fig. 4.2] indicate that both $\eta_p^*$ and $\Psi_1^*$ are independent of shear rate.

Figures 4.3 and 4.4 show the shear rate dependent viscosity and first normal stress difference coefficient for FENE-P and FENE models, respectively. The results are plotted for a finite extensibility parameter $b_{\mathbf{M}} = 18.33$ which is equivalent to $b = 50$ used by Herrchen and Ottinger [1997]. The results in both Figures 4.3 and 4.4 show
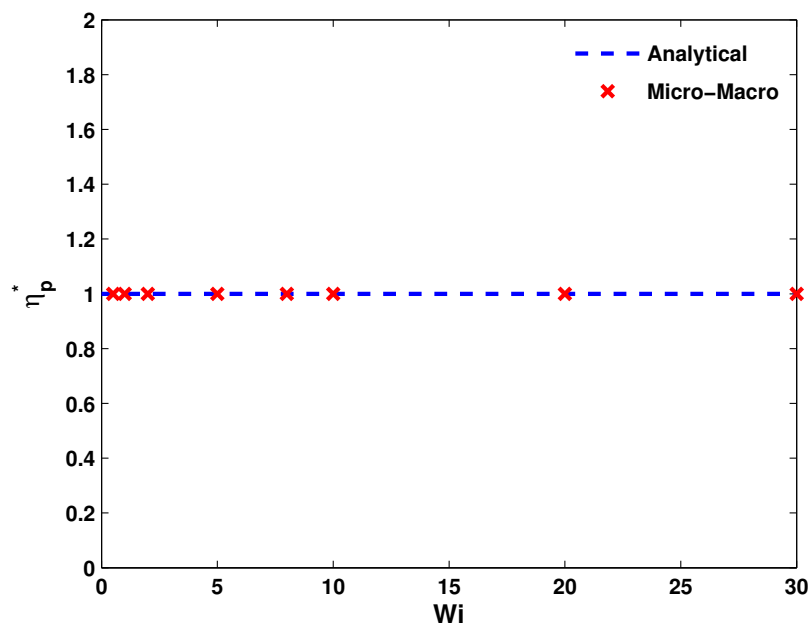
(a) Viscosity
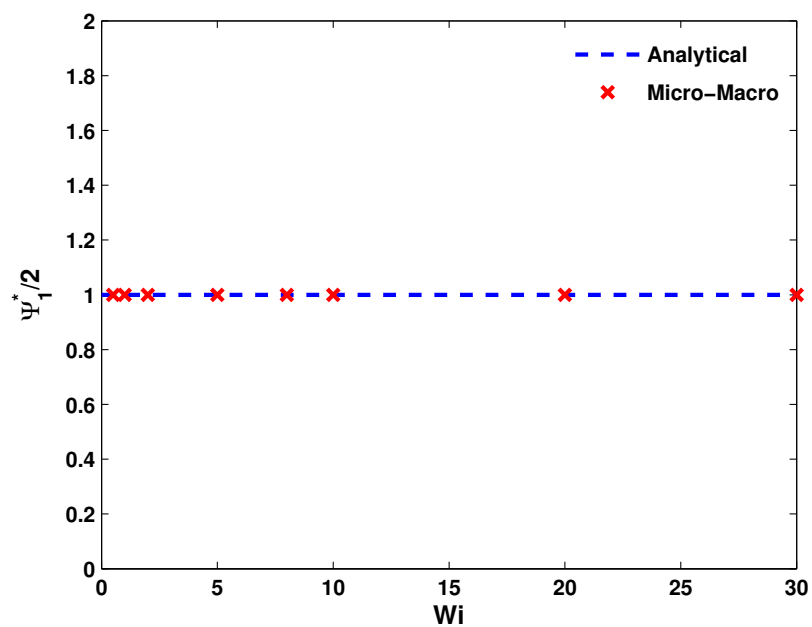


(b) First Normal Stress Difference Coefficient

Figure 4.2: Steady shear viscosity (a) and first normal stress difference coefficient (b) for Hookean dumbbells as a function of $Wi$ using the Micro-Macro approach. $Re = 0.0$, $\beta = 1.0$, $N_f = 4000$, $\Delta t = 0.01$.

a good agreement with the homogeneous results of Herrchen and Ottinger [1997].

As can be seen from Figs. 4.3 and 4.4, FENE and FENE-P models exhibit very similar steady state response in shear flow. Both material functions, $\eta^*$ and $\Psi_1^*$, approach a constant value at low shear rates and decrease at high shear rates according to a power law. The rate of decline for the first normal stress coefficient is greater than for the viscosity.

Figure 4.5 shows the response of material functions for Hookean dumbbells with hydrodynamic interactions with HI parameter $h^* = 0.15$. We find a good agreement between the micro-macro computations and BDS results by Prabhakar and Prakash [2002]. It is evident from Figs. 4.3-4.5 that the FENE-P and FENE model show greater shear thinning compared to the Hookean dumbbells with HI.

In this section we have shown that the response of material functions for a steady shear flow computed using the micro-macro method are in good agreement with the published results for different microscopic constitutive models.

## 4.3  Steady Poiseuille Flow

For Poiseuille flow, the pressure drop per unit length $(-\nabla p/L)$ was always maintained as $-\nabla p/L = 1$. Various $Wi$ at different locations in the $y$-direction, were obtained by varying the value of $\lambda_\eta$. The steady state computations of Poiseuille flow at different $Wi$ is then compared with the steady state Couette flow computations carried out at all these $Wi$.

Figures 4.3-4.5 compare results of Poiseuille flow with Couette flow using the FENE-P, FENE and Hookean dumbbells with HI constitutive models. It is evident from these figures that, given a $Wi$, identical results are obtained in Poiseuille and Couette flow.

## 4.4  Start-Up of Couette Flow

In this section, the transient results for various microscopic constitutive equations are presented for the start-up of Couette flow. For dilute solutions, both the velocity and the stress profile are monitored as a function of time. For ultra-dilute solutions,
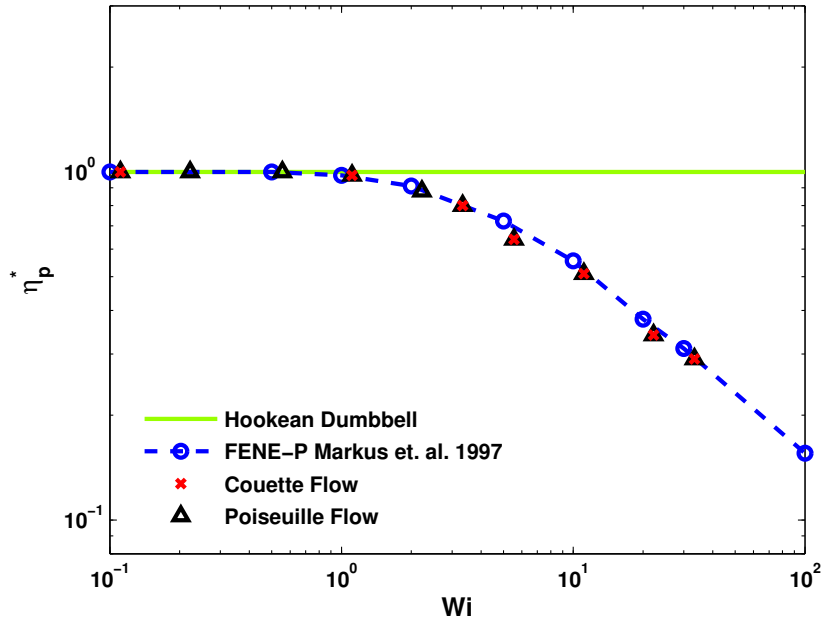
(a) Viscosity
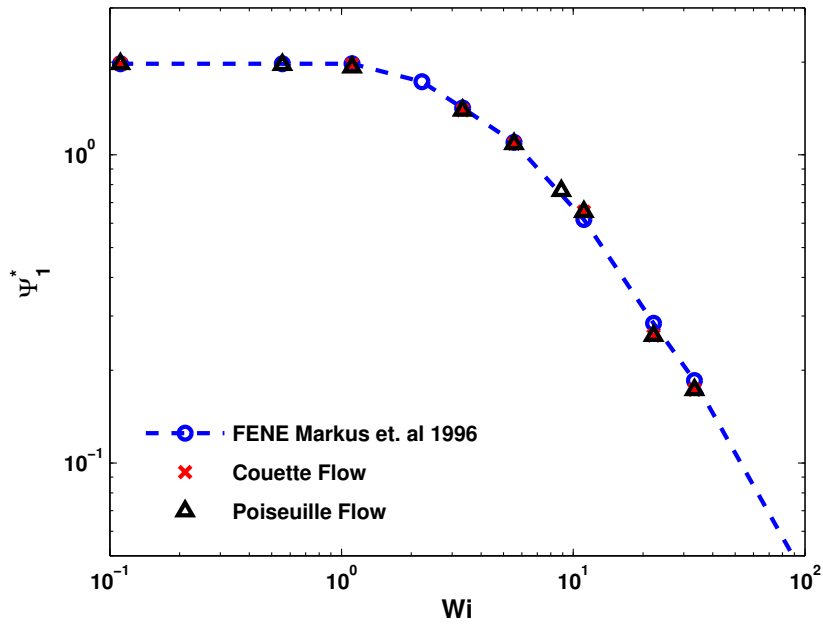


(b) First Normal Stress Difference Coefficient

Figure 4.3: Steady shear viscosity (a) and first normal stress difference coefficient (b) for FENE-P dumbbells as a function of $Wi$ using Micro-Macro approach. $Re = 0.0$, $\beta = 1.0$, $N_f = 4000$, $\Delta t = 0.01$, $b_{\mathbf{M}} = 18.333$.
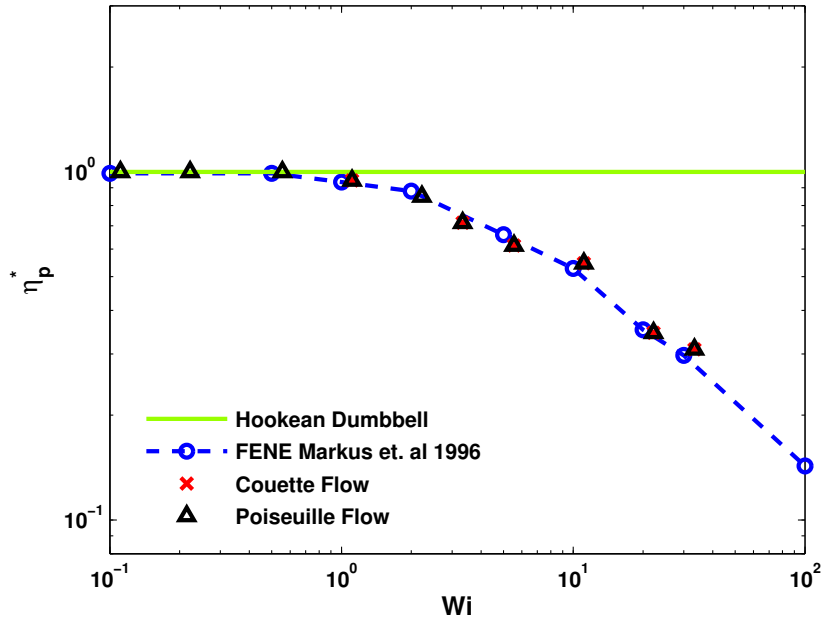
(a) Viscosity
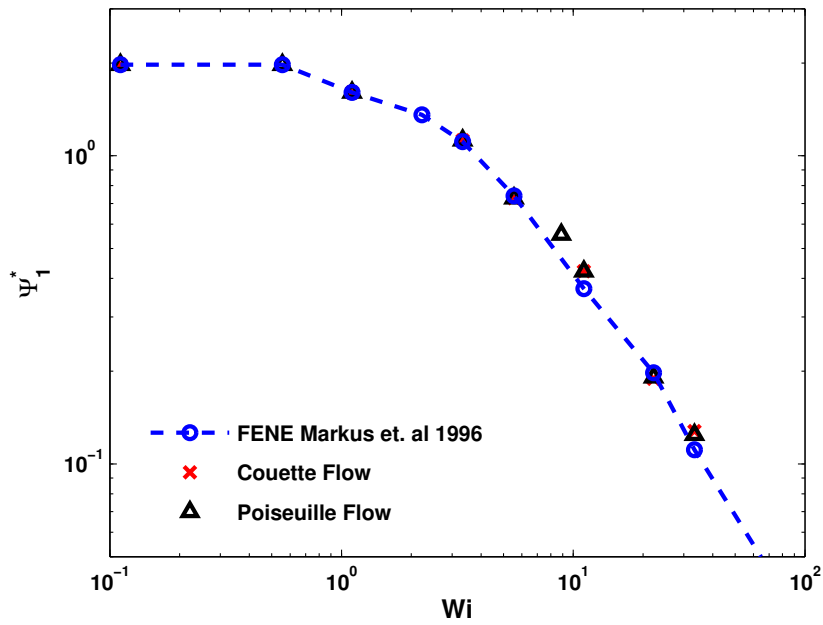


(b) First Normal Stress Difference Coefficient

Figure 4.4: Steady shear viscosity (a) and first normal stress difference coefficient (b) for FENE dumbbells as a function of $Wi$ using the micro-macro approach. The Collocation method is used to compute results using the micro-macro method. $Re = 0.0$, $\beta = 1.0$, $N_f = 4000$, $\Delta t = 0.01$, $b_{\mathbf{M}} = 18.33$.
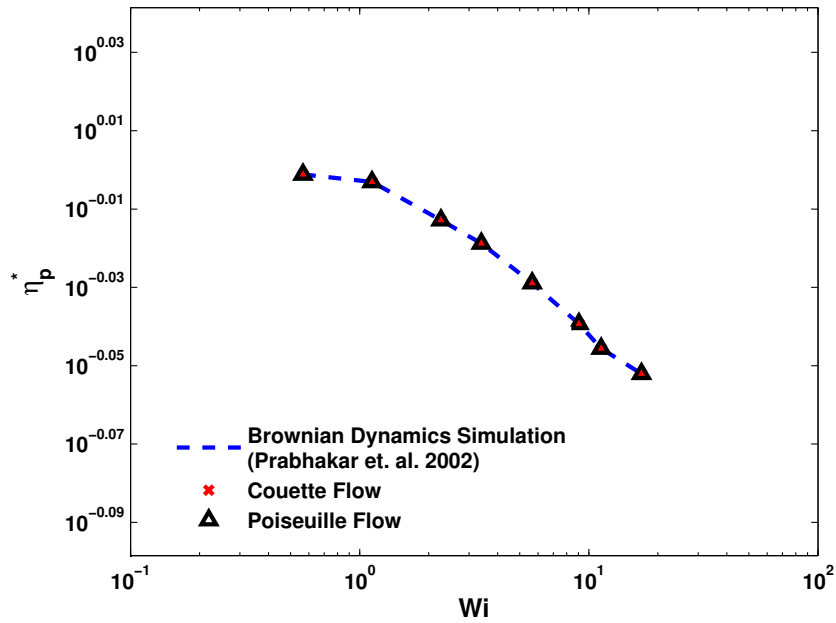
(a) Viscosity
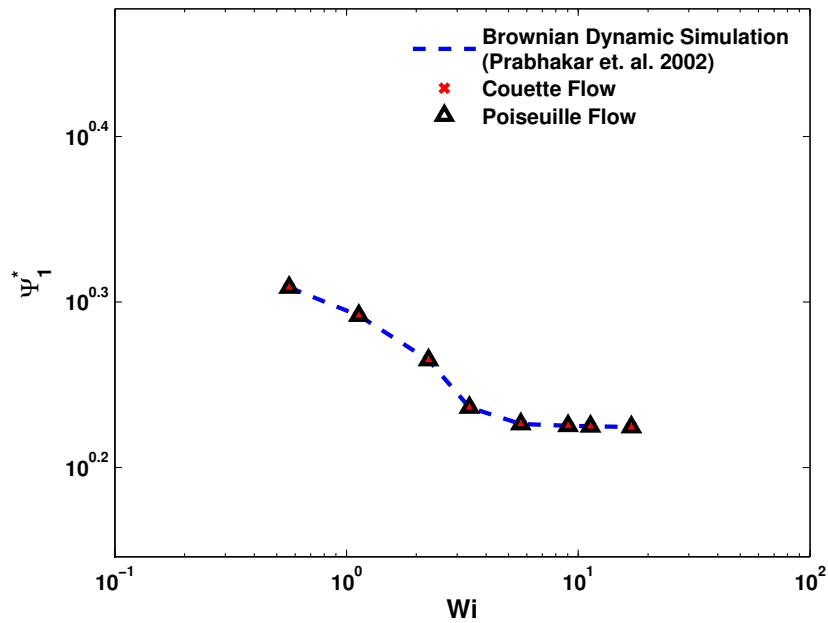


(b) First Normal tress Difference Coefficient

Figure 4.5: Steady shear viscosity (a) and first normal stress difference coefficient (b) for Hookean dumbbells with hydrodynamic interactions as a function of $Wi$ using micro-macro approach. The Collocation method is used to compute results using the micro-macro method. $Re = 0.0$, $\beta = 1.0$, $N_f = 4000$, $\Delta t = 0.01$, $h^* = 0.15$.

though it is in principal possible to impose a time dependent velocity profile, we have monitored the development of the stress profile for a velocity profile that is maintained constant at the steady state value from time $t = 0$.

Figure 4.6 shows the development of velocity and polymer stress profiles for different dimensionless parameters used earlier by Tomea et al. [2002] for a dilute solution of an Oldroyd-B fluid. The results obtained here using the macroscopic and micro-macro approached are displayed in Fig. 4.6 along with the results of Tomea et al. [2002]. The results clearly demonstrate the validity of the time integration numerical schemes developed for both the micro-macro and macroscopic approaches for different dimensionless parameters.

For FENE dumbbells, computations of start-up of Coeutte flows using the BCF method is tested with the published CONFFESSIT results by Laso and Ottinger [1993] for a set of dimensionless parameters, $Re = 1.2757$, $\beta = 0.0521$, $Wi = 49.62$, $b_{\mathbf{M}} = 18.33$. The FENE-P results are compared with the results obtained using the conformation tensor based constitutive models. Though results for Hookean dumbbell with HI are not available, simulations are carried out for the same set of dimensionless parameters for the sake of comparison. Figures 4.7 and 4.8 display the development of velocity profiles at three different locations between the plates for different microscopic constitutive models used in this work. While the results from Hookean dumbbells [see Fig. 4.7(a)] are in good agreement with the equivalent conformation tensor based models, Hookean dumbbells with HI do not show any different behaviour from Hookean dumbbells without HI [see Fig. 4.7(b)]. Similarly for the FENE-P dumbbell, as seen in Fig. 4.8(a), results for both the macroscopic and micro-macro computations are in good agreement. It is also evident from the development of velocity for FENE dumbbells in Fig. 4.8(b) that the BCF method is as accurate as the CONFFESSIT method.

It can seen from Figs. 4.7 and 4.8 that the dynamic response of various constitutive equations is totally different from each other except for the dumbbells with and without HI. Especially the response of the linearized FENE model, namely, the FENE-P model, is dramatically different from that of the FENE model. Both the duration of the velocity overshoot, number of overshoots and the time at which the maximum in velocity overshoot is reached are overestimated by the FENE-P
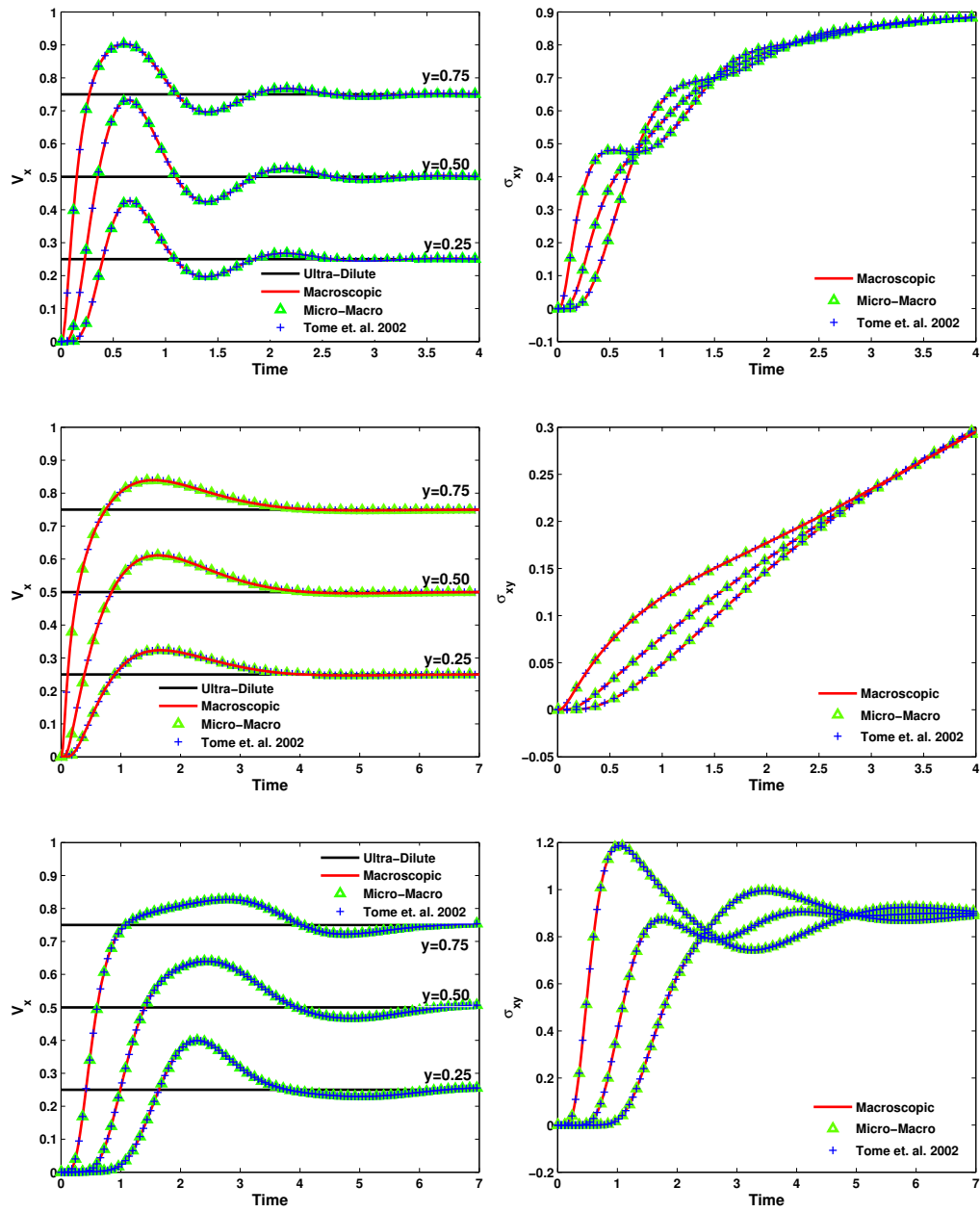
Figure 4.6: Development of velocity and stress profiles for an Oldroyd-B fluid using the micro-macro and macroscopic approaches. (a) $Re = 0.5$, $\beta = 0.1$, $Wi = 1.0$, (b) $Re = 0.5$, $\beta = 0.1$, $Wi = 10$, (c) $Re = 5$, $\beta = 0.1$, $Wi = 1.0$. $N_f = 4000$, $\Delta t = 0.01$.

approximation. The FENE-P linearization leads to more oscillatory behavior in the velocity, which is also the case with the Oldroyd-B model. It should be noted that as the zero shear rate viscosity of both FENE and FENE-P fluids is different, different $\eta_s$ and $\rho$ are used in order to keep the dimensionless parameters same. These different features of FENE-P and FENE dumbbells have been earlier pointed out by Laso and Ottinger [1993] in their CONFFESSIT computations of start-up of Couette flow.

Figures 4.9 and 4.10 shows the development of shear stress on the bottom plate as a function of time for different constitutive models. The difference between the stress evolution computed using different models is striking. While for the Oldroyd-B model, the stress is still growing (as in the case of Hookean dumbbells with HI), the FENE-P model shows larger overshoot compared to the FENE model. The maximum shear stress predicted by the FENE-P model is roughly two times more than it is for FENE dumbbells. The comparison between the micro-macro and macroscopic results for linear dumbbell are excellent. The asymptotic values for the stress for start-up flow calculations are identical to the steady-state values of homogeneous flow for ultra-dilute solutions with time independent velocity field, although it takes considerably longer for the FENE-P dumbbells to reach the steady state. The oscillations that appear in the start-up problem for dilute solutions through the coupling of inertial and elastic effects are absent for ultra-dilute solutions. The difference in behavior between steady and start-up of Couette flow is more pronounced for the more oscillatory FENE-P model.

Figures 4.11 and 4.12 displays the time evolution of first normal stress difference for different constitutive models. Once again, while for the Hookean dumbbells the stress difference increases with time due to the unbounded length of the molecule, for both FENE and FENE-P models, the normal stress difference seems to reached their final steady state values. Similar to the shear stress, there are two additional peaks in the FENE-P model and a much larger overshoot in the value of normal stress difference.
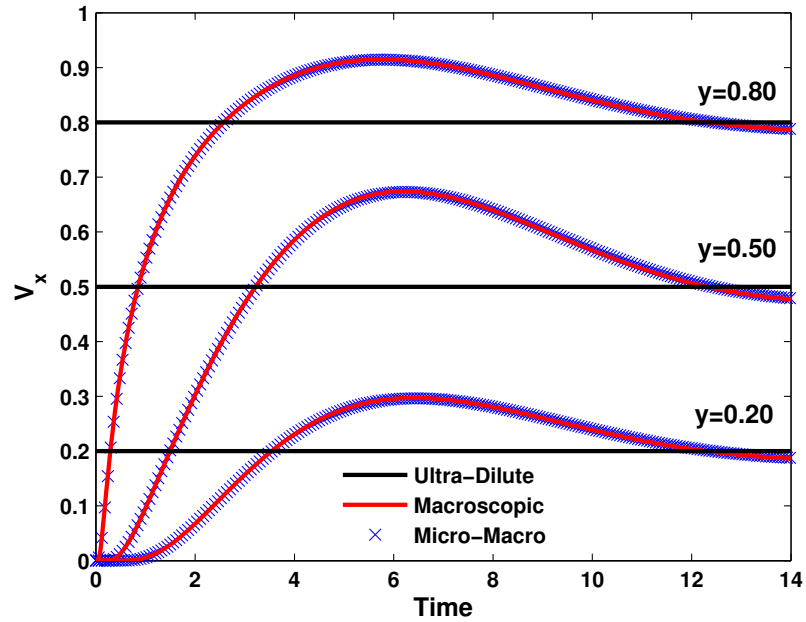
(a) Hookean Dumbbells
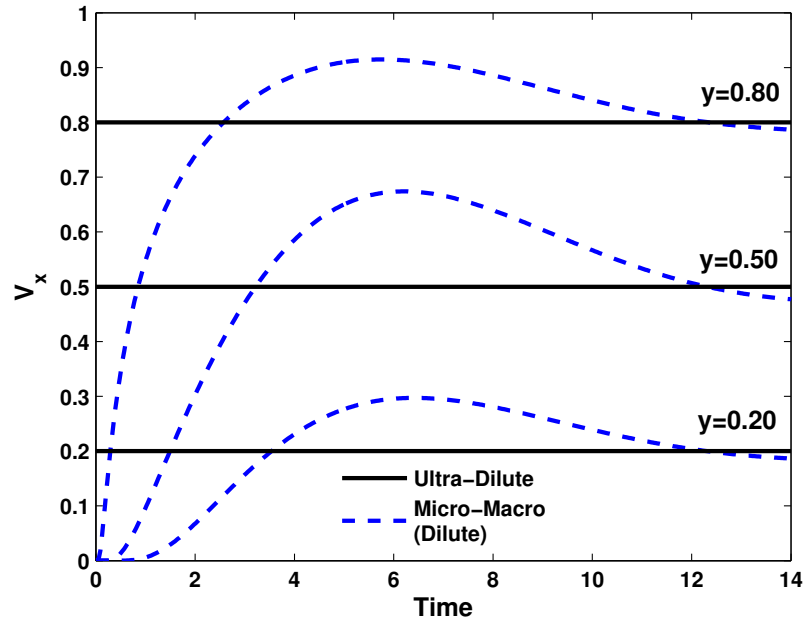


(b) Hookean Dumbbells with HI

Figure 4.7: Development of velocity profile Hookean dumbbells (a) and dumbbells with hydrodynamic interactions (b) using the micro-macro and macroscopic approach. The Collocation method is used to compute results using the micro-macro method for HI. $Re = 1.2757$, $\beta = 0.0521$, $Wi = 49.62$, $h^* = 0.15$, $\Delta t = 0.01$, $N_f = 4000$.
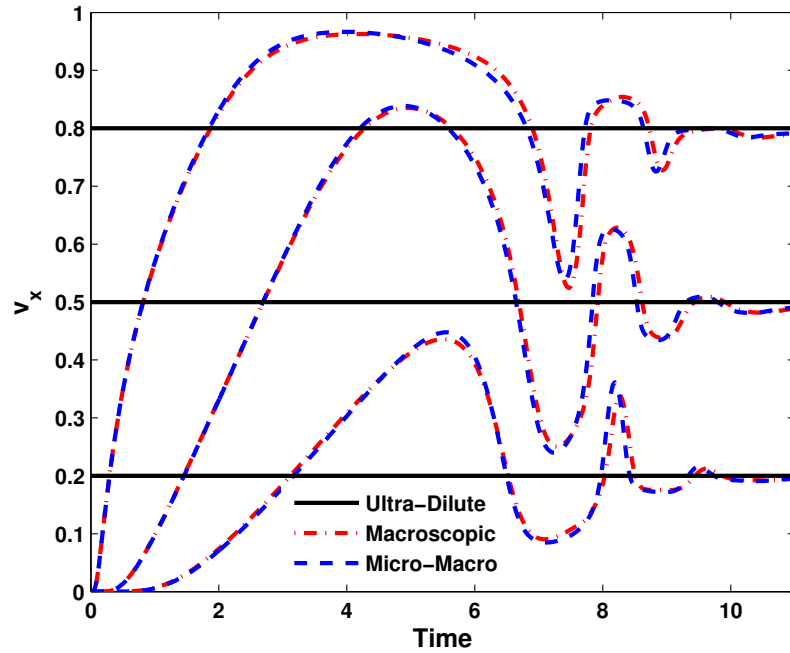
(a) FENE-P Dumbbells
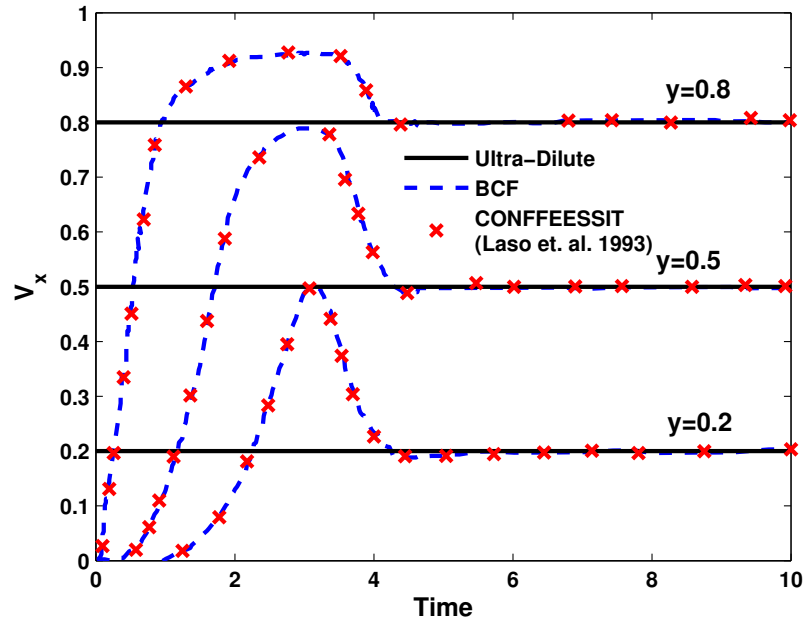


(b) FENE Dumbbells

Figure 4.8: Development of velocity profile for FENE-P (a) and FENE (b) fluid. For FENE-P fluid results are presented using both micro-macro and macroscopic approach. The Collocation method is used to compute results using the micro-macro method for FENE dumbbell model. $Re = 1.2757$, $\beta = 0.0521$, $Wi = 49.62$, $b_{\mathbf{M}} = 55$, $\Delta t = 0.01$, $N_f = 4000$
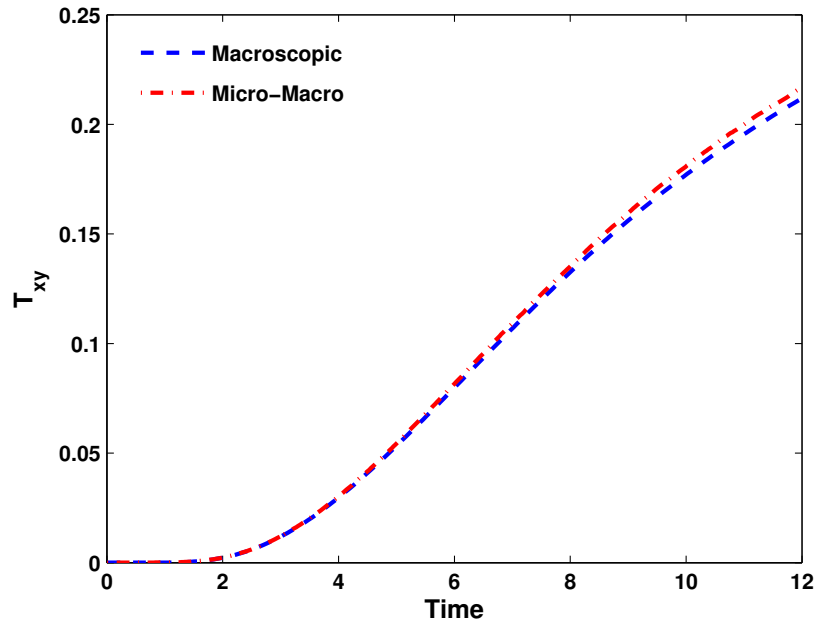
(a) Hookean Dumbbell
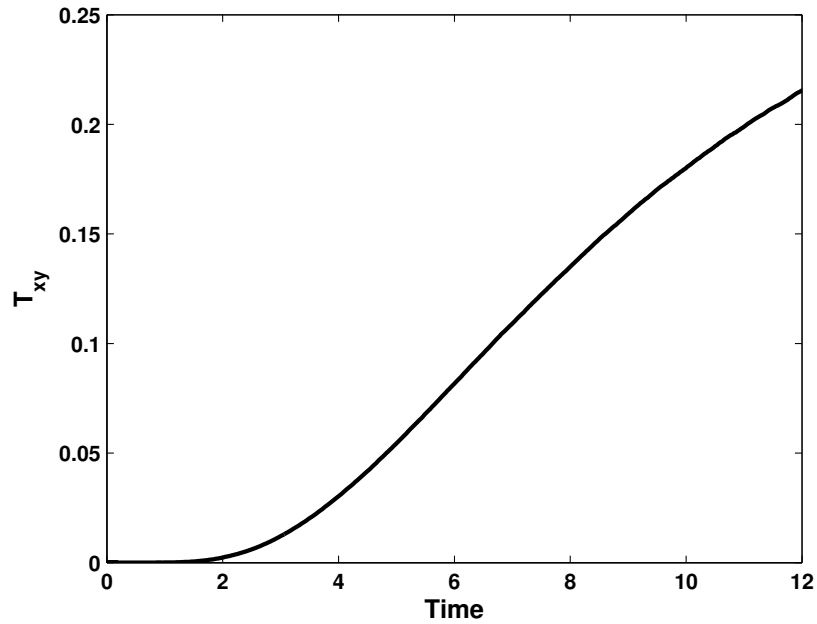


(b) Hookean Dumbbell with HI

Figure 4.9: Development of shear stress on the bottom plate for Hookean dumbbell (a) and Hookean dumbbells with HI (b) fluid. For Hookean dumbbells results are presented using both micro-macro and macroscopic approach. $Re = 1.2757$, $\beta = 0.0521$, $Wi = 49.62$, $\Delta t = 0.01$, $N_f = 4000$ $h^* = 0.15$

(a) FENE-P Dumbbbells
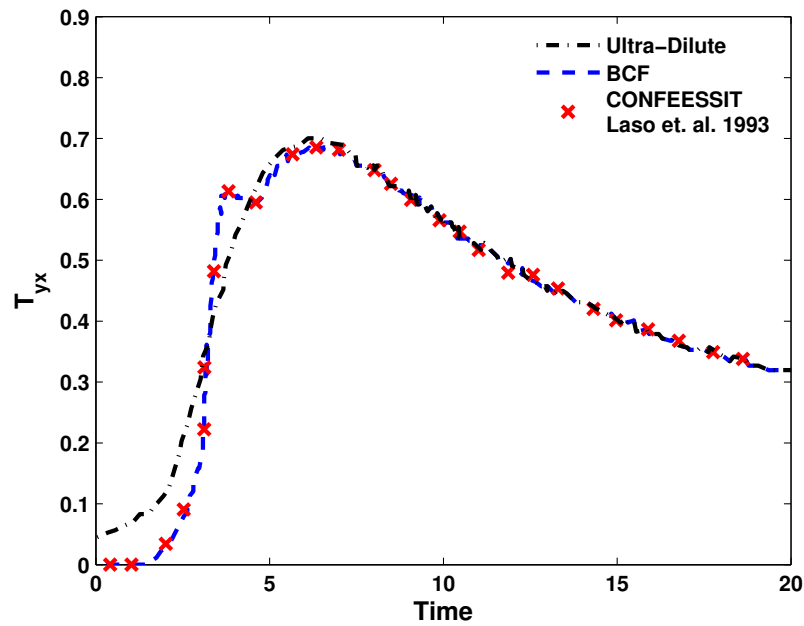


(b) FENE Dumbbells

Figure 4.10: Development of shear stress on the bottom plate for FENE-P (a) and FENE (b) fluid. For FENE-P fluid results are presented using both micro-macro and macroscopic approach. The Collocation method is used to compute results using the micro-macro method for FENE dumbbell model. (a) $Re = 1.2757$, $\beta = 0.0521$, $Wi = 49.62$, $b_{\mathbf{M}} = 55$, $\Delta t = 0.01$, $N_f = 4000$
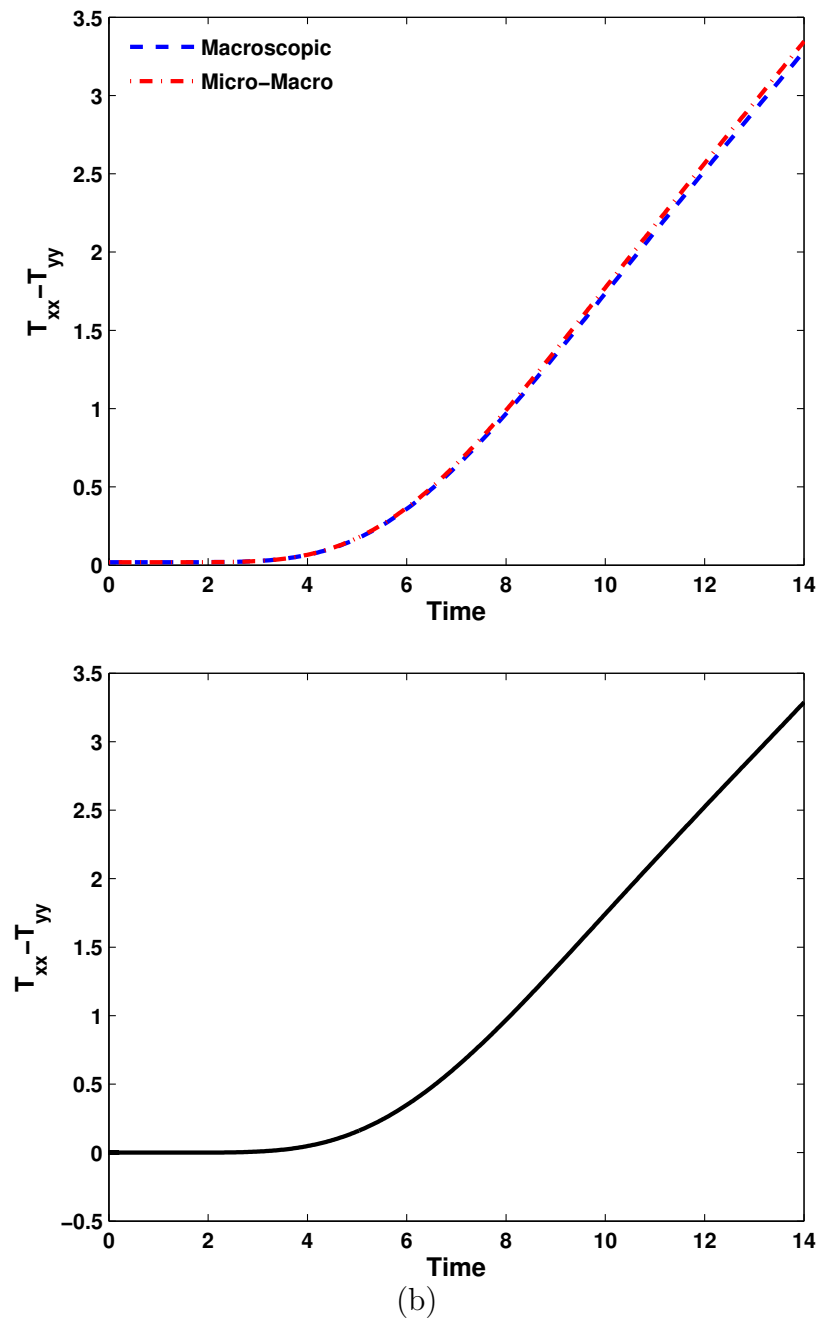
Figure 4.11: Development of normal stress on the bottom plate for Hookean dumb-bell (a) and Hookean dumbbells with HI (b) fluid. For Hookean dumbbells results are presented using both Micro-Macro and Macroscopic approach. $Re = 1.2757$, $\beta = 0.0521$, $Wi = 49.62$, $\Delta t = 0.01$, $N_f = 4000$ $h^* = 0.15$
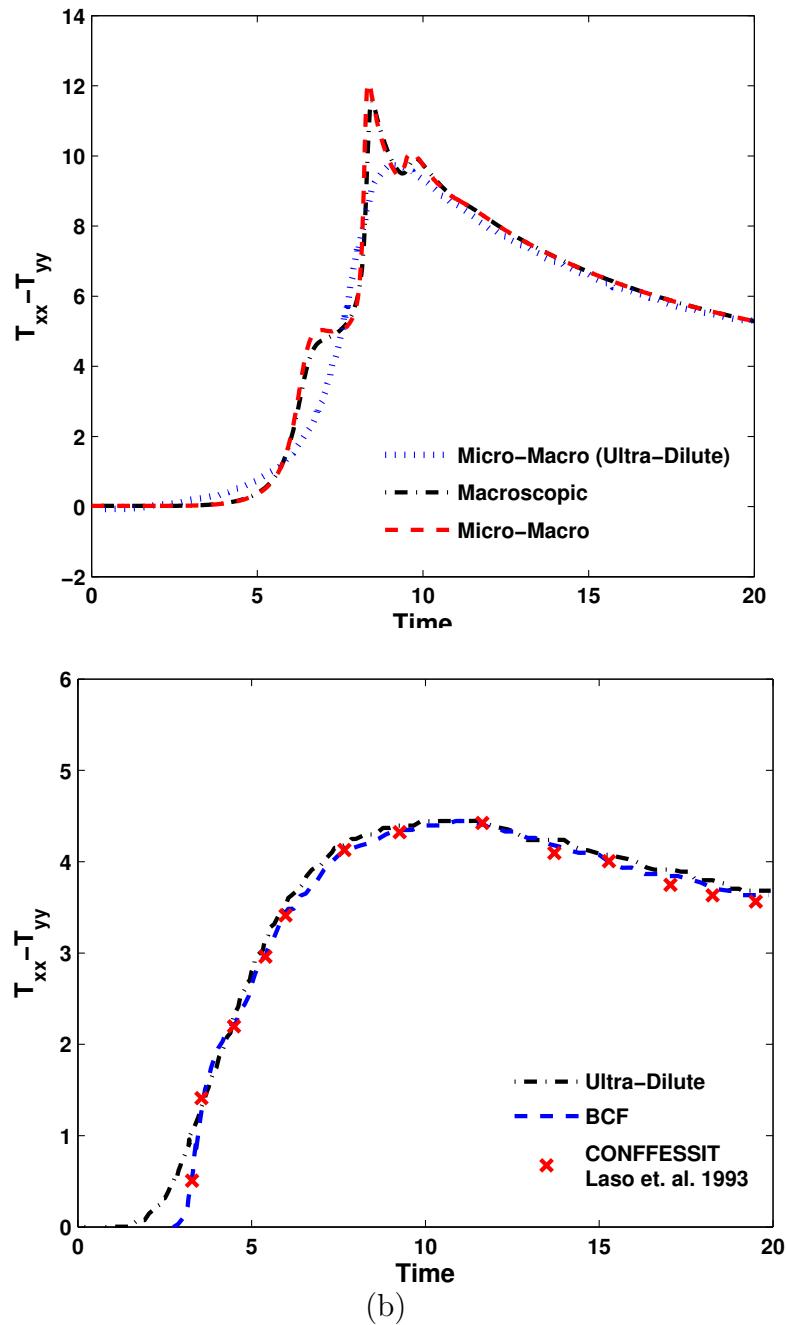
Figure 4.12: Development of normal stress on the bottom plate for FENE-P (a) and FENE (b) fluid. For FENE-P fluid results are presented using both micro-macro and macroscopic approach. The Collocation method is used to compute results using the micro-macro method for FENE dumbbell model. (a) $Re = 1.2757$, $\beta = 0.0521$, $Wi = 49.62$, $b_{\mathbf{M}} = 55$, $\Delta t = 0.01$, $N_f = 4000$

## 4.5   Conclusion

In this section, we have compared the results for flow between two parallel plates computed using the micro-macro algorithms developed in this work. We have found excellent agreement between the micro-macro and macroscopic results for linear dumbbell models. For FENE dumbbells the results of Laso and Ottinger [1993] has been reproduced with the algorithms developed in this work.

# Chapter 5

# Computation of Steady Viscoelastic Free Surface Flow Using the Macroscopic Approach

In this chapter, the macroscopic approach developed in chapter 2 is used to solve an example of a free surface flow. Free surface flows occur when a layer of liquid meets a gas at an interface. Such flows arise in a variety of commercial applications, such as coating (e.g. slot coating, roll coating etc.), ink-jet printing, fiber spinning, and micropipetting. The free surface flow studied in this work is the flow in the downstream section of a slot coater. The results presented in this chapter address some problems that have not been considered in the earlier work on viscoelastic slot coating flow by Lee et al. [2002]; Pasquali and Scriven [2002] and Romero et al. [2004].

Slot coating belongs to a class of coating flows known as pre-metered coating, where the thickness of the coated layer is predetermined. In pre-metered coating, all the liquid fed into the coating die by a metering device e.g., a displacement pump, is deposited on the substrate (see Fig. 5.1). As a result, the average film thickness is predetermined for a given feed flow rate, coating width in the cross-web direction, and substrate speed, and is consequently ideal for high precision coating. The average film thickness is independent of the rheological properties of the coating liquid.
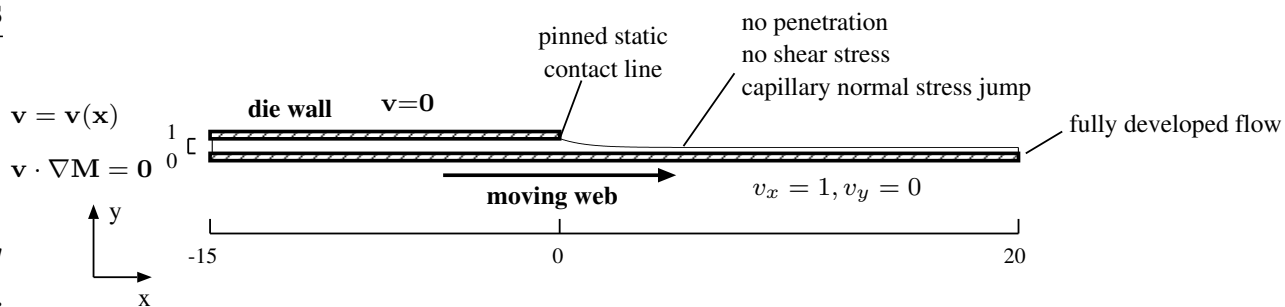
Figure 5.1: Flow domain and boundary conditions used in analyzing the flow of viscoelastic liquid in the downstream section of a slot coater.

Frequently, coating applications involve liquids that are viscoelastic due to the presence of polymer as final product or as rheology modifier (e.g. ink-jet printing). Most of these flows are time dependent and their dynamics are controlled by the elasticity and capillarity of the liquid. The competition among viscous, capillary and elastic forces (also inertial forces if the Reynolds number $Re >> 0$) determine the range of parameters in which the flow is stable and steady. Although the coating thickness is independent of the non-Newtonian nature of the liquid, the flow in the coating bead and subsequently, the uniformity of the liquid layer can be affected by the rheological properties of the liquid [Romero et al., 2004].

Due to the existence of a variety of industrial applications of coating flows, numerous researchers have focused their attention on steady Newtonian coating flows [Carvalho and Kheshgi, 2000; Carvalho and Scriven, 1997a,b, 1999; Christodoulou and Scriven, 1992; Gates, 1999; Musson, 2001; Ruschak, 1976; Saito and Scriven, 1981; Sartor, 1990; Silliman and Scriven, 1980] and on understanding the dynamics of stable Newtonian coating flows [Coyle et al., 1990; Greener et al., 1980; Mill and South, 1967; Pearson, 1960; Pitts and Greiller, 1961; Savage, 1984]. However, studies related to viscoelastic coating flows have only recently been attempted and are limited [Bajaj et al., 2004, 2005; Bhatara et al., 2004, 2005; Lee et al., 2002; Pasquali and Scriven, 2002; Romero et al., 2004; Zevallos et al., 2005]. For slot coating flow in particular, calculations of steady Newtonian [Carvalho and Kheshgi, 2000; Gates, 1999; Musson, 2001; Saito and Scriven, 1981; Sartor, 1990; Silliman and Scriven, 1980] and viscoelastic flows [Lee et al., 2002; Pasquali and Scriven, 2002; Romero et al., 2004] have been reported in literature. To some extent, the

limited number of studies in the area, specially for viscoelastic coating flow, can be attributed to the presence of a free surface in such flows. The computational method discussed in detail in chapter 2 is used here to solve viscoelastic free surface flows.

A careful investigation of the work by Pasquali and Scriven [2002] and Lee et al. [2002] reveal the following aspects of slot coating flows:

Pasquali and Scriven [2002] found that for an ultra - dilute polymer solution, recirculation under the die strongly affects the computations at high $Wi$. In ultra-dilute solutions, the presence of polymer molecules doesn't affect the flow field and the conservation equations are decoupled from the conformation tensor equation. Pasquali and Scriven [2002] observed that when the recirculation under the die lip was absent, all models failed at a relatively low value of $Wi$ number because of the singularity in the velocity gradient at the contact line [Salamon et al., 1995, 1997a,b]. However, when recirculation was present, much higher $Wi$ could be achieved. The mode of failure was found to be independent of the model details i.e. the smallest eigenvalue of the conformation tensor reached zero in the region of strong extensional flow under the stretching section of the free surface. An important observation was that in the presence of recirculation, the maximum $Wi$ achieved in all calculations was shown to increase as the model used to represent the polymer molecules captured the underlying physics more accurately. This suggests that shortcomings of these models could be due to the use of approximate non-linear kinetic theory based relations leading to a poor physical description of polymer molecules in solution.

Lee et al. [2002] observed that for dilute polymer solutions (in which case the conservation equations are coupled with the conformation tensor equation), viscoelasticity increases the meniscus invasion and thus, reduces the angle of separation at the static contact line. They identified meniscus invasion as a possible mechanism for the onset of ribbing instabilities. A recent study by Romero et al. [2004] has verified experimentally and theoretically that the viscoelastic nature of the fluid significantly reduces the contact angle due to meniscus invasion, leading to a non-uniform coating. Both Lee et al. [2002] and Pasquali and Scriven [2002] observed the formation of elastic stress boundary layers under the free surface and the failure of the numerical method at high $Wi$.

While the coupling between flow and the flow induced microstructure in slot

coating flow is yet to be examined, a recent study on roll coating flow of dilute polymer solutions by Zevallos et al. [2005] has revealed that the presence of polymers can dramatically change the nature of the flow field (e.g. velocity field, recirculation etc.) which ultimately leads to flow instabilities. This kind of behaviour is not expected for ultra-dilute solution as the flow field is independent of the elastic stress. The strange behavior shown by dilute polymer solutions can be attributed to the strong coupling between the velocity field and the elastic stress. Zevallos et al. [2005] have established that for a given flow condition and $Wi$ in viscoelastic roll coating flows, there is always a critical Capillary number (defined as the ratio of viscous to surface forces) beyond which the normal stress difference at the stagnation point becomes positive and recirculation, which is present at low $Ca$, completely disappears. Due to the disappearance of recirculation, the flow close to the stagnation point becomes stronger and consequently, the normal stress difference at the free surface increases dramatically. This explains how liquid elasticity makes roll coating flow unstable at a much lower $Ca$ than the $Ca$ achieved in the Newtonian case [Graham, 2003; Zevallos et al., 2005].

Although the flow computations by Pasquali and Scriven [2002], Lee et al. [2002] and Zevallos et al. [2005] are significant contributions to the understanding of the role of viscoelsaticity on slot coating flows and in general on free surface flows, the following questions remain unanswered:

- How does the behaviour of ultra-dilute polymer solutions differ from that of dilute solutions, for instance with regard to the mode of failure of numerical simulations at high $Wi$ number, the effect of static contact line on flow computations etc.?

- How do the viscoelastic properties of the fluid affect the macroscopic properties of flow such as, the velocity field, recirculation under the die, the location of the stagnation point etc.?

- Does the change in the flow behaviour affect the stability of slot coating flow?

- How does the ratio of polymer to solvent viscosity affect the flow behaviour?

In order to examine the above listed issues arising from the study of Pasquali and Scriven [2002] and Lee et al. [2002], simulations for both dilute and ultra-dilute

Table 5.1: Meshes used for slot coating flow computations.

| Mesh | Number of Elements | Number of Nodes | Degrees of Freedom Macroscopic Simulations $(\mathbf{x}, \mathbf{v}, p, \mathbf{M}, \mathbf{L})$ |
|------|------|------|------|
| M1 | 550 | 2311 | 15712 |
| M2 | 1096 | 4539 | 30836 |
| M3 | 2100 | 8611 | 58392 |
| M4 | 4105 | 16717 | 113215 |

solutions are carried out here for a wide range of parameters. The results presented in the next few sections are an attempt to clearly identify the role of viscoelasticiy on slot coating flows. In particular, we have extended the earlier work on slot coating flow by Pasquali and Scriven [2002] and Lee et al. [2002] to investigate the effect of viscosity ratio on both macroscopic and microscopic properties. The computed flow and stress fields are analyzed to understand the role of viscoelasticity on the stability of slot coating flows using the stability criteria proposed by Graham [2003].

All simulations are preformed at $Re = 0$ and at a dimensionless flow rate less then 0.33, for which a recirculation region is always present in the flow domain [Pasquali and Scriven, 2002]. The dimensionless numbers that are varied in this work are $Ca$, $\beta$, $Wi$ and $Ec$.

## 5.1  Mesh Convergence

The numerical solutions were tested for convergence on four different meshes. Details of the meshes, namely M1, M2, M3 and M4, are given in Table 5.1. The most important distinction between the four meshes is the density of element distribution in the vicinity of the static contact line and in the region of the air/fluid interface.

Figure 5.2 displays the zoomed images of the meshes near the contact line.

As the viscosity ratio is an important parameter in this study, we show the mesh convergence for all 4 values of $\beta$ namely, $\beta = 0.25$, 0.51, 0.75 and 1.0 used in this work. While for $\beta < 1$ the evolution equations for the conformation tensor are coupled with the mass, momentum and mesh equations, for $\beta = 1$ (which corresponds
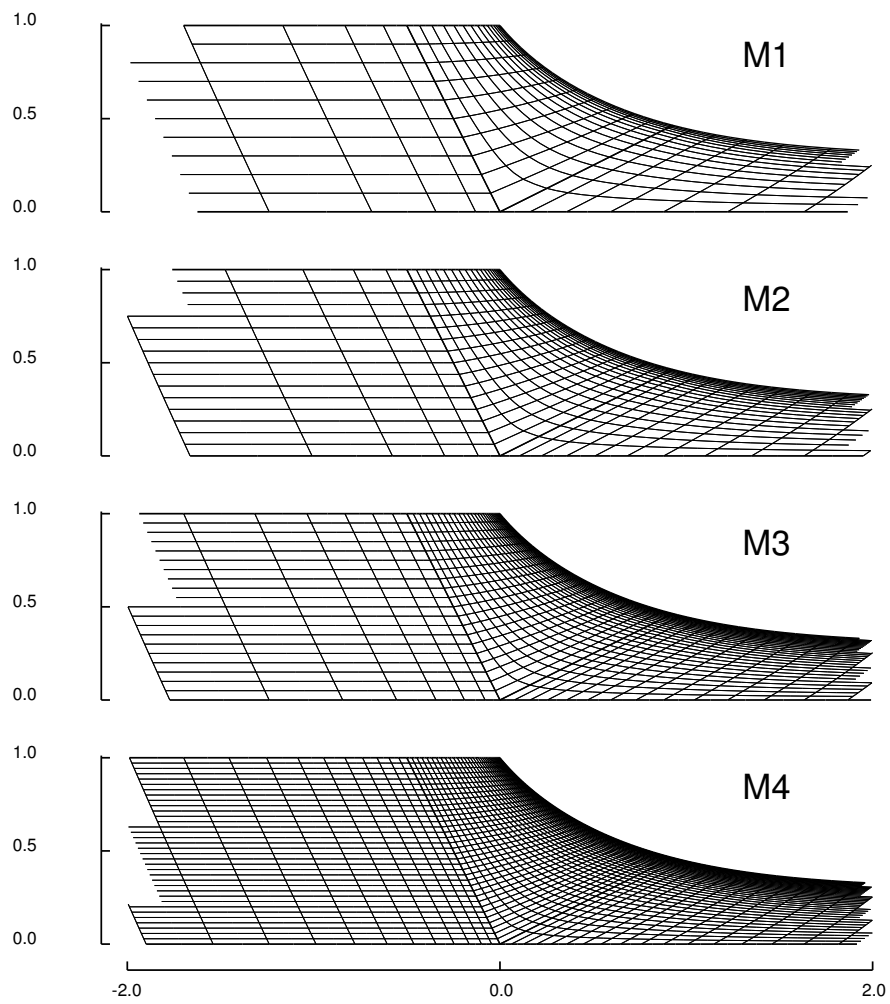
Figure 5.2: Meshes used in analyzing the downstream section of slot coater

to an ultra-dilute solution), obtained by setting $\eta_p = 0$, the evolution equation for the conformation tensor is decoupled from conservation and mesh equations. The molecular conformation is computed by solving the coupled set of equations for both the Oldroyd-B and FENE-P constitutive equations in the case of dilute solutions and by solving only the conformation tensor equation for a given flow field in the case of ultra-dilute solutions.

All the mesh convergence results are presented in terms of the eigenvalues of the conformation tensor. The orthonormal eigenvectors $\mathbf{m}_i$ of the conformation dyadic $\mathbf{M}$ represent three orthonormal directions along which molecules are stretched or contracted. The corresponding eigenvalues represents the square of the principal stretch ratios of flowing polymer molecules. Eigenvalues of the conformation tensor are always real and positive because the conformation tensor is symmetric and positive definite [Pasquali and Scriven, 2002].

Figures 5.3 and 5.4 show the largest and the smallest eigenvalues of the conformation tensor in the flow domain as a function of $Wi$ for an Oldroyd-B fluid for different values of $\beta$. While the largest eigenvalue (stretch of the molecule) grows rapidly with increasing $Wi$, the minimum eigenvalue decreases with increasing $Wi$. As shown in Fig. 5.4, computations using different meshes breakdown at different values of $Wi$ i.e., the smallest eigenvalue of the conformation tensor becomes negative in certain regions of the flow field [Pasquali and Scriven, 2002]. Figure 5.4 also demonstrates an important difference between the computations for ultra-dilute solutions and those for dilute solutions. For an ultra-dilute solution, the maximum $Wi$ at which the smallest eigenvalue becomes negative increases significantly with mesh refinement as shown in Fig. 5.4(d). However, the maximum $Wi$ for dilute solutions remains relatively insensitive to mesh refinement and decreases significantly with reducing viscosity ratio $\beta$. The reason for the decrease in maximum $Wi$ with viscosity ratio will be discussed shortly. It is also evident from Fig. 5.4 that mesh convergence is obtained at least up to $Wi = 2.0$ for all $\beta$ values.

Mesh convergence for the FENE-P model is depicted in Figs. 5.5 and 5.6 for different values of $\beta$ in terms of the largest and the smallest eigenvalues of the conformation tensor, respectively. The behaviour of the FENE-P model is similar to that of the Oldroyd-B model except that the largest eigenvalues reaches its maximum
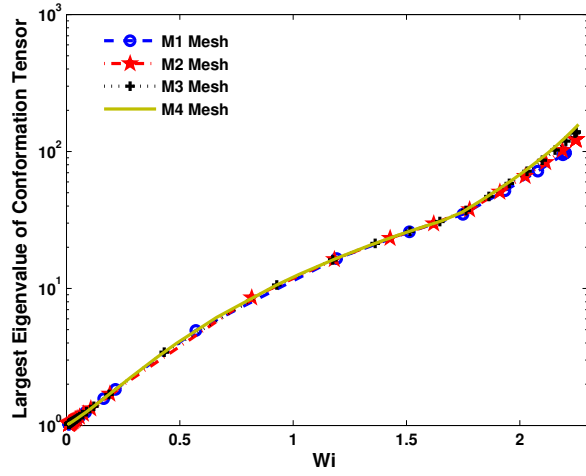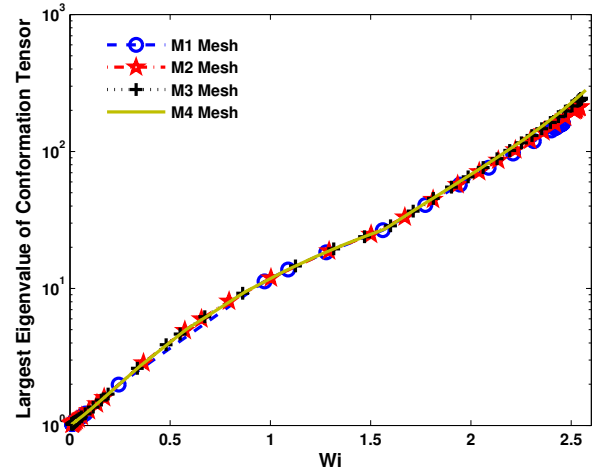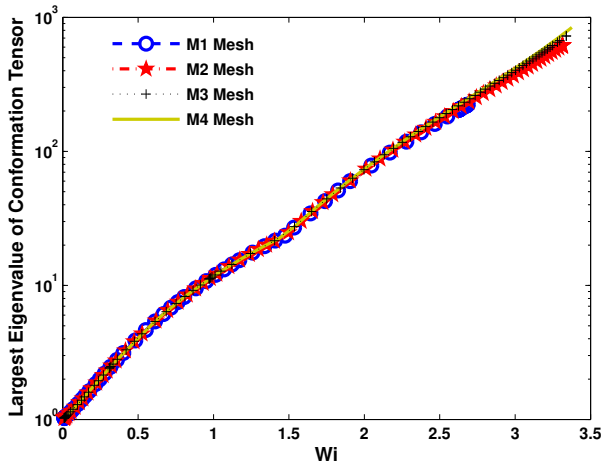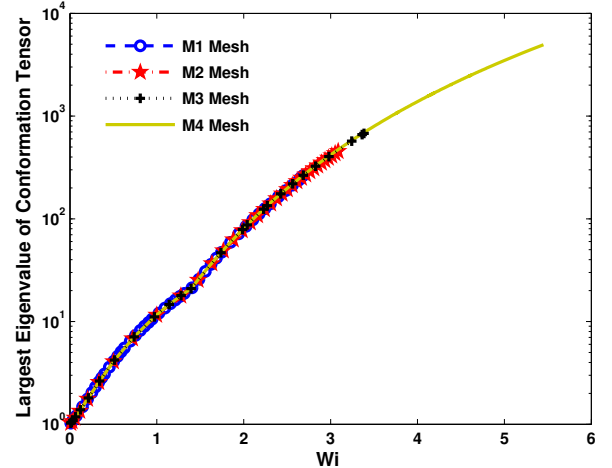
Figure 5.3: Largest eigenvalues of the conformation tensor in the flow domain for an Oldroyd-B fluid. $Ca = 0.1$, $Q = 0.3$.
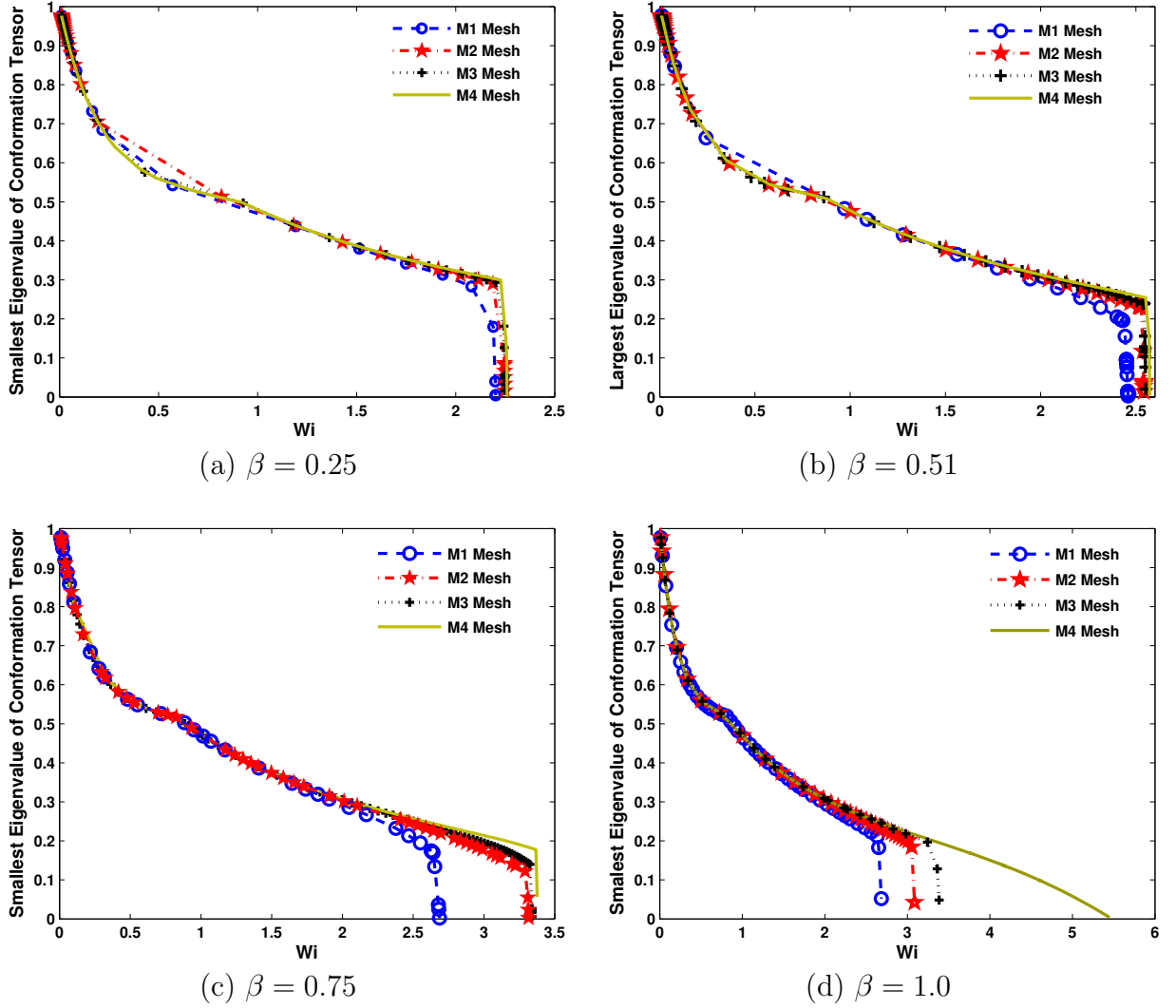
Figure 5.4: Smallest eigenvalues of the conformation tensor in the flow domain for an Oldroyd-B fluid. $Ca = 0.1$, $Q = 0.3$.

value (which is equal to $b_{\mathbf{M}}$, the finite extensibility parameter) at a higher $Wi$.

A striking difference between the computations of ultra-dilute and dilute solutions is that while the maximum $Wi$ strongly depends upon the constitutive model for ultra-dilute solutions, for dilute solutions, however, the constitutive model has little or no effect on the maximum $Wi$ for the set of parameters studied here. The maximum $Wi$ for an ultra-dilute solution of an Oldroyd-B fluid is $\sim 5.45$, it increase to $\sim 10$ for the FENE-P model [see Figs. 5.6(d) & Figs. 5.6(d)] which is quantitatively consistent with the finding of Pasquali and Scriven [2002].

The FENE-P model also predicts that the out-of-plane eigenvalue of the conformation tensor can be driven away from its equilibrium value in a two dimensional flow as depicted in Fig. 5.7 [Pasquali and Scriven, 2002]. Basically, the out-of-plane eigenvalue contacts much more slowly than the in-plane eigenvalue. The mesh convergence is evident from Fig. 5.7.

Figure 5.8 shows that for both the Oldroyd-B and the FENE-P fluid, stress boundary layers are formed under the stretching section of the free surface at higher $Wi$. While moving from the web to the free surface, the elastic stress grows sharply at high $Wi$ number in the vicinity of the free surface. Figures 5.9 and 5.10 are further evidence of the formation of stress boundary layers. Figures 5.9 and 5.10 show the evolution of the $xx$ component of elastic stress with increasing $Wi$ for both the Oldroyd-B and the FENE-P fluid. More refined meshes are required to resolve stress boundary layers close to the free surface at higher $Wi$.

## 5.2   Effect of Viscosity Ratio on the Stretch of Polymer Molecules

In the previous section we showed the mesh convergence of our results for different values of $\beta$ in terms of the eigenvalues of the conformation tensor. In this section, we present the effect of viscosity ratio on the stretch of polymer molecules. We show that the $\beta$ dependence of the rate of stretching is a function of $Wi$.

Figures 5.11 and 5.12 show the effect of the viscosity ratio $\beta$ on the stretch of the polymer molecules as a function of $Wi$ for an Oldroyd-B fluid. It is worth mentioning that these figures display the largest and smallest stretch in the whole flow domain

(a) $\beta = 0.25$

(b) $\beta = 0.51$

(c) $\beta = 0.75$

(d) $\beta = 1.0$
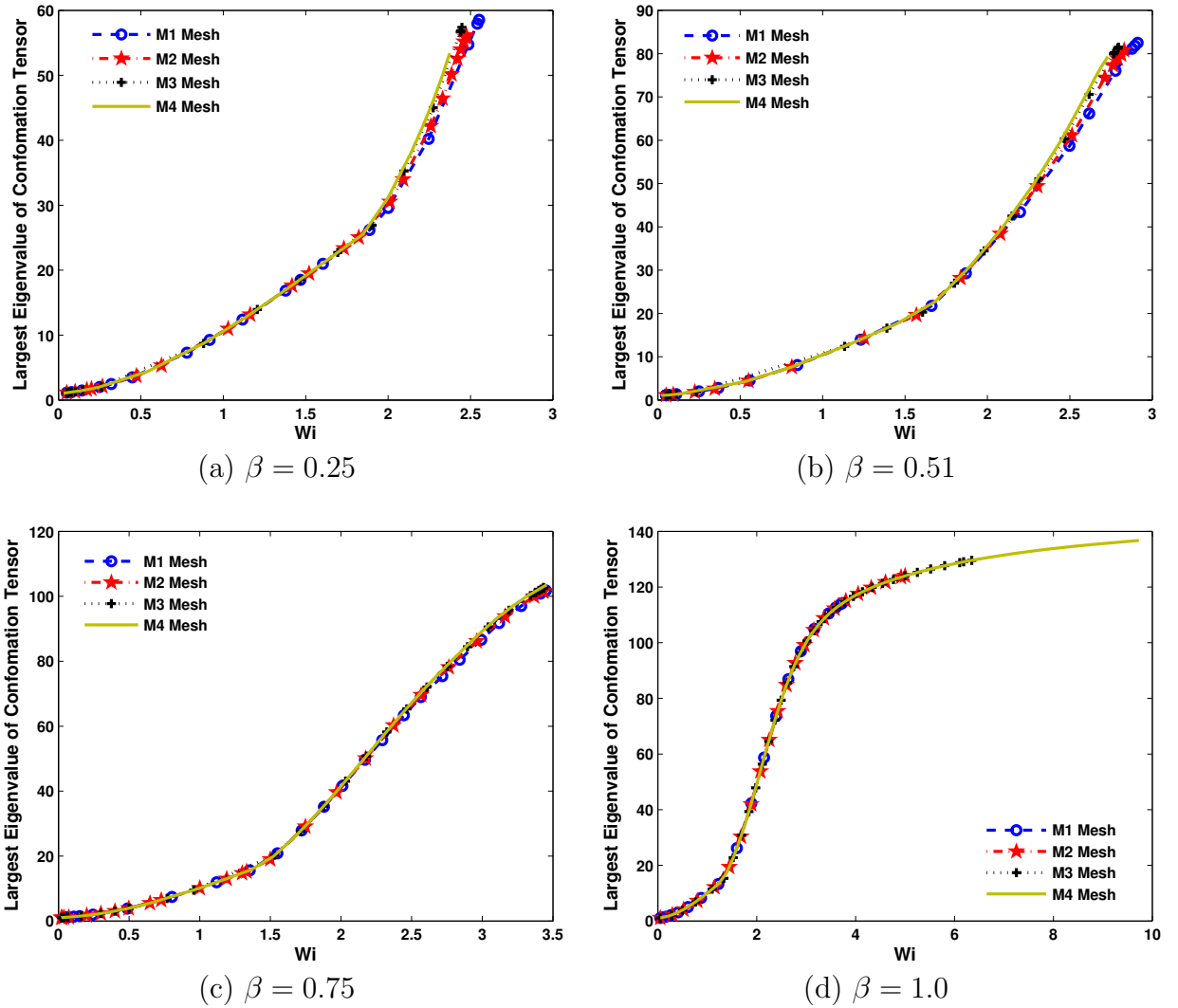
Figure 5.5: Largest eigenvalues of the conformation tensor in the flow domain for the FENE-P fluid. $Ca = 0.1$, $Q = 0.3$, $b_{\mathbf{M}} = 50$.

(a) $\beta = 0.25$

(b) $\beta = 0.51$

(c) $\beta = 0.75$

(d) $\beta = 1.0$
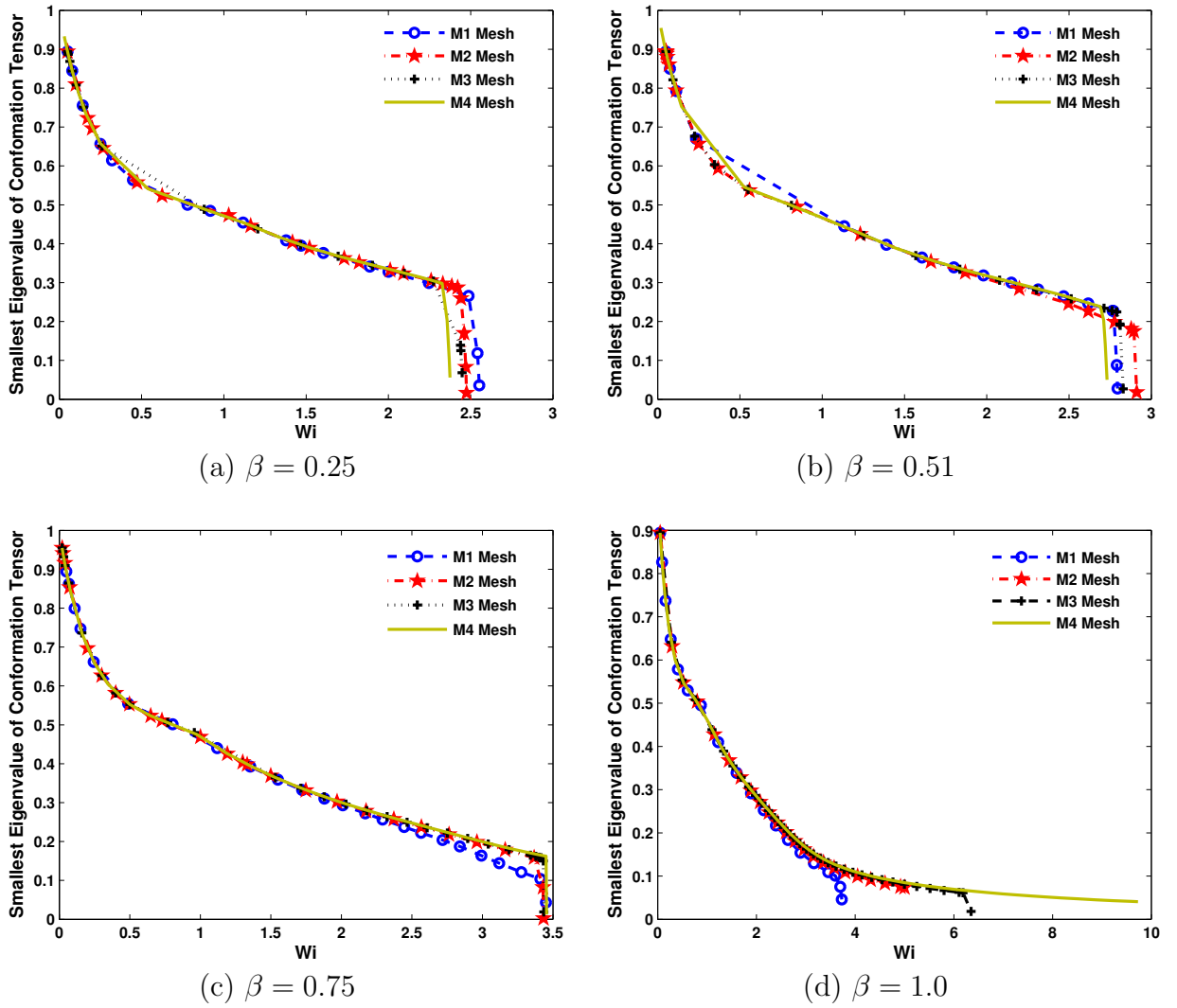
Figure 5.6: Smallest eigenvalues of the conformation tensor in the flow domain for the FENE-P fluid. $Ca = 0.1$, $Q = 0.3$, $b_{\mathbf{M}} = 50$.
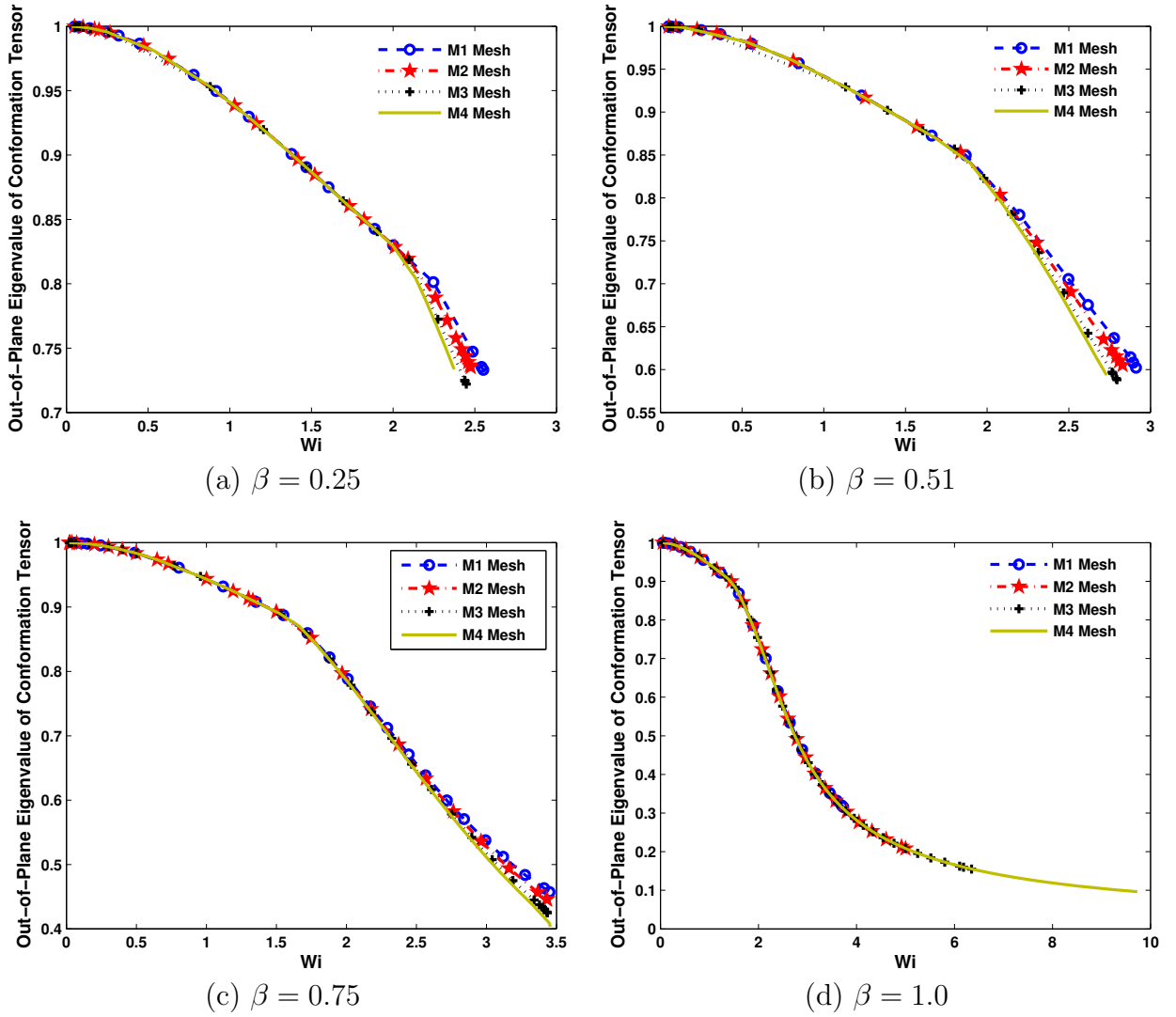
Figure 5.7: Out-of-plane eigenvalues of the conformation tensor in the flow domain for the FENE-P fluid. $Ca = 0.1$, $Q = 0.3$, $b_{\mathbf{M}} = 50$.
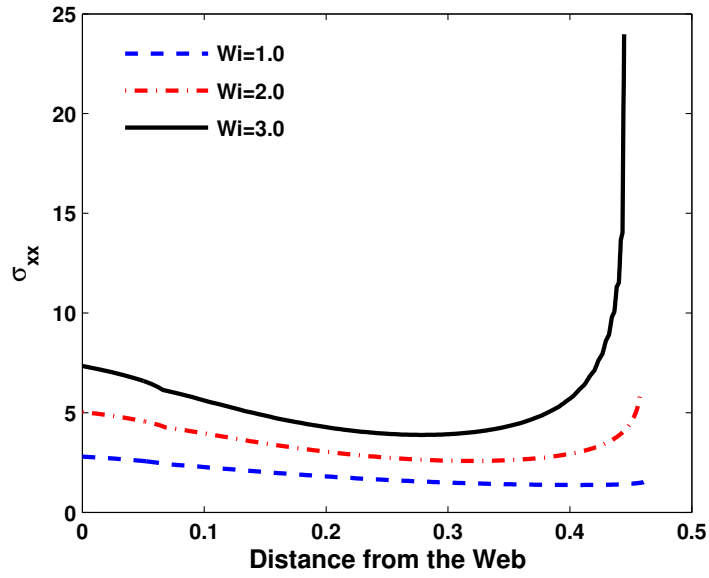
(a) Oldroyd-B
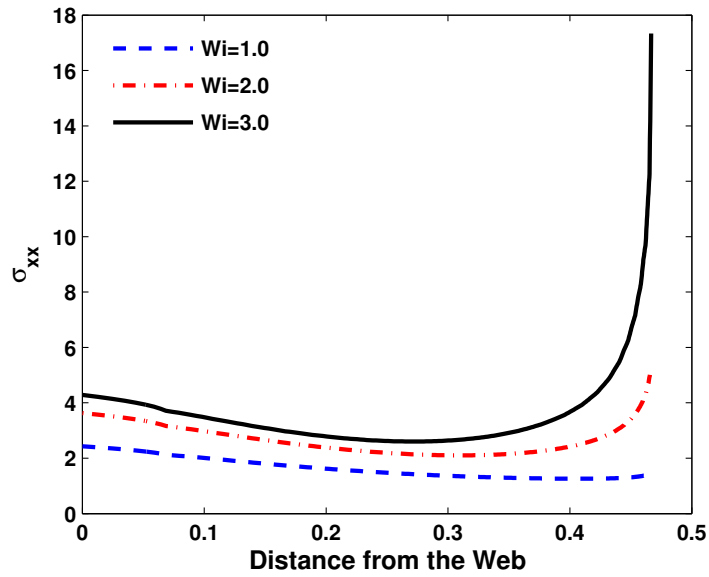


(b) FENE-P

Figure 5.8: $xx$ component of elastic stress (a) for Oldroyd-B and (b) for FENE-P fluid. Distance is measured from the web to the free surface. $Ca = 0.1$, $Q = 0.3$, $\beta = 0.75$, $b_{\mathbf{M}} = 50$
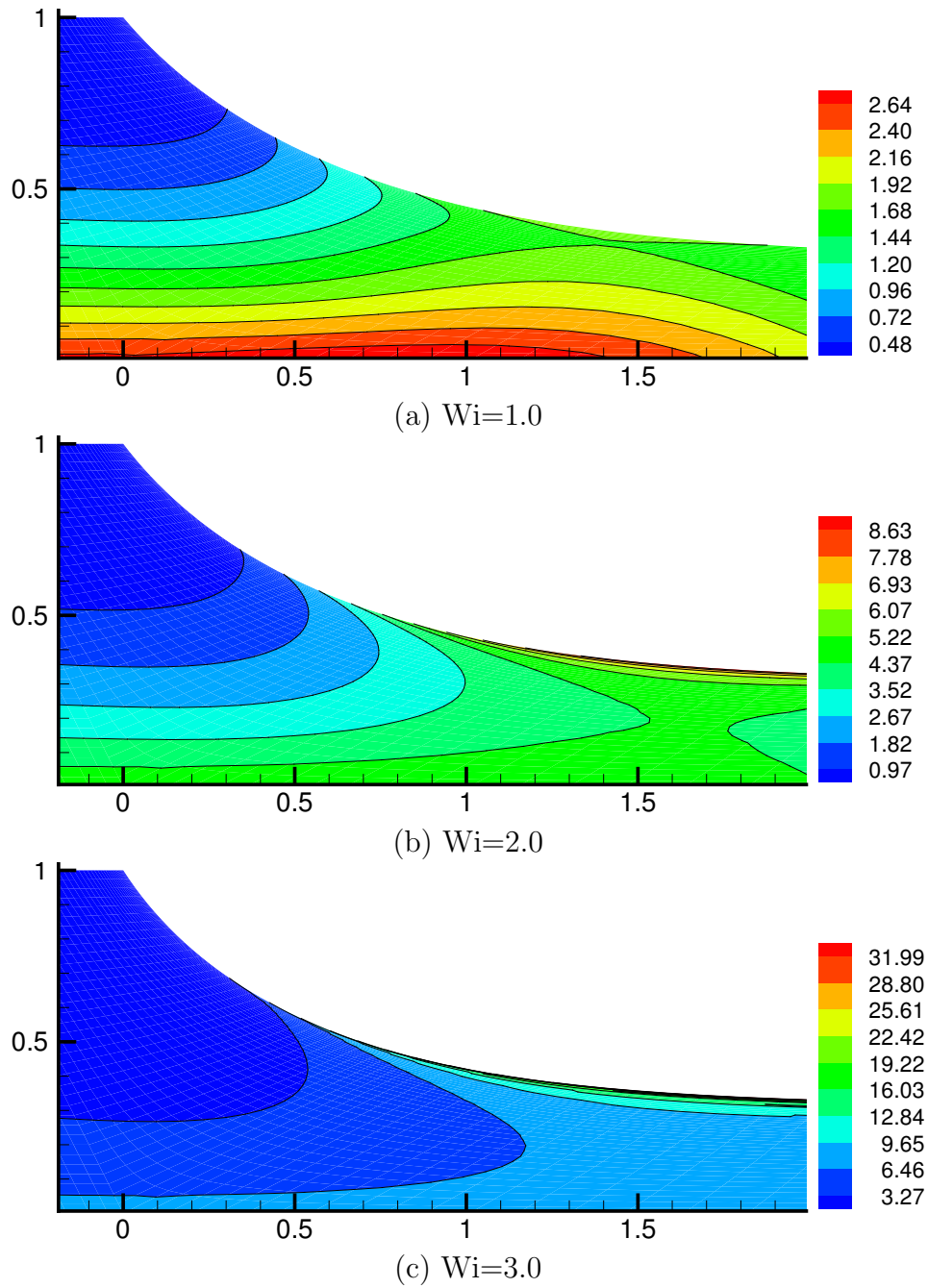
Figure 5.9: Evolution of the $xx$ component of the elastic stress ($\sigma_{xx}$) as a function of $Wi$ for an Oldroyd-B fluid. $Ca = 0.1$, $Q = 0.3$, $\beta = 0.75$.

(a) Wi=1.0

(b) Wi=2.0

(c) Wi=3.0
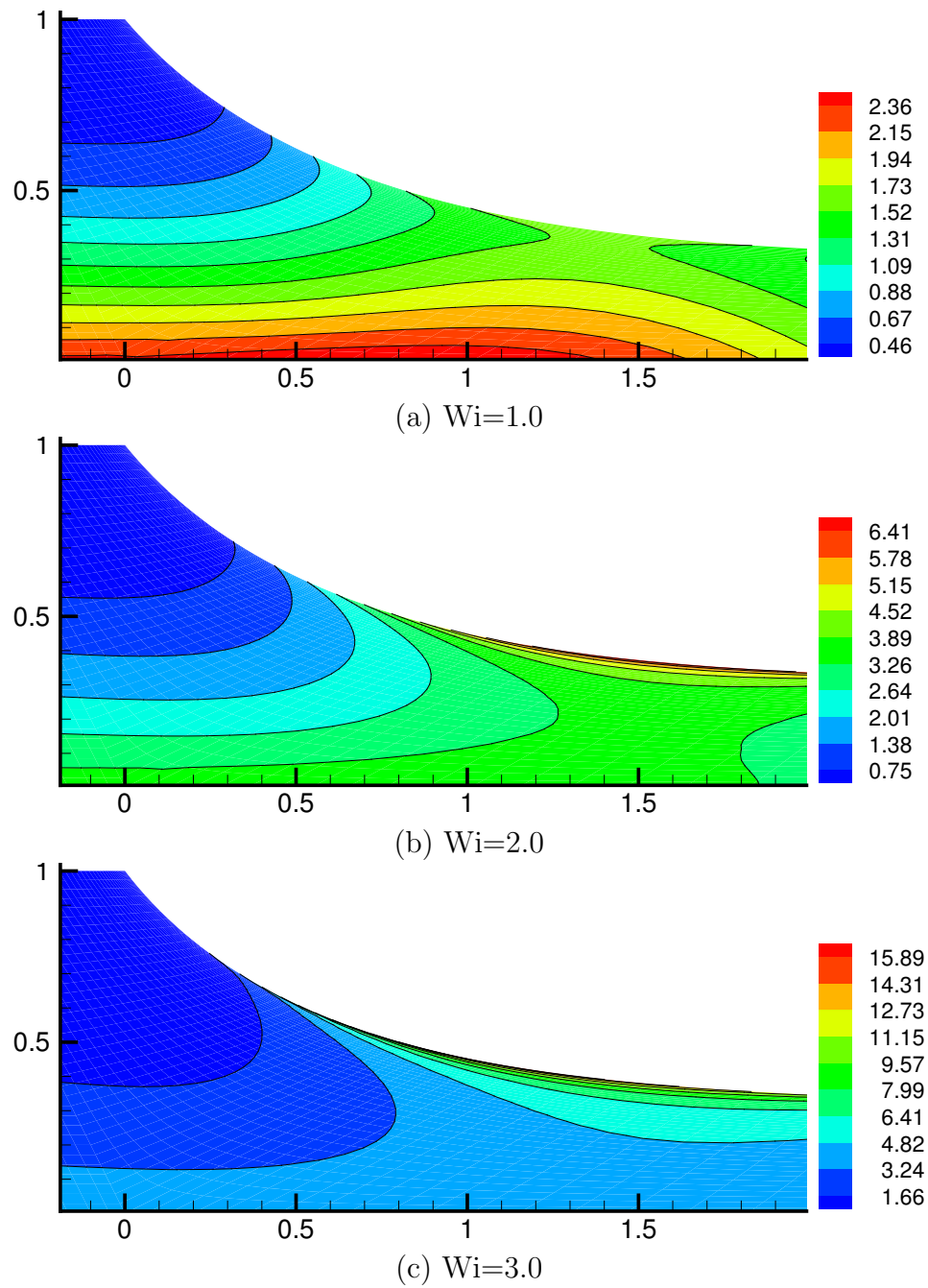
Figure 5.10: Evolution of the $xx$ component of the elastic stress ($\sigma_{xx}$) as a function of $Wi$ for the FENE-P fluid. $Ca = 0.1$, $Q = 0.3$, $\beta = 0.75$, $b_{\mathbf{M}} = 50$.

(irrespective of the actual position where it occurs). Because of the number of subtle features in Fig. 5.11, Fig. 5.12 displays the same data broken up into different regimes of magnitude of $Wi$. It is evident from the Fig. 5.11(a) that for a $Wi$ smaller than $\sim 1.5$, the rate of stretching (the largest eigenvalue of the conformation tensor) is independent of the viscosity ratio $\beta$ [more clearly shown in Fig. 5.12(a)]. Beyond $Wi=1.5$, a dependence on $\beta$ kicks in. As can be seen from Fig 5.12(b), the rate of stretching appears to decrease with increasing concentration (which correspondence to decreasing $\beta$). For $Wi > 2$, curves for different $\beta$ diverge sharply. The curves for smaller $\beta$ diverge more rapidly [see Fig. 5.12(e)]. Figure 5.11(b) which shows the change in smallest eigenvalue with $Wi$ for different $\beta$ reveals that $Wi$ at which the rate of stretching diverges corresponds to minimum eigenvalue becoming zero and the conformation tensor eventually loosing its positive definiteness [see Fig. 5.12(f)]. This implies that the $Wi$ at which the stretch starts to diverge, the gradient in the stress at the free surface becomes too steep to be captured with the most refined mesh (M4) used in this study. Hence, it can be concluded that for a $Wi < 1.5$, stretch of molecules is independent of viscosity ratio and for a $Wi > 1.5$ the rate of stretching decreases with increasing $Wi$ as the polymer solution become more and more concentrated (viscosity ratio $\beta$ goes from 1 to 0.25).

A careful investigation of Fig. 5.11(b) reveals that similar to the largest eigenvalue, the rate of change of the smallest eigenvalue with $Wi$ is different on the either side of $Wi \sim 0.7$ [more clearly shown in Figs. 5.12(b) & 5.12(d)] . The values $Wi \sim 1.5$ and $Wi \sim 0.7$, around which rate of stretching (i.e. the largest and smallest eigenvalue of the conformation tensor respectively) is different, are independent of the constitutive equation as shown in Figs. 5.13(a) and 5.13(b) for FENE-P model.

Figure 5.13(c) shows that the rate of change of the out-of-plane eigenvalue of the conformation tensor, predicted by the FENE-P model, becomes $\beta$ dependent around $Wi \sim 1.7$.

The two different regimes of the rate of stretching near the critical $Wi$, for a given $\beta$, can be explained by looking at the actual spatial position of the largest and smallest eigenvalues of the conformation tensor in the flow domain [Figs. 5.14(a)-5.14(d)]. The y-coordinate of the location of the largest and smallest eigenvalue in the flow domain [Figs. 5.14(a)-5.14(b)] reveals why the rate of stretching is different

around $Wi \sim 1.5$ and $Wi \sim 0.7$ for largest and smallest eigenvalues respectively. For $Wi < 1.5$, the largest eigenvalue remains at $Y = 0$ (on the moving web) independent of the viscosity ratio. On the web, the stretch of the molecules is dominated by shearing flow kinematics. With an increase in $Wi$ beyond 1.5, the largest eigenvalue abruptly jumps from $Y = 0$ to the free surface as shown in Fig. 5.14(d). The free surface profile in Fig. 5.14(d) is plotted for $\beta = 0.25$, $Wi = 2.0$. On the free surface, the flow kinematics is extensional in nature. Different flow kinematics at the web and the free surface lead to the different rates of stretching around $Wi \sim 1.5$ for a given $\beta$.

The transition in position of the smallest eigenvalue from the web to the free surface occurs at $Wi \sim 0.7$. However, the position of the smallest eigenvalue once more abruptly changes [see Fig. 5.14(b)] from the free surface to the static contact line when the smallest eigenvalue becomes very close to zero in strong extensional flows. The conformation tensor always losses it positive definiteness at the static contact line for $\beta < 1$ which is different from simulation of ultra-dilute solutions $\beta = 1$ where the conformation tensor losses it positive definiteness under the stretching section of the free surface as predicted earlier by Pasquali and Scriven [2002]. The behaviour of position of eigenvalues for FENE-P model with $b_{\mathbf{M}} = 50$ virtually coincides with those obtained with the Oldroyd-B model.

The contours plots displayed in Fig. 5.15 also demonstrate that for $Wi < 1.5$, molecules are predominantly stretched on the moving web [see Figure 5.15(a)] and for $Wi > 1.5$, molecules are stretched under the free surface [see Figure 5.15(b)]. Similar observations for smallest eigenvalue are evident from Figs. 5.15(c) & 5.15(d)

The x-coordinate of the largest [Figs. 5.16(a)] and the smallest [Figs. 5.16(b)] eigenvalues indicate that the position of both the eigenvalues on the free surface moves back (towards the die wall) as $Wi$ increase for all $\beta$ values. This can be understood by considering the position of the maximum molecular extension rate as shown in Fig. 5.17. Pasquali and Scriven [2002] have defined the mean ensemble molecular extension and shear rates as

$$\dot{\epsilon} \equiv |\mathbf{m}_3\mathbf{m}_3 : \mathbf{D}|; \quad \dot{\gamma} \equiv |\mathbf{m}_1\mathbf{m}_3 : \mathbf{D}| \tag{5.1}$$

where $\mathbf{m}_1$ and $\mathbf{m}_3$ are the eigenvectors associated with the smallest and largest

eigenvalues of the conformation tensor, respectively. For an Oldroyd-B fluid, the maximum molecular shear rate always remains on the web for all $Wi$ as previously shown by Pasquali and Scriven [2002] and Romero et al. [2004] and as shown in Fig. 5.17(a).

Figure 5.17(b) shows the evolution of the location of the maximum molecular extension rate as a function of $Wi$. At low $Wi$, the molecules stretch predominantly near the web where the rate of strain is highest and the flow is dominated by shear flow. At high $Wi$, the polymer molecules becomes more and more stretched and a thin layer of high molecular extension grows at the free surface. The maximum molecular extension rate always occur under the stretching section of the free surface i.e. downstream to the stagnation as shown in Fig. 5.18. An abrupt change in the position of the molecular extension rate explains why the largest and smallest eigenvalues of conformation tensor unexpectedly changes their positions from the moving web to the free surface.

An another observation from Figure 5.17(b) is that the molecular extension rate moves back towards to the static contact line, which explains behavior of the the x-position of the largest and smallest eigenvalues of the conformation tensor in Fig. 5.16.

## 5.3 Effect of Viscosity Ratio on Macroscopic Flow Properties

The strong extensional nature of flow close to the free surface strongly affects the flow field in the vicinity of the static contact line. The change in the flow behavior is analyzed here in terms of the stability criterion proposed by Graham [2003] and later used by Zevallos et al. [2005]. Although in a more conventional approach to the analysis of the stability of two dimensional flows, conservation equations are solved with respect to infinitesimal three-dimensional perturbations, we have restricted our discussion to the simple stability criteria proposed by Graham [2003] which analyzes the flow field close to the free surface in order to extract critical conditions.

Zevallos et al. [2005] combined the stability criteria proposed by Pitts and Greiller [1961] for Newtonian film splitting flow with the stability mechanism proposed by

Graham [2003] for viscoelastic free surface flows. The combined stability criteria proposed by Zevallos et al. [2005] is

$$\frac{dT_{rr}}{dr} - \rho g_r = H(\sigma_{\theta\theta} - \sigma_{rr}) - \rho g_r < \varsigma(\frac{dH}{dr} + N^2) \tag{5.2}$$

where, $H$ is the in-plane curvature of the film splitting meniscus, $r$ is the coordinate along the normal to the free surface (as shown in Fig. 5.19), $\sigma_{\theta\theta}$ is component of elastic stress along the free surface, $\sigma_{rr}$ is component of elastic stress along the normal to the free surface and $N$ is the wave number of the perturbation. The key idea of this analysis is the introduction of a local coordinate system at the free surface, allowing the incorporation of the normal stress difference at the free surface in the radial component of the momentum balance equation. This criteria correctly identifies the competition of forces at the free surface. While the large normal stress difference at the free surface destabilizes the flow, the capillary forces and the meniscus curvature variation with free surface position counteract this effect to stabilize the flow. Note that the $dH/dr$ term is irrelevant in slot coating flows.

Zevallos et al. [2005] studied viscoelastic roll coating flows in terms of Eq. (5.2) by assuming $dH/dr$ and $N$ to be zero, which implies that the the sign of normal stress difference dictates the flow stability in the absence of gravity. They showed that for given flow conditions, an increase in $Wi$ leads to a positive normal stress difference at the stagnation point causing recirculation to completely disappear.

The evolution of the difference between the normal stress components in the streamline direction $T_{tt}$ and perpendicular to streamline direction $T_{nn}$ along the free surface, as a function of $Wi$, is portrayed in Fig. 5.20. Fig. 5.20(b), the zoomed image of Fig. 5.20(a), is presented in order to show the normal stress difference behavior close to the static contact line. The normal stresses are a combination of pressure, normal viscous stresses and normal viscoelastic stresses. As discussed above the normal stress difference is the driving force for the meniscus instability [Graham, 2003; Romero et al., 2004]. With an increase in $Wi$ number, the normal stress difference along the free surface grows. An important observation from Fig. 5.20(b) is that close to the static contact line, the normal stress difference is negative ($T_{nn} > T_{tt}$) for small $Wi$ number. An increase in $Wi$ beyond $\sim 1$ eventually makes the normal stress in the streamline direction higher than the normal stress perpendicular to

the streamlines. As a result, the normal stress difference close to the contact line becomes positive. This flow state is the one at which the stagnation point moves from the free surface to the die wall. Romero et al. [2004] have predicted that in roll coating flows, for a given $Ca$, there is always a $Wi$ at which the value of $(T_{tt} - T_{nn})$ becomes positive which leads to a complete elimination of the recirculation present in the flow domain for a Newtonian liquid. Figure 5.21 shows the normal stress difference for the FENE-P model at $Wi = 2.0$. As expected the normal stress difference for the FENE-P model is smaller than for the Oldryod-B model because of the finite extensibility of molecules.

Figure 5.22 displays the effect of the viscosity ratio on normal stress difference at two different $Wi$ ($Wi = 0.5, 2.0$), for an Oldroyd-B liquid. Figures 5.22(c) and 5.22(d) are the zoomed images of Figures 5.22(a) and 5.22(b), respectively, and are presented here to show the stress field close to the static contact line. It is evident from Figs. 5.22(a) and 5.22(b) that for a given $Wi$, the normal stress difference increases with decreasing $\beta$. However, Fig. 5.22(c) indicates that for a given $Wi$, a reduction in $\beta$ leads to a positive normal stress difference in the vicinity of the static contact line. Similar behavior was observed for the FENE-P model.

Figure 5.23(a) shows the effect of viscosity ratio on the shape of the free surface (more clearly shown in Fig. 5.23(b) & Figure 5.23(c), the zoomed images of Fig. 5.23(a)). For the parameters studied in this work, the shape of the free surface is not significantly affected by the viscoelasticity. However we find, as Lee et al. [2002] and Romero et al. [2004] have predicted previously, the free surface moves into the die as viscoelasticity increases, close to the static contact line. Movement of the free surface causes a reduction in the contact angle and ultimately the detachment of the free surface from the die wall. A more detailed discussion on the effect of viscoelascity on contact angle will be presented shortly.

Figure 5.24 shows the effect of viscosity ratio on the largest eigenvalue of the rate of strain tensor. By decreasing the viscosity ratio, the largest eigenvalue of the rate of strain tensor decreases which explains the decrease in the rate of stretching with decreasing viscosity ratio [see Figs. 5.11 and 5.13].

Figure 5.25 shows the position of the stagnation point for an Oldroyd-B liquid as a function of $Wi$ number. For $Wi < 1$, the stagnation point is always on the

free surface. At $Wi \sim 1$, the stagnation point moves to the static contact line and with further increase in $Wi$ ($Wi > 1$), the stagnation point moves to the die wall. It is worth mentioning that as long as $(T_{nn} - T_{tt})$ is negative [see Fig. 5.20 (b)], the stagnation point is on the free surface and when the $(T_{nn} - T_{tt})$ becomes positive, the stagnation point jumps to the die wall. The strong extensional stresses arising from the viscoelastic nature of the fluid pulls the liquid out of the recirculation region and the recirculation zone shrinks as depicted in Fig. 5.26. For $Wi > 1$, the recirculation region attached to the static contact line completely disappears.

The effect of the viscosity ratio and the constitutive model on the size of the recirculation zone is shown in Fig. 5.27. Due to the higher normal stress difference at smaller $\beta$, the recirculation zone size is much smaller for $\beta = 0.25$ than it is for $\beta = 0.75$. For $Wi = 2.0$, the stagnation point has moved to $x = -0.5$ at $\beta = 0.25$ from $x = -0.24$ at $\beta = 0.75$ as shown in Fig. 5.27. Similar behavior can be seen for the FENE-P model.

The consequence of the shrinking of the recirculation zone is that it exposes the geometric singularity that is present in slot coating flows. In slot coating flows, a geometric singularity arises due to the imposition of an inappropriate boundary condition on the die wall and the free surface. While moving from the die wall to the free surface, the boundary condition changes from a no-slip boundary at the die wall to the shear-free condition on the free surface. Pasquali and Scriven [2002] predicted that for an ultra-dilute solution, the geometric singularity at the static contact line does not affect viscoelastic flow calculations when recirculation is present under the die (which occurs for $Q < 0.33$). An analysis of the flow field for an Oldroyd-B liquid near corners (formed by the intersection of a slip surface with either a no-slip or a shear-free boundary) by Salamon et al. [1997a] revealed that for dilute and ultra-dilute solutions both stress and flow fields have a singularity at the point of intersection of the free surface and the solid surface in the absence of the recirculation. They found that the strength of the singularity depends upon the dimensionless solvent viscosity (defined as $\beta$ in this work) and in particular, for dilute solutions, the singularity in the rate-of-strain and elastic stress fields scale with $1/\beta$

At high $Wi$, the recirculation region close to static contact line disappears and

thus exposes the geometric singularity to a recirculation free flow which is relatively strong. Both the field variables the rate-of-strain and the conformation tensor for the Oldroyd-B and the FENE-P liquids are plotted in Figs. 5.28 and 5.29, respectively, as a function of the x-position along the free surface. It is evident that the field variables become singular as the static contact line is approached. It should be noted that at $Wi = 2.0$, the recirculation has completely disappeared from the vicinity of the static contact line for all values of $\beta$ studied in this work [see Fig. 5.27]. It is also clear from the Fig. 5.28 that the strength of singularity is much higher for a smaller $\beta$ value which is consistent with the findings of Salamon et al. [1997a].

The relatively higher strength of the singularity in field variables and the requirement of refined meshes to capture higher normal stresses along the free surface explains why the conformation tensor becomes negative definite at a much smaller $Wi$ for decreasing values of $\beta$ [see Fig. 5.4 & 5.6].
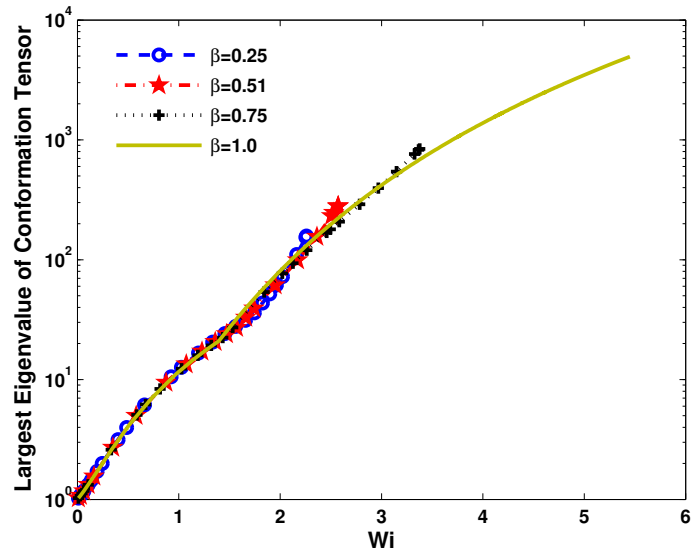
(a) Largest Eigenvalue
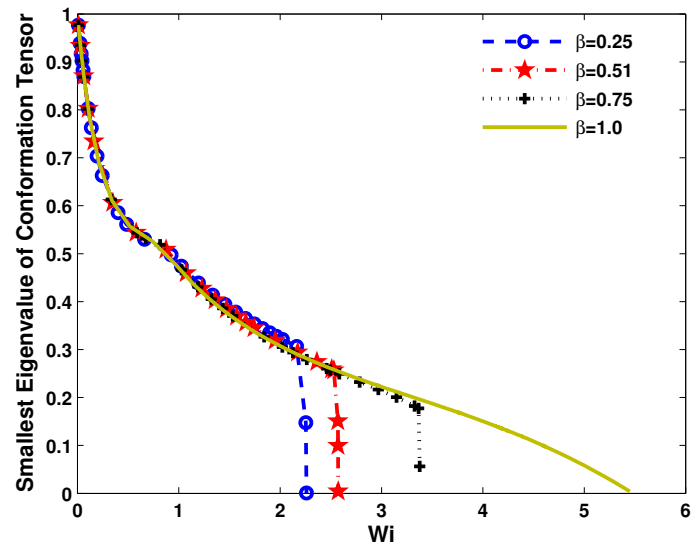


(a) Smallest Eigenvalue

Figure 5.11: Effect of viscosity ratio ($\beta$) on the stretch (largest eigenvalue on top and smallest eigenvalue at the bottom) of the molecule for an Oldryod-B fluid. $Ca = 0.1$, $Q = 0.3$.
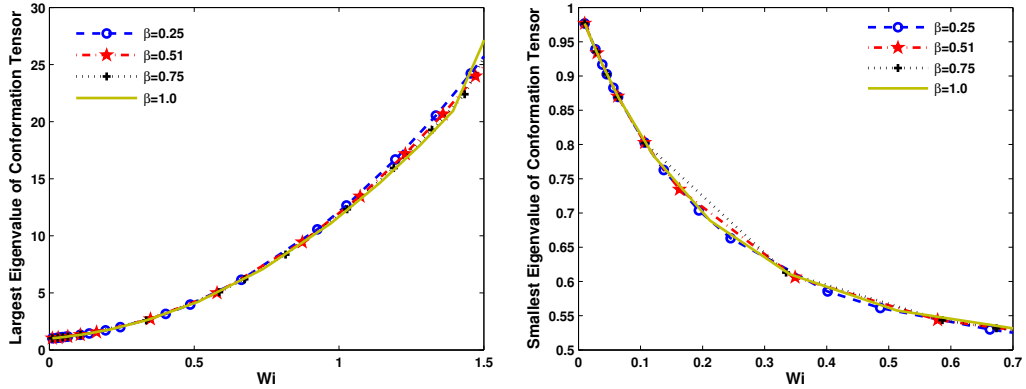
(a) Largest Eigenvalue, $Wi <\sim 1.5$  (b) Smallest Eigenvalue, $Wi >\sim 0.7$
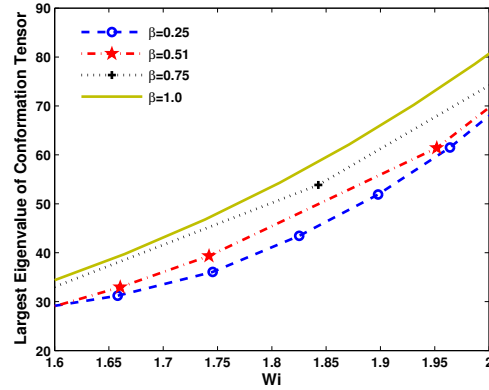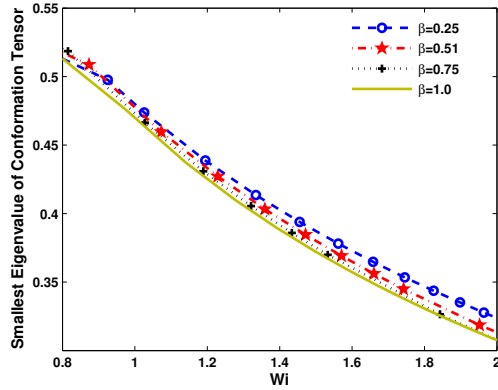
(c) Largest Eigenvalue $Wi >\sim 1.5$  (d) Smallest Eigenvalue, $Wi >\sim 0.7$
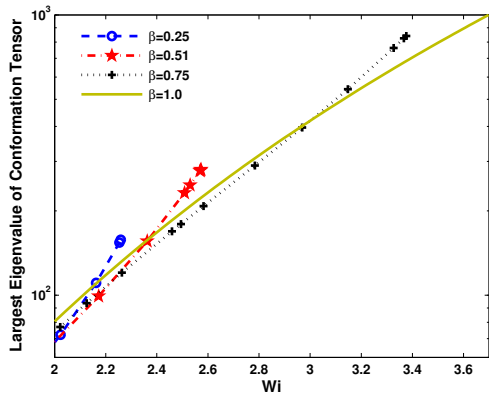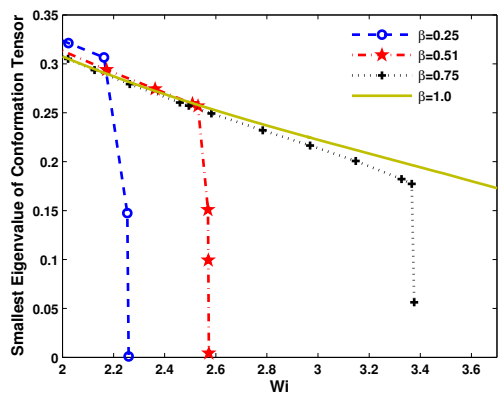
(e) Largest Eigenvalue $Wi >\sim 2$  (f) Smallest Eigenvalue, $Wi >\sim 2.0$

Figure 5.12: Effect of viscosity ratio ($\beta$) on the stretch of the molecule for an Oldroyd-B fluid. Zoomed images of Fig. 5.11 $Ca = 0.1$, $Q = 0.3$.
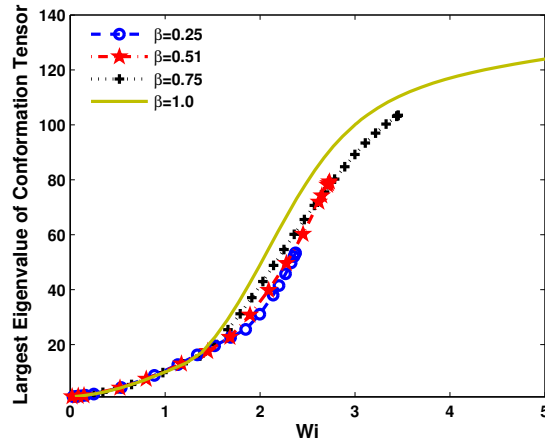
(a) Largest Eigenvalue
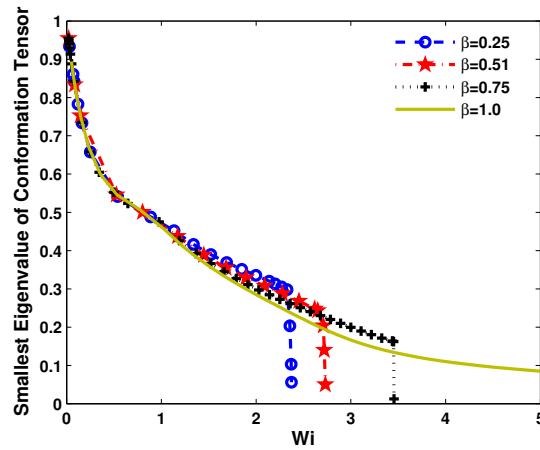


(b) Smallest Eigenvalue
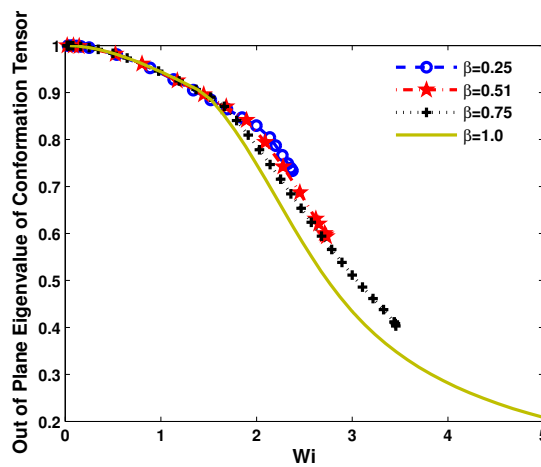


(c) Out-of-Plane Eigenvalue

Figure 5.13: Effect of viscosity ratio ($\beta$) on the stretch of the molecule for a FENE-P fluid. For $\beta = 1$, the stretch is plotted up to $Wi = 5$. Note that the maximum $Wi$ for $\beta = 1$ is $\sim 10$ as shown in Fig. 5.4. $Ca = 0.1$, $Q = 0.3$, $b_{\mathbf{M}} = 50$.
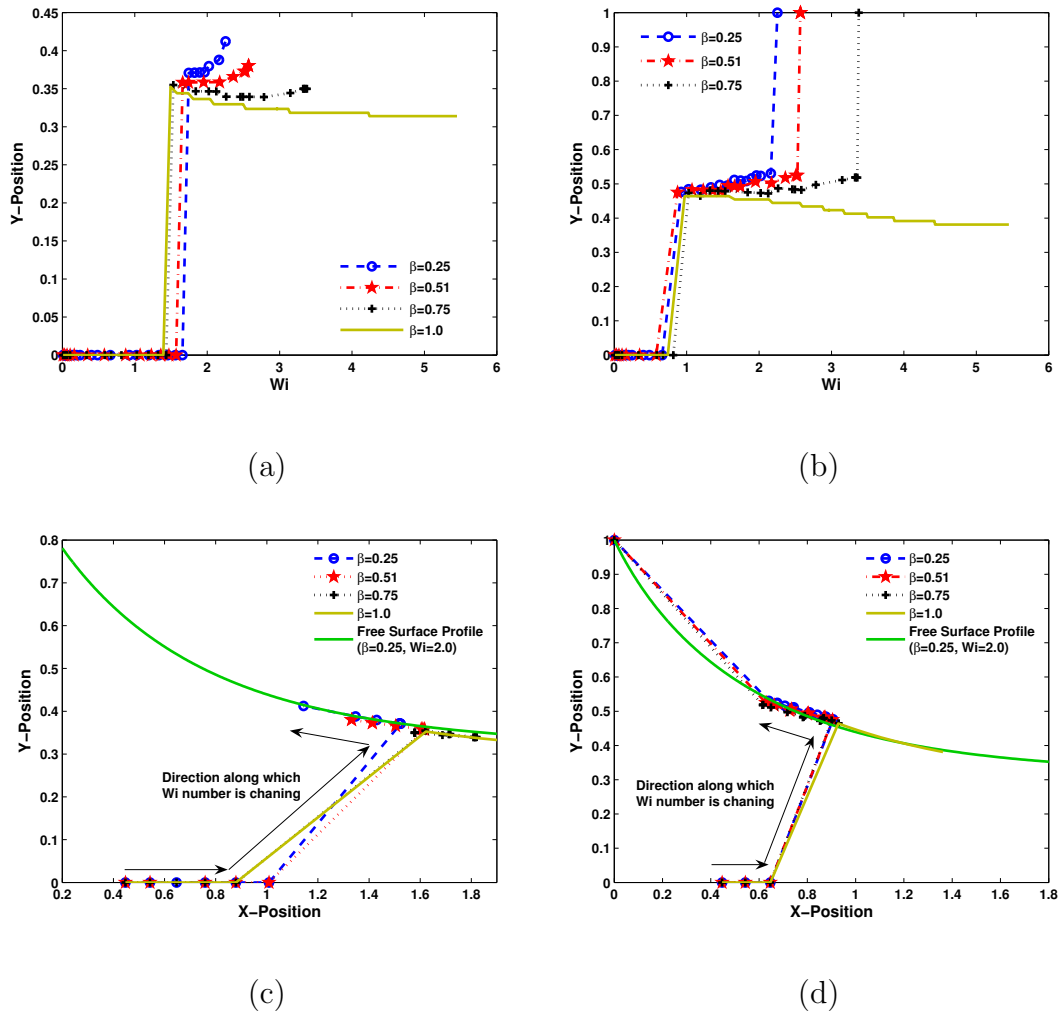
Figure 5.14: Change in spatial position of the location of the largest (a & c) and smallest (b & d) eigenvalues of the conformation tensor as a function of *Wi* for an Oldroyd-B fluid. $Ca = 0.1$, $Q = 0.3$.

(a) Wi=0.5 (Largest Eigenvalue)

(b) Wi=2.0 (Largest Eigenvalue)

(c) Wi=0.5 (Smallest Eigenvalue)

(d) Wi=2.0 (Smallest Eigenvalue)
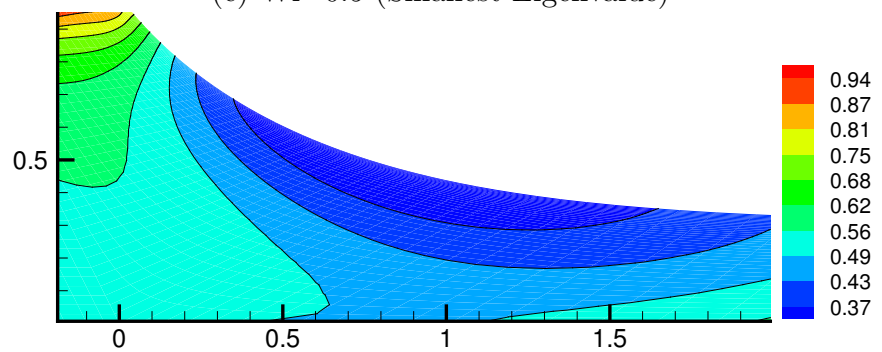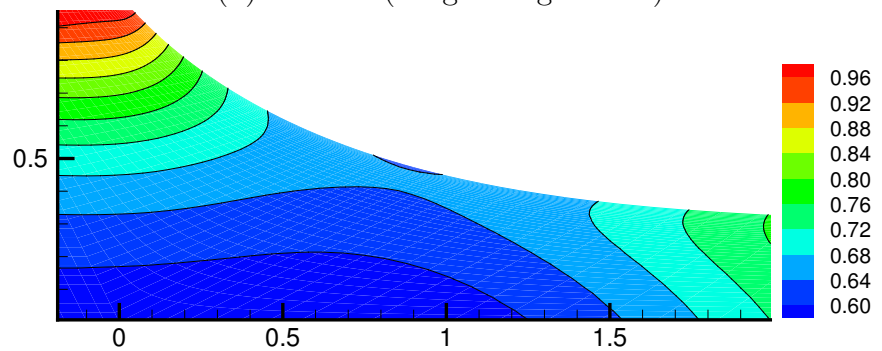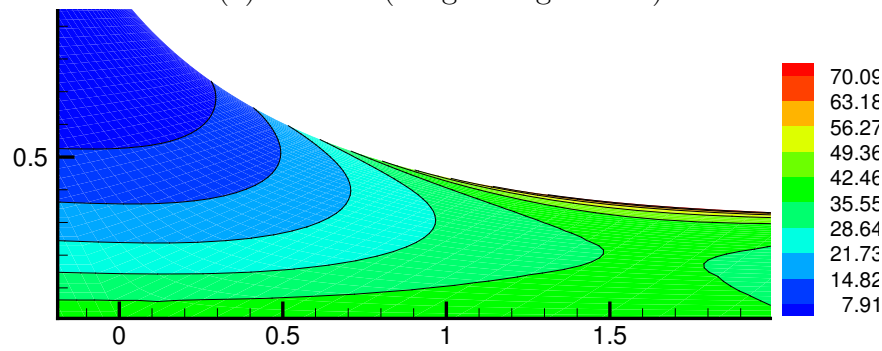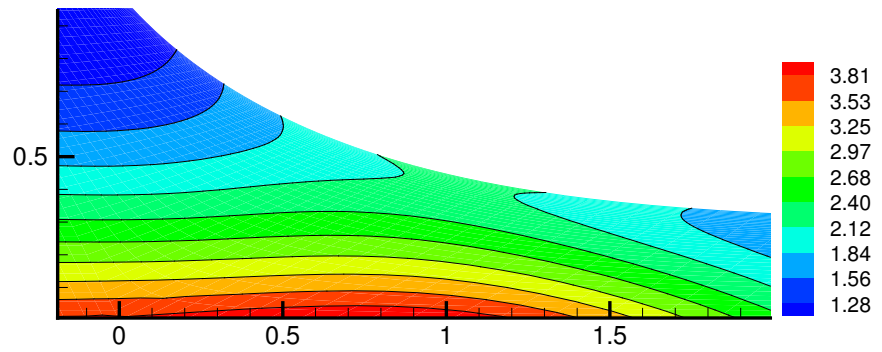
Figure 5.15: Contours of the stretch of the polymer molecules (largest eigenvalue in a & b and smallest eigenvalue in c & d) for an Oldroyd-B fluid. $Ca = 0.1$, $Q = 0.3$, $\beta = 0.75$.
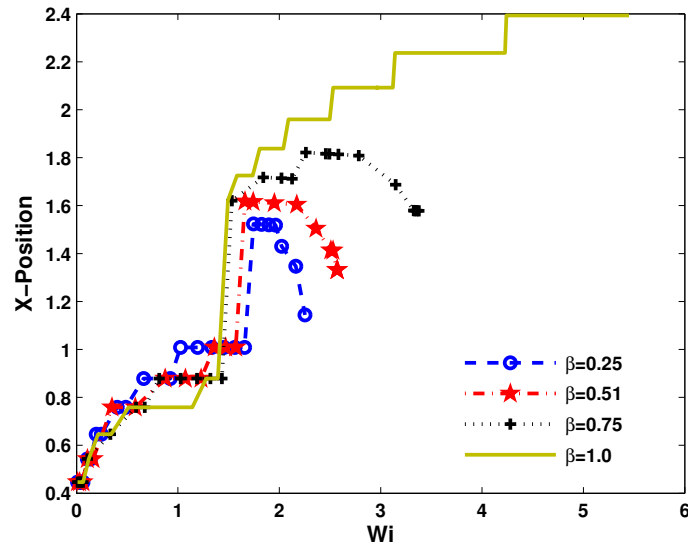
(a) Largest Eigenvalue
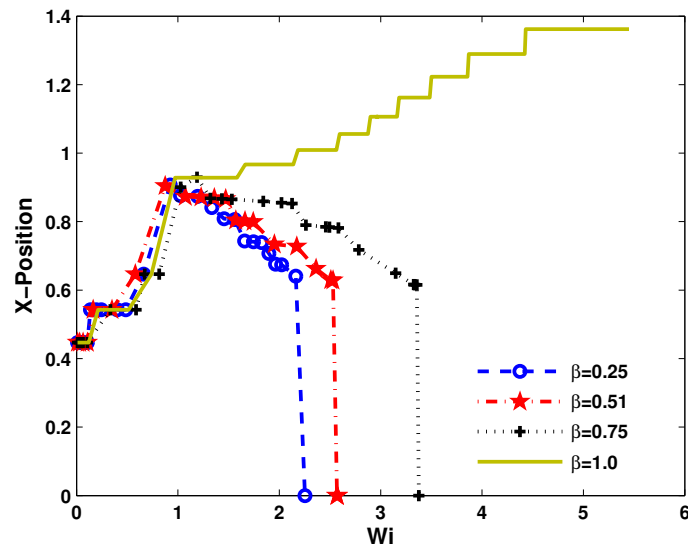


(b) Smallest Eigenvalue

Figure 5.16: Change in the X position of the location of the largest (Top) and smallest (Bottom) eigenvalues of the conformation tensor as a function of $Wi$ for an Oldroyd-B fluid. $Ca = 0.1$, $Q = 0.3$.
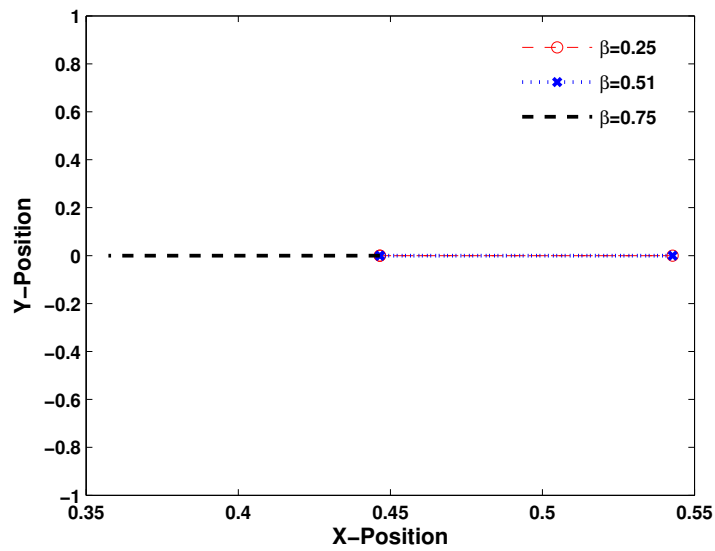
(a) Molecular Shear Rate
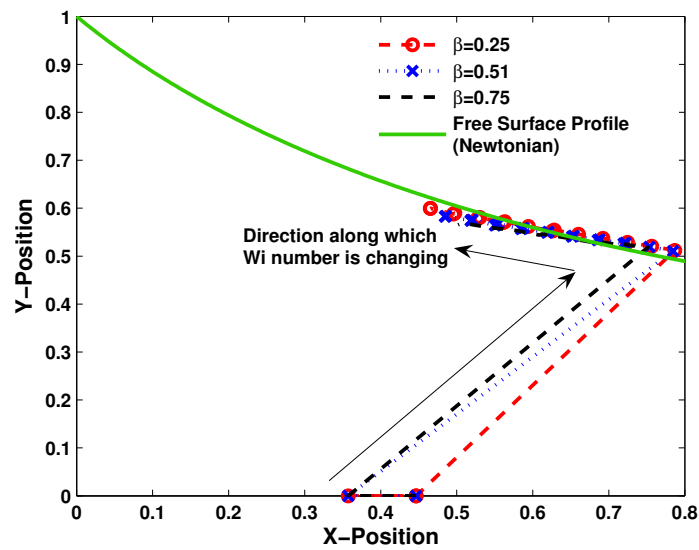


(b) Molecular Extension Rate

Figure 5.17: Change in the spacial position of the maximum molecular shear (top) and extension rate (bottom) with $Wi$ number for different values of $\beta$. $Ca = 0.1$, $Q = 0.3$.
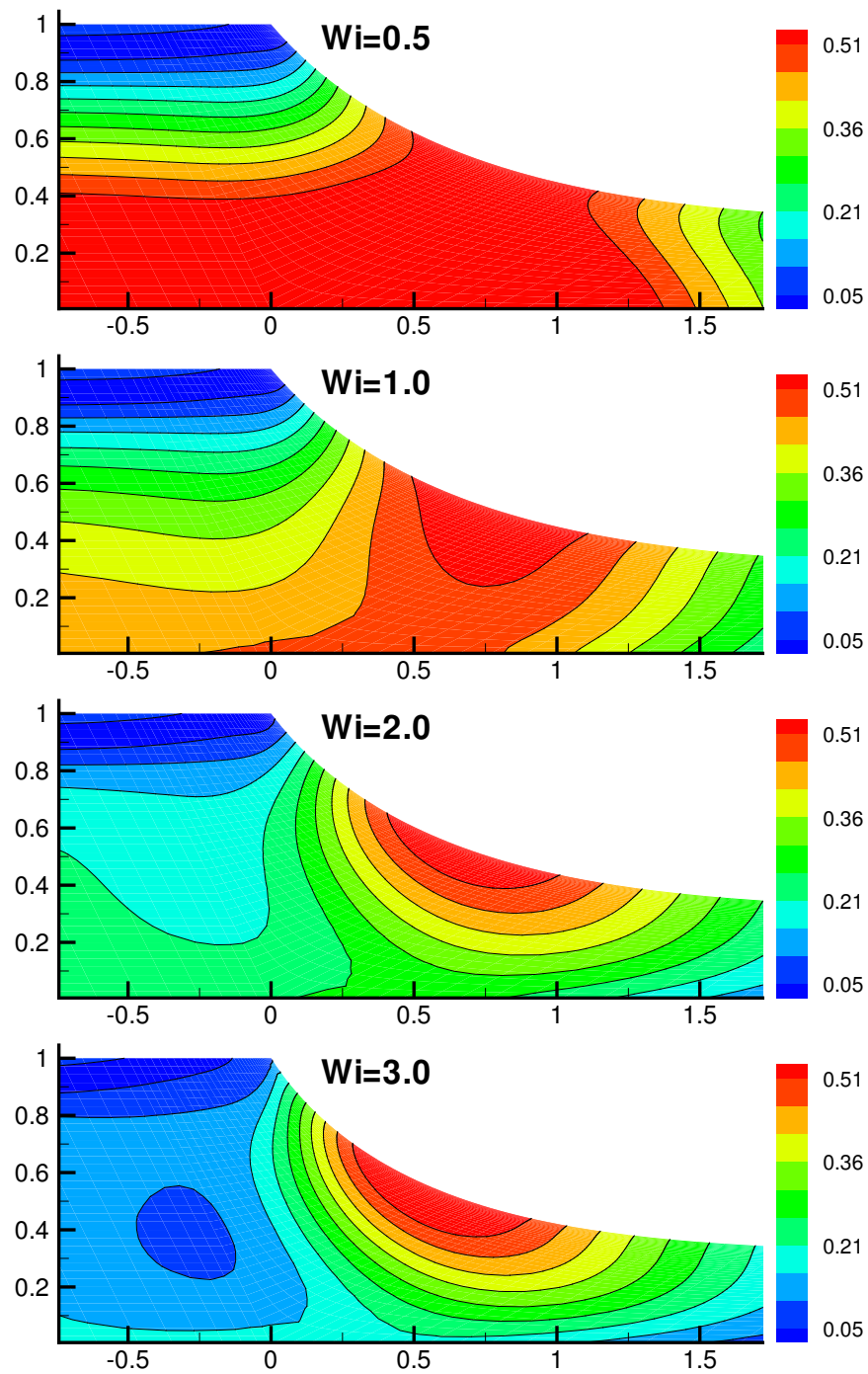
Figure 5.18: Molecular extension rate as a function of *Wi* number for Oldroyd-B liquid. $Ca = 0.1$, $Q = 0.3$, $\beta = 0.75$.
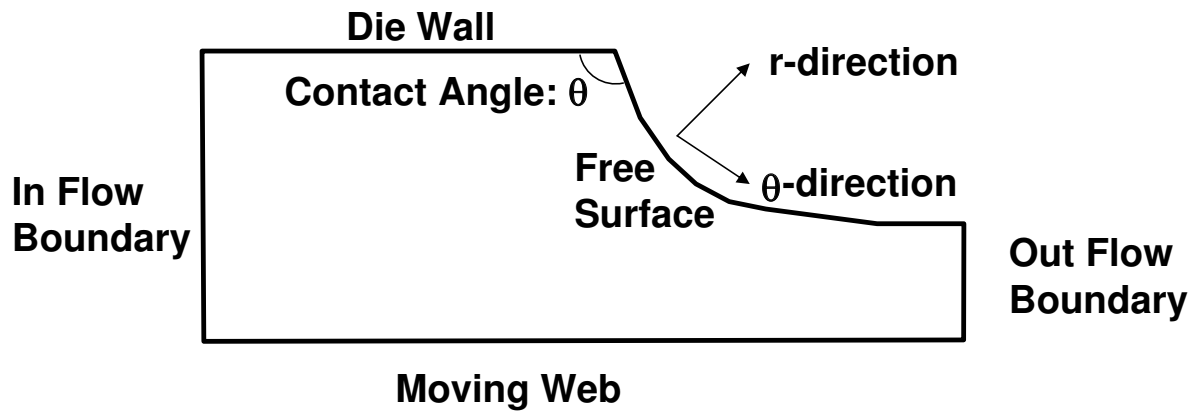
Figure 5.19: Schematic of the local coordinates (r, $\theta$) used by Graham [2003] to analyze free surface flow instabilities. Figure also shows the contact angle (the angle between the die wall and the free surface).



(a)                                        (b)
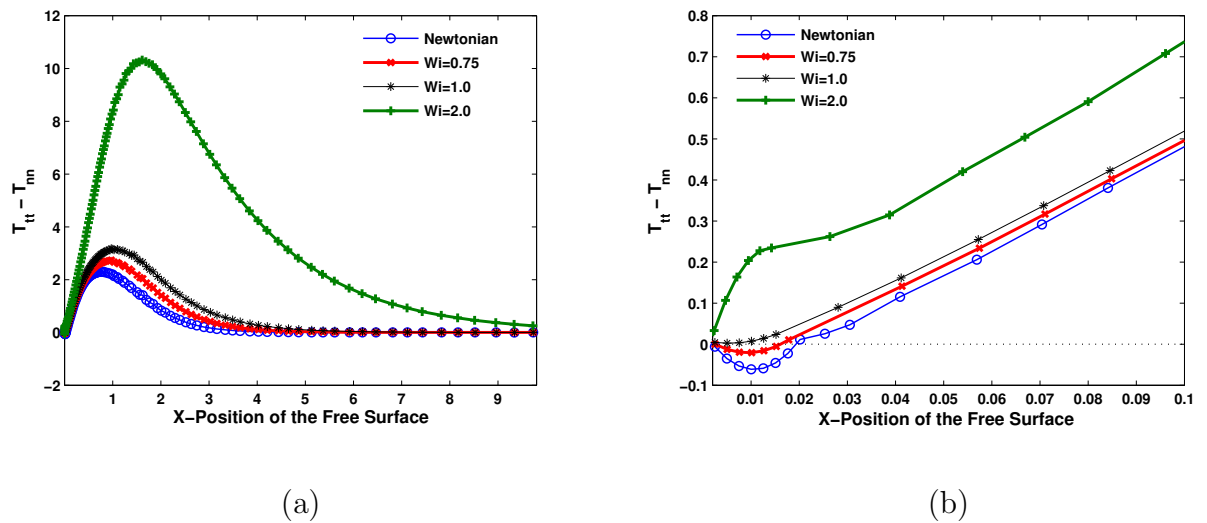
Figure 5.20: Normal stress difference along the free surface as a function of $Wi$ for an Oldroyd-B fluid. Figure (b) shows the zoomed image of (a) closed to the static contact line. $Ca = 0.1$, $Q = 0.3$, $\beta = 0.75$.
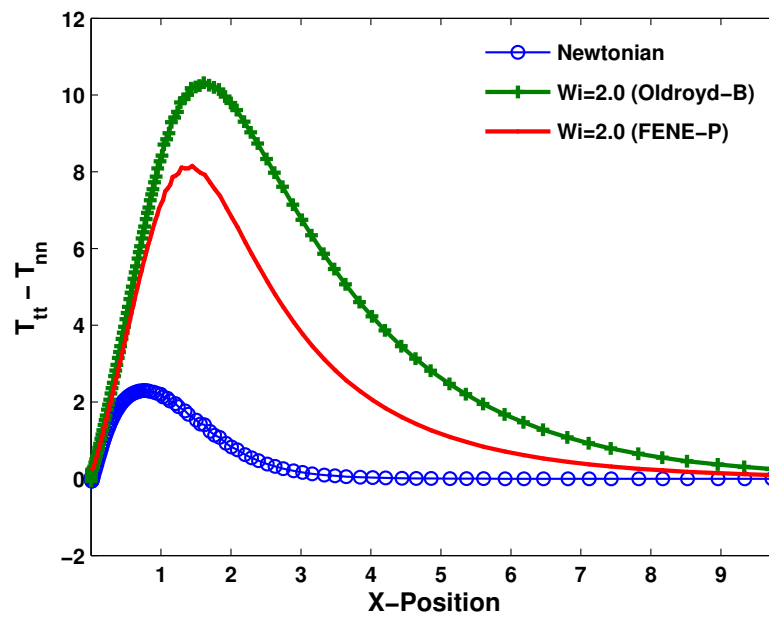
Figure 5.21: Normal stress difference along the free surface for different constitutive equations. $Ca = 0.1$, $Q = 0.3$, $\beta = 0.75$, $b_{\mathbf{M}} = 50$.
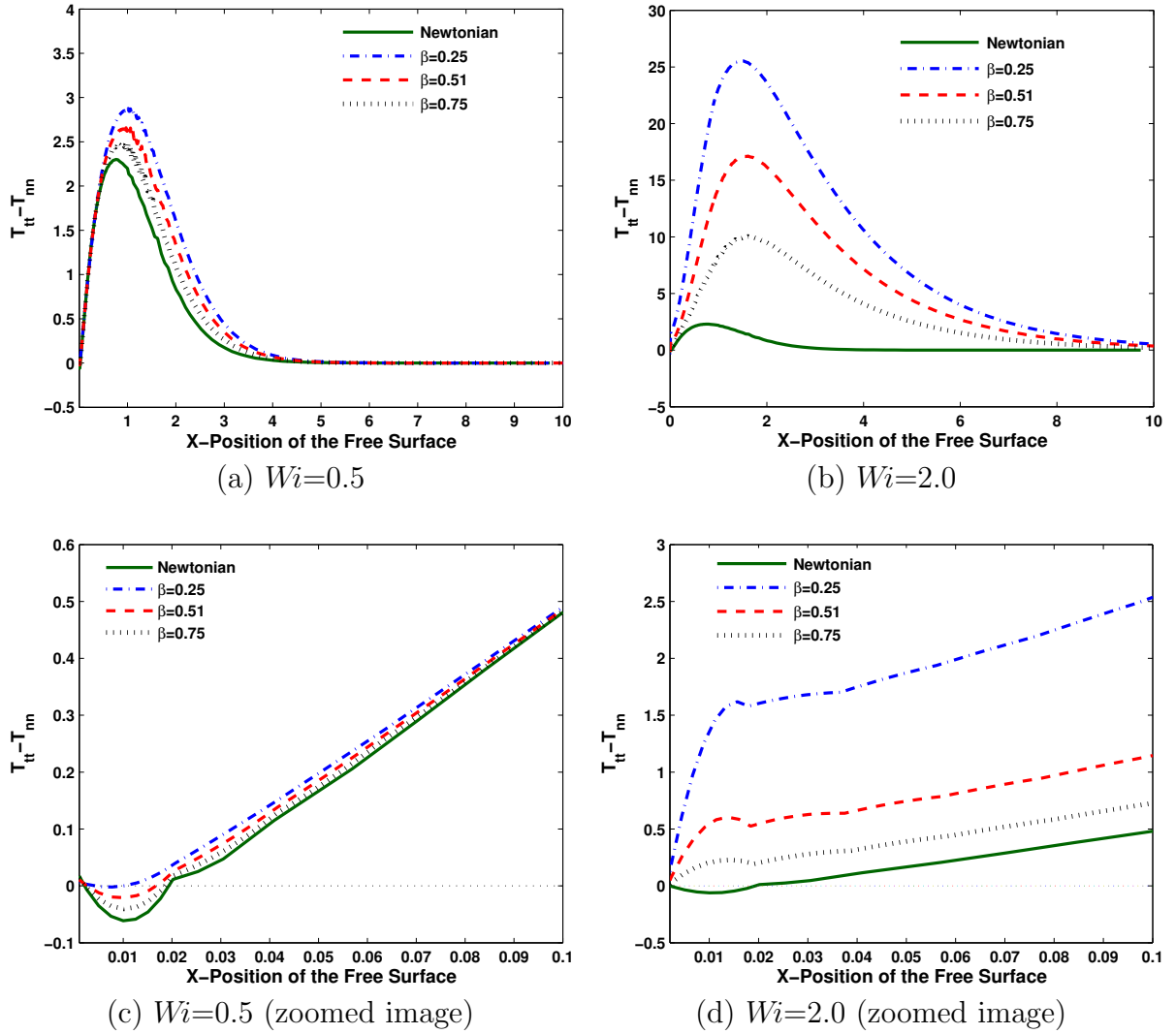
Figure 5.22: Normal stress difference along the free surface as a function of viscosity ratio for an Oldroyd-B fluid. $Ca = 0.1$, $Q = 0.3$.
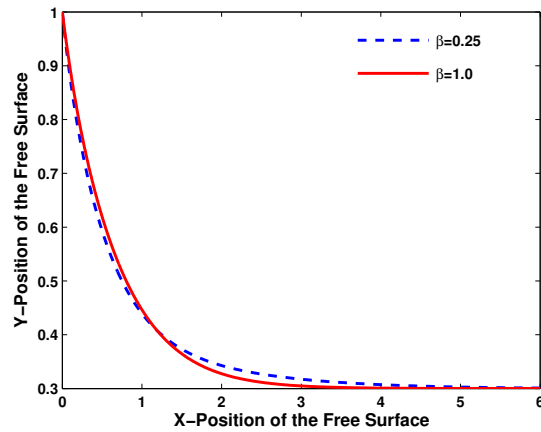
(a)
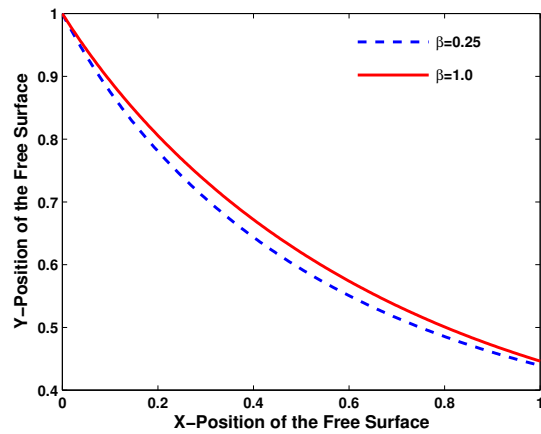


(b) Zoomed image of (a) close to the contact line ($x = 0$)
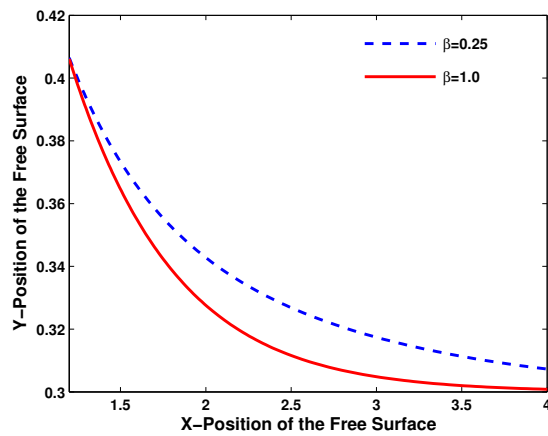


(c) Zoomed image of (a) downstream the contact line

Figure 5.23: Effect of polymer viscosity on the shape of the free surface for an Oldroyd-B fluid. $Wi = 2.0$, $Ca = 0.1$, $Q = 0.3$ .
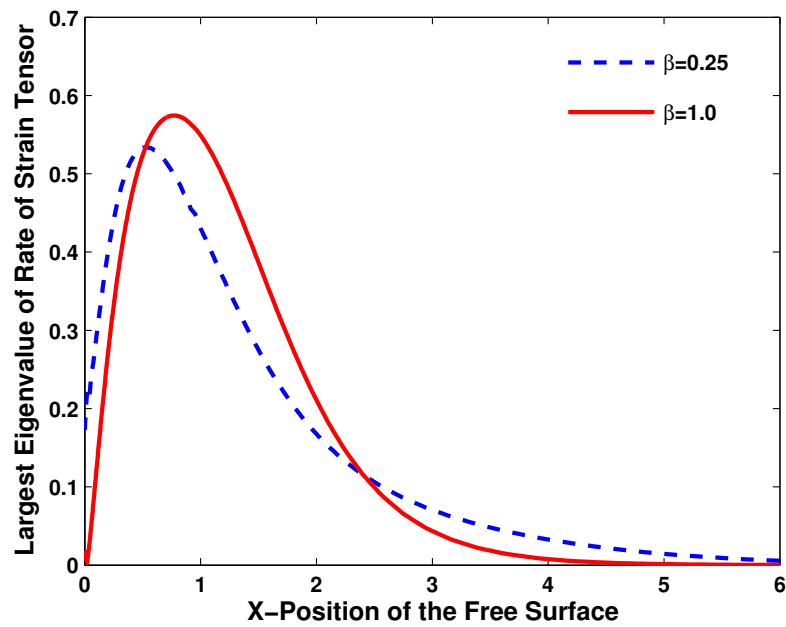
Figure 5.24: Effect of viscosity ratio on the largest eigenvalue of the rate of strain-rate tensor along the free surface for an Oldryod-B fluid. $Wi = 2.0$, $Ca = 0.1$, $Q = 0.3$.
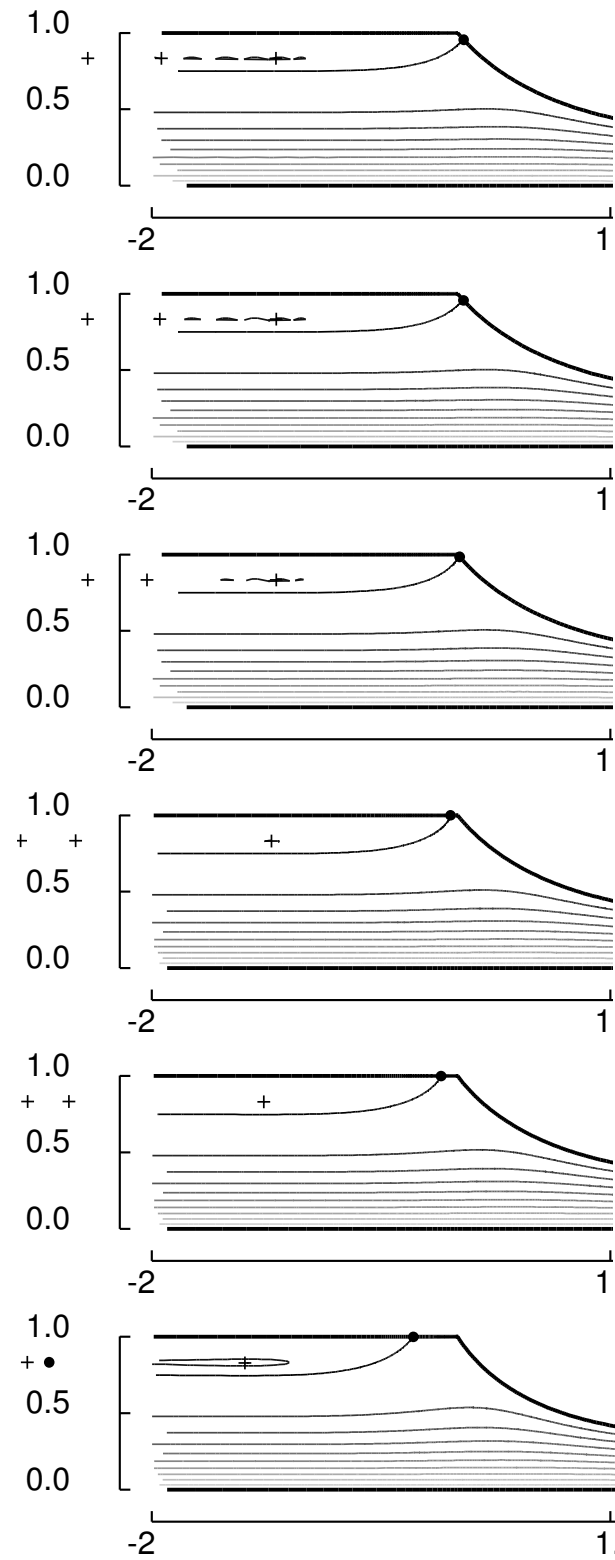
Figure 5.25: Movement of the stagnation point for an Oldroyd-B liquid. The dark filled circle denotes the stagnation point. $Ca = 0.1$, $Q = 0.3$, $\beta = 0.75$. From top to bottom $Wi = 0.0$ (Newtonian), $Wi = 0.75$, $Wi = 1.0$, $Wi = 1.5$, $Wi = 2.0$, $Wi = 3.0$
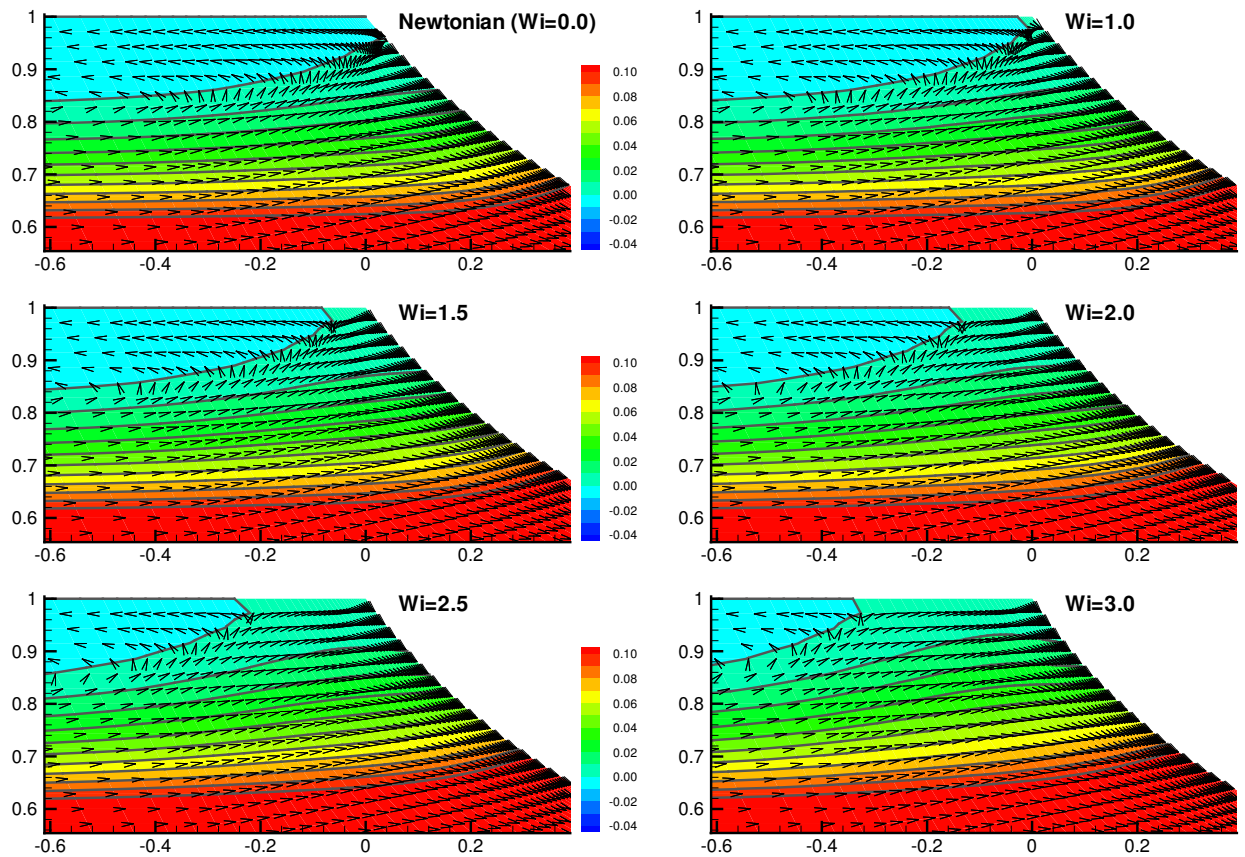
Figure 5.26: Change in velocity profile by changing the $Wi$ for Oldroyd-B. $Ca = 0.1$, $Q = 0.3$, $\beta = 0.75$.
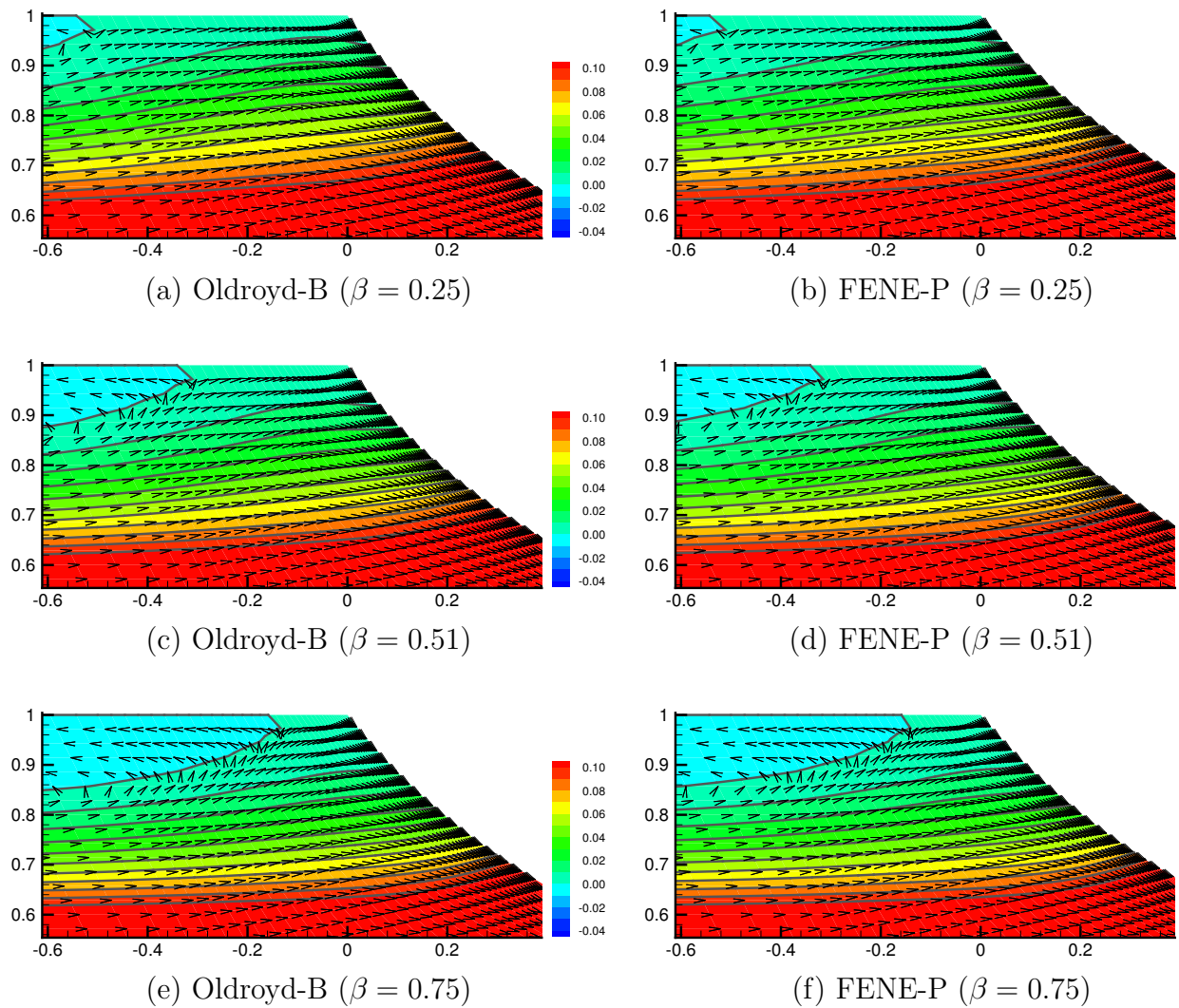
Figure 5.27:   Change in velocity profile by changing the viscosity ratio for the Oldroyd-B and the FENE-P fluid. $Wi = 2.0$, $Ca = 0.1$, $Q = 0.3$, $b_{\mathbf{M}} = 50$.
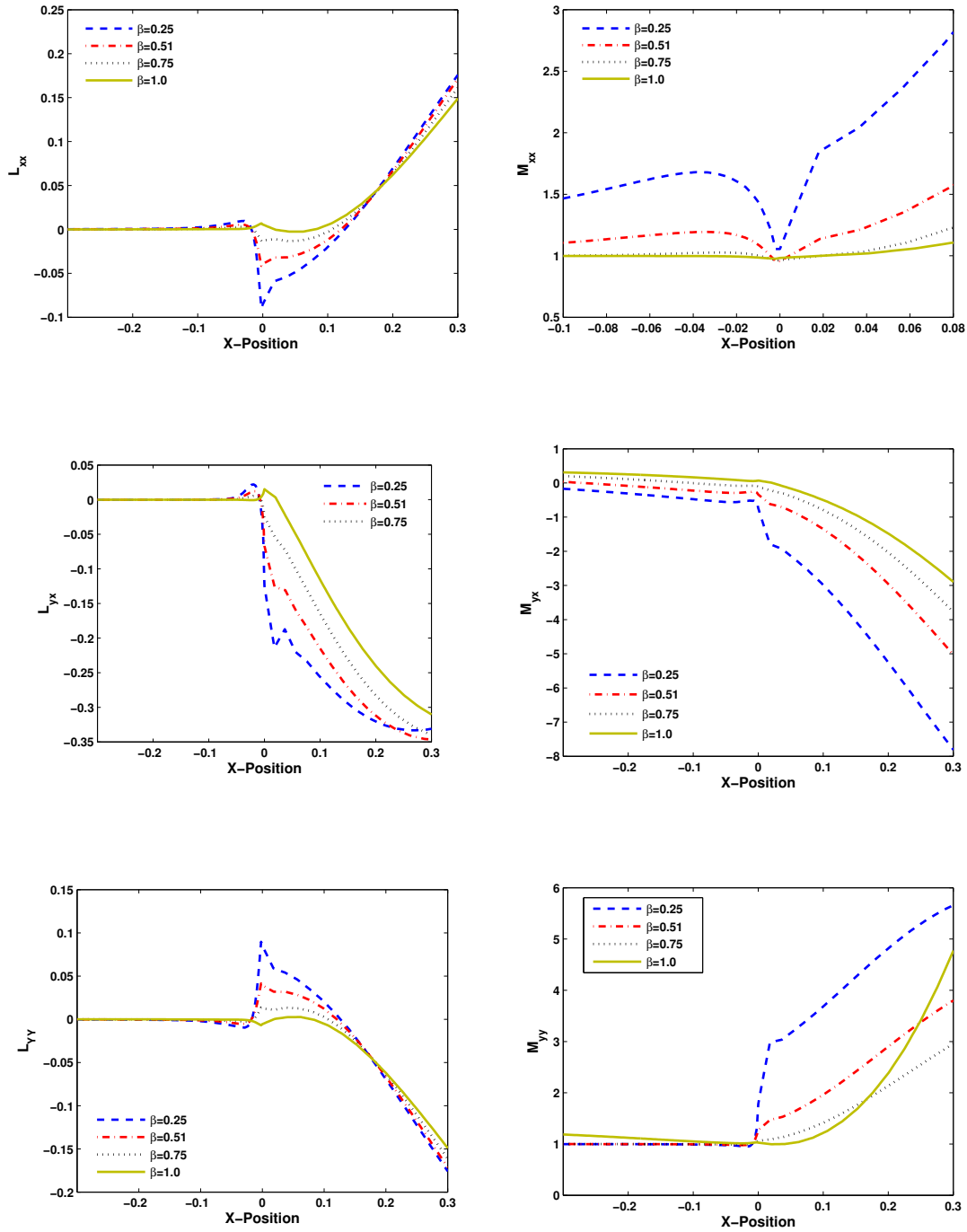
Figure 5.28: Components of velocity gradient (Left) and conformation tensor (Right) for an Oldroyd-B fluid. X-axis shows the x-coordinate of the position while moving from the die wall to the free surface. $X = 0$ is static contact line. $Wi = 2.0$, $Ca = 0.1$, $Q = 0.3$.

## 5.4   Effect of $Ca$ Number

Here, we analyze the effect of $Ca$ on various microscopic and macroscopic flow properties. Two different Capillary number namely, $Ca = 0.1$ and $Ca = 0.5$ are chosen for this.

Figure 5.30 shows the effect of $Ca$ on the free surface shape for a Newtonian liquid. An increase in $Ca$, from 0.1 to 0.5, causes an increase in adverse pressure gradient at the meniscus. Hence, for a given surface tension, the free surface curves more in order to balance the increased pressure gradient and the free surface moves into the die (meniscus invasion).

The meniscus invasion cause the rate of strain or the velocity gradient to increase as shown in Fig. 5.31(a). Figures 5.31(b) & 5.31(c) show the contours of the largest eigenvalue of the rate of strain tensor for a Newtonian liquid. It is evident from Figs. 5.31(b) & 5.31(c) that the maximum rate of strain is always on the moving web under the stretching section of the free surface.

The increase in the rate of strain by increasing the $Ca$ significantly affects the flow behaviour of viscoelastic liquid. Figure 5.32 shows the effect of $Ca$ on the stretch of polymer molecules and the normal stress difference along the streamlines on the free surface for an Oldroyd-B fluid. As expected, because of the higher rate of strain, both the stretch and the stress are much higher for $Ca = 0.5$ compared to those for $Ca = 0.1$.

The normal stress difference arising because of the viscoelastic nature of the fluid contributes to the net pressure gradient at the free surface. In order to balance the increased pressure gradient due to the viscoealasticiy of the fluid, the free surface has to curve more compared to that for a Newtonian liquid. The effect of viscoelasticity on meniscus invasion is displayed in Fig. 5.33 for two different $Ca$. While at smaller $Ca$, the surface forces are high enough to balance the increased pressure difference without much change in the curvature of the free surface [shown in Fig. 5.33 (a)], at high $Ca$ number (smaller surface forces), the free surface has to curve more for viscoelastic liquids compared to that for Newtonian fluids [shown in Fig. 5.33 (b)].

The effect of the $Ca$ on the size of the recirculation zone is displayed in Fig. 5.34. It is clear from the figure that the reduction in the size of the recirculation zone for viscoelastic liquids at high $Ca$ is much more compared to its size reduction for smaller
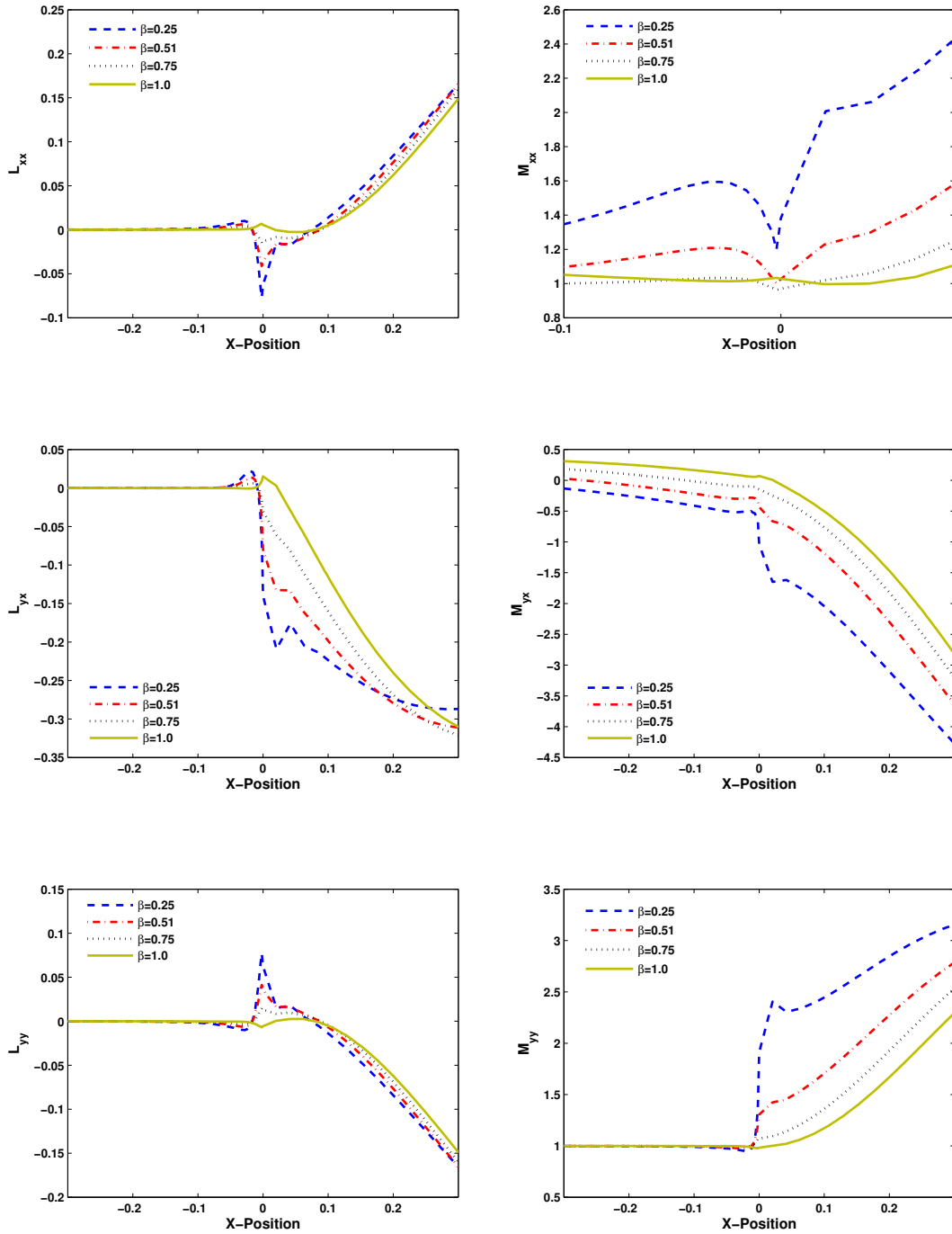
Figure 5.29: Components of velocity gradient (Left) and conformation tensor (Right) for the FENE-P fluid. X-axis shows the x-coordinate of the position while moving from the die wall to the free surface. $X = 0$ is static contact line. $Wi = 2.0$, $Ca = 0.1$, $Q = 0.3$, $b_\mathbf{M} = 50$.
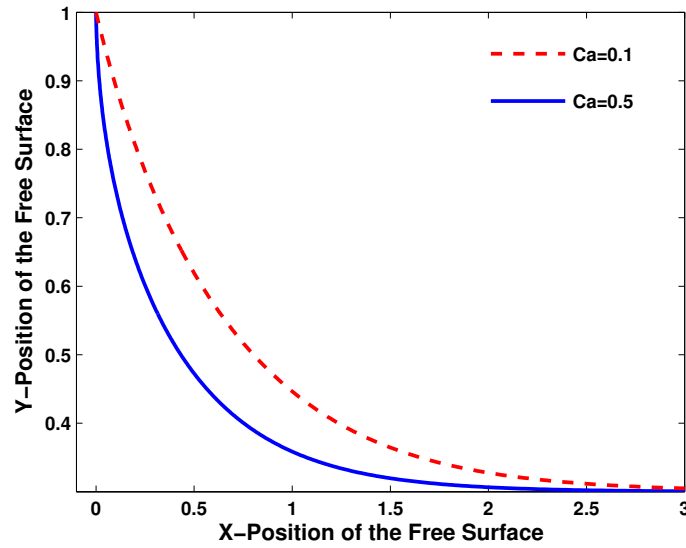
Figure 5.30: Effect of $Ca$ number on the free surface shape for Newtonian fluid. $Q = 0.3$.

$Ca$ which can be attributed to the higher normal stress difference for $Ca = 0.5$.

## 5.5   Low Flow Limit of Slot Coating Flows

The viscoelastic nature of the coating fluid not only affects the flow behavior but also the so called low-flow limit of slot coating. The low-flow limit is an important operating limit in designing the coating window, and is defined as the minimum thickness that can be coated at a given substrate speed [Carvalho and Kheshgi, 2000; Higgins and Scriven, 1980; Romero et al., 2004; Ruschak, 1976]. Knowledge of the coating window is necessary in order to predict whether the coating operation can be used at a given production rate for uniform coating. Carvalho and Kheshgi [2000] and Romero et al. [2004] have discussed the design of a stable coating window for slot coating flows. The threshold on the low-flow limit is described by the viscocapillary model first proposed by Landau and Levich [1942]. Ruschak [1976] extended the work of Landau and Levich [1942] and showed that the critical gap to thickness ratio is given by

$$\frac{t_{\min}}{H_0} = \frac{1}{1 + 1.49 Ca^{-2/3}} \tag{5.3}$$
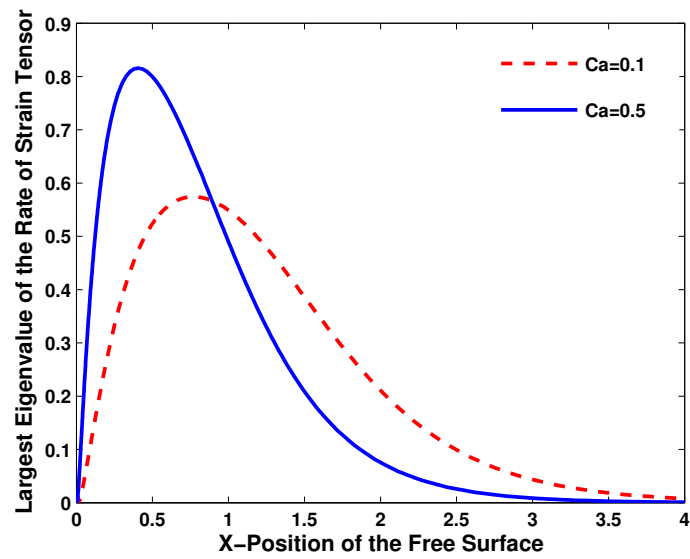
(a)
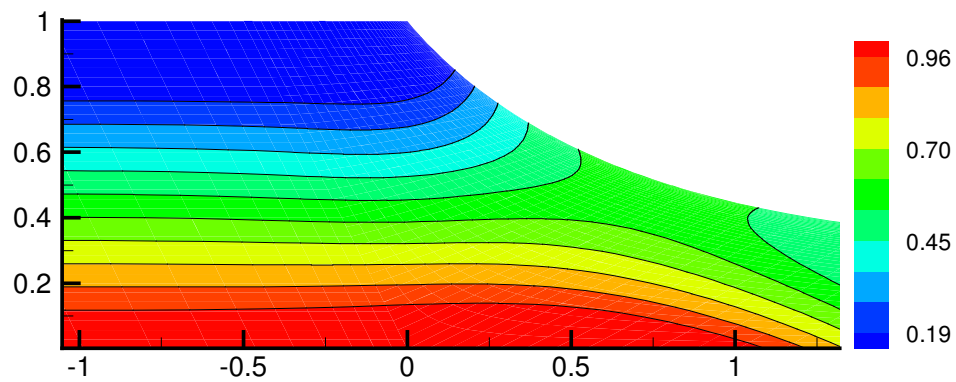


(b)
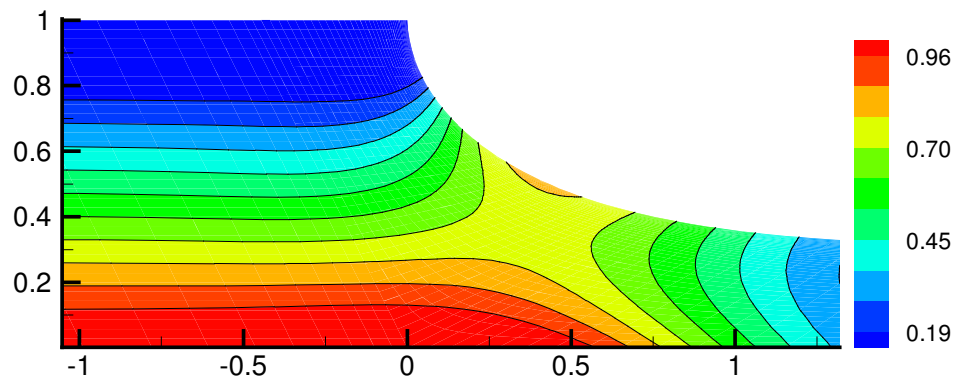


(c)

Figure 5.31: Effect of $Ca$ number on the rate of strain for Newtonian fluid. (a) Line plot of the largest eigenvalue of rate of strain tensor. (b) & (c) Contour plots of the largest eigenvalue of rate of strain tensor for $Ca$=0.1 and $Ca$=0.5, respectively. $Q = 0.3$.
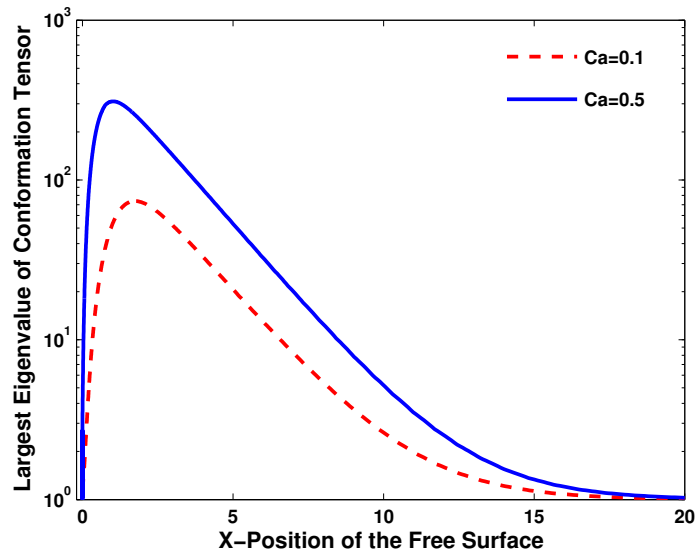
(a) Largest eigenvalue of the conformation tensor along the free surface
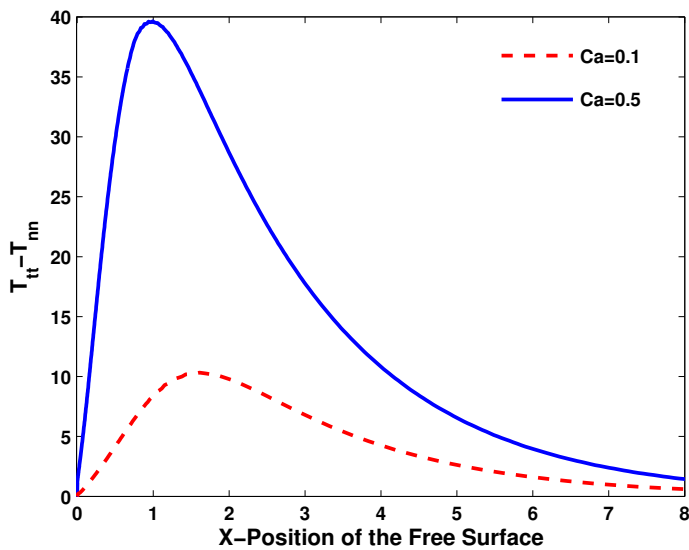


(b) Hoop stress along the free surface

Figure 5.32: Effect of $Ca$ number on the stretch and the normal stress difference for an Oldroyd-B fluid. $Wi = 2.0$, $Q = 0.3$, $\beta = 0.75$.
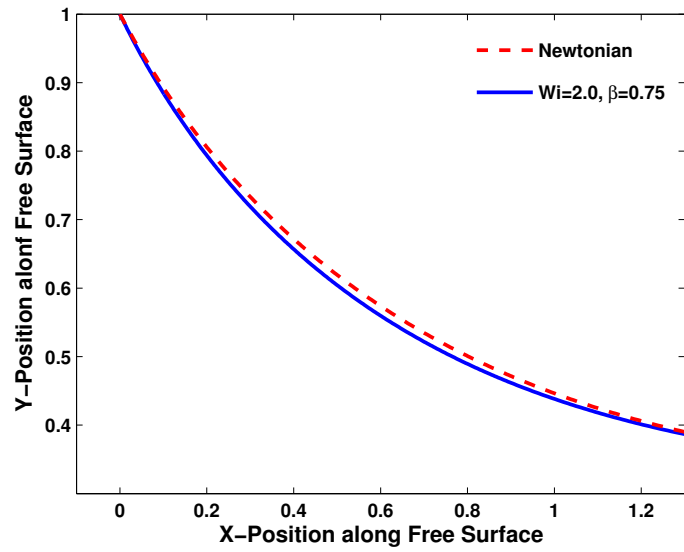
(a) $Ca$=0.1
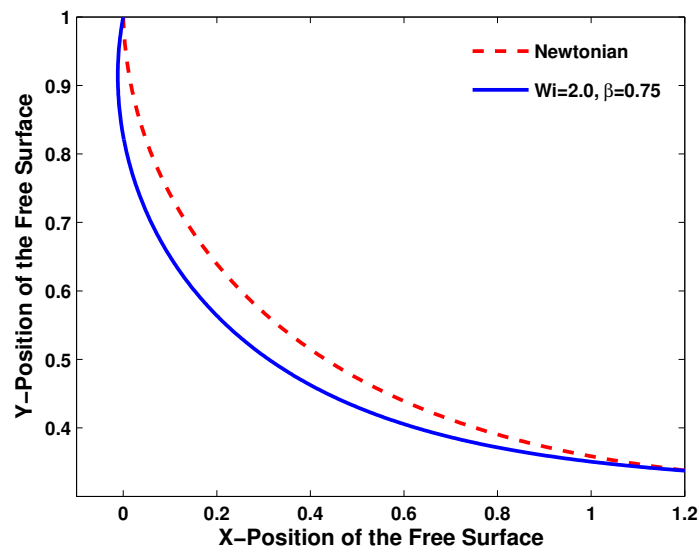


(b) $Ca$=0.5

Figure 5.33: Effect of $Ca$ number on free surface shape for and Oldyod-B fluid. $Wi$=2.0, $Q = 0.3$, $\beta = 0.75$.

(a) Newtonian, $Ca = 0.1$

(b) $Wi = 2.0$, $\beta = 0.75$, $Ca = 0.1$

(c) Newtonian, $Ca = 0.5$

(d) $Wi = 2.0$, $\beta = 0.75$, $Ca = 0.5$
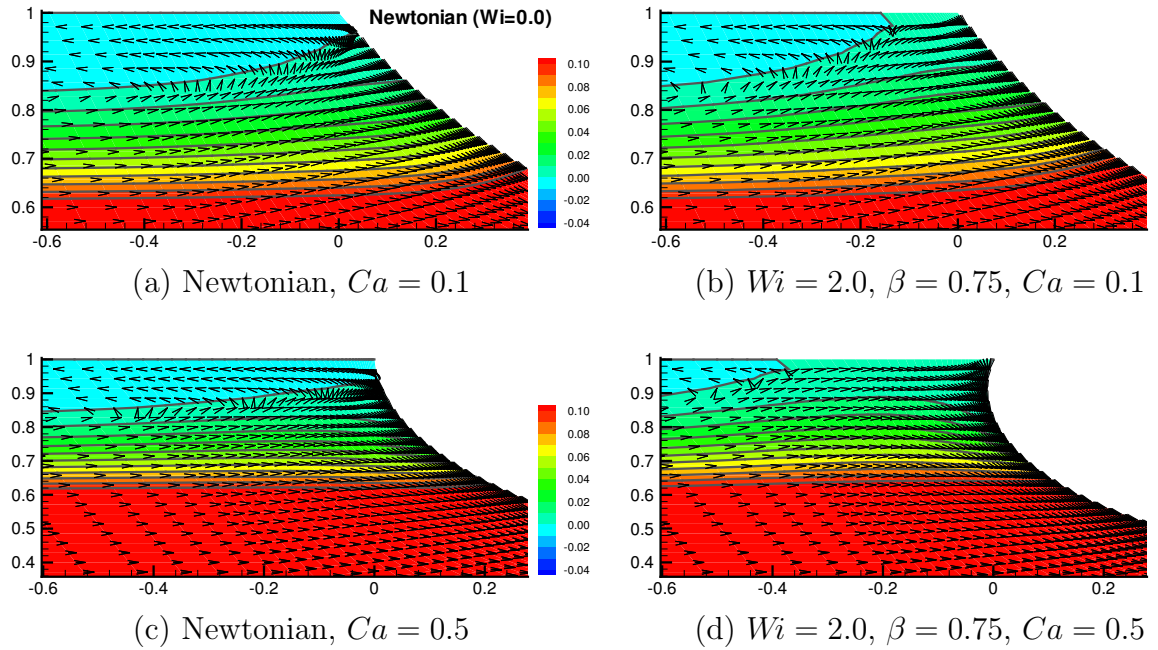
Figure 5.34: Change in velocity profile by changing the $Ca$ number for an Oldroyd-B fluid. $Q = 0.3$.

According to the viscocapillary model, above the critical gap to thickness ratio, two-dimensional steady flow cannot exist. Equation (5.3) is strictly valid only when $Ca << 1$, $Re << 1$. Carvalho and Kheshgi [2000] have extended the work on the low-flow limit of Landau and Levich [1942] and Ruschak [1976] by conducting experiments and by carrying out numerical simulations for much higher values of $Re$ and $Ca$ for a Newtonian liquid. Both experiment and numerical results predict that the viscocapillary model is useful for low $Ca$ and $Re$. However, it becomes increasingly ineffective for higher values of $Ca$ and $Re$. Carvalho and Kheshgi [2000] found that at higher $Ca$, the viscocapillary model proposed by Landau and Levich [1942] underpredicts the low flow limit for inertialess flows. Romero et al. [2004] further extended the work of Carvalho and Kheshgi [2000] to viscoelastic liquids and predicted that the critical conditions for the onset of the low-flow limit are strong functions of the viscoelasticity of the fluid and the viscosity ratio. They demonstrate that viscoelasticity reduces the size of the coating window. Romero et al. [2004] used a power-law constitutive equation in their model to accurately capture the behaviour of the viscoelastic liquid used in performing their experiments. However, in this work

two more traditional and widely used constitutive models, namely Oldroyd-B and FENE-P, are used to investigate the effect of viscoelasticity on the low-flow limit in terms of the Elastocapillary number, $Ec = Wi/Ca = \lambda\varsigma/(\eta_{\text{s}} + \eta_{\text{p,0}})L$. The advantage of the Elastocapillary number is that it is a function of only fluid properties and slot width and is independent of the web velocity. This is unlike the $Ca$ and $Wi$, which both depend on the web velocity, making it difficult to hold one of them constant while varying the other through a variation in the web velocity. Hence, to investigate the effect of viscoelasticity on low flow limit of inertialess slot coating flow, the parameter space which is to be explored is either a combination of $Ec$, $Ca$ and $\beta$ or a combination of $Ec$, $Wi$ and $\beta$. Both of these equivalent combinations ensure that all the necessary forces have been taken into account and the web velocity is related solely to a single parameter. The use of $Ec$ in this work is similar to the use of the property number ($P_p = Re/Ca$) defined by Carvalho and Kheshgi [2000] to investigate the effect of inertial forces on the low flow limit.

Figure 5.35 shows the evolution of streamlines as a function of dimensionless coating thickness for a Newtonian and an Oldroyd-B liquid for $Ca = 0.75, Ec = 2.0$ and $\beta = 0.75$.

It is clear from Fig. 5.35 that as the dimensionless coating thickness ($H_0/t$) falls, the free surface becomes more curved and the contact angle ($\theta$) between the free surface and the die wall diminishes. The contact ($\theta$) is pictorially shown is Fig. 5.19. Figure 5.35 shows that viscoelasticity can lead to a significant reduction in the coating thickness. However, the steepness in the reduction in the contact angle for viscoelastic liquids is a function of $Ca$ for a given $\beta$ and $Ec$ as shown in Figure 5.36. For a given dimensionless coating thickness, $\beta$, and $Ec$, the static contact angle $\theta$ decreases as $Ca$ increases for both Newtonian and Oldroyd-B liquids as predicted earlier by Carvalho and Kheshgi [2000]; Saito and Scriven [1981] and Romero et al. [2004]. At low $Ca$ surface tension forces are strong and hence, the free surface does not need to curve much in order to balance the adverse pressure gradient at the free surface even for viscoelastic liquids with $Ec$ of the order of $\sim 2$. At higher $Ca$ (lower surface forces), as the normal stresses arising due to the viscoelastic nature of the fluid ($Ec > 0$) contribute to the net pressure gradient at the free surface, the free surface curves more for viscoelastic liquids in order to balance
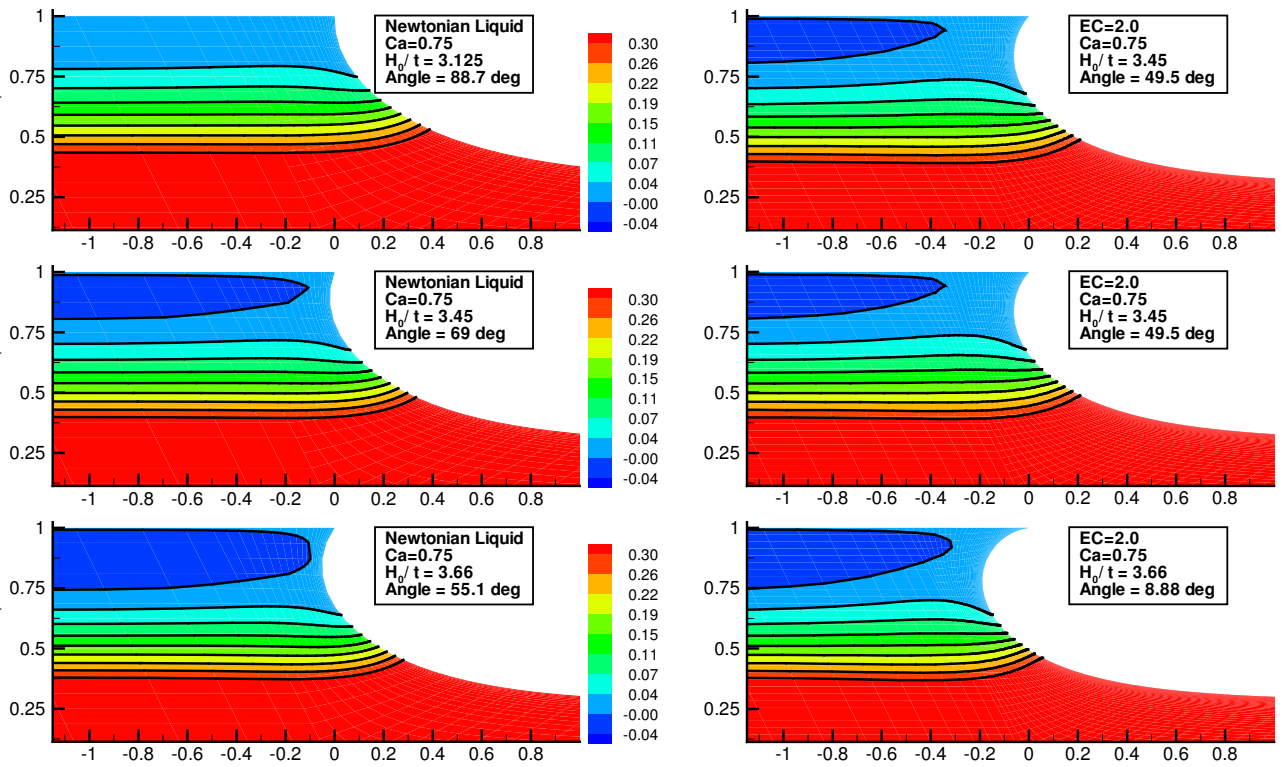
Figure 5.35: Evolution of streamlines with the change in the dimensionless coating thickness $(H_0/t)$. The Newtonian flow profile is on the left for $Ca = 0.75$ and flow profile for an Oldroyd-B liquid is on the right for $Ca = 0.75$, $Ec = 2.0$ and $\beta = 0.75$.
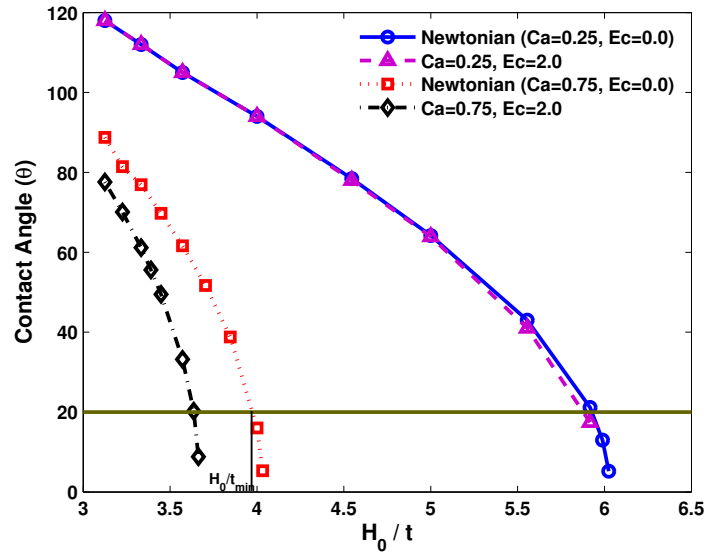
Figure 5.36: Change in the contact angle with the change in dimensionless coating thickness ($H_0/t$) for a Newtonian and an Oldroyd-B fluid. Figure shows the effect of $Ca$ on contact angle. $H_0/t_{\min}$ shown is the figure is used to predict the low-flow limit. $\beta = 0.75$.

the adverse pressure gradient as compared to the Newtonian liquid. Romero et al. [2004] have suggested that the mechanism responsible for a change in the static contact angle is the formation of stress boundary layers at the free surface. We have also observed the formation of stress boundary layers in our simulations (see Fig. 5.8). An increase in $Ec$ or decrease in the viscosity ratio $\beta$, increases the normal stresses close to the free surface at a given $Ca$ and dimensionless coating thickness and hence, the computed contact angle decreases more rapidly. The effect of $\beta$ is portrayed in Figure 5.37.

Figure 5.38 shows the effect of finite extensibility of the polymer molecules on the contact angle. For the FENE-P model the normal stresses at the free surface are smaller (due to shear thinning) than the stresses predicted by the Olydroyd-B model, and hence the change in contact angle for the FENE-P model is less steep compared to the change in contact angle for the Oldroyd-B model.

It has been established earlier by Romero et al. [2004] that the critical conditions for the low-flow limit obtained by solving only the downstream section of a slot coater are virtually the same as those predicted for the full slot coater [Carvalho
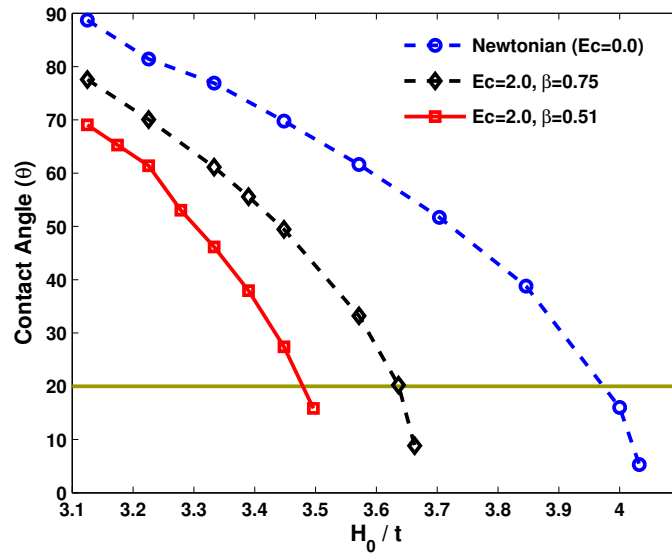
Figure 5.37: Change in the contact angle with the change in dimensionless coating thickness ($H_0/t$) for a Newtonian and an Oldroyd-B fluid for different viscosity ratio $\beta$. $Ca$=0.75
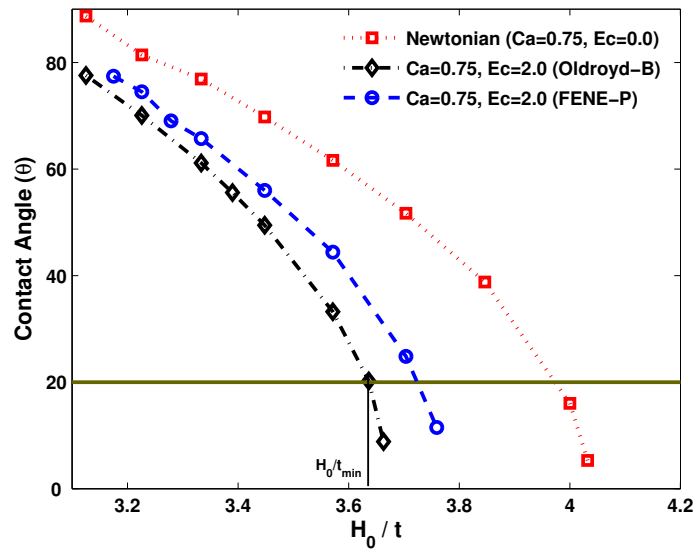


Figure 5.38: Change in the contact angle with the change in dimensionless coating thickness ($H_0/t$) for different constitutive models. $H_0/t_{\min}$ shown is the figure is used to predict the low-flow limit. $\beta = 0.75, b_{\mathbf{M}} = 50$
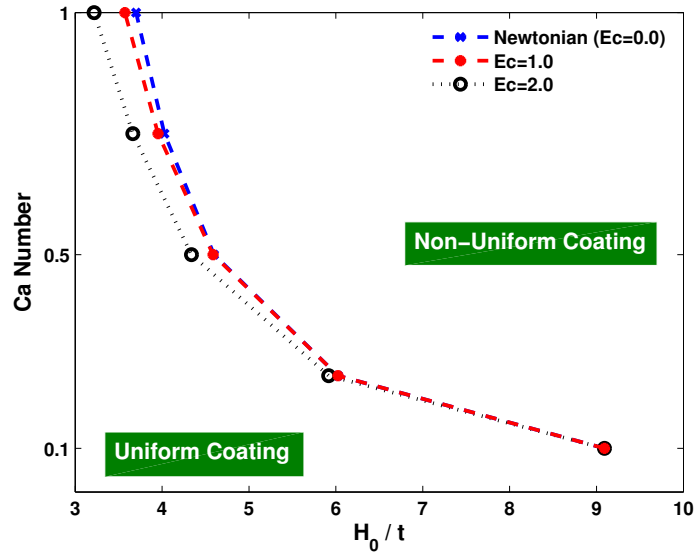
Figure 5.39: Effect of viscoelasticy ($Ec$) of an Oldroyd-B fluid on the size of coating window. $\beta = 0.75$

and Kheshgi, 2000; Romero et al., 2004] for $Ca$ of order $\sim 1$ and inertialess flows ($Re = 0$). As only the downstream section of the slot coater has been analyzed in this work, the low-flow limit computed here is limited to the range of $Ca$ from $Ca = 0.1$ up to 1 and for inertialess flows.

Following Romero et al. [2004], the onset of the low-flow limit at a given $Ca$ is determined theoretically by predicting the dimensionless coating thickness at which the static contact angle falls below $20^0$ as shown in Fig. 5.36. Figure 5.39 displays the critical conditions for low-flow limit. For the Oldroyd-B model, the onset of the low-flow limit occurs at a smaller dimensionless coating thickness for all values of $Ec$ and $\beta$ studied in work [see Fig. 5.39 and 5.40]. The minimum film thickness that can be coated increases as the liquid becomes more viscoelastic. A reduction in the size of the coating window has been reported earlier by Romero et al. [2004] for extensional thickening liquids both experimentally and theoretically.

Rheological properties of liquids, such as shear thinning strongly the affects size of the coating window. Figure 5.41 compares the critical conditions for different constitutive models. As predicted, for the FENE-P model the onset of the low flow limit occurs at a higher dimensionless coating thickness compared to the Oldroyd-B
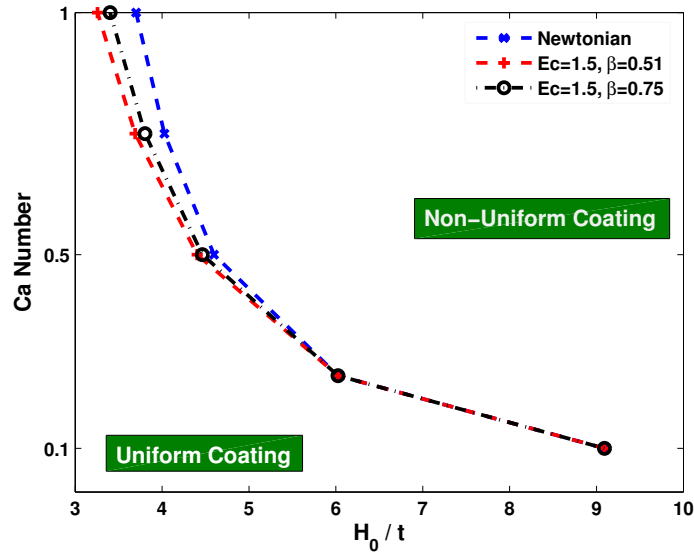
Figure 5.40: Effect of viscosity ratio $\beta$ for an Oldroyd-B fluid on the size of the Coating window.

model because of smaller normal stresses.

## 5.6   Conclusion

In this chapter, we have investigated the flow behavior of Oldroyd-B and FENE-P liquids in the downstream section of a slot coating flow using the DEVSS-TG finite element method coupled with elliptic mesh generation methodology developed in chapter 2. We have found that the flow behavior of the ultra-dilute solution is dramatically different from that of dilute solutions. Our simulation indicates that at low $Wi$ ($Wi < 1.5$), polymer molecules are predominantly stretched at the web in shear dominated flow. At higher $Wi$ ($Wi > 1.5$), the extensional nature of flow at the free surface governs the rate of stretching of polymer molecules. It is found that the change in the flow kinematics governing the rate of stretching of polymers is independent of the viscosity ratio and constitutive equation i.e. largest eigenvalue changes its position from the web to the free surface at roughly the same $Wi$ for all viscosity ratios. The extensional nature of the flow in the stretching section of the free surface leads to the formation of normal stress boundary layers
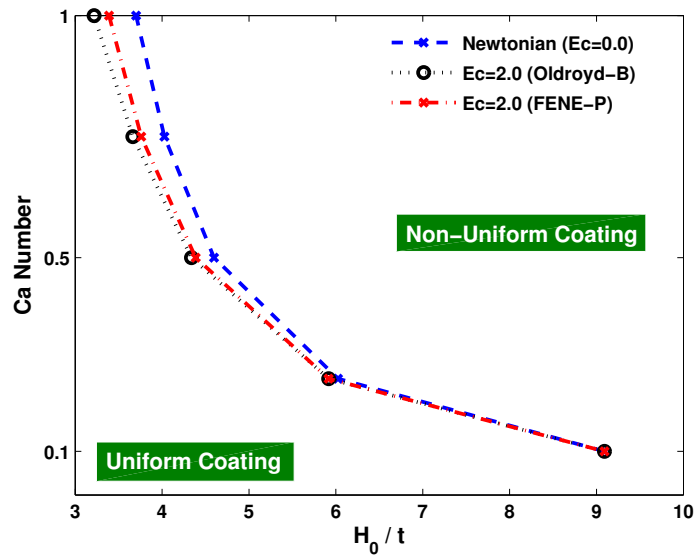
Figure 5.41: Coating window for different constitutive models. $\beta = 0.75, b_{\mathbf{M}} = 50$

at the free surface. The high normal stresses at the free surface tends to pulls the liquid away from the recirculation region present in a Newtonian flow. As a result the recirculation zone diminishes in size, and flow close to the static contact line becomes stronger. The stagnation point moves from the free surface to the die wall and the normal stress difference close to the static contact line becomes positive. Reduction in the size of the recirculation zone exposes the singularity present in slot coating flows, which causes the velocity gradient and the conformation tensor to become singular. The strength of the singularity in the field variables grows with decreasing viscosity ratio. We have also investigated the effects of viscoelasticity and viscosity ratio on the low-flow limit of slot coating flows. We have found that for viscoelastic liquids, the minimum coating thickness is higher than the coating thickness for Newtonian liquids. As a result the coating window for a uniform coating shrinks in size compared to Newtonian liquids.

# Chapter 6

# Computation of Viscoelastic Free Surface Flow Using the Micro-Macro Approach

In this chapter, the micro-macro approach developed in chapter 3 is used to solve the slot coating flow of viscoelastic liquids. The results presented in this chapter are compared with the steady state results presented in chapter 5 for linear dumbbell models. Computations are also carried out for non-linear dumbbells and detailed comparison between transient computations using the micro-macro and macroscopic approaches is presented.

In recent years, macroscopic methods for computing viscoelastic flows have attracted considerable interest. Basically, their computational requirements are comparatively less intense than micro-macro methods, which enables a more thorough exploration of parameter space to be carried out. However, as it well known, and has been demonstrated in chapter 5, macroscopic methods either fail to converge or give unphysical results beyond a certain $Wi$. In this regard, micro-macro methods have been considered a breakthrough since they permit the use of non-linear constitutive models (for which no closed-form equations exist) that have been shown recently to accurately describe experimentally observed features in homogeneous flows [Cifre and De la Torre, 1999; DE Gennes, 1979; Hsieh et al., 2003; Knudsen et al., 1996; Larson et al., 1999, 1997; Magda et al., 1988; Prabhakar, 2005; Schroeder et al.,

2003, 2004; Sunthar and Prakash, 2005].

Despite the potential for micro-macro methods to incorporate such non-linear models, their use so far has largely been limited to examining the predictions of linear dumbbell models (for which an exact closed-form equation exist) in confined flow [Fan et al., 1999a; Feigl et al., 1995; Halin et al., 1998; Hu et al., 2005; Hulsen et al., 1997; Laso and Ottinger, 1993; Laso et al., 1997; Somasi and Khomami, 2000, 2001; Van Heel et al., 1990]. The exception is the application of the CONNFFESSIT method to solve transient free surface problems by Cormenz et al. [2002] andGrande et al. [2003]. In particular, the validity of micro-macro methods in a variety of flows, for Weissenberg numbers that are approximately similar in magnitude to those explored in macroscopic simulations, has been established. Although Hulsen et al. [1997] have shown that the micro-macro method remains numerically stable at a higher $Wi$ in the flow-around a cylinder problem compared to the macroscopic approach, mesh convergence of the high Weissenberg number solution has not yet been established.

It is clearly worthwhile to examine the performance of advanced and efficient micro-macro methods such as BCF, using accurate constitutive models that incorporate FENE force, hydrodynamic interactions etc. in complex flows. While the computation of large scale viscoelastic flows using bead-spring and bead-rod models are still beyond currently available computational resources, a coarser representation of polymer molecule, namely, a dumbbell model, can be used address the following questions:

- Can the BCF method predict the basic macroscopic features of viscoelastic flows discussed in chapter 5 (using equivalent microscopic constitutive equations) for free surface flows?

- Do the micro-macro simulations using the BCF method remain numerically stable and mesh converged at high $Wi$ for complex free surface flows?

- What is the effect of non-linearities in various microscopic constitutive models on free surface flows within the framework of the BCF approach?

In this chapter, these issues have been examined.

Table 6.1: Meshes used for slot coating flow computations using the Micro-Macro approach.

| Mesh | Number of Elements | Number of Nodes | Degrees of Freedom for Micro-Macro Simulations |
|---|---|---|---|
| M1 | 550 | 2311 | 10894 ($\mathbf{x}, \mathbf{v}, p$) and 1818 ($\mathbf{Q}$) |
| M2 | 1096 | 4539 | 21444 ($\mathbf{x}, \mathbf{v}, p$) and 3522 ($\mathbf{Q}$) |

## 6.1  Linear Dumbbell Models

As this work represents the first attempt to extend the BCF method to solve complex free surface flows, we validate our numerical scheme by comparing results for linear dumbbell models using the macroscopic and the micro-macro method for both ultra-dilute and dilute polymer solutions. The Hookean and FENE-P dumbbell representation of polymer molecules in the micro-macro approach are equivalent to the Oldroyd-B and FENE-P constitutive equations in macroscopic approach. Hence, we anticipate that results using both methods should agree for linear dumbbell models. An important aspect of macroscopic simulations is that steady states can be computed directly by dropping the time derivatives of velocity and conformation tensor in the momentum and conformation tensor equations, respectively. However, this is not possible with the micro-macro approach. Except where explicitly indicated, all steady-state micro-macro computations (obtained with actually running transient simulations for the given parameters) are compared with the macroscopic steady computations obtained by dropping time derivative terms.

The convergence of the numerical solutions using the micro-macro approach is tested on two different meshes (M1 and M2). Details of the meshes M1 and M2 are given in Table 6.1. These meshes are the same as the ones used for macroscopic computations.

Figures 6.1 and 6.2 compare the largest and smallest eigenvalues of the conformation tensor for a Hookean dumbbell model using the micro-macro and the macroscopic approaches for different viscosity ratios. The micro-macro results are computed with the M1 mesh and the macroscopic results are computed using the M4 mesh. The steady state values reported using the micro-macro approach are

a time and ensemble-average over all the Brownian configuration fields after the system reaches a stationary state. The error bars are smaller than the size of the symbols. Figure 6.2 for the smallest eigenvalues, clearly indicates that computations using the micro-macro method are numerically stable at much higher $Wi$ than those for the macroscopic method for all $\beta$ values. The minimum eigenvalue computed by the macroscopic approach becomes negative at high $Wi$ in certain regions of flow leading to a negative definite conformation tensor. However, the inherent positive definiteness of the conformation tensor in the micro-macro approach ensures a positive smallest eigenvalue at all $Wi$. Although results have been reported using the mesh M2 in Figs. 6.1(d) and 6.2(d) for an ultra-dilute solution, the computations at much higher $Wi$ and with more refined meshes were not attempted primarily because of the intense computational requirements.

The computations using the micro-macro approach for Hookean dumbbells depart from the macroscopic computations at different $Wi$ for different viscosity ratios, i.e. for $\beta = 1$ (ultra-dilute solution), the micro-macro results depart from the macroscopic computations at $Wi \sim 3$, while for $\beta = 0.25$, the results start departing at $Wi \sim 2$, beyond which the smallest eigenvalue using the macroscopic method drops quickly to zero. Figures 6.1(d) and 6.2(d) also show the mesh convergence of the micro-macro results for specific case of ultra-dilute solutions ($\beta = 1$).

The micro-macro simulations of FENE-P dumbbells (see Fig. 6.3, 6.4 and 6.5) show a qualitative behavior similar to Hookean dumbbells in terms of the numerical stability at high $Wi$. For ultra-dilute solutions of FENE-P dumbbells, a numerically stable and mesh converged solution at $Wi$ as high as $\sim 12$ is achieved compared to the solution using the macroscopic approach which fails at $Wi \sim 8$ for the M4 mesh and at $Wi \sim 3$ for the M1 mesh. For all values of $\beta$, a good agreement is seen between the results using the macroscopic and the micro-macro approach.

For ultra-dilute solutions ($\beta = 1$), an increase in $Wi$ beyond 3 significantly increases the computational cost for Hookean dumbbell models and several relaxation times must be computed before a steady state is achieved irrespective of the initial condition on the configuration fields. However, for FENE-P dumbbells, a zero order continuation in $Wi$ (where the initial condition for dumbbell configurations at high $Wi$ is chosen to be the non-equilibrium configurations of dumbbells at low $Wi$) is
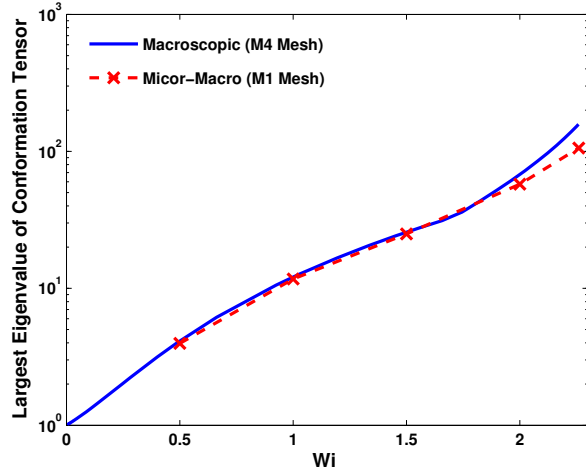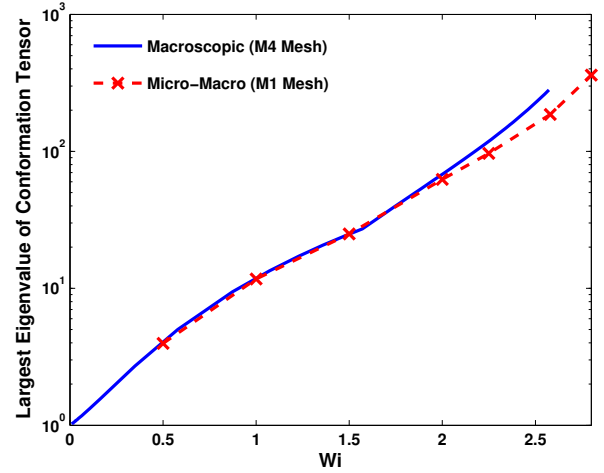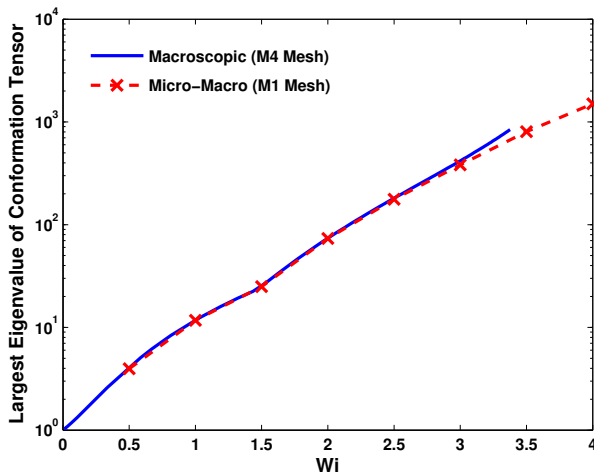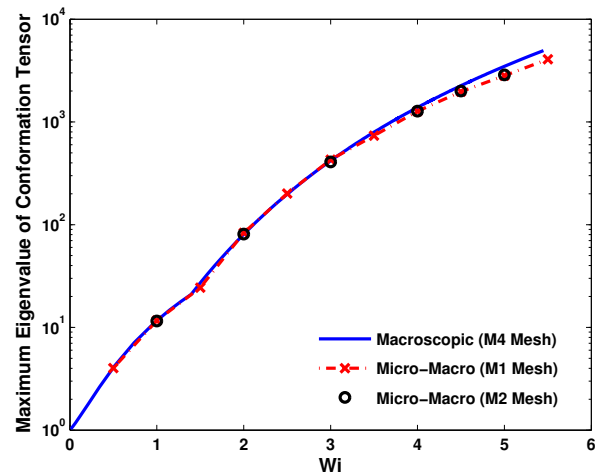
Figure 6.1: Largest eigenvalue of the conformation tensor in the flow domain for Hookean dumbbells using the Macroscopic and Micro-Macro approach. Macroscopic results are obtained using the M4 mesh and Micro-Macro results are obtained using the M1 mesh. The results for $\beta = 1.0$ are also reported for the M2 mesh. $Ca = 0.1$, $Q = 0.3$, $N_f = 2000$.
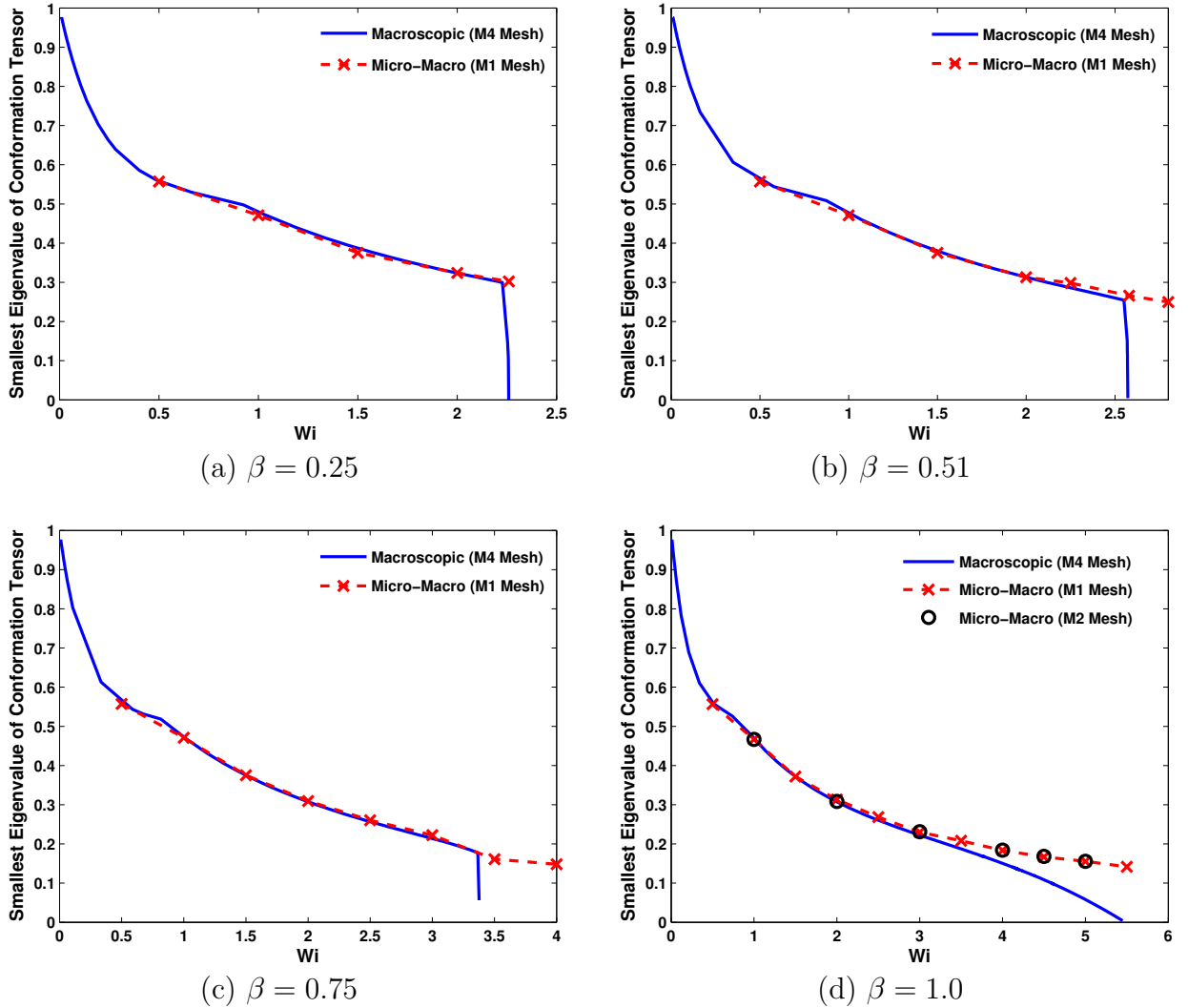
Figure 6.2: Smallest eigenvalue of the conformation tensor in the flow domain for Hookean dumbbells using the Macroscopic and Micro-Macro approach. Macroscopic results are obtained using the M4 mesh and Micro-Macro results are obtained using the M1 mesh. The results for $\beta = 1.0$ are also reported for the M2 mesh. $Ca = 0.1$, $Q = 0.3$, $N_f = 2000$.
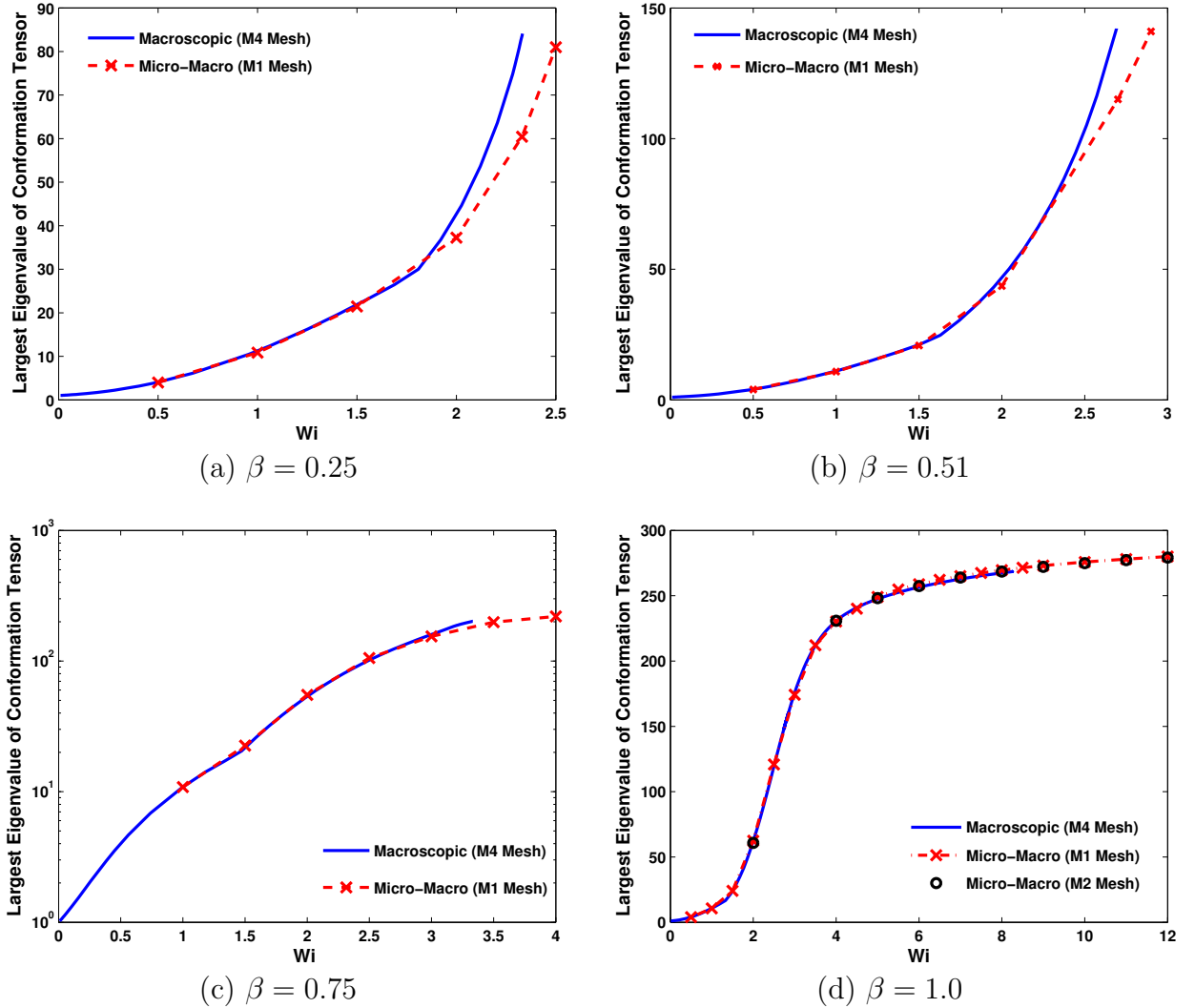
Figure 6.3: Largest eigenvalue of the conformation tensor in the flow domain for FENE-P dumbbells using the Macroscopic and Micro-Macro approach. Macroscopic results are obtained using the M4 mesh and Micro-Macro results are obtained using the M1 mesh. The results for $\beta = 1.0$ are also reported for the M2 mesh. $Ca = 0.1$, $Q = 0.3$, $b_{\mathbf{M}} = 100$, $N_f = 2000$.
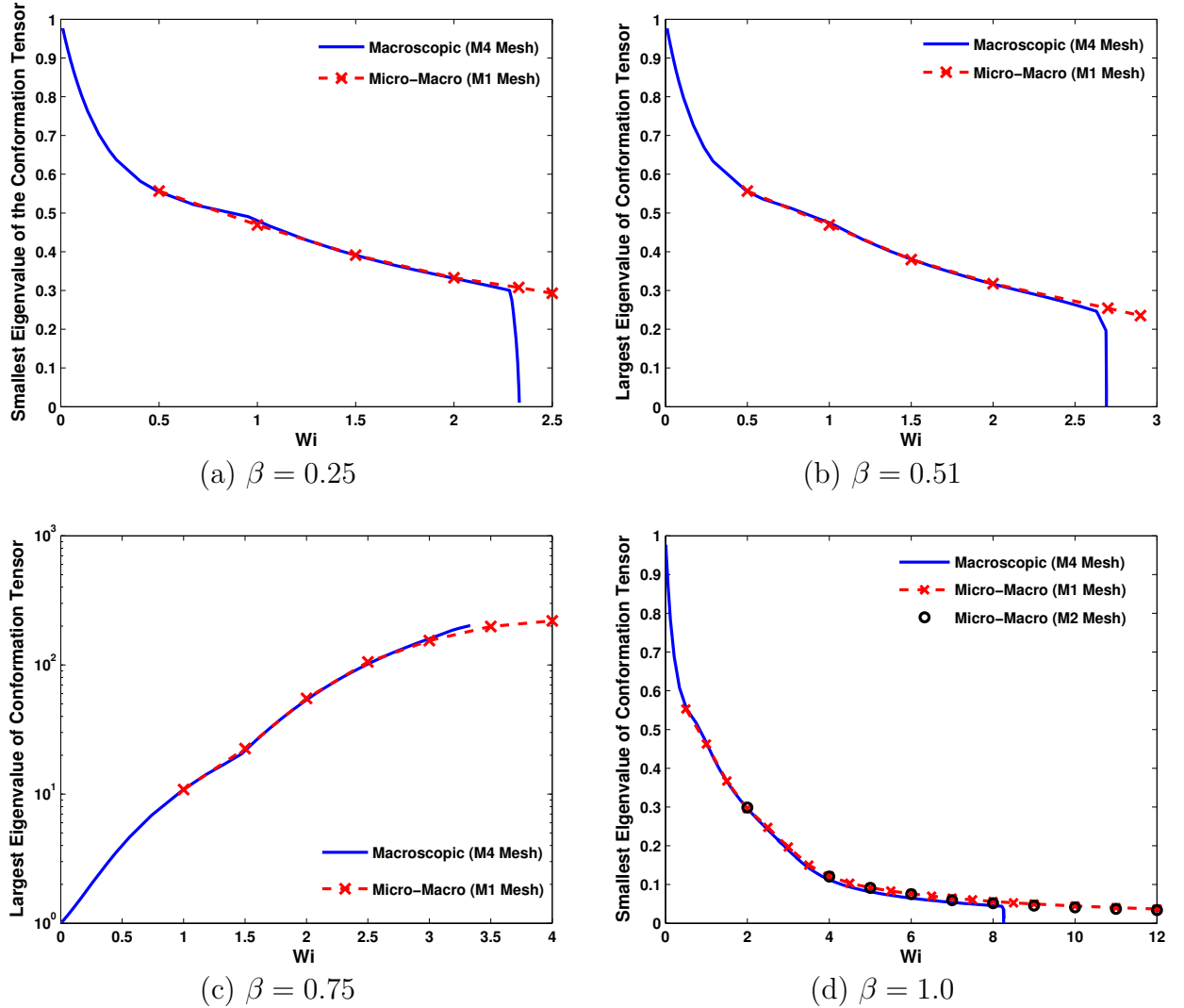
Figure 6.4: Smallest eigenvalue of the conformation tensor in the flow domain for FENE-P dumbbells using the Macroscopic and Micro-Macro approach. Macroscopic results are obtained using the M4 mesh and Micro-Macro results are obtained using the M1 mesh. The results for $\beta = 1.0$ are also reported for the M2 mesh. $Ca = 0.1$, $Q = 0.3$, $b_{\mathbf{M}} = 100$, $N_f = 2000$.
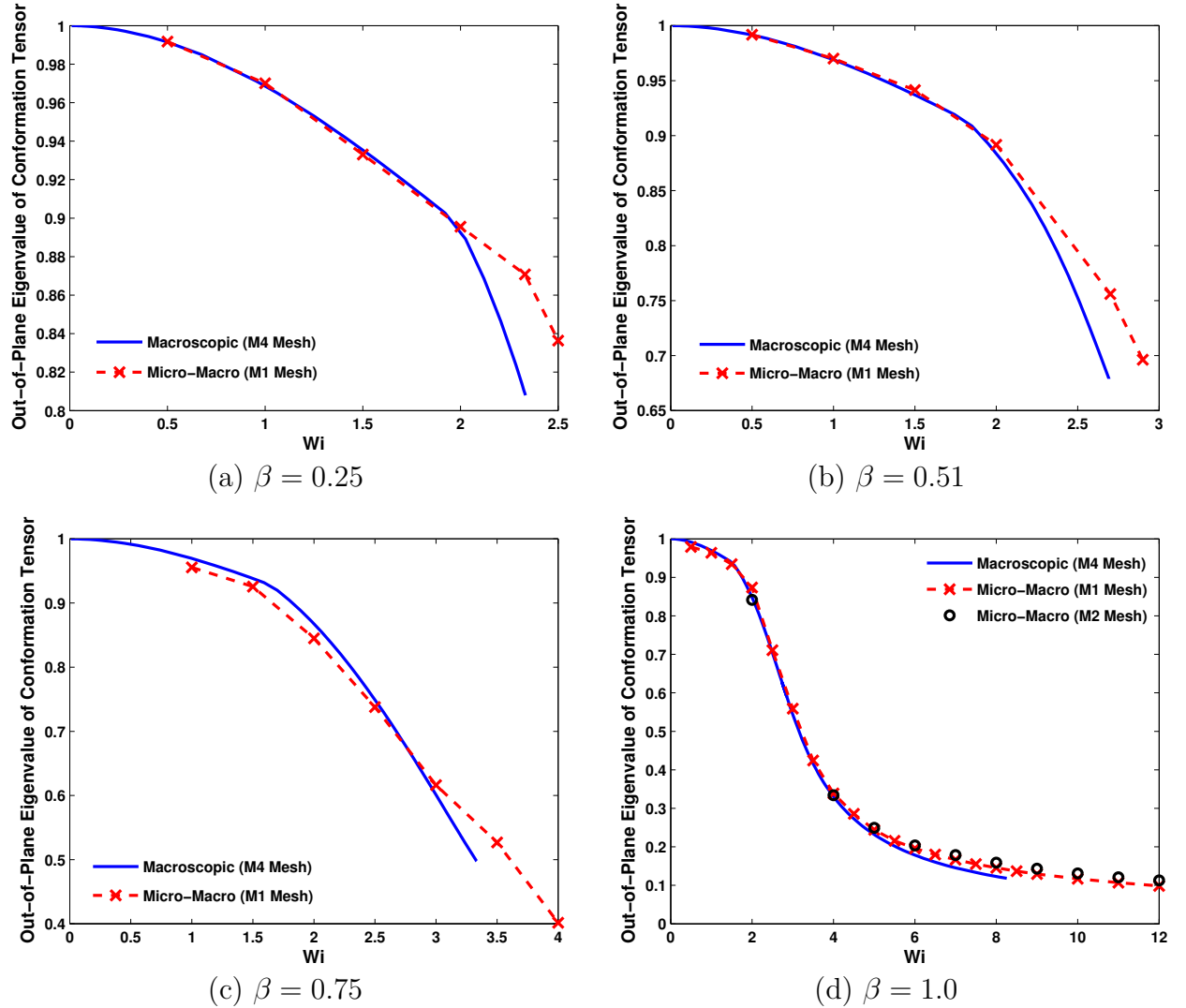
Figure 6.5: Out-of-plane eigenvalues of the conformation tensor in the flow domain for FENE-P dumbbells using the Macroscopic and Micro-Macro approach. Macroscopic results are obtained using the M4 mesh and Micro-Macro results are obtained using the M1 mesh. The results for $\beta = 1.0$ are also reported for the M2 mesh. $Ca = 0.1$, $Q = 0.3$, $b_{\mathbf{M}} = 100$, $N_f = 2000$.

found to speed up computations at high $Wi$. The significant reduction in the computational cost for FENE-P dumbbells is due to the finite extensibility of polymer molecules which ensures that at high $Wi$ there is a relatively smaller change in the almost fully stretched dumbbells by increasing $Wi$. The zero order continuation has no effect on computations using Hookean dumbbells, specially at high $Wi$.

For dilute solutions ($\beta < 1.0$), computations are far more expensive compared to the computational cost for ultra-dilute solutions. The computational cost for dilute solutions depends strongly on the viscosity ratio ($\beta$). An important difference between the computations of dilute and ultra-dilute solutions is that the micro-macro computations of dilute polymer solutions result in temporal fluctuations in all field variables such as velocity, coating thickness etc. The intensity of these fluctuations is very high at initial times and strongly depend upon the initial conditions used for configurations fields. The fluctuations at initial times grow as the viscosity ratio decreases and it takes longer time to reach a stationary state for lower $\beta$ values.

Figure 6.6 shows the fluctuations in the coating thickness for Hookean dumbbells at $Wi = 2.0$ for different values of the viscosity ratios. It is clear from the figure that the coating thickness at $\beta = 0.25$ shows much more pronounced fluctuations compared to $\beta = 0.75$. For $\beta = 1.0$, the evolution of polymer conformation is not coupled with other field variables and hence, the coating thickness doesn't show any fluctuations.

Figure 6.7 shows the contours of the $xx$ component of elastic stress for a Hookean dumbbell model. An increase in $Wi$ results in the formation of stress boundary layers under the free surface, similar to the earlier predictions of the macroscopic approach. The stress contours in Fig. 6.7 are similar to the ones in Fig. 5.9, except that contours in Fig. 6.7 are not as smooth due to the coarseness of the mesh used for micro-macro computations. The maximum stress level at different $Wi$ is also slightly smaller for micro-macro computations, due also to the difference in the meshes used for the two approaches.

Figure 6.8 compares contour plots of the largest and smallest eigenvalues of the conformation tensor with the results for the macroscopic method on the same mesh (M1). Clearly, the results for the micro-macro method agree closely with macroscopic results for the same mesh.
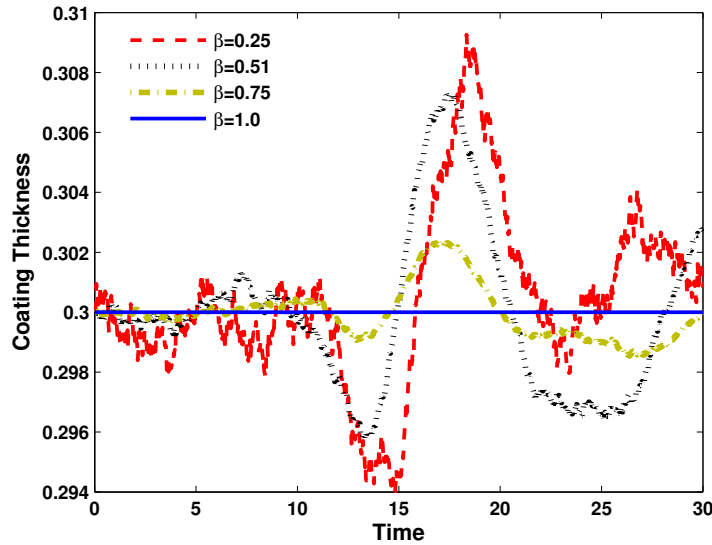
Figure 6.6: Temporal fluctuations in the coating thickness for different viscosity ratios using the Micro-Macro approach for Hookean dumbbells. Computations are carried out with the M1 mesh. $Wi = 2.0$, $Ca = 0.1$, $Q = 0.3$, $N_f = 2000$, $\Delta t = 0.02$.

Figure 6.9 examines the time step convergence of steady state results obtained with the micro-macro method for Hookean dumbbells in terms of the largest eigenvalue of the conformation tensor. It is clear that within statistical error bars the largest eigenvalue of the conformation tensor at steady state, for a time step of 0.02 is identical to that obtained for a time step of 0.0075. The eigenvalue for both time steps eventually coincide with the final steady state value obtained using the macroscopic Oldroyd-B model. The steady state value for the higher time step (0.05) settles down to a lower value than the one obtained using the Oldroyd-B model, but it remains within error bars. Error bars in Figs. 6.1-6.5 are smaller than those displayed in Fig. 6.9, because error bars for steady state averages in these figures are evaluated by carrying out time and ensemble-averages over all the configuration fields compared to the error bars for transient averages in Fig. 6.9 which are evaluated only by ensemble-averaging.

Hereafter, all reported micro-macro simulations have been carried out with $\Delta t = 0.02$ unless otherwise specified.

Figure 6.10 displays the sensitivity of the micro-macro solution to ensemble size. Ensemble sizes of 500, 1000 and 2000 dumbbells are chosen to run simulations for a

(a) $Wi$=1.0

(b) $Wi$=2.0

(b) $Wi$=3.0
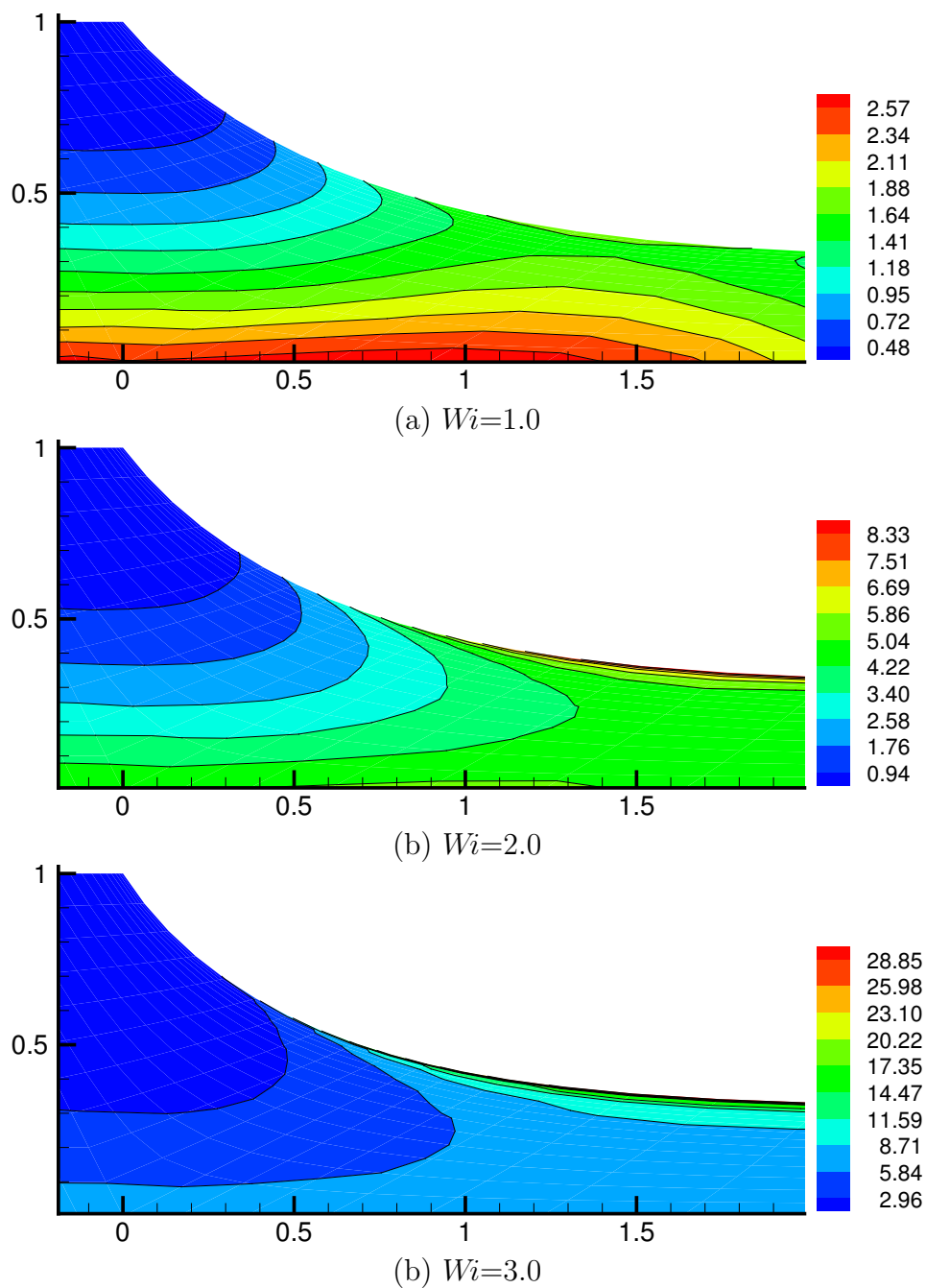
Figure 6.7: Evolution of the $xx$ component of the elastic stress $(\sigma_{xx})$ as a function of $Wi$ for Hookean dumbbells. $Ca = 0.1$, $Q = 0.3$, $\beta = 0.75$, $N_f = 2000$.
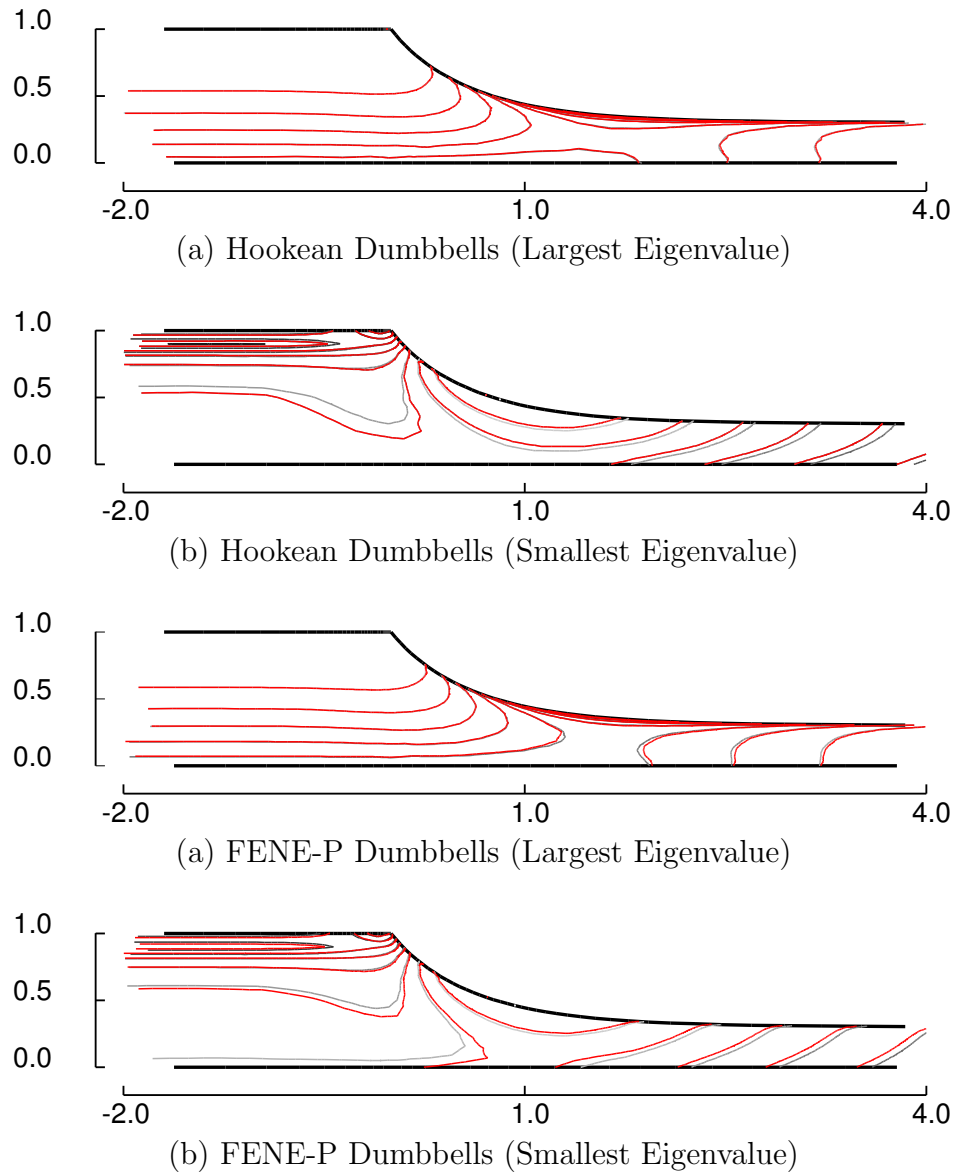
Figure 6.8: Comparison of contours of the largest (Left) and smallest (Right) eigen-values of the conformation tensor. The Macroscopic results are represented by grey lines and the Micro-Macro results are by red lines. [(a) & (b)] Oldroyd-B and [(c) & (d)] FENE-P. $Wi = 2.0$, $Ca = 0.1$, $Q = 0.3$, $\beta = 0.75$, $b_{\mathbf{M}} = 100$, $N_f = 2000$.
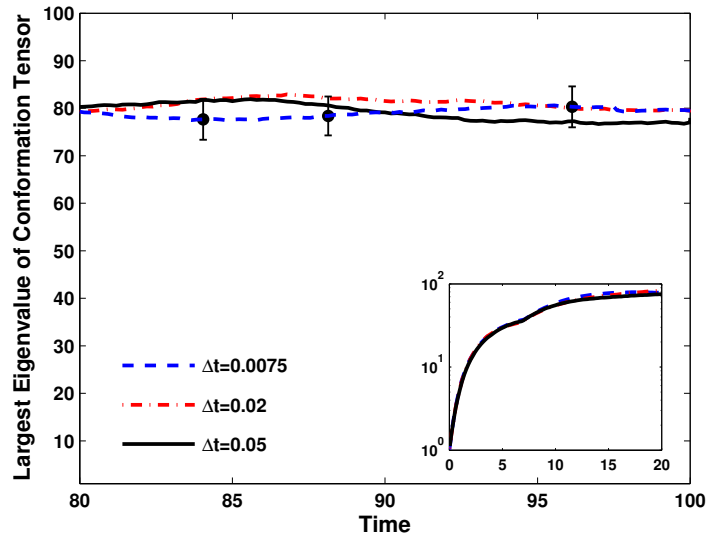
Figure 6.9: Time step convergence of the Micro-Macro method for Hookean dumbbells for an ultra-dilute solution. Inset shows the change in the eigenvalue at initial times. Computations are carried out with the M1 mesh. $Wi = 2.0$, $Ca = 0.1$, $Q = 0.3$, $\beta = 1.0$, $N_f = 2000$

particular case of $Wi = 2.0$ and $\beta = 1.0$. As expected, the solution gets increasingly more accurate as the ensemble size increases i.e. the number of dumbbells or the number of trajectories increases. The temporal fluctuations in the largest eigenvalue of the conformation tensor are more pronounced for an ensemble size of 500 than for an ensemble size of 1000 or 2000. Here, an ensemble size of 2000 dumbbells is chosen for all the micro-macro computations in order to have a smaller variance in the field variables.

The mesh convergence of the evolution of the largest eigenvalue of the conformation tensor for Hookean dumbbells for two different ensemble sizes using the micro-macro approach is shown in Figs. 6.11. Note that Figs. 6.1(d)-6.5(d) demonstrate the mesh convergence of the steady state results. It is evident that in order to the address the issue of mesh convergence, a sufficiently large ensemble of configuration fields must be chosen. For $N_f = 1000$, the presence of large fluctuations prevents a clear demonstration of mesh convergence. For $N_f = 2000$, mesh convergence is evident.

Figure 6.12 shows the numerical stability of the proposed fully implicit scheme
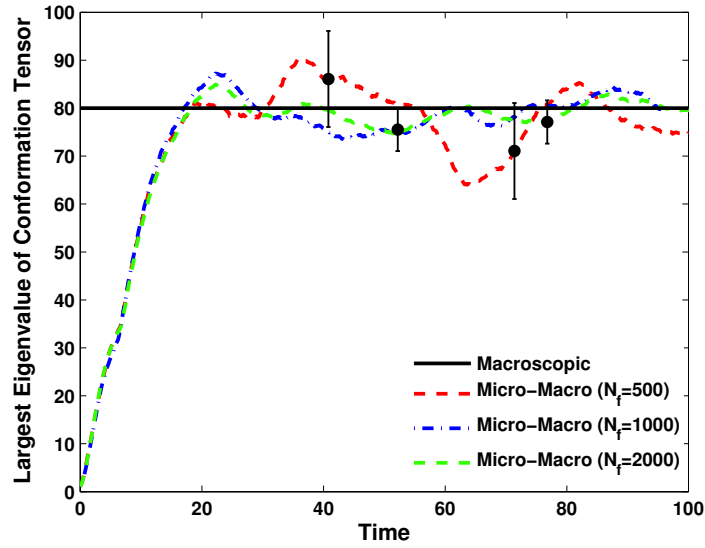
Figure 6.10: Effect of the ensemble size (Micro-Macro approach) on the largest eigenvalue of the conformation tensor for Hookean dumbbells in an ultra-dilute solution. Computations are carried out with the M1 mesh. Error bars are shown for $N_f = 500$ and $N_f = 2000$. $Ca = 0.1$, $Q = 0.3$, $Wi = 2.0$, $\beta = 1.0$, $\Delta t = 0.02$.
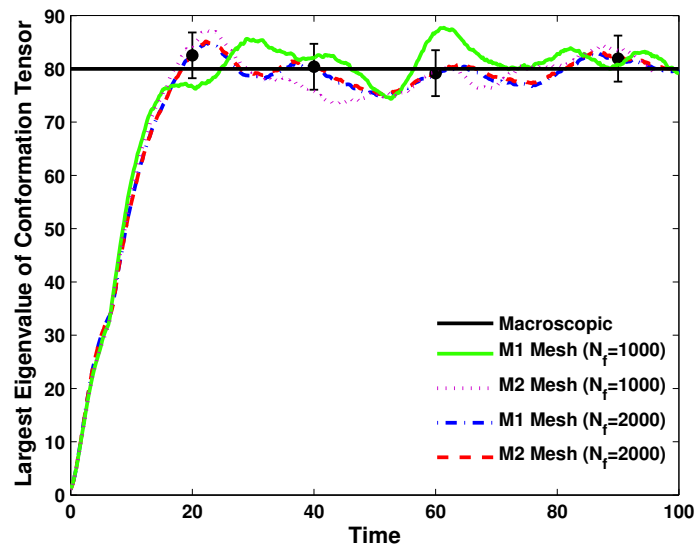


Figure 6.11: Mesh convergence of Micro-Macro approach for Hookean dumbbells for an ultra-dilute solution. Figures shows mesh convergence for two different ensemble sizes. $Ca = 0.1$, $Q = 0.3$, $Wi = 2.0$, $\beta = 1.0$, $\Delta t = 0.02$, $N_f = 2000$.
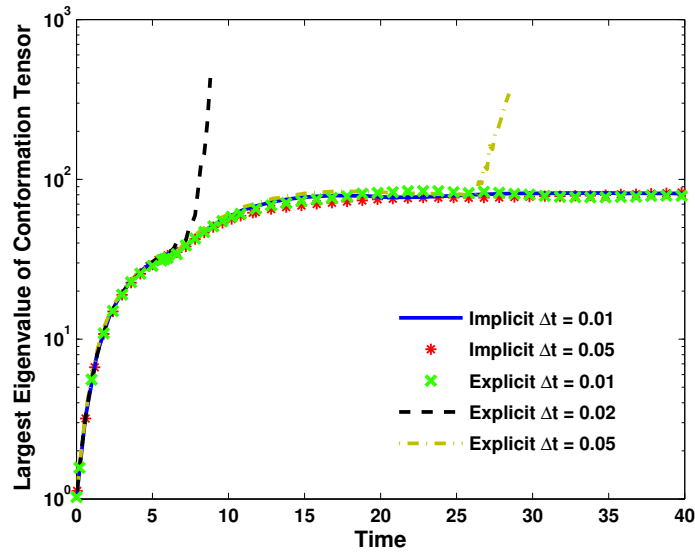
Figure 6.12: Comparison of the solution obtained using the explicit Euler scheme and the fully implicit scheme for Hookean dumbbells $Wi = 2.0$, $Ca = 0.1$, $Q = 0.3$, $\beta = 0.75$, $N_f = 2000$. Computations are carried out with the M1 mesh.

compared to the explicit Euler scheme at $Wi = 2.0$ and $\beta = 0.75$ for three different time steps, namely $\Delta t = 0.01, 0.02$ & $0.05$. It is clear that both implicit and explicit schemes are stable for $\Delta t = 0.01$. However, when the time step is increased to $0.02$ or $0.05$, only implicit scheme remains stable.

Figure 6.13 displays the effect of the upwind parameter (which appears in the SUPG finite element scheme used to spatially discretize the conformation tensor [Eq. (2.4)] and configuration fields [Eq. (3.15)] equations) on the largest eigenvalue of the conformation tensor. The computation using the macroscopic approach depends strongly on $h$ when $h > 0.01$ and is virtually independent of $h$ when $h < 0.01$. In contract to the macroscopic approach, micro-micro computations seem to be almost independent of $h$, reflecting the stability and accuracy of micro-macro computations.

Figure 6.14 shows the components of the conformation tensor $M_{xx}$, $M_{xy}$ and $M_{yy}$ along the free surface for Hookean and FENE-P dumbbells. We see that the results of micro-macro method compare very well with the macroscopic method.

Table 6.2 has comparisons of the memory and the CPU time requirements for steady state slot coating flow computations using the macroscopic and micro-macro methods for a Hookean dumbbell model. It is evident from Table 6.2 that the CPU
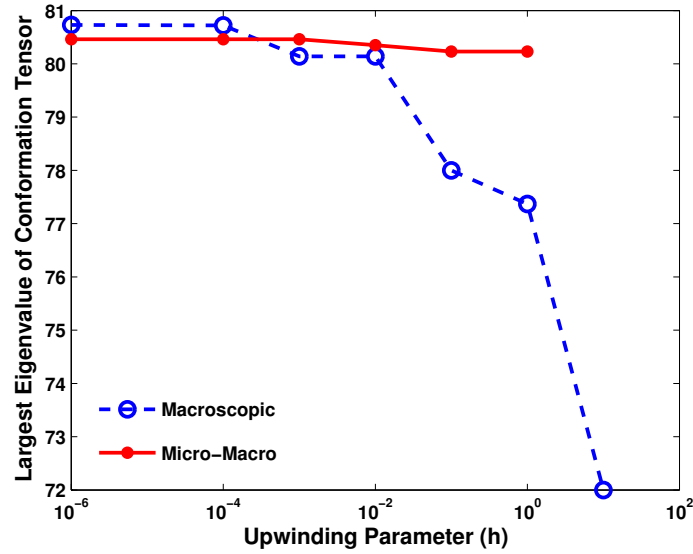
Figure 6.13: Effect of SUPG parameter ($h$) on the largest eigenvalue of the conformation tensor using the Macroscopic and Micro-Macro computations for Hookean dumbbells. $Wi = 2.0$, $Ca = 0.1$, $Q = 0.3$, $\beta = 1.0$, $N_f = 2000$, $\Delta t = 0.02$.

time requirements for the micro-macro approach are much more demanding than the macroscopic approach especially when compared on a single processor and on the same Mesh. However, the micro-macro method can easily be parallelized and the wall time drops significantly after parallelization. Table 6.2 also compares the memory and the CPU time requirements to solve the BCF equation using the explicit Euler scheme and the proposed fully implicit scheme for the Hookean dumbbell model. Note that explicit computations are done with a time step 0.01, as the explicit scheme is unstable for time step size 0.02. Although the CPU time required for a single time step is the same for both the explicit scheme and the fully implicit scheme, the total CPU time required to reach steady state is much smaller for the implicit scheme as a relatively much higher time step size can be used while maintaining the same accuracy as the explicit scheme.

It is worth mentioning that the CPU time and memory requirements are independent of the type of microscopic constitutive equation (for a linear dumbbell model) for free surface flow computations using the fully implicit scheme. However, for confined flow problems (fixed mesh), the CPU time required depends upon the type of microscopic constitutive equation used i.e. computations using Hookean
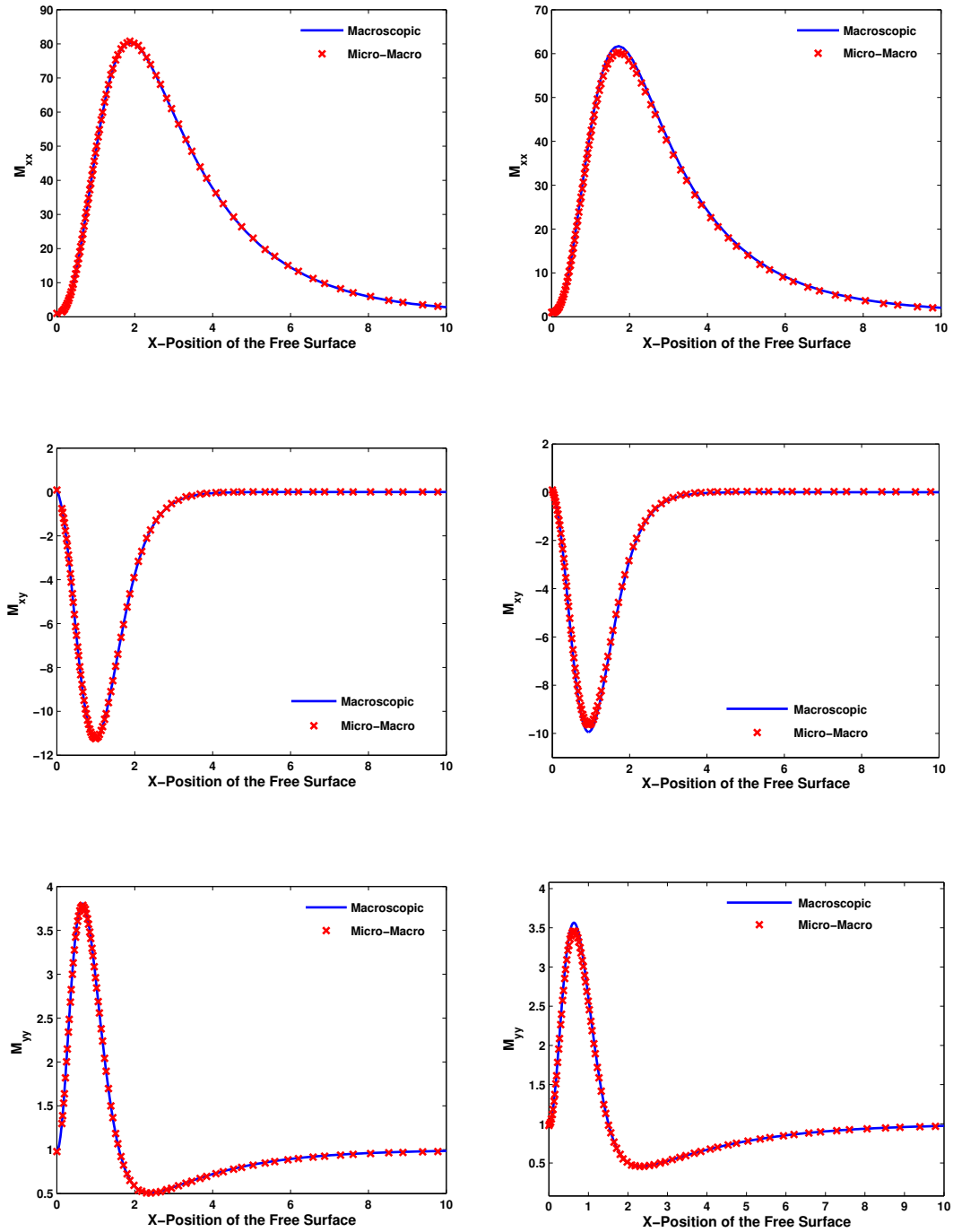
Figure 6.14: Comparison of the components of conformation tensor $M_{xx}$, $M_{xy}$ and $M_{yy}$ along the free surface. Macroscopic results are for M4 mesh and Micro-Macro results are for M1 mesh. $Wi = 2.0$, $Ca = 0.1$, $Q = 0.3$, $\beta = 0.75$, $b_{\mathbf{M}} = 100$, $N_f = 2000$.

Table 6.2: Comparison of CPU time and memory requirements for the macroscopic and the micro-macro method. $Wi = 2.0$, $\beta = 0.75$, $N_f = 2000$. The Micro-Macro values are for M1 mesh.

| Constitutive Equation | Number of Processors | Time Steps | CPU Time | Wall Time | Memory (Mb) |
|---|---|---|---|---|---|
| Macroscopic (M1 Mesh) | 1 | Steady State | 90 sec | 90 sec | 147 |
| Macroscopic (M4 Mesh) | 1 | Steady State | 90 mins | 90 mins | 2000 |
| Micro-Macro (Exp. Euler - $\Delta t = 0.02$) | 1 | Unstable | - | - | - |
| Micro-Macro (Exp. Euler - $\Delta t = 0.01$) | 1 | 1000 | 32 hrs | 32 hrs | 150 |
| Micro-Macro (Imp. Euler - $\Delta t = 0.02$) | 1 | 1000 | 32 hrs | 32 hrs | 150 |
| Micro-Macro (Imp. Euler - $\Delta t = 0.02$) | 8 | 1000 | 32 hrs | 4 hrs | 150 |

dumbbells are less expensive compared to a FENE-P model because the mass-matrix [Eq. (3.32)] is independent of the configurations of the dumbbells and hence it is not required to be factorized at each time step [see Eqs. (3.26) and (3.27)].

Recall the discussion in section 5 regarding the rate of stretching of polymer molecules being different around $Wi \sim 1.5$ due to the movement of the largest and the smallest eigenvalue from the web to the free surface. It is evident from Fig. 6.25 that the micro-macro computations show a similar behavior. Figure 6.25 displays the contours of largest and smallest eigenvalue at two different $Wi$ namely $Wi = 0.5$ and $Wi = 2.0$ for Hookean dumbbells. We see that both the eigenvalues change their spatial position with an increase in $Wi$ from $Wi = 0.5$ to $Wi = 2.0$. Clearly Fig. 6.25 is in excellent agreement with the macroscopic results portrayed in Fig. 5.15.

Another observation from macroscopic computations in chapter 5 is that the rate of stretching decreases with decreasing viscosity ratio beyond $Wi \sim 1.5$. A similar behaviour can also be observed from Fig. 6.16 for micro-macro computations. Figure 6.16 shows the effect of the viscosity ratio ($\beta$) on the stretch of molecules along the free surface. As expected, the Hookean dumbbell model predicts higher stretch along the free surface when compared to the FENE-P model. The behavior
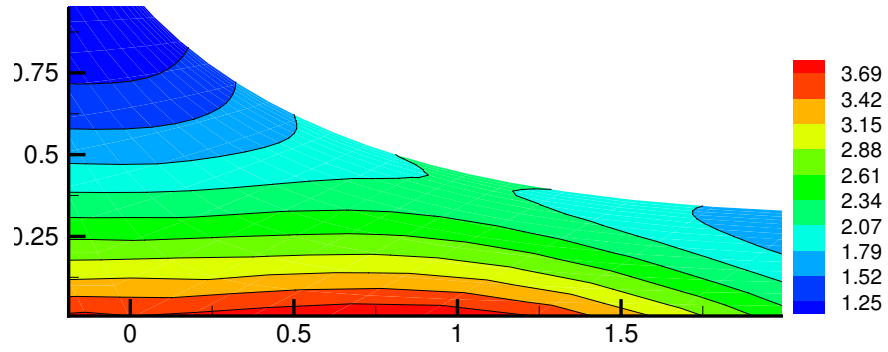
(a) $Wi$=0.5 (Largest Eigenvalue)
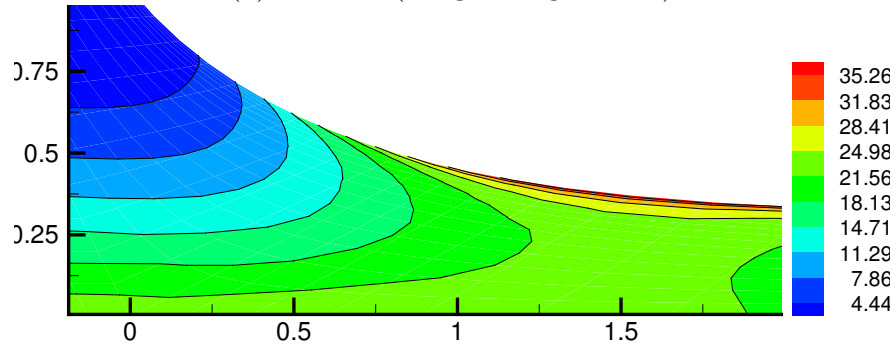
(b) $Wi$=2.0 (Largest Eigenvalue)
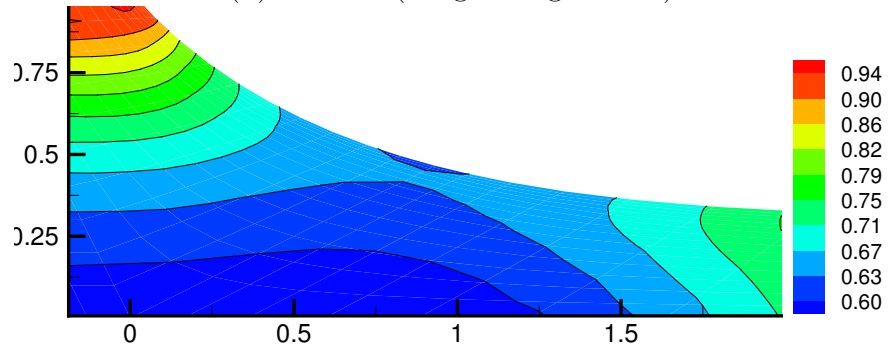
(c) $Wi$=0.5 (Smallest Eigenvalue)
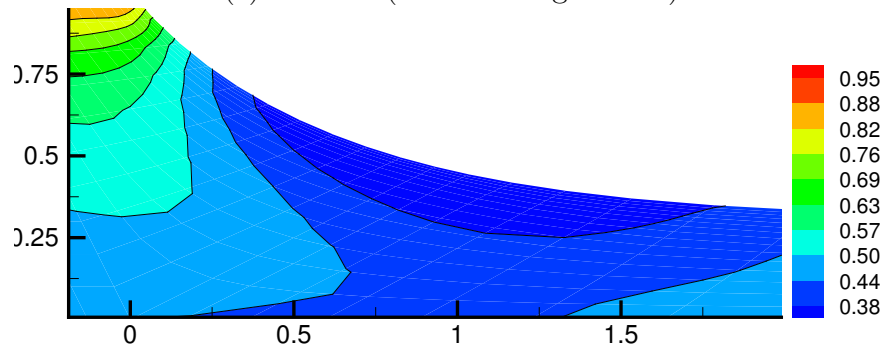
(d) $Wi$=2.0 (Smallest Eigenvalue)

Figure 6.15: Contours of the stretch of the polymer molecules (largest eigenvalue in a & b and smallest eigenvalue in c & d) for dumbbells dumbbells. $Ca = 0.1$, $Q = 0.3$, $\beta = 0.75$, $N_f = 2000$.
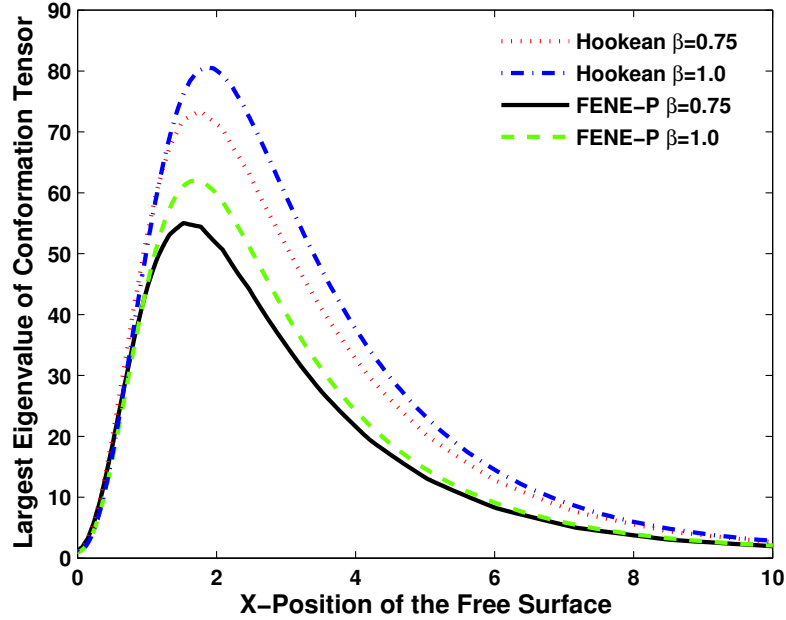
Figure 6.16: Effect of viscosity ratio on stretch of the molecules for Hookean and FENE-P dumbbells using the Micro-Macro approach. Computations are carried out with the M1 mesh. $Wi = 2.0$, $Ca = 0.1$, $Q = 0.3$, $b_{\mathbf{M}} = 100$, $N_f = 2000$.

of the smallest eigenvalue is similar to that of the largest eigenvalue.

The failure of macroscopic computations for dilute solutions at high $Wi$ is due to the singular behaviour of various field variables at the static contact line (discussed in detail in chapter 5). The micro-macro computations, however, remain numerically stable at all values of $Wi$ and $\beta$ as displayed in Figs. 6.1-6.5. Figure 6.17 compares the strength of singularity at the static contact line for $Wi = 2.0$ and $\beta = 0.25$ for the macroscopic and micro-macro computations. It is evident from Fig. 6.17 that the singularity in both the conformation tensor and the velocity gradient is much more pronounced for macroscopic computations. The micro-macro computations show a much smoother velocity gradient close to the static contact line. In recirculation free flows near corners, Salamon et al. [1997a] argue that the strength of singularities grow by mesh refinement [also shown by Pasquali and Scriven [2002]]. It can be seen from Fig. 6.17 that for macroscopic computations the singular nature of field variables are stronger for M4 mesh than is for M1 mesh. At this point it is not clear how the flow computations using the micro-macro approach circumvent the problems associated with the presence of the geometric singularity at the static

contact line in slot coating flow. A careful investigation with much more refined meshes needs to be carried out to fully understand the source of stability provided by micro-macro methods.

In this section we have compared computations of linear dumbbell models using the micro-macro approach with computations of their equivalent constitutive models in the conformation tensor based macroscopic approach. We have shown that the results using the micro-macro method remain numerically stable at higher $Wi$ compared to the flow computations using the macroscopic method even on a much coarser mesh (mesh M1 in the micro-macro approach compared to the M4 mesh in the macroscopic approach) with the same accuracy.

## 6.2   Non-Linear Dumbbell Models

In this section, we present results using non-linear dumbbell models. Since there are no equivalent constitutive equations for FENE dumbbells and models with hydrodynamic interactions, we only compare results for the non-linear dumbbell models with the results for linear dumbbell models.

Figure 6.18 shows the change in the largest and the smallest eigenvalue of conformation tensor with $Wi$ for two different values of the viscosity ratio ($\beta = 0.75$, and $\beta = 1$) for FENE dumbbells. The results for FENE-P dumbbells are also presented for comparison. For non-linear dumbbells, flow computations for smaller $\beta$ values were not carried out purely because of computational requirements. As will be discussed shortly, computations for non-linear dumbbells are significantly more expensive than for linear dumbbell models.

For $\beta = 1$, we have also reported results for an M2 mesh to show mesh convergence of our computations [see Figs. 6.18(c) and 6.18(d)]. For any given value of $Wi$, the FENE model predicts a smaller molecular stretch compared to the stretch of FENE-P dumbbells for both dilute and ultra-dilute solutions. Similar to the results for linear dumbbell models, results for non-linear dumbbells remain numerically stable for all values of $Wi$, i.e. the conformation tensor remains positive definite in the entire flow domain. It is worth mentioning that FENE dumbbells are simulated
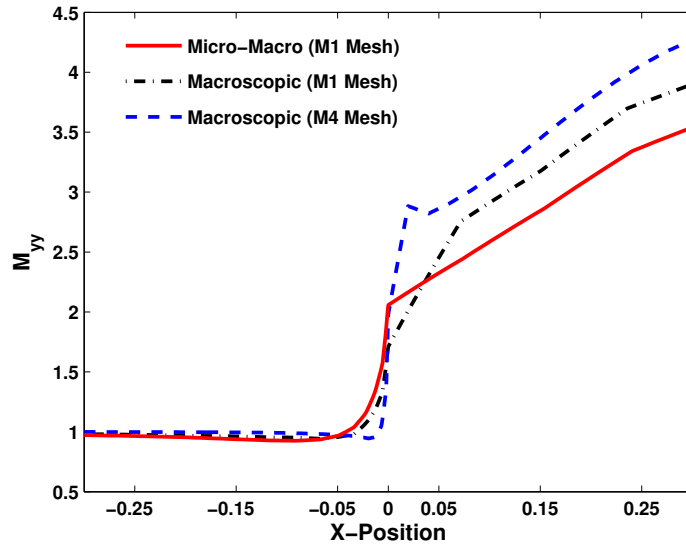
(a) $yy$ Component of the Conformation Tensor
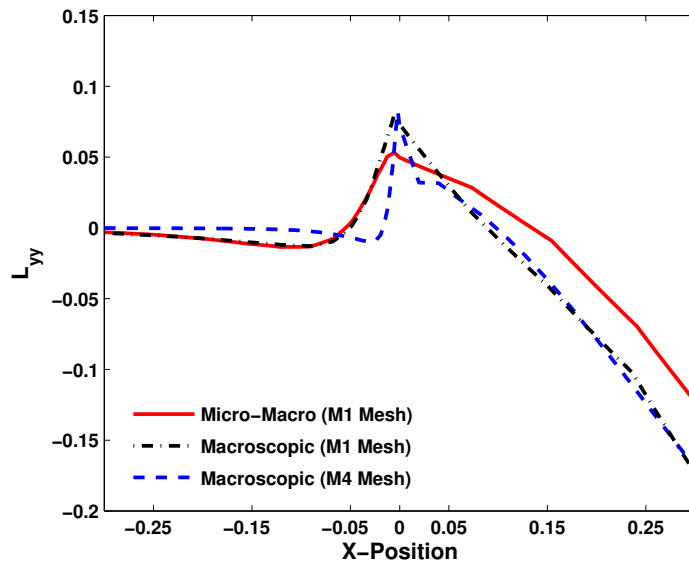


(b) $yy$ Component of the Rate of Stain Tensor

Figure 6.17: $yy$ component of the conformation tensor and rate of strain tensor for a Hookean dumbbell model. Results for Oldroyd-B model on two different meshes are also presented for comparison. Micro-Macro results are carried out with the M1 mesh. $Wi = 2.0$, $Ca = 0.1$, $Q = 0.3$, $\beta = 0.25$, $N_f = 2000$.

using the collocation method discussed in chapter 3. The equivalence of the collocation method and the Newton's method for non-linear dumbbells will be discussed shortly.

Figure 6.19 shows that similar to the FENE-P model, the FENE model also predicts that the out-of-plane eigenvalue of the conformation tensor can be driven away from its equilibrium value in two dimensional flows [Pasquali and Scriven, 2002]. The out-of-plane eigenvalue for FENE dumbbells contracts much more slowly than for FENE-P dumbbells. Mesh convergence is evident from Fig. 6.19(b).

Figure 6.20 displays the change in the largest and smallest eigenvalue of the conformation tensor with $Wi$ for Hookean dumbbells with hydrodynamic interactions for two different values of viscosity ratio ($\beta = 0.75$, and $\beta = 1$). The mesh convergence of the computations are evident from Figs. 6.18(c) and 6.18(d). For any given value of $Wi$, Hookean dumbbells with hydrodynamic interactions are predicted to have smaller stretch compared to the stretch of Hookean dumbbells without hydrodynamic interactions, for both dilute and ultra-dilute solutions.

As in the case of linear dumbbell models, stress boundary layers are formed under the free surface at high $Wi$. The growth of stress boundary layers with $Wi$ is shown in Figs. 6.21 and 6.22. The FENE model predicts smaller maximum stress compared to the FENE-P model [see Fig. 5.10] and the Hookean dumbbell model with hydrodynamic interactions predicts a smaller maximum stress compared to the Hookean dumbbells without hydrodynamic interactions [see Fig. 5.9].

Figure 6.23 shows the components of the conformation tensor $M_{xx}$, $M_{xy}$ and $M_{yy}$ along the free surface computed using Newton's method and the collocation method for FENE dumbbells and Hookean dumbbells with hydrodynamic interactions. It is observed that both methods give identical results. The local values of components of the conformation tensor differ by less than $10^{-5}$ between the two methods.

Figure 6.24 displays the ratio of CPU times using the Newton's method and the collocation method as a function of $Wi$ for non-linear dumbbell models. We observe that for Hookean dumbbells with hydrodynamic interactions, the collocation method is approximately 3 times faster than the Newton's method at any given time step and is independent of $Wi$. For FENE dumbbells, the ratio of CPU times is a strong function of $Wi$. For $Wi < 1.5$, the collocation method is approximately 3 times faster
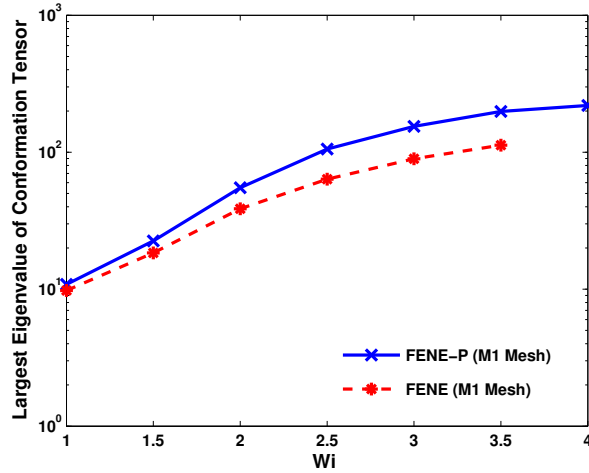
(a) Largest Eigenvalue ($\beta = 0.75$)     (b) Largest Eigenvalue ($\beta = 1.0$)
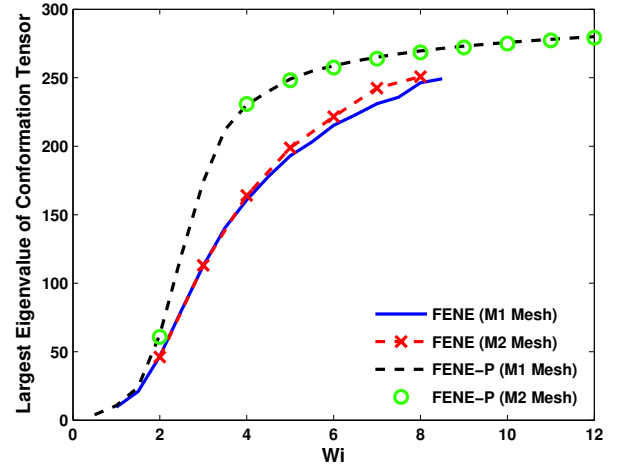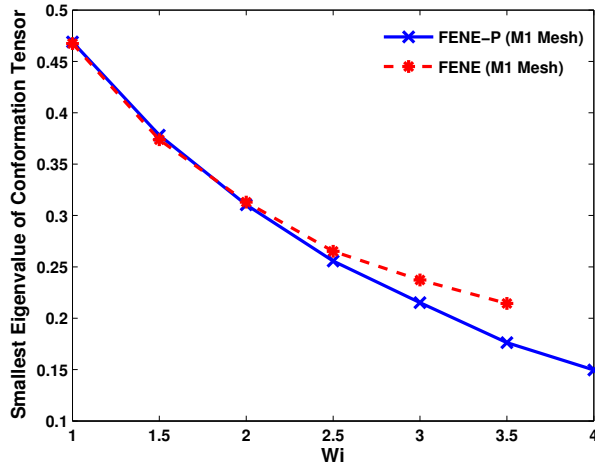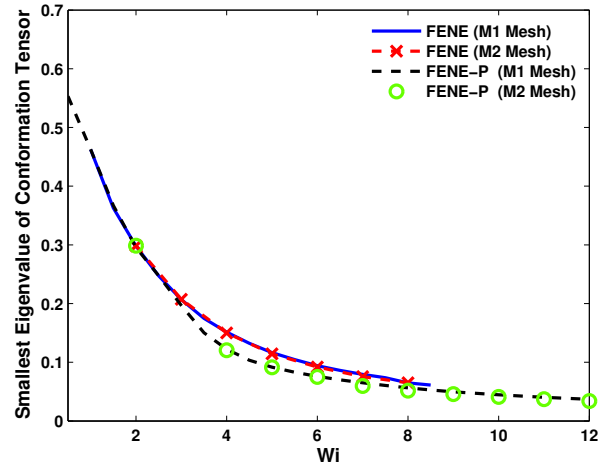
(c) Smallest Eigenvalue ($\beta = 0.75$)     (d) Smallest Eigenvalue ($\beta = 1.0$)

Figure 6.18: Largest (top) and smallest eigenvalue (bottom) of the conformation tensor in the flow domain for non-linear FENE dumbbells. Results for FENE-P dumbbells are also reported for comparison. For FENE dumbbells results are obtained with the M1 mesh using the Collocation method. The results for $\beta = 1.0$ are also reported for the M2 mesh using the Collocation method. $Ca = 0.1$, $Q = 0.3$, $b_{\mathbf{M}} = 100$, $N_f = 2000$.
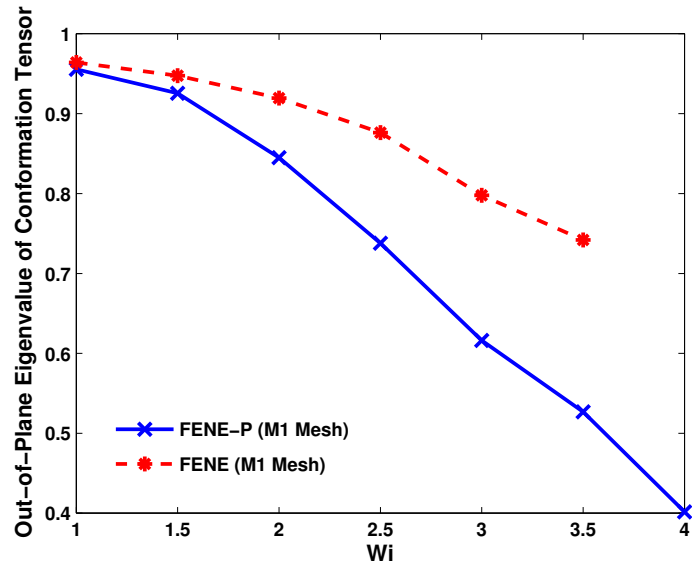
(b) $\beta = 0.75$
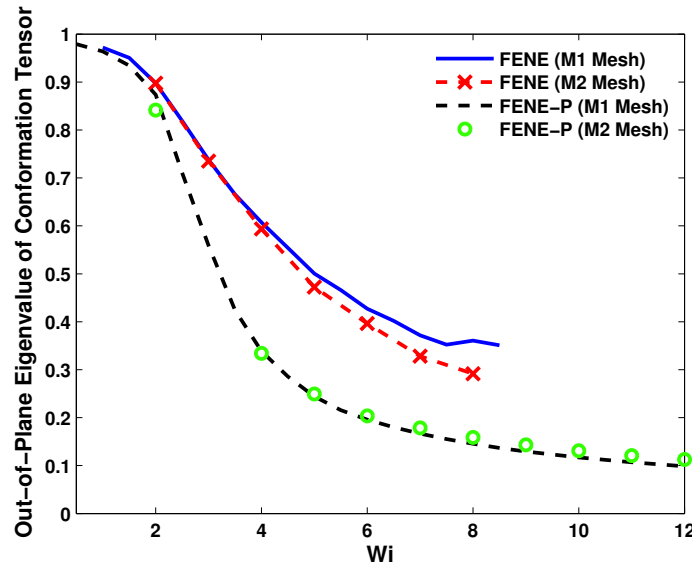


(d) $\beta = 1.0$

Figure 6.19: Out-of-plane eigenvalues of the conformation tensor in the flow domain for non-linear FENE dumbbells. Results for FENE-P dumbbells are also reported for comparison. For FENE dumbbells results are obtained with the M1 mesh using the Collocation method. The results for $\beta = 1.0$ are also reported for the M2 mesh using the Collocation method. $Ca = 0.1$, $Q = 0.3$, $b_{\mathbf{M}} = 100$, $N_f = 2000$.
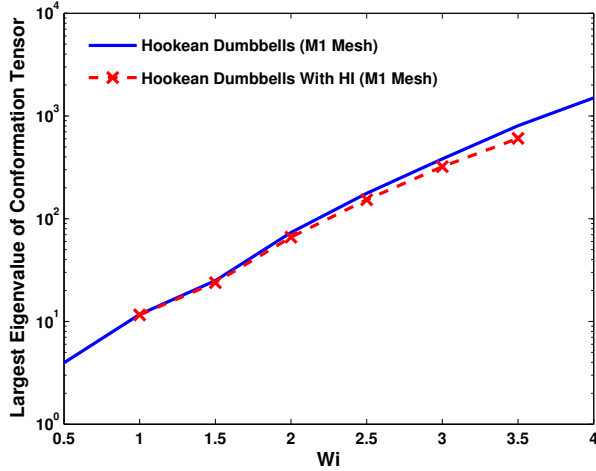
(a) Largest Eigenvalue ($\beta = 0.75$)    (b) Largest Eigenvalue ($\beta = 1.0$)
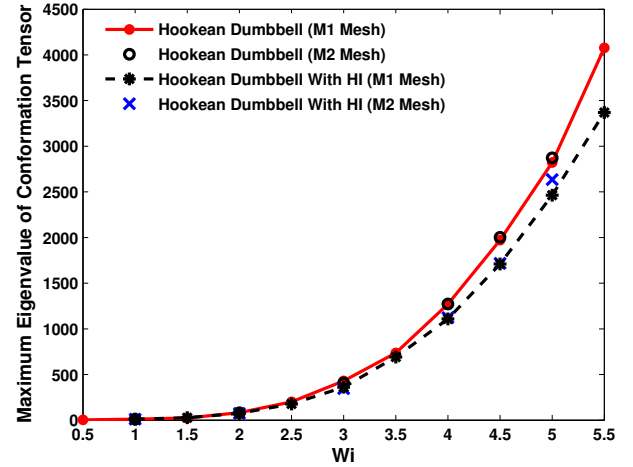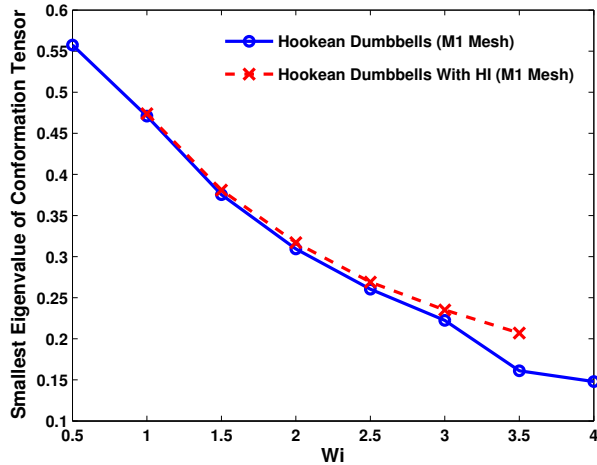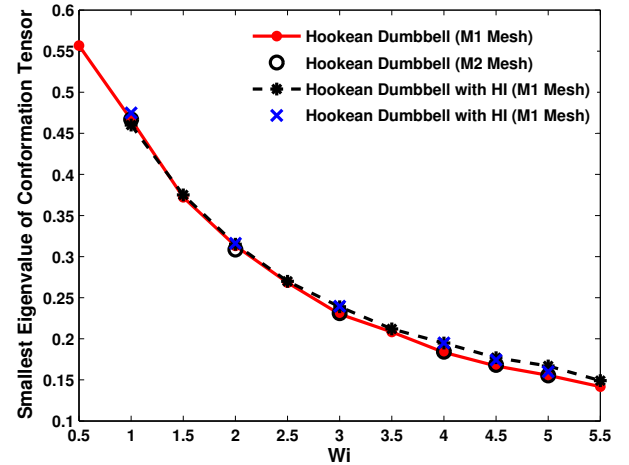
(c) Smallest Eigenvalue ($\beta = 0.75$)    (d) Smallest Eigenvalue ($\beta = 1.0$)

Figure 6.20: Largest (top) and smallest eigenvalue (bottom) of the conformation tensor in the flow domain for Hookean dumbbells with hydrodynamic interactions. Results for Hookean dumbbells without HI are also reported for comparison. For dumbbells with hydrodynamic interactions results are obtained with the M1 mesh using the Collocation method. The results for $\beta = 1.0$ are also reported for the M2 mesh using the Collocation method. $Ca = 0.1$, $Q = 0.3$, $N_f = 2000$.
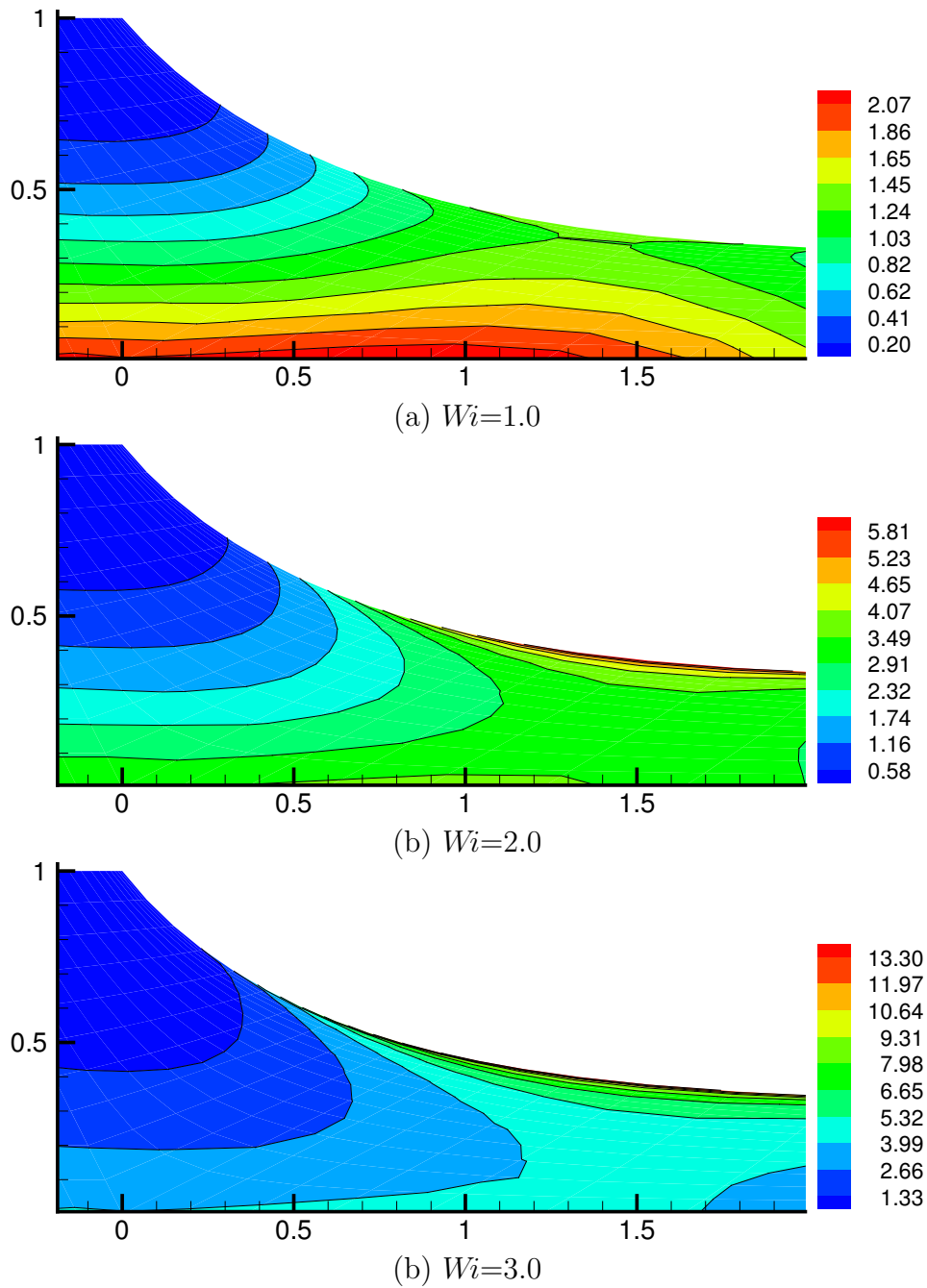
Figure 6.21: Evolution of the $xx$ component of the elastic stress ($\sigma_{xx}$) as a function of $Wi$ for FENE dumbbells. $Ca = 0.1$, $Q = 0.3$, $\beta = 0.75$, $b_{\mathbf{M}} = 100$, $N_f = 2000$.
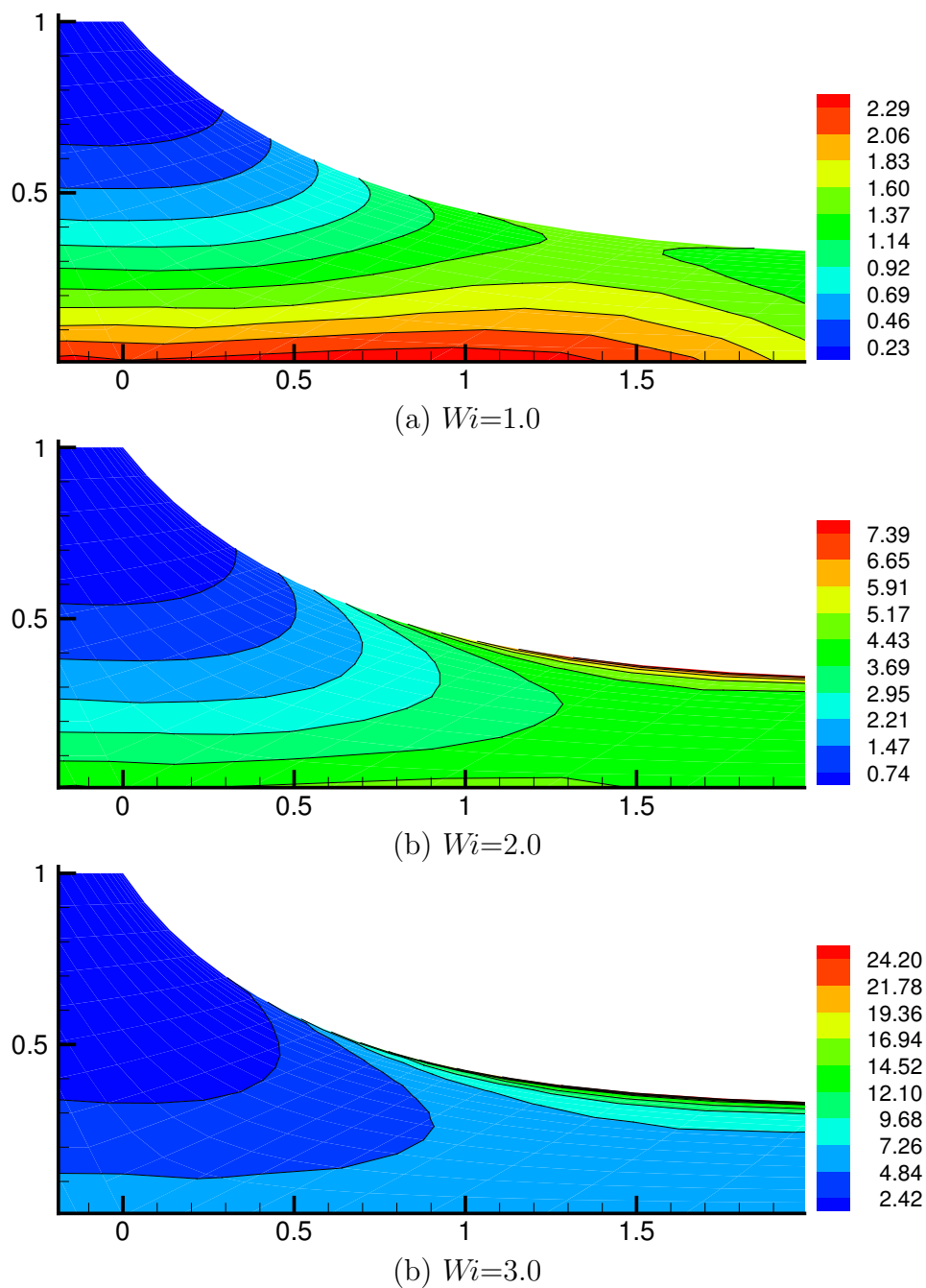
Figure 6.22: Evolution of the $xx$ component of the elastic stress ($\sigma_{xx}$) as a function of $Wi$ for Hookean dumbbells with hydrodynamic interactions. $Ca = 0.1$, $Q = 0.3$, $\beta = 0.75$, $N_f = 2000$, $h^* = 0.14$.
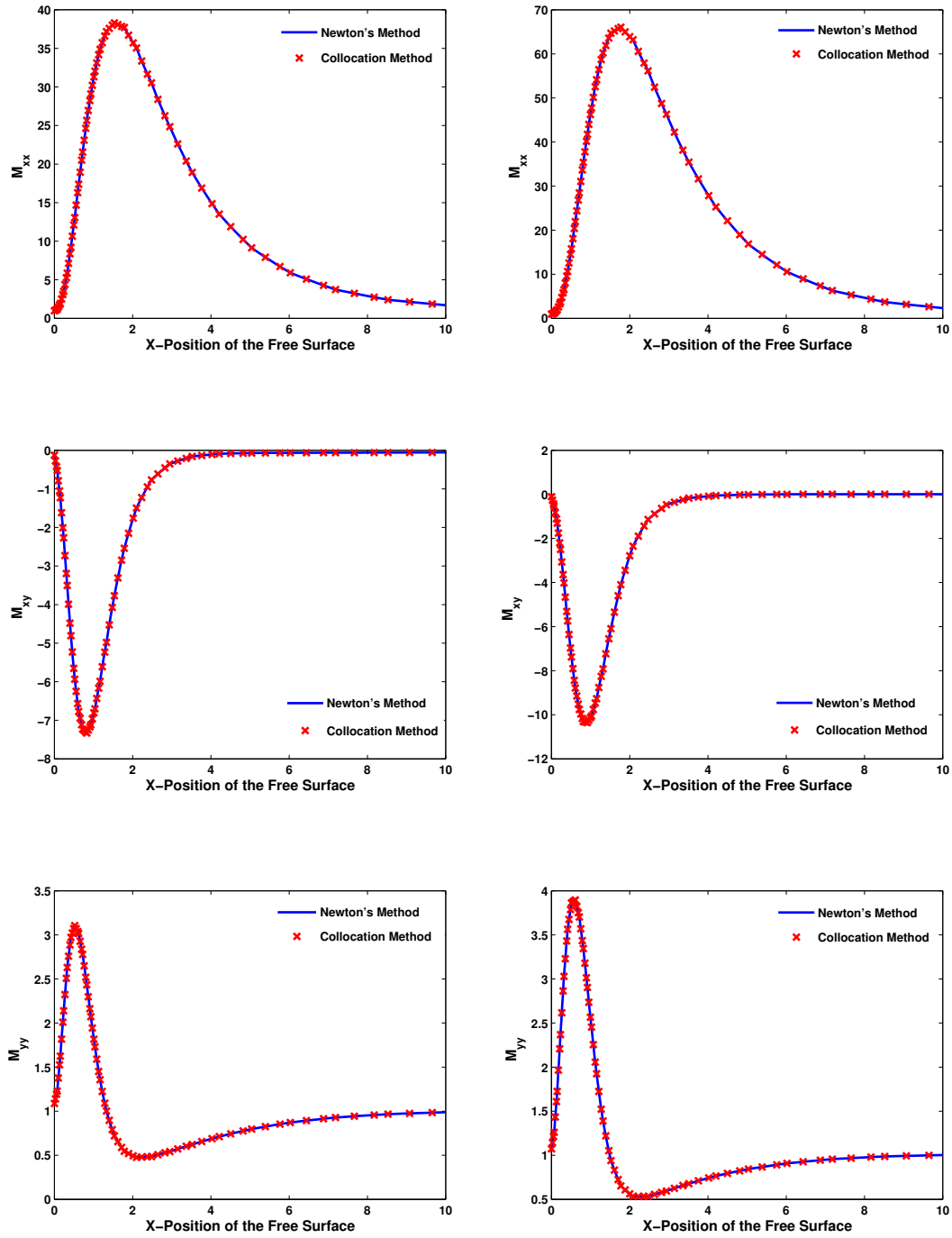
Figure 6.23: Comparison of the components of conformation tensor: $M_{xx}$, $M_{xy}$ and $M_{yy}$ computed using the Newton's method and the collocation method. FENE Dumbbells (Left) and Hookean Dumbbells with hydrodynamic interactions (Right). $Wi = 2$, $Ca = 0.1$, $Q = 0.3$, $\beta = 0.75$, $b_{\mathbf{M}} = 100$, $N_f = 2000$, $h^* = 0.14$.

than the Newton's method. As $Wi$ increases beyond 1.5 the collocation method becomes much more CPU efficient. It is worth mentioning that the CPU time required for the collocation method is relatively insensitive to the values of $Wi$ and the constitutive models for the parameters used in this work. For stiffer dumbbells ($b_{\mathbf{M}} \sim 20-30$), the time required for FENE dumbbells using the collocation method might differ significantly from that of the non-FENE dumbbells (Hookean dumbbells with HI) as the number of iterations to solve the cubic equation using the Newton's method increase as dumbbells gets stiffer. A look up table scheme proposed by Somasi and Khomami [2000] to solve cubic equation in the case of stiff dumbbells would be more appropriate.

For FENE dumbbells, the CPU time required for the Newton's method increases with increasing $Wi$ (and hence the ratio of CPU times) since it takes more and more Newton iterations for the Newton's method to converge. The increase in the time required for Newton's method to converge by increasing $Wi$ can be attributed to the finite extensibility of the molecules which makes the system of equations stiffer at high $Wi$. It is also observed in our simulations that in the case of FENE dumbbells, many of the dumbbells are stretched beyond the maximum length $\sqrt{b}$ for $Wi > 2$ during the course of Newton's iterations requiring the configuration vectors of these dumbbells to be reset in order to get a physically meaningful spring force law.

Table 6.3 compares the memory and the CPU time requirements for the micro-macro computations using linear and non-linear dumbbell models. The computations for non-linear dumbbell models using the collocation method are almost twice as expensive as computations for linear dumbbell models both in terms of the CPU time and memory requirements. The memory and CPU time required for non-linear dumbbell models are controlled by storage and evaluation of the configuration fields at the predictor step which is not required in the scheme used for linear dumbbell models in this work. For non-linear dumbbell models, while the required CPU time depends upon the numerical scheme (either the collocation or Newton's method), the memory requirements are the same (independent of the numerical method).

Figure 6.25 shows the effect of $Wi$ on the relative positions of largest and smallest eigenvalues of the conformation tensor in the flow domain for FENE dumbbells. As in the case of a linear dumbbell model, the non-linear constitutive models also show
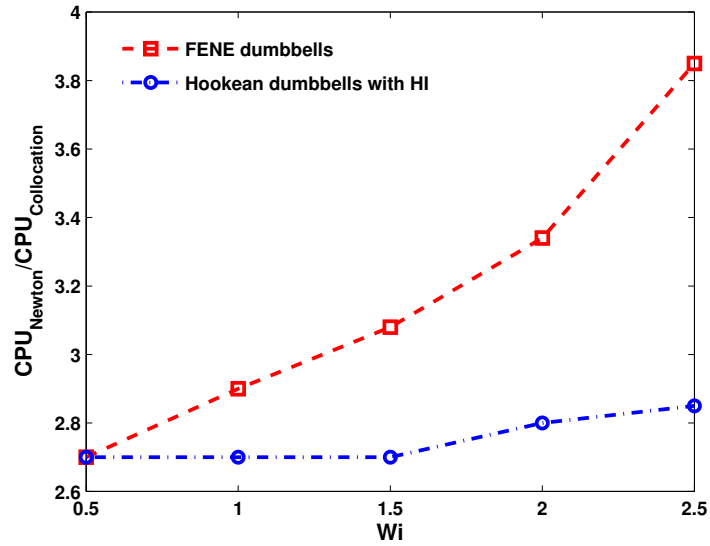
Figure 6.24: Comparison of CPU time requirement for the computations of FENE dumbbells and Hookean dumbbells with hydrodynamic interactions using the Newton's method and the Collocation method. Computations are carried out with the M1 mesh. $Ca = 0.1$, $Q = 0.3$, $\beta = 0.75$, $b_\mathbf{M} = 100$, $N_f = 2000$, $h^* = 0.14$, $\Delta t = 0.02$.

Table 6.3: Comparison of CPU time requirements for linear and non-linear dumbbell models for M1 mesh. $Wi = 2.0$, $\beta = 0.75$, $\Delta t = 0.02$, $N_f = 2000$

| Constitutive Equation | Number of Processors | Time Steps | CPU Time | Wall Time | Memory (Mb) |
|---|---|---|---|---|---|
| Linear dumbbells | 8 | 1000 | 32 hrs | 4 hrs | 147 |
| Non-linear dumbbells with Newton's method | 8 | 1000 | 224 hrs | 28 hrs | 285 |
| Non-linear dumbbells with Collocation method | 8 | 1000 | 64 hrs | 8 hrs | 285 |

that at smaller $Wi$ ($Wi \sim< 1.5$), molecules are stretched predominantly on the web and at higher $Wi$ ($Wi \sim< 1.5$), the largest stretch is on the free surface. The contours for Hookean dumbbells with hydrodynamic interactions show virtually the same behaviour.

Figure 6.26 displays the effect of the viscosity ratio on the stretch of polymer molecules along the free surface. Qualitatively, the behavoiur shown by the non-linear dumbbells are similar to that of linear dumbbell models. An increase in the viscosity ratio increases the stretch of the molecules for both FENE and the Hookean dumbbells with hydrodynamic interactions.

Figures 6.27 examines the effect of different constitutive models used in this study on the largest eigenvalue of the dimensionless stress tensor along the free surface. The stress, a macroscopic property, appears relatively unaffected by the presence of different non-linear phenomenon (except perhaps for FENE model, which has maximum difference of about 40% from other models). In other words, Hookean dumbbells, Hookean dumbbells with hydrodynamic interactions, and FENE-P dumbbells exhibit nearly similar stresses along the free surface. A similar conclusion can be drawn from Fig. 6.28 which shows the velocity contours (a macroscopic property) of viscoelastic liquids for different constitutive models. As discussed in section 5, the viscoelasticity of the coating fluid pulls the liquid out of the recirculation zone (present under the die for Newtonian liquids) because of a positive hoop stress. Similar behavior is observed with the micro-macro method using different constitutive models. It is evident from Fig. 6.28 that the velocity is relatively independent of constitutive models.

On the other hand, the stretch of the polymer, a microscopic property, is significantly different for different constitutive models as shown in Fig. 6.29. The Peterlin approximation to the FENE dumbbell model over-predicts the stretch. The inclusion of hydrodynamic interactions appears to reduce the stretch in comparison with the pure Hookean dumbbell model. The inaccurate prediction of stretch and orientation of polymer molecules might lead to a conclusion of the existence of various instabilities such as non-uniform coating in slot coating flows, which are not in actuality.
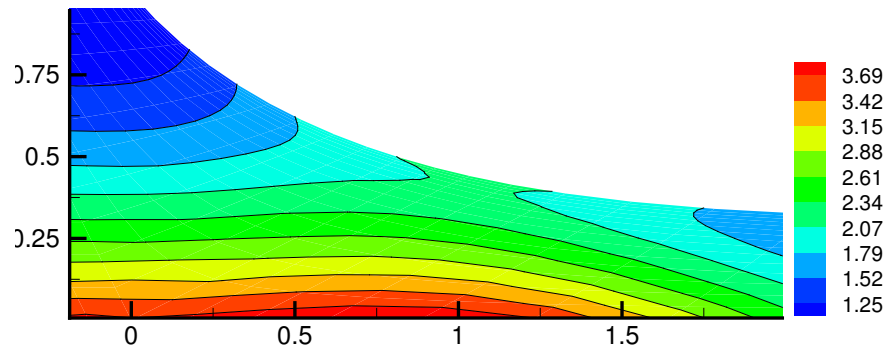
(a) $Wi$=0.5 (Largest Eigenvalue)
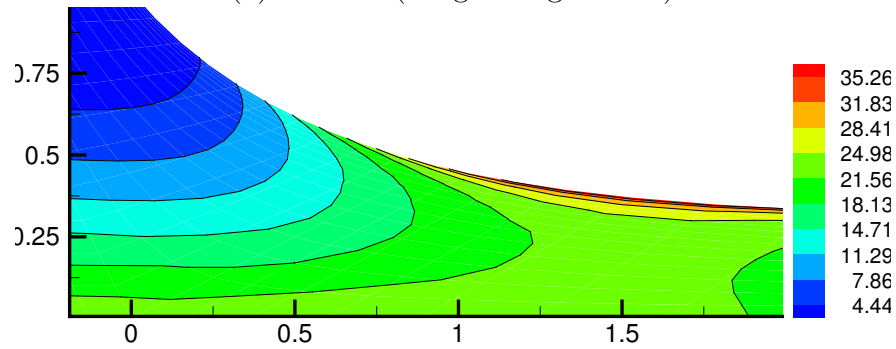
(b) $Wi$=2.0 (Largest Eigenvalue)
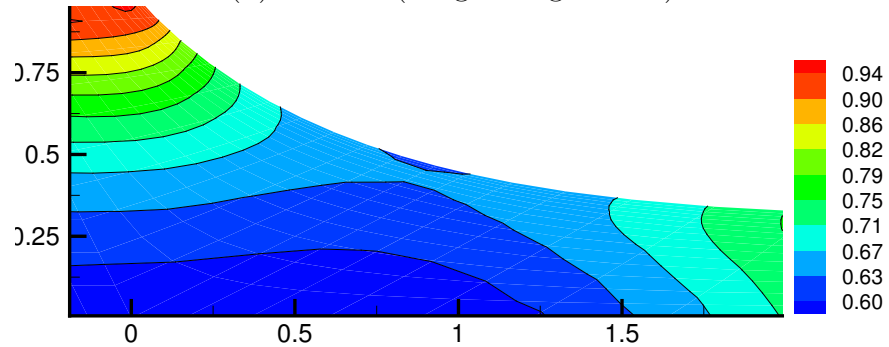
(c) $Wi$=0.5 (Smallest Eigenvalue)
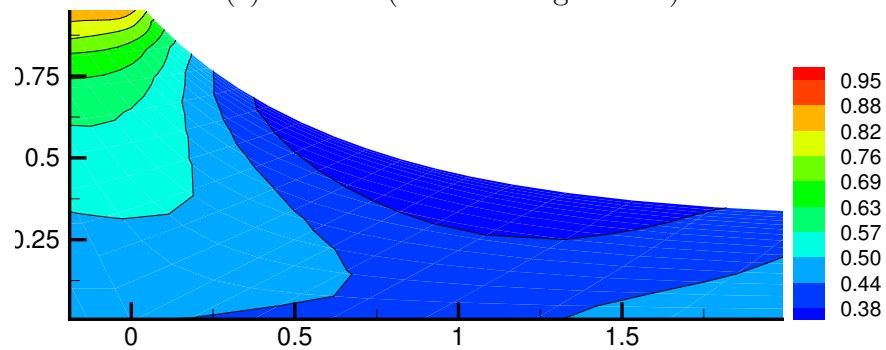
(d) $Wi$=2.0 (Smallest Eigenvalue)

Figure 6.25: Contours of the stretch of the polymer molecules (largest eigenvalue in a & b and smallest eigenvalue in c & d) for FENE dumbbells. $Ca = 0.1$, $Q = 0.3$, $\beta = 0.75$, $b_{\mathbf{M}} = 100$, $N_f = 2000$.
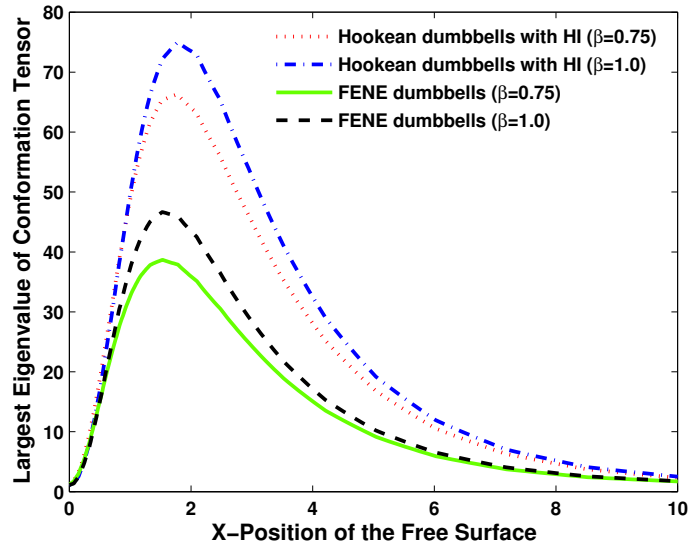
Figure 6.26: Effect of viscosity ratio on the stretch of the molecules for Hookean dumbbells with hydrodynamic interactions and FENE dumbbells. $Wi = 2.0$, $Ca = 0.1$, $Q = 0.3$, $b_{\mathbf{M}} = 100$, $N_f = 2000$.
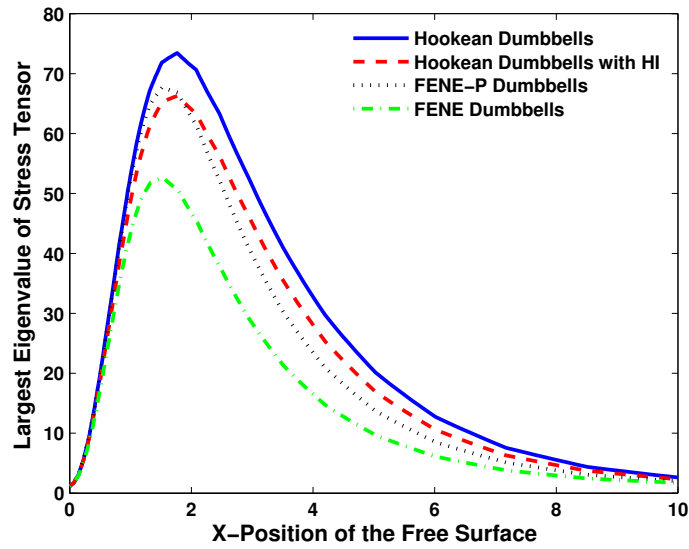


Figure 6.27: Largest eigenvalue of the dimensionless stress tensor $(\lambda\,\sigma/\eta_{p,0})$ along the free surface for different constitutive models. $Wi = 2.0$, $Ca = 0.1$, $Q = 0.3$, $\beta = 0.75$, $b_{\mathbf{M}} = 100$, $N_f = 2000$, $h^* = 0.14$
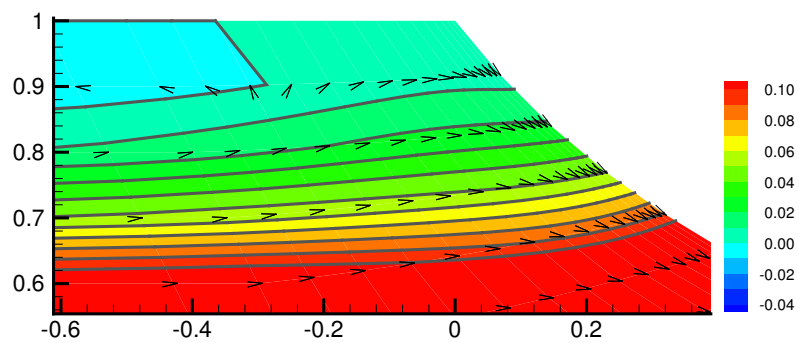
(a) Hookean Dumbbells
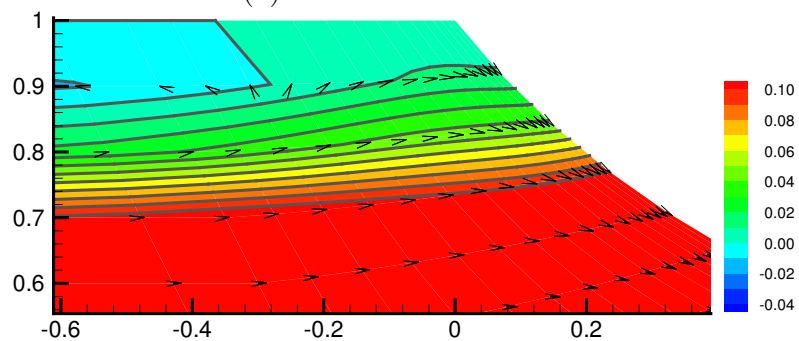
(b) Hookean Dumbbells with Hydrodynamic Interactions
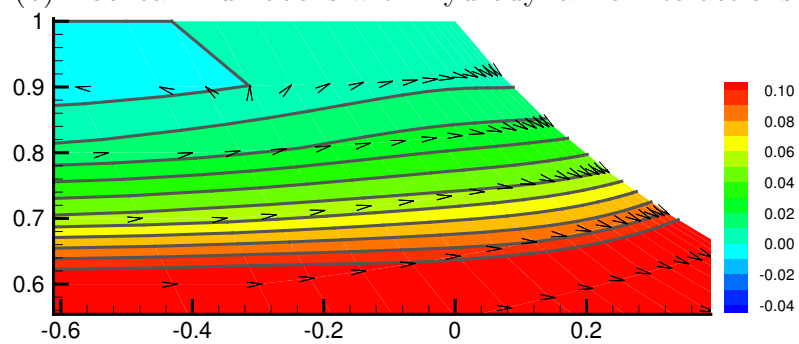
(c) FENE-P Dumbbells
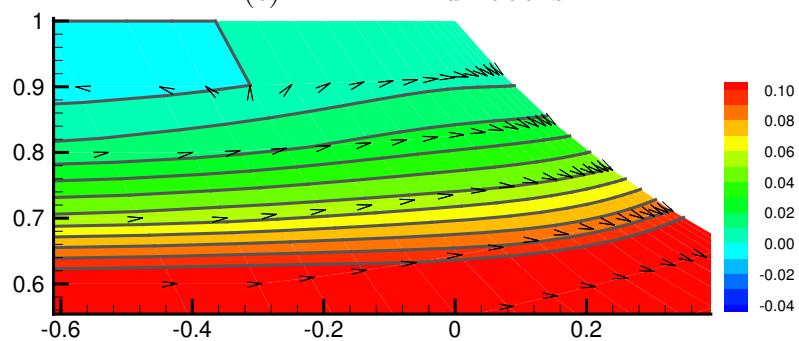
(d) FENE Dumbbells

Figure 6.28: Velocity contours for different constitutive models. $Wi = 2.0$, $Ca = 0.1$, $Q = 0.3$, $\beta = 0.75$, $b_{\mathbf{M}} = 100$, $N_f = 2000$.
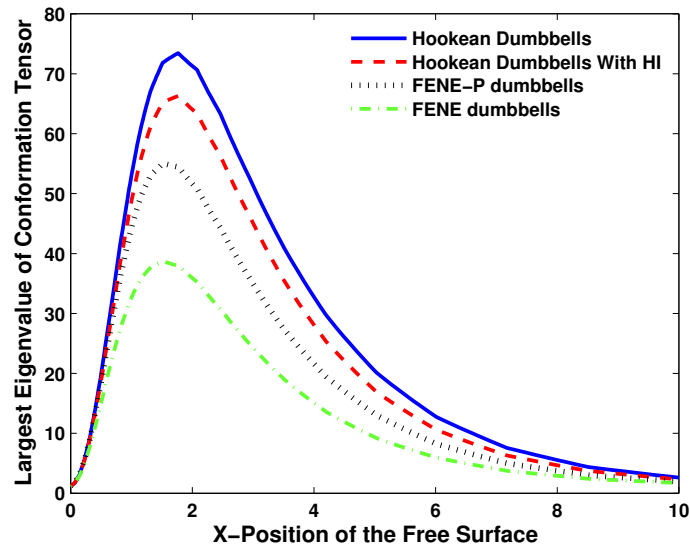
Figure 6.29: Stretch (Largest eigenvalue of the conformation tensor) of polymer molecules along free surface for different constitutive models. $Wi = 2$, $Ca = 0.1$, $Q = 0.3$, $\beta = 0.75$, $b_{\mathbf{M}} = 100$, $N_f = 2000$, $h^* = 0.14$.

## 6.3   Transient Free Surface Flow

In this section, the evolution of molecular conformation in the downstream section of a slot coater is studied as the flow evolves from one steady state to another after a gradual change of the dimensionless flow rate from 0.3 to 0.27 at $Wi$=2.0 and $\beta = 0.75$. The initial condition for all the transient simulations is the solution of the flow equations at dimensionless flow rate 0.3, $Wi = 2.0$ and $\beta = 0.75$. The flow rate is gradually changed over a period of $3\lambda$ while keeping all other parameters fixed. The gradual change in flow rate ensures a divergence free velocity at each time step which is necessary to calculate the flow field at a subsequent time step [Gresho et al., 1979].

Figure 6.30 displays the change in the largest eigenvalue of the conformation tensor by changing the flow rate for an Oldroyd-B fluid and Hookean dumbbell model. Changing the flow rate from 0.30 to 0.27 increases the local velocity gradient under the die lip because the free surface moves inward for a constant web velocity. As a result molecules at a lower flow (0.27) rate are more stretched compared to the those at a higher flow rate (0.30). The results using the macroscopic Oldroyd-B
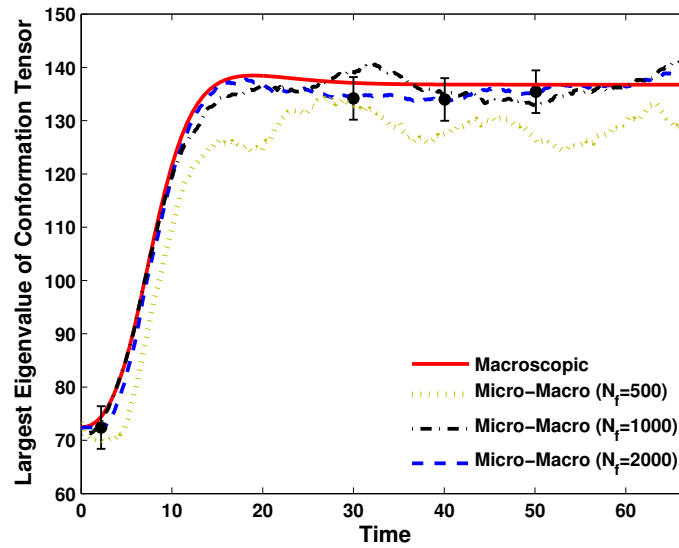
Figure 6.30: Change in the largest eigenvalues of the conformation tensor by changing the flow rate for the Hookean dumbbell model. $Wi = 2.0$, $Ca = 0.1$, $Q = 0.3$, $\beta = 0.75$, $N_f = 2000$, $\Delta t = 0.01$. Micro-Macro and Macroscopic computations are carried out with the M1 and M4 mesh, respectively

model in Figure 6.30 are for a time step $\Delta t = 0.01$. The time step convergence of macroscopic results are shown in Fig. 6.31. Hereafter, $\Delta t = 0.01$ for macroscopic results unless otherwise specified.

The mesh convergence of the transient results are shown in Figure 6.32. It is evident that results using the mesh M1 are significantly different from M2, M3 and M4 meshes, specially the evolution of smallest eigenvalue of the conformation tensor as shown in Fig 6.32b.

Transient results calculated using the micro-macro method are subject to statistical fluctuations due to the finite ensemble size of the configuration fields. Figure 6.30 shows that by increasing the size of the ensemble from 500 to 2000, the statistical error bar gets smaller as the variance is inversely proportional to the square root of the number of trajectories. The results show good comparison between the macroscopic and micro-macro method within statistical error.

Figure 6.33 shows the time step convergence of the micro-macro results reported in Fig. 6.30. It is evident from the Fig. 6.33 that as the time step size gets smaller, the solution gets increasingly more accurate. The results using a time step of $\Delta t = 0.01$
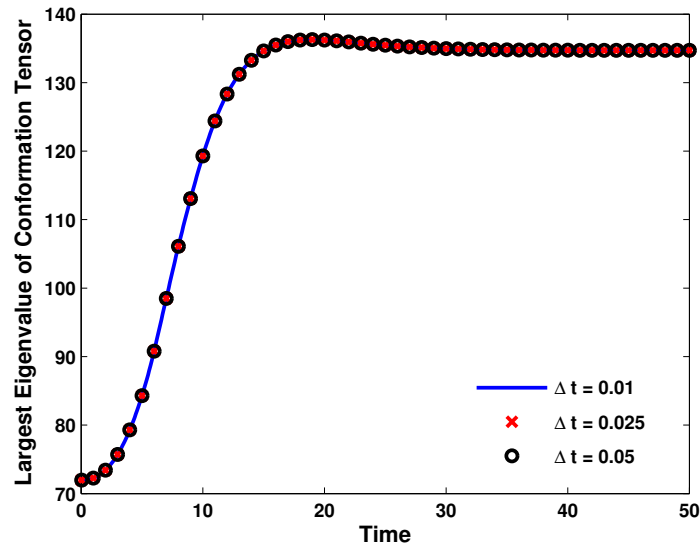
Figure 6.31: Time step convergence of the change in the largest eigenvalues of the conformation tensor by changing the flow rate for Oldroyd-B model. $Wi = 2.0$, $Ca = 0.1$, $Q = 0.3$, $\beta = 0.75$. Computations are carried out with the M1 mesh.

are very close to the results using $\Delta t = 0.0075$. Hence, $\Delta t = 0.01$ is used hereafter.

Figure 6.34 displays the change in the smallest eigenvalue of the conformation tensor by changing the flow rate for an Oldroyd-B fluid and Hookean dumbbell model. The results using the macroscopic approach for the smallest eigenvalue are obtained with the M4 mesh since the smallest eigenvalue computed using the M1 mesh at $Wi = 2.0$ is significantly different from the computed using M4 mesh [see Fig. 6.32]. It is evident from Fig. 6.34 that the micro-macro computations are more accurate than than the macroscopic computations on coarse meshes i.e. the smallest eigenvalue predicted by the M1 mesh using macro-macro approach is as accurate as the smallest eigenvalue predicted by the macroscopic approach using the M3 and M4 meshes.

Figure 6.35 shows the change in the coating thickness with time at the outflow plane. It should be noted that although the flow rate is changed at $t = 0$ the coating thickness starts changing only after $t \sim 30$. This in explained in Fig. 6.36 which shows the change in y-position of the free surface with time at different x-positions along the free surface. As shown in the Fig. 6.36, a front develops at the contact line and propagates downstream like a wave. Figure 6.36 shows that we have a good
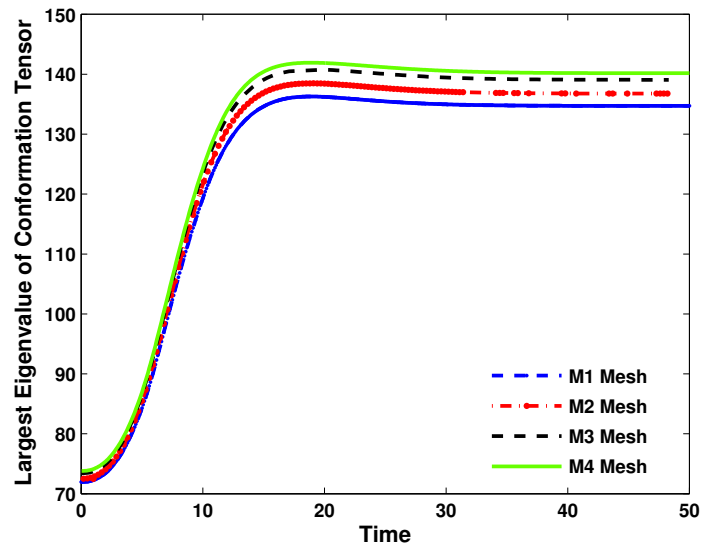
(a) Largest Eigenvalue
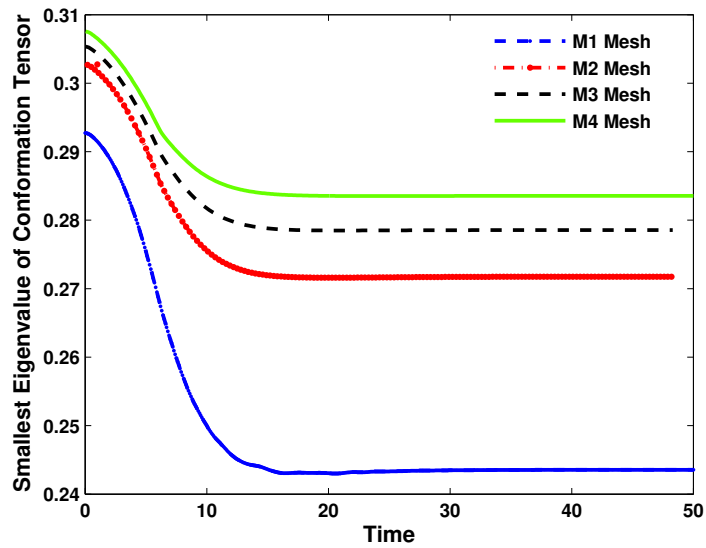


(b) Smallest Eigenvalue

Figure 6.32: Mesh convergence of transient results for macroscopic computations. $Wi = 2.0$, $Ca = 0.1$, $Q = 0.3$, $\beta = 0.75$.
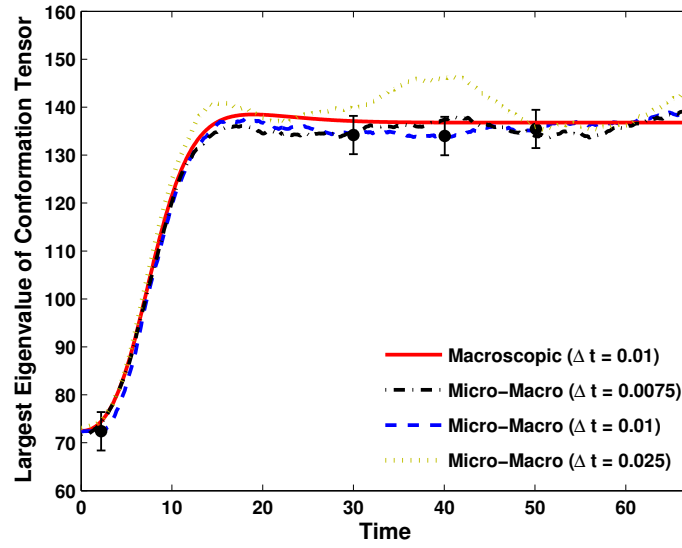
Figure 6.33: Time step convergence of the change in the largest eigenvalues of the conformation tensor by changing the flow rate for Hookean dumbbell model. $Wi = 2.0$, $Ca = 0.1$, $Q = 0.3$, $\beta = 0.75$, $N_f = 2000$. Computations are carried out with the M1 mesh.
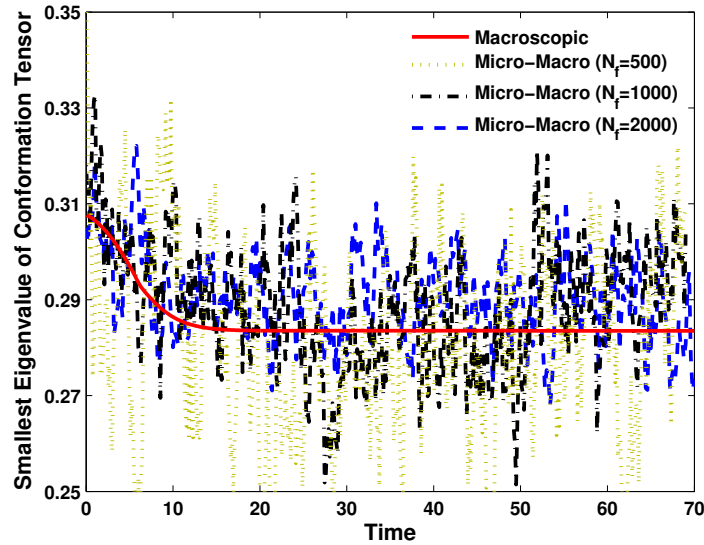


Figure 6.34: Change in the smallest eigenvalues of the conformation tensor by changing the flow rate for the Hookean dumbbell model. $Wi = 2.0$, $Ca = 0.1$, $Q = 0.3$, $\beta = 0.75$, $N_f = 2000$, $\Delta t = 0.01$. The Micro-Macro computations are carried out with the M1 mesh and Macroscopic are carried out with the M4 mesh.
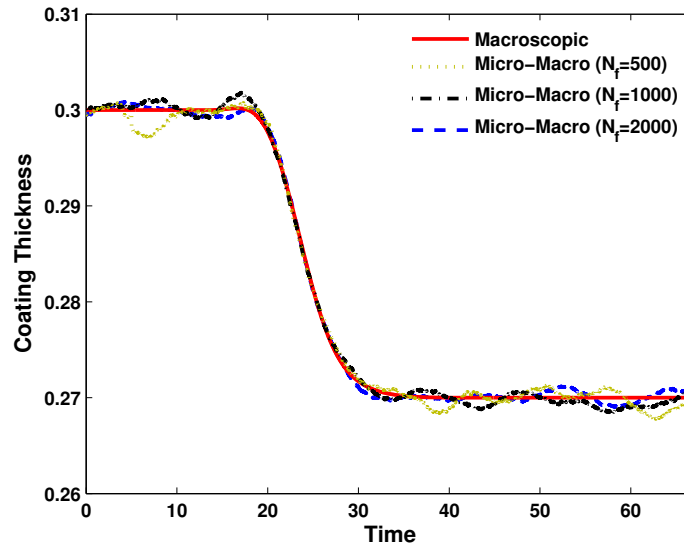
Figure 6.35: Change in the coating thickness by changing the flow rate for the Hookean dumbbell model. $Wi = 2.0$, $Ca = 0.1$, $Q = 0.3$, $\beta = 0.75$, $N_f = 2000$, $\Delta t = 0.01$. Computations are carried out with the M1 mesh.

agreement between the micro-macro and macroscopic methods for transients flows.

Figure 6.37 displays snap shots of the contours of velocity at different times. The contours in Fig. 6.37 are not as smooth as the one displayed in Figs. 5.27 and 5.26 which can be attributed to the coarseness of the mesh (M1 mesh is used for Fig. 6.37 and M4 mesh is used for Figs. 5.27 and 5.26). As the flow decrease from $Q = 0.3$ to $0.27$, recirculation under the die increase. At a given $Wi$ and viscosity ratio, the strength of recirculation is much higher for a smaller flow rate. As shown in Fig. 6.37, the micro-macro results compare very well with the macroscopic results.

The transient results for FENE-P model using the macroscopic and micro-macro approach are shown in Fig. 6.38. The FENE-P model shows almost the same behavior as the Hookean dumbbell model and good agreement is observed between macroscopic and micro-macro results.

## 6.4   Conclusion

In this chapter, we have computed the transient free surface flow using the BCF based micro-macro approach. This method involves Brownian dynamics simulation
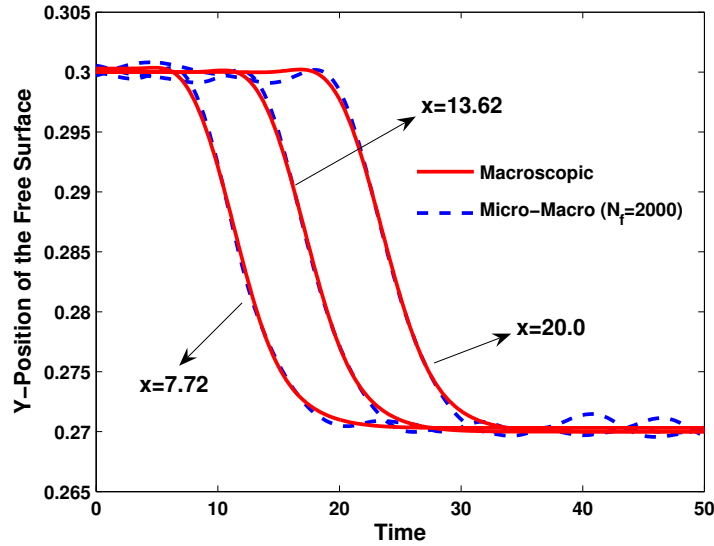
Figure 6.36: Change in the Y-position of the free surface at different X-positions along the free surface. Solid lines are for Oldroyd-B model (Macroscopic) and dotted lines are for the Hookean dumbbell model (Micro-Macro). $Wi = 2.0$, $Ca = 0.1$, $Q = 0.3$, $\beta = 0.75$, $\Delta t = 0.01$, $N_f = 2000$. Computations are carried out with the M1 mesh.

of the motion of polymer molecules coupled together with a time dependent finite element algorithm for the solution of the macroscopic conservation equations. We have validated our method by comparing the flow behavior in the downstream section of a slot coater for linear dumbbell models i.e. Hookean and FENE-P dumbbell with their equivalent macroscopic closed form constitutive equations in a conformation tensor based formulation. We found excellent agreement between the results from the BCF approach and the results using the macroscopic approach. An important observation was that the computations using the BCF method were stable at higher $Wi$ and on a relatively coarser mesh when compared to the computations using the macroscopic approach. We have shown that the proposed fully implicit scheme is more stable than the explicit Euler scheme used in literature with no additional computational and memory requirements for the solution of free surface flows.

We have further computed the complex free surface flow problem by using FENE dumbbells and dumbbells with hydrodynamic interactions, for which no closed-form
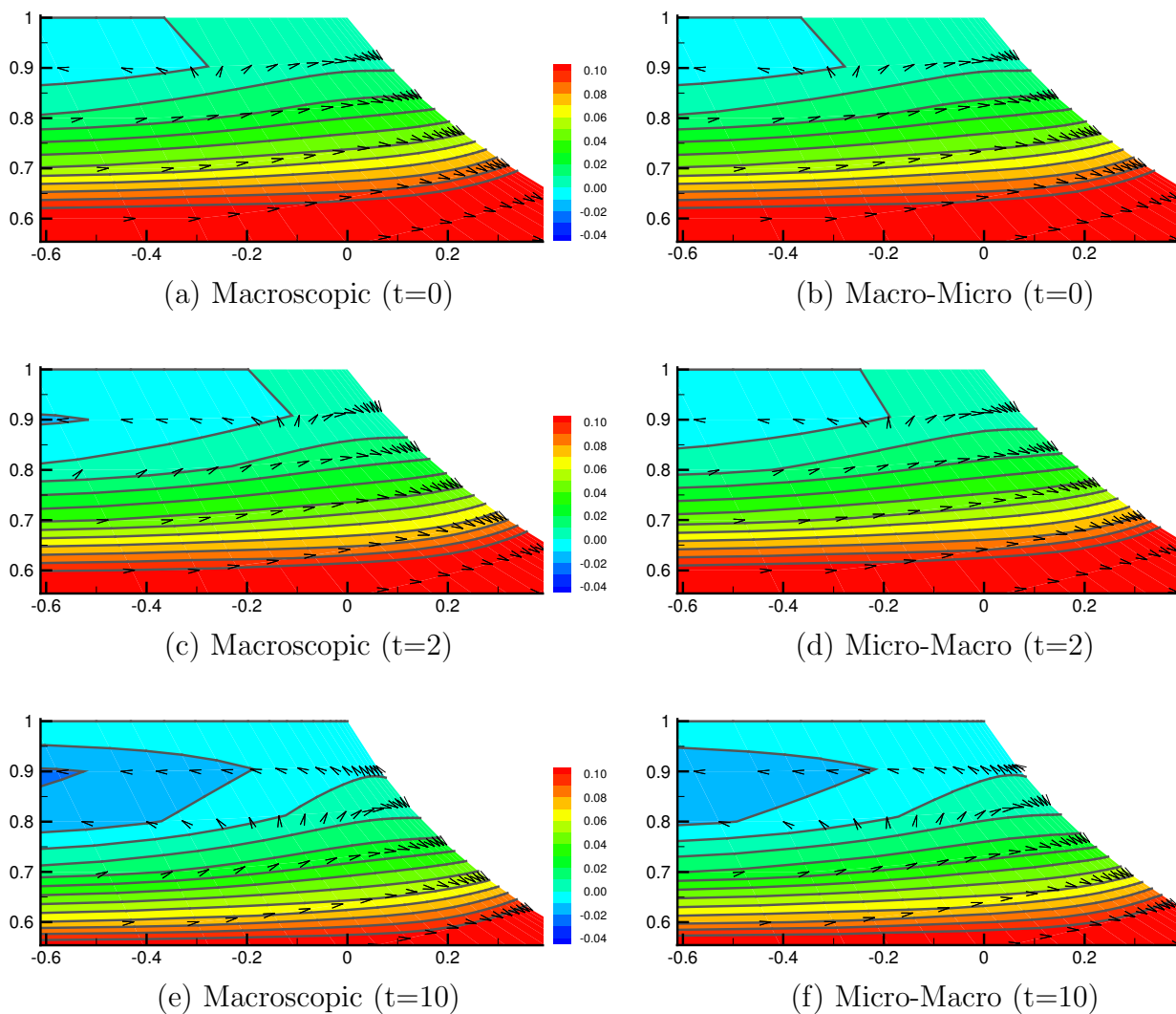
Figure 6.37: Change in velocity profile by changing the dimensionless flow rate from $Q = 0.3$ to $Q = 0.27$ for an Oldroyd-B fluid using the Macroscopic (left) and Micro-Macro approach (right). Computations are carried out with the M1 mesh. $Wi = 2.0$, $Ca = 0.1$, $\beta = 0.75$, $N_f = 2000$, $\Delta t = 0.01$.
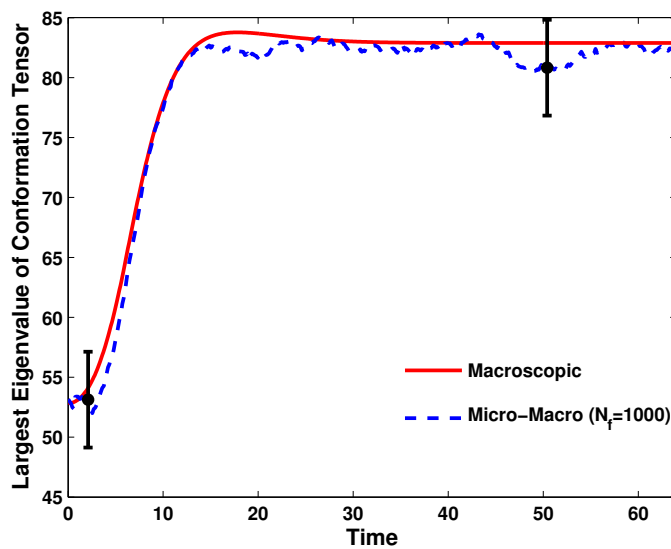
(a) Largest Eigenvalue
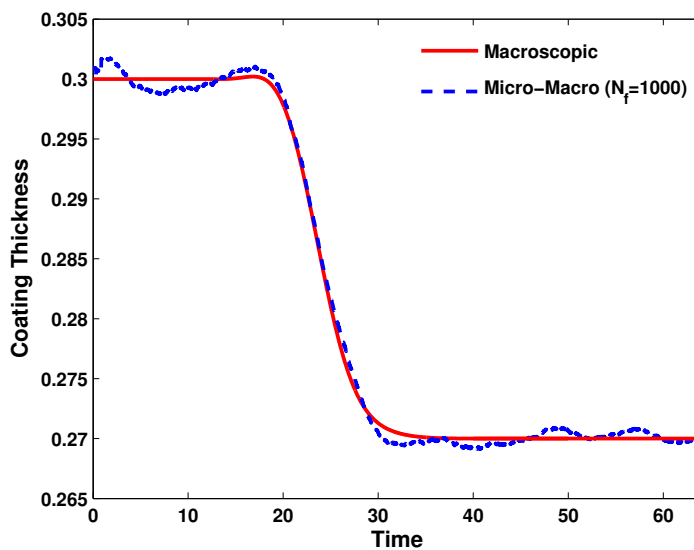


(b) Coating Thickness

Figure 6.38: Change in the largest eigenvalue of the conformation tensor and the coating thickness for the FENE-P model. Computations are carried out with the M1 mesh. $Wi = 2.0$, $Ca = 0.1$, $\beta = 0.75$, $b_{\mathbf{M}}=100$, $N_f = 2000$, $\Delta t = 0.01$.

constitutive equations exist. Two different algorithms to solve the non-linear dumb-bell models namely, Newton's method and a novel least-squares and collocation method discussed in chapter 3, were examined. We have shown that both algorithms give identical results. However, the collocation method is fast and computation-ally efficient when compared to Newton's method. We found significant differences between the stretch of the polymers at the free surface for different microscopic constitutive models.

# Chapter 7

# Conclusions

The objective of this work has been to use a multiscale simulation strategy to compute transient viscoelastic free surface flows of dilute and ultra-dilute polymer solutions. Two different multiscale methods, namely, conformation tensor based approach and micro-macro approach based on the Brownian configuration fields method, have been used for this purpose. In general, multiscale methods for modeling viscoelastic flows are superior to conventional macroscopic methods as they account for the microstructure of flowing polymer molecules. However, a distinct advantage of the micro-macro method over other methods is that it avoids the need for a closed-form constitutive model and hence, more accurate polymer models that incorporate effects such as finite extensibility and other non-linear solvent mediated interactions like hydrodynamic and excluded-volume interactions (for which no closed-form equations exist) can be simulated. This work is the first ever application of the BCF method to solve viscoelastic free surface flows.

In the conformation tensor based approach, two different constitutive models, namely, an Oldroyd-B and a FENE-P model, were used for viscoelastic flow computations. In the BCF method used in this work, polymer molecules were represented by a dumbbell model with both linear and non-linear springs, and hydrodynamic interactions between beads was incorporated. The linear dumbbell models i.e. Hookean and FENE-P dumbbells, are equivalent to the Oldroyd-B and FENE-P constitutive models in the conformation tensor based formulation.

The following different solutions strategies were developed and implemented to

177

compute viscoelastic flow with the micro-macro and conformation tensor based approaches:

- The DEVSS-TG finite element method coupled with the elliptic mesh generation methodology was implemented to study steady state free surface flow using the conformation tensor approach.

- An unconditionally stable fully implicit time integration scheme was implemented to study transient free surface flow using the conformation tensor approach.

- For micro-macro flow computations, the Galerkin finite element method was implemented for macroscopic conservation and mapping equations.

- An unconditionally stable fully implicit simulation algorithm was developed for linear dumbbell models.

- Two different algorithms to solve non-linear dumbbell models, namely, Newton's method and a novel least-squares and collocation method, were developed. The least-squares and collocation scheme is an extension of the predictor-corrector scheme proposed by Somasi and Khomami [2000] to solve nonhomogeneous flows.

- A new way of imposing boundary conditions on the BCF equation was developed. The new boundary condition is independent of the initial condition on configuration fields and the microscopic constitutive model.

Simulations for a wide range of parameters were carried out to understand the role of viscoelasticity on slot coating flows using both the micro-macro and conformation tensor based approach. The key findings of this work are as follows:

- The computations of both dilute and ultra-dilute solutions suggest that the flow behaviour of a dilute polymer solution is completely different from that of an ultra-dilute solution, for instance with regard to the mode of failure of numerical simulations at high $Wi$ number, the effect of the static contact line on flow computations etc. We found that flow computations of ultra-dilute

polymer solutions are very strongly dependent on mesh refinement and constitutive model, i.e., the maximum $Wi$ which corresponds to a stable numerical solution increases with mesh refinement and with the use of a more accurate constitutive equation. On the contrary, the simulations for dilute polymer solutions are independent of mesh refinement and constitutive equation. Out study has clearly demonstrated the difference between dilute and ultra-dilute flow computations.

- It was found that for $Wi < 1.5$ the rate of stretching of polymer molecules is independent of viscosity ratio. The rate of stretching decreases with viscosity ratio as $Wi$ goes beyond 1.5. Two different regimes of rate of stretching in our simulations indicate the existence of two different flow kinematics governing the rate of stretching. At low $Wi$ ($Wi < 1.5$), polymer molecules are predominantly stretched at the web in shear dominated flow. At higher $Wi$ ($Wi > 1.5$), the extensional nature of flow at the free surface governs the rate of stretching of polymer molecules. It is found the value $Wi = 1.5$, around which different flow kinematics govern the rate of stretching, is independent of the viscosity ratio and constitutive equation i.e. largest eigenvalue changes its position from the web to the free surface at roughly the same $Wi$ for all viscosity ratios.

- For dilute polymer solutions, at high $Wi$, the position of the smallest eigenvalue of the conformation tensor abruptly jumps to the static contact line (which is a geometric singularity in slot coating) at high $Wi$ just before numerical simulations fail. On the other hand, the position of the smallest eigenvalue always remains on the free surface at high $Wi$ for ultra-dilute solutions. This is an important observation as it suggests that the mode of failure in the case of dilute polymer solutions is the presence of the static contact line and for ultra-dilute solutions, it is the inability of the mesh to capture stress boundary layers close to the free surface.

- The extensional nature of the flow in the stretching section of the free surface leads to the formation of normal stress boundary layers at the free surface. While the formation of these stress boundary layers can be captured with mesh refinement in the case of ultra-dilute solutions, a completely different

flow behaviour under the die and close to the static contact line accounts for the independence of flow computations with mesh refinement for dilute solutions. For ultra-dilute solutions the flow field is not affected by the presence of polymer molecules. For dilute solutions, the high normal stresses at the free surface tends to pulls the liquid away from the recirculation region present in a Newtonian flow. As a result the recirculation zone diminishes in size, and flow close to the static contact line becomes stronger. The stagnation point moves from the free surface to the die wall and the normal stress difference close to the static contact line becomes positive. The reduction in the size of the recirculation zone exposes the singularity present in slot coating flows, which causes the field variables such as the velocity gradient and conformation tensor to become singular. It was found that the strength of the singularity in the field variables grows with decreasing viscosity ratio.

- At a given $Ca$ and viscosity ratio, the increased normal stress difference along the free surface at high $Wi$ causes the free surface to move into the die (meniscus invasion) and hence reduce the contact angle for dilute polymer solutions. An increase in $Ca$ was found to increase the normal stresses due to the increase in the rate of strain tensor along the free surface which consequently results in a further reduction in the contact angle.

- A reduction in the contact angle at high $Wi$ affects the low-flow limit of slot coating flows. We have found that for viscoelastic liquids, the minimum coating thickness is higher than the coating thickness for Newtonian liquids. As a result the coating window for a uniform coating shrinks in size compared to Newtonian liquids.

- Unlike conformation tensor based computations, the micro-macro computations were found to be numerically stable at much higher $Wi$ for both dilute and ultra-dilute solutions. One of the key features of micro-macro simulations in this work is that the stability and accuracy of the computations were obtained on relatively coarse meshes making the micro-macro simulations viable for large scale complex flow simulations with more accurate microscopic constitutive equations. In principle the micro-macro approach can be used as

an alternative numerical method to overcome the high Weissenberg number problem.

- Excellent agreement was found for different parameters between the micro-macro results for linear dumbbell models and their equivalent conformation tensor based constitutive models. The fully implicit scheme developed for linear dumbbell models was found to be stable and accurate at much higher time steps compared to micro-macro simulations using an explicit scheme, with no additional computational and memory requirements for the solution of free surface flows.

- Two different algorithms to solve non-linear dumbbell models, namely, Newton's method and a novel least-squares and collocation method were examined for viscoelastic free surface flows of FENE dumbbells and dumbbells with hydrodynamic interactions. We have shown that both algorithms give identical results and remain numerically stable for all $Wi$ studied in this work. The collocation method was found to be fast and computationally efficient compared to Newton's method.

- We found that there were significant differences between the stretch of polymers (a microscopic property) at the free surface for different microscopic constitutive models while the macroscopic properties (i.e. velocity and stress profile) are almost unaffected. The inaccurate predictions of stretch and orientation of polymer molecules might lead to inaccurate predictions of the existence of various instabilities such as non-uniform coating in slot coating flows.

- The computations of transient free surface flows in this work further established the accuracy, stability and viability of micro-macro methods for large scale simulations.

This work provides a comprehensive study of the effect of viscoelasticy on slot coating flows. Although with the micro-macro method developed in this work, it is possible to capture, at least qualitatively, the behavior of real polymer molecules in solution, several further improvements and future research is possible.

- The stability and the accuracy of micro-macro methods at high $Wi$ needs to be investigated much more closely before such schemes are claimed to resolve the solution of the high Weissenberg number problem encountered in viscoelastic flow simulations.

- The ability of the micro-macro approach to overcome problems associated with the presence geometric singularity is required to be investigated with more refined meshes.

- While with adequate computational resources, this method can in principle be used for solving complex flow problems by incorporating the most accurate models presently available (which are based on bead-rod and bead-spring models with non-linear interactions and many degrees of freedom) it is yet to be shown that micro-macro methods can lead to significantly better predictions of industrial flows.

- Due to the intense computational requirement of micro-macro methods compared to macroscopic methods, computational and memory efficient methods such as *closure approximations for bead-spring models* [Prabhakar, 2005; Siginer et al., 1999] can be used in the context of large scale simulations.

# Appendix A

# Interfacial transport phenomena and Differential geometry

In this appendix, we discuss a systematic procedure to derive free surface boundary conditions outlined in chapter 2. Although these boundary conditions have been discussed in details in literature, here we summarize the elements that go into the derivation of these boundary conditions in a concise manner. The text book by Slattery [1990] has been used to derive most of the equations presented in chapter. In addition, we have also discussed, in brief, the basics of differential geometry which is a preliminary requirement to understand mass and momentum balance at interface.

Phase interface is defined as the region separating two phases in which properties and behavior of the material differ from those of adjoining phases. There are two continuum models for the phase interface. One model represents it as three dimensional region and other as a two dimensional surface.

## A.1   Three-dimensional interfacial region

Density and concentration of various species are observed to be appreciably different in the neighborhood of an interface than that of away from the interface. In three dimensional interfacial region model, as critical point approaches, the density is observed to be a continuous function of position in the direction normal to the
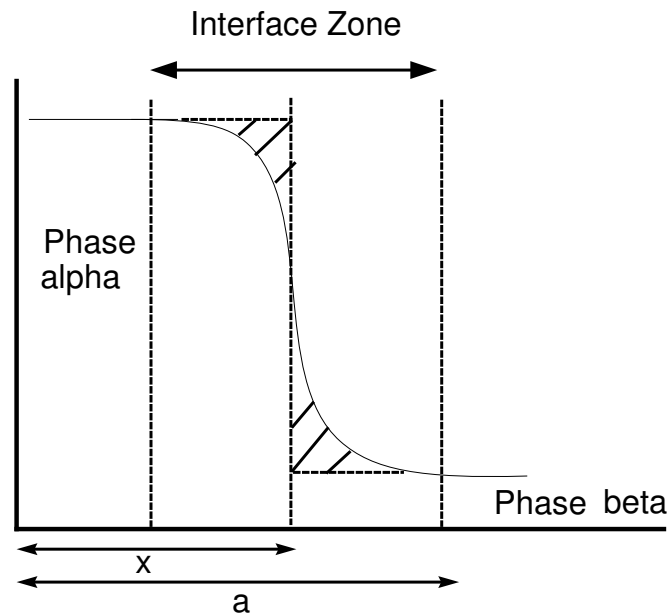
Figure A.1: Gibbs dividing surface

interface. Thus, the interface can be regarded as a three-dimensional region, the thickness of which may be of several molecular diameters or more. The stress deformation behavior in such a region could be described by assuming that stress tensor is a function of the rate of deformation tensor, the gradient of density and the second gradient of density. As the thickness of the region approaches zero, the results take the same form as that obtained when uniform tension is assumed to act on a two dimensional surface separating the two phase. The problem with this model is that there is no way by which one can study the stress and velocity distributions in a very thin interfacial region.

## A.2   Two dimensional model or Dividing surface

In two dimensional model, the phase interface is assumed to ba a hypothetical two dimensional dividing surface that lies within or near the interfacial region and separates two homogeneous phases. Effects of adjoining phases on the interface are taken into account by assigning excess mass or energy to the interface.

## A.2.1 Concept of Surface Excess Properties

In a system of two phases $\alpha$ and $\beta$, while moving from one phase to the other through the interface zone, all *extensive* properties vary in a smooth way from the values in $\alpha$ phase to corresponding values in the $\beta$ phase. Gibbs modelled the above system by considering it to consist of three parts [Gupta, 2000].

1. Part one consists of pure $\alpha$ phase.

2. Part two consists of pure $\beta$ phase.

3. Part three consists of an imaginary surface separating the two phases.

This imaginary dividing surface is a mathematical surface of zero thickness. Properties of the bulk phases in these models are considered to be identical to those of the bulk phases without any interface. The deficit or the excess property compared to the actual value of the property is assigned to the interface to ensure that an extensive property remains the same in the two representation. Thus, for a profile shown in the figure for unit cross-sectional area, if the actual amount present for species $i$ is $M_i$, then the quantity assigned to the interface, $\Gamma_i^\sigma$, per unit area is given by,

$$\Gamma_i^\sigma = M_i - [x\, n_i^\alpha + (a - x)\, n_i^\beta] \tag{A.1}$$

where $n_i^\alpha$ and $n_i^\beta$ are the densities of species $i$ in $\alpha$ and $\beta$ phases respectively.

## A.2.2 Gibbs equation

For a small change in the total energy of a system shown in Fig. A.1,

$$\begin{aligned}
dE = {} & T\, ds^\alpha + T\, ds^\beta + T\, ds^\sigma \\
& + \sum_i \mu_i\, dn_i^\alpha + \sum_i \mu_i\, dn_i^\beta + \sum_i \mu_i\, dn_i^\sigma \\
& - P^\alpha\, dV^\alpha - P^\beta\, dV^\beta + \sigma\, dA
\end{aligned} \tag{A.2}$$

where $S^i\, \{i = \alpha, \beta\}$ is the entropy associated with the phases $\alpha$ and $\beta$, $S^\sigma$ is the entropy associated with the dividing surface, $P^i\{i = \alpha, \beta\}$ is the pressure in two bulk phases, $T$ is the temperature of the system. $\mu^i$ is the chemical potential of the

system, $\sigma$ is the surface tension, $V^\alpha$ and $V^\beta$ are the volumes of two bulk phases, $A$ is the interfacial area and $E$ is the total energy of the system. Here, $P^\alpha$ is taken to be different from $P^\beta$ to allow for pressure jump across a curved interface. For pure phases,

$$dE^\alpha = T\,ds^\alpha + \sum_i \mu_i\,dn_i^\alpha - P^\alpha\,dV^\alpha$$

and

$$dE^\beta = T\,ds^\beta + \sum_i \mu_i\,dn_i^\beta - P^\beta\,dV^\beta$$

since

$$dE = dE^\alpha + dE^\beta + dE^\sigma$$

where $dE^i\,\{i = \alpha, \beta\}$ is the energy change associated with the $\alpha$ and $\beta$ phases respectively. Thus, we can say that

$$dE^\sigma = T\,ds^\sigma + \sum_i \mu_i\,dn_i^\sigma + \sigma\,dA \tag{A.3}$$

From Eq. (A.3), the Gibbs-Duhem equation can be written as,

$$S^\sigma\,dT + \sum_i n_i^\sigma\,d\mu_i + A\,d\sigma = 0 \tag{A.4}$$

For a binary system at constant temperature, Eq. (A.4) reduces to

$$d\sigma = -\Gamma_1^\sigma\,d\mu_1 - \Gamma_2^\sigma\,d\mu_2$$

where $\Gamma_i^\sigma = n_i/A$ (excess concentration per unit area)

The mathematical dividing surface is located in such a way that $\Gamma_1^\sigma$ is zero which implies that the excess concentration of species 1 on interface is zero and hence, species 1 remains entirely in bulk. In other words, it requires that the shaded area on either side of dividing surface to be equal, which means that rate of mass transfer from the interface is equal and nothing accumulates on the interface implying

$$d\sigma = -\Gamma_2^{(1)\sigma}\,d\mu_2 \tag{A.5}$$

Here, $\Gamma_2^{(1)\sigma}$ represents the excess concentration of solute 2 on the interface where the dividing surface is located such that the excess quantity of species 1 in the interface zone is zero. As

$$\mu_2 = \mu_2^0 + RT \log a_2 \tag{A.6}$$

$\Gamma_2^{(1)\sigma}$ can be written as

$$\Gamma_2^{(1)\sigma} = -\frac{1}{RT} \left( \frac{\partial \sigma}{\partial \log a_2} \right)_T \tag{A.7}$$

Equation (A.7) is the Gibbs equation which relates the change in interfacial tension per unit change in $\log a_2$ to the excess concentration of solute 2 on the interface. In the limit of dilute solutions of species 2 in 1, $\log a_2$ can be replaced by $\log c_2$ [Gupta, 2000]. Thus,

$$\Gamma_2^{(1)\sigma} = -\frac{1}{RT} \left( \frac{\partial \sigma}{\partial \log c_2} \right)_T \tag{A.8}$$

The above equation is used to calculate the excess concentration per unit interfacial area associated with the interface and can be use in context of the interfacial mass density.

## A.3 Introduction to differential geometry

A surface is the locus of a point whose position is a function of two parameters $y^1$ and $y^2$. Thus,

$$\mathbf{z} = \mathbf{p}^\sigma(y^1, y^2) \tag{A.9}$$

where $\mathbf{z}$ is the position vector. Since two numbers $y^1$ and $y^2$ uniquely determine a point on the surface, these are called surface coordinates. A $y^1$ coordinate curve is a line on the surface along which $y^1$ varies while $y^2$ takes a fixed value. Similarly, $y^2$ coordinate curve is the one along which $y^2$ varies while $y^1$ assumes a constant value. Eq. (A.9) can be represented as three scalar equations. By eliminating $y^1$ and $y^2$ from two of these and substituting in third equation gives one scalar equation,

$$f(\mathbf{z}) = 0$$

These surface coordinates can be related to the cuvilinear coordinetes of a point in three dimensional space as

$$z_i = z_i(x^1, x^2, x^3)$$

and

$$z_i = z_i(y^1, y^2)$$

it can be written as

$$x^r = x^r(y^1, y^2)$$

where $x^r$ are the curvilinear coordinates.

## A.3.1 Natural basis

In space a spatial vector field is nothing but the spatial vector-valued function of position in space. Spatial vector fields on the surface is defined as spatial vector-valued functions of position on a surface. The natural basis is defined as,

$$\mathbf{a}_\alpha = \frac{\partial \mathbf{p}^\sigma}{\partial y^\alpha} = \frac{\partial \mathbf{z}}{\partial y^\alpha} = \frac{\partial x^i}{\partial y^\alpha} \mathbf{g_i} \tag{A.10}$$

At every point on the surface, the values of these spatial vector fields are tangent to the $y^\alpha$ coordinate curves and therefore tangent to the surface. Definition of $\mathbf{a}_\alpha$ on the surface is parallel to the definition of $\mathbf{g}_i$ in space. If $\boldsymbol{\xi}$ is the unit normal to the surface, then vector fields $\mathbf{a_1}, \mathbf{a_2}$ and $\boldsymbol{\xi}$ are linearly independent and thus, form a basis for the spatial vector fields on the surface. We can define

$$\begin{aligned}
a_{\alpha\beta} &= \mathbf{a}_\alpha \cdot \mathbf{a}_\beta \\
&= \frac{\partial x^i}{\partial y^\alpha} \frac{\partial x^j}{\partial y^\beta} \mathbf{g}_i \cdot \mathbf{g}_j \\
&= \frac{\partial x^i}{\partial y^\alpha} \frac{\partial x^j}{\partial y^\beta} g_{ij}
\end{aligned} \tag{A.11}$$

where $a_{\alpha\beta}$ are the covariant components of the surface metric tensor. The determinant can also be constructed as

$$a = det(a_{\alpha\beta}) \tag{A.12}$$

It can be written that

$$a^{\alpha\beta} \, a_{\beta\gamma} = a_{\gamma\beta} \, a^{\beta\alpha} = \delta^{\alpha}_{\gamma} \tag{A.13}$$

Where $\delta^{\alpha}_{\gamma}$ is the Kronecker delta.

### A.3.2 Surface gradient of scalar field

The surface gradient of a scaler field $\phi$ is a tangential vector field denoted by $\boldsymbol{\nabla}_{\sigma}\phi$ and specified by defining its inner product with an arbitrary tangential vector field $\mathbf{c}$:

$$\boldsymbol{\nabla}_{\sigma}\phi(y^1, y^2) \cdot \mathbf{c} = c^{\alpha} \frac{\partial \phi}{\partial y^{\alpha}} (y^1, y^2) \tag{A.14}$$

If $\mathbf{c}$ is an arbitrary vector field and if $\mathbf{c} = \mathbf{a}_{\beta}$

$$\boldsymbol{\nabla}_{\sigma}\phi \cdot \mathbf{a}_{\beta} = \frac{\partial \phi}{\partial y^{\beta}} \tag{A.15}$$

Since $\boldsymbol{\nabla}_{\sigma}\phi$ is defined as a tangential vector field, it can be written that

$$\boldsymbol{\nabla}_{\sigma}\phi = \frac{\partial \phi}{\partial y^{\alpha}} \, a^{\alpha\beta} \, \mathbf{a}_{\beta} \tag{A.16}$$

### A.3.3 Dual basis

The dual tangential vector fields $\mathbf{a}^{\alpha}$ are defined as the surface gradients of the surface coordinates as

$$\mathbf{a}^{\alpha} \equiv \boldsymbol{\nabla}_{\sigma} y^{\alpha} \tag{A.17}$$

Thus, using the definition of surface gradient it can be written

$$\mathbf{a}^{\alpha} = a^{\alpha\beta} \, \mathbf{a}_{\beta}$$
$$\mathbf{a}_{\alpha} = a_{\alpha\beta} \, \mathbf{a}^{\beta} \tag{A.18}$$

## A.3.4 Projection tensor

The projection tensor $\mathbf{P}$ is a tangential second-order tensor field that transforms every tangential vector field into itself. Hence,

$$\mathbf{P} \cdot \mathbf{a}_\beta = \mathbf{a}_\beta \tag{A.19}$$

$$\mathbf{P} = \mathbf{a}_\beta\, \mathbf{a}^\beta = a_{\alpha\beta}\, \mathbf{a}^\alpha\, \mathbf{a}^\beta \tag{A.20}$$

Since $\mathbf{a}_1$, $\mathbf{a}_2$, and $\boldsymbol{\xi}$ are linearly independent vectors, they form a basis for spatial vector field on the surface. If $\mathbf{v}$ is any spatial vector field on the surface, $\mathbf{v}$ can be written as

$$\mathbf{v} = v^\alpha\, \mathbf{a}_\alpha + v_{(\xi)}\, \boldsymbol{\xi} \tag{A.21}$$

which implies

$$\mathbf{v} = (\mathbf{v} \cdot \mathbf{a}^\alpha)\, \mathbf{a}_\alpha + v_{(\xi)}\, \boldsymbol{\xi} \tag{A.22}$$

or

$$\mathbf{I} \cdot \mathbf{v} = \mathbf{v} \cdot \mathbf{P} + (\mathbf{v} \cdot \boldsymbol{\xi})\, \boldsymbol{\xi}$$

or

$$\mathbf{I} \cdot \mathbf{v} = (\mathbf{P} + \boldsymbol{\xi}\, \boldsymbol{\xi}) \cdot \mathbf{v}$$

Since $\mathbf{v}$ is any spatial vector field on the surface

$$\mathbf{I} = \mathbf{P} + \boldsymbol{\xi}\, \boldsymbol{\xi}$$

or the alternative interpretation of the projection tensor is

$$\mathbf{P} = \mathbf{I} - \boldsymbol{\xi}\, \boldsymbol{\xi}$$

The projection tenser plays the role of an identity tensor for the set of all tangential vector fields and its dot product with any spatial vector field gives the tangential component of the spatial vector field.

## A.3.5 Surface gradient of vector field

The surface gradient of a spatial vector field $\mathbf{v}$ is a tangential vector field denoted by $\boldsymbol{\nabla}_\sigma \mathbf{v}$ and specified by defining its inner product with an arbitrary tangential vector field $\mathbf{c}$:

$$\boldsymbol{\nabla}_\sigma \mathbf{v} \cdot \mathbf{c} = c^\alpha \frac{\partial \mathbf{v}}{\partial y^\alpha} \tag{A.23}$$

if $\mathbf{c}$ is an arbitrary vector field and we take $\mathbf{c} = \mathbf{a}_\beta$

$$\boldsymbol{\nabla}_\sigma \mathbf{v} \cdot \mathbf{a}_\beta = \frac{\partial \mathbf{v}}{\partial y^\beta} \tag{A.24}$$

Since $\boldsymbol{\nabla}_\sigma \mathbf{v}$ is defined as the tangential vector field, we can write

$$\boldsymbol{\nabla}_\sigma \mathbf{v} = \frac{\partial \mathbf{v}}{\partial y^\beta} \mathbf{a}_\beta \tag{A.25}$$

For instance, the surface gradient of the position vector field $\mathbf{p}^{(\sigma)}$ is

$$\boldsymbol{\nabla}_\sigma \mathbf{p}^{(\sigma)} = \frac{\partial \mathbf{p}^{(\sigma)}}{\partial y^\beta} \mathbf{a}_\beta = \mathbf{a}^\beta \mathbf{a}_\beta = \mathbf{P} \tag{A.26}$$

Equation (A.26) gives an alternative expression for the projection tensor.

## A.3.6 Surface divergence of vector field

Surface divergence of a spatial vector field is defined as

$$\mathrm{div}_\sigma \mathbf{v} = \mathrm{tr}(\boldsymbol{\nabla}_\sigma \mathbf{v}) \tag{A.27}$$

The trace of $\boldsymbol{\nabla}_\sigma \mathbf{v}$ can be evaluated as

$$
\begin{aligned}
\mathrm{tr}(\boldsymbol{\nabla}_\sigma \mathbf{v}) &= \frac{\partial v_\alpha}{\partial y^\beta}\,\mathrm{tr}(\mathbf{a}_\alpha\,\mathbf{a}^\beta) \\
&= \frac{\partial v_\alpha}{\partial y^\beta}\,\mathrm{tr}(P_\alpha^\beta) \\
&= \frac{\partial v_\alpha}{\partial y^\alpha}
\end{aligned}
\tag{A.28}
$$

Thus, from Eqs. (A.27) and (A.37)

$$
\mathrm{div}_\sigma \mathbf{v} = \frac{\partial v_\alpha}{\partial y^\alpha}
\tag{A.29}
$$

or

$$
\mathrm{div}_\sigma \mathbf{v} = \frac{\partial \mathbf{v}}{\partial y^\alpha}\,.\,\mathbf{a}^\alpha
$$

## A.3.7   Vector field is explicit function of position in space

Here we find out that how the surface gradient is expressed in terms of the components of $\mathbf{v}$ where $\mathbf{v}$ is an explicit function of curvilinear coordinates $(x^1, x^2, x^3)$,

$$
\mathbf{v} = \mathbf{v}(x^1, x^2, x^3)
$$

The surface gradient of $\mathbf{v}$ is

$$
\begin{aligned}
\boldsymbol{\nabla}_\sigma \mathbf{v} &= \frac{\partial \mathbf{v}}{\partial x^i}\,\frac{\partial x^i}{\partial y^\alpha}\,\mathbf{a}^\alpha \\
&= \frac{\partial \mathbf{v}}{\partial x^i}\,(\mathbf{g}^i\,.\,\mathbf{a}_\alpha)\,\mathbf{a}^\alpha \\
&= \boldsymbol{\nabla}\mathbf{v}\,.\,\mathbf{P}
\end{aligned}
\tag{A.30}
$$

$\mathbf{v}$ can be written as $\mathbf{v} = v^i \, \mathbf{g}_i$, which can be substituted in Eq. (A.30)

$$\begin{aligned}
\boldsymbol{\nabla}_\sigma \mathbf{v} &= \frac{\partial(v^i \, \mathbf{g}_i)}{\partial x^j} \frac{\partial x^j}{\partial y^\alpha} \mathbf{a}^\alpha \\
&= \frac{\partial v^i}{\partial x^j} \frac{\partial x^j}{\partial y^\alpha} \mathbf{g}_i \, \mathbf{a}^\alpha + v^i \frac{\partial \mathbf{g}_i}{\partial x^j} \frac{\partial x^j}{\partial y^\alpha} \mathbf{a}^\alpha
\end{aligned} \tag{A.31}$$

By the definition of christoffel symbol of second kind

$$\frac{\partial \mathbf{g}_i}{\partial x^j} = \left\{ \begin{matrix} m \\ j\ i \end{matrix} \right\} \mathbf{g}_m \tag{A.32}$$

From Eqs. (A.31) and (A.32)

$$\begin{aligned}
\boldsymbol{\nabla}_\sigma \mathbf{v} &= \frac{\partial v^i}{\partial x^j} \frac{\partial x^j}{\partial y^\alpha} \mathbf{g}_i \, \mathbf{a}^\alpha + v^i \frac{\partial x^j}{\partial y^\alpha} \left\{ \begin{matrix} m \\ j\ i \end{matrix} \right\} \mathbf{g}_m \, \mathbf{a}^\alpha \\
&= v^i_{\ ,j} \frac{\partial x^j}{\partial y^\alpha} \mathbf{g}_i \, \mathbf{a}^\alpha
\end{aligned} \tag{A.33}$$

where $v^i_{\ ,j}$ is given by

$$v^i_{\ ,j} = \frac{\partial v^i}{\partial x^j} + \left\{ \begin{matrix} m \\ j\ i \end{matrix} \right\} v^m \tag{A.34}$$

also surface divergence of $\mathbf{v}$ can be written as

$$\begin{aligned}
\mathrm{div}_\sigma \mathbf{v} &= \mathrm{tr}(\boldsymbol{\nabla}_\sigma \mathbf{v}) \\
&= \mathrm{tr}(\boldsymbol{\nabla}\mathbf{v} \cdot \mathbf{P})
\end{aligned} \tag{A.35}$$

It is necessary to convert surface basis vector to spatial basis vector in order to derive Eq. (A.35). Following results are useful in deriving Eq. (A.35):

$$\begin{aligned}
\mathbf{a}_\alpha &= \frac{\partial \mathbf{p}^{(\sigma)}}{\partial y^\alpha} \\
&= \frac{\partial x^j}{\partial y^\alpha} \mathbf{g_j} \\
\mathbf{a}^\alpha &= a^{\alpha\beta} \frac{\partial x^i}{\partial y^\alpha} \mathbf{g_i} \\
\mathbf{g}_i \, \mathbf{a}^\alpha &= a^{\alpha\beta} \frac{\partial x^i}{\partial y^\alpha} \mathbf{g}_i \mathbf{g}_j
\end{aligned} \tag{A.36}$$

Thus, we can write

$$
\begin{aligned}
\operatorname{tr}(\mathbf{g}_i \, \mathbf{a}^\alpha) &= a^{\alpha\beta} \, \frac{\partial x^i}{\partial y^\alpha} \operatorname{tr}(\mathbf{g}_i \mathbf{g}_j) \\
&= a^{\alpha\beta} \, \frac{\partial x^i}{\partial y^\alpha} \, (\mathbf{g}_i \cdot \mathbf{g}_j) \\
&= a^{\alpha\beta} \, \frac{\partial x^i}{\partial y^\alpha} \, g_{ij}
\end{aligned}
\tag{A.37}
$$

So from Eqs. (A.33), (A.35) and (A.37), it can be shown that

$$
\operatorname{div}_\sigma \mathbf{v} = v^i_{\,,j} \, g_{jk} \, a^{\alpha\beta} \frac{\partial x^i}{\partial y^\alpha} \frac{\partial x^j}{\partial y^\beta}
\tag{A.38}
$$

where $v^i_{\,,j}$ is given by Eq. (A.34).

## A.3.8 Vector field is explicit function of position on surface

In this section, we find out that how the surface gradient is expressed in terms of the components of $\mathbf{w}$ where $\mathbf{w}$ is an explicit function of positions $(y^1, y^2)$ on surface:

$$
\mathbf{v} = \mathbf{v}(x^1, x^2, x^3)
$$

If $\mathbf{w}$ is given in terms of natural basis fields for some natural curvilinear coordinate system, then

$$
\mathbf{w} = w_i \, \mathbf{g}^i
$$

The surface gradient takes the following form:

$$
\begin{aligned}
\boldsymbol{\nabla}_\sigma \mathbf{w} &= \frac{\partial (w^i \, \mathbf{g}_i)}{\partial y^\alpha} \mathbf{a}^\alpha \\
&= \frac{\partial w^i}{\partial y^\alpha} \, \mathbf{g}_i \, \mathbf{a}^\alpha + w^i \, \frac{\partial \mathbf{g}_i}{\partial x^j} \frac{\partial x^j}{\partial y^\alpha} \, \mathbf{a}^\alpha
\end{aligned}
\tag{A.39}
$$

Using Eq. (A.32), the above equation can be simplified as

$$
\boldsymbol{\nabla}_\sigma \mathbf{w} = w^i_{\,,\alpha} \mathbf{g}_i \, \mathbf{a}^\alpha
\tag{A.40}
$$

where $w^i_{,\alpha}$, known as surface covariant derivative of $w^i$ and defined as

$$w^i_{,\alpha} = \frac{\partial w^i}{\partial y^\alpha} + \begin{Bmatrix} i \\ j\ m \end{Bmatrix} w^m \frac{\partial x^j}{\partial y^\alpha} \tag{A.41}$$

$\mathbf{w}$ can be written in terms of tangential and normal components as follows:

$$\mathbf{w} = w^\alpha \, \mathbf{a}_\alpha + w_{(\xi)} \, \boldsymbol{\xi} \tag{A.42}$$

The surface gradient consequently, becomes

$$\boldsymbol{\nabla}_\sigma \mathbf{w} = \frac{\partial w^\alpha}{\partial y^\beta} \, \mathbf{a}_\alpha \, \mathbf{a}^\beta + w^\alpha \frac{\partial \mathbf{a}_\alpha}{\partial y^\beta} \, \mathbf{a}^\beta + \frac{\partial w_{(\xi)}}{\partial y^\beta} \, \boldsymbol{\xi} \, \mathbf{a}^\beta + w_{(\xi)} \frac{\partial \boldsymbol{\xi}}{\partial y^\beta} \, \mathbf{a}^\beta \tag{A.43}$$

Equation (A.43) can be written in a more convenient form using the following results.

1. The second term of Eq. (A.43) can be written as

$$\begin{aligned} \frac{\partial \mathbf{a}_\alpha}{\partial y^\beta} &= \frac{\partial}{\partial y^\beta} \left( \frac{\partial x^i}{\partial y^\beta} \, \mathbf{g}_i \right) \\ &= \left( \frac{\partial^2 x^i}{\partial y^\beta \, \partial y^\beta} + \frac{\partial x^j}{\partial y^\beta} \frac{\partial x^m}{\partial y^\alpha} \begin{Bmatrix} i \\ j\ m \end{Bmatrix} \right) \mathbf{g}_i \end{aligned} \tag{A.44}$$

Equation (A.32) has been used to derive the above result.

2. Natural basis function can also be represent in terms of surface basis function and normal to surface $\boldsymbol{\xi}$

$$\begin{aligned} \mathbf{g}_i &= \mathbf{I} \cdot \mathbf{g}_i \\ &= (\mathbf{P} + \boldsymbol{\xi} \, \boldsymbol{\xi}) \cdot \mathbf{g}_i \\ &= (\mathbf{a}_\mu \, \mathbf{a}^\mu + \boldsymbol{\xi} \, \boldsymbol{\xi}) \cdot \mathbf{g}_i \\ &= \left( \mathbf{a}_\mu \, a^{\mu\nu} \frac{\partial x^k}{\partial y^\nu} \mathbf{g}_k + \boldsymbol{\xi} \, \boldsymbol{\xi} \right) \cdot \mathbf{g}_i \\ &= a^{\mu\nu} \frac{\partial x^k}{\partial y^\nu} \, g_{ik} \mathbf{a}_\mu + \xi_i \, \boldsymbol{\xi} \end{aligned} \tag{A.45}$$

Substituting Eq. (A.45) into Eq. (A.44)

$$\frac{\partial \mathbf{a}_\alpha}{\partial y^\beta} = \left\{ \begin{matrix} \mu \\ \beta\ \alpha \end{matrix} \right\}_a \mathbf{a}_\mu + B_{\beta\alpha}\,\boldsymbol{\xi} \tag{A.46}$$

where

$$\left\{ \begin{matrix} \mu \\ \beta\ \alpha \end{matrix} \right\}_a = \left( \frac{\partial^2 x^i}{\partial y^\beta\,\partial y^\alpha} + \frac{\partial x^j}{\partial y^\beta}\frac{\partial x^m}{\partial y^\alpha} \left\{ \begin{matrix} i \\ j\ m \end{matrix} \right\} \right) a^{\mu\nu} \frac{\partial x^k}{\partial y^\nu}\, g_{ik} \tag{A.47}$$

is the surface Christoffel symbol of the second kind and

$$B_{\beta\alpha} = \left( \frac{\partial^2 x^i}{\partial y^\beta\,\partial y^\beta} + \frac{\partial x^j}{\partial y^\beta}\frac{\partial x^m}{\partial y^\alpha} \left\{ \begin{matrix} i \\ j\ m \end{matrix} \right\} \right) \xi_i \tag{A.48}$$

are the components of the symmetric second groundform tangential tensor field which is related to the radius of curvature of the surface.

$$\mathbf{B} \equiv B_{\beta\alpha}\,\mathbf{a}^\alpha\,\mathbf{a}^\beta \tag{A.49}$$

3. The last term of Eq. (A.43):

$$\mathbf{a}_\gamma\,.\,\boldsymbol{\xi} = 0$$

and

$$\boldsymbol{\xi}\,.\,\boldsymbol{\xi} = 1 \tag{A.50}$$

Differenting these equations with respect to the surface coordinate $y^\beta$, we get

$$\mathbf{a}_\gamma\,.\,\frac{\partial \boldsymbol{\xi}}{\partial y^\beta} = -B_{\gamma\beta} \tag{A.51}$$

and

$$\boldsymbol{\xi}\,.\,\frac{\partial \boldsymbol{\xi}}{\partial y^\beta} = 0 \tag{A.52}$$

from above equations it can be concluded that $(\partial \boldsymbol{\xi}/\partial y^\beta)$ is a tangential vector field and hence

$$\frac{\partial \boldsymbol{\xi}}{\partial y^\beta} = -B_{\gamma\beta}\, \mathbf{a}^\gamma \tag{A.53}$$

Substituting Eqs. (A.46) and (A.53) in Eq. (A.43),

$$\boldsymbol{\nabla}_\sigma \mathbf{w} = \frac{\partial w^\alpha}{\partial y^\beta}\, \mathbf{a}_\alpha\, \mathbf{a}^\beta + \{\}w^\alpha\, \mathbf{a}_\mu\, \mathbf{a}^\beta + B_{\beta\alpha}w^\alpha \boldsymbol{\xi}\mathbf{a}^\beta + \frac{\partial w_{(\xi)}}{\partial y^\beta}\, \boldsymbol{\xi}\, \mathbf{a}^\beta + w_{(\xi)}B_{\gamma\beta}\mathbf{a}^\gamma\mathbf{a}^\beta$$

$$= w^\alpha_{,\beta}\mathbf{a}_\alpha\, \mathbf{a}^\beta + \boldsymbol{\xi}\,(\mathbf{B}\,.\,\mathbf{w}) + \boldsymbol{\xi}\boldsymbol{\nabla}_\sigma w_{(\xi)} - w_{(\xi)}\mathbf{B} \tag{A.54}$$

where $w^\alpha_{,\beta}$ is the surface covariant derivative of $w^\alpha$ and is defined as,

$$w^\alpha_{,\beta} = \frac{\partial w^\alpha}{\partial y^\beta} + \left\{\begin{matrix} \mu \\ \beta\ \alpha \end{matrix}\right\}_a w^\mu \tag{A.55}$$

It can be proved by simple algebra that

$$\mathbf{P}\,.\,\boldsymbol{\nabla}_\sigma(\mathbf{P}\,.\,\mathbf{w}) = w^\alpha_{,\beta}\mathbf{a}_\alpha\, \mathbf{a}^\beta$$

Using the above result, Eq. (A.54) can be written as

$$\boldsymbol{\nabla}_\sigma \mathbf{w} = \mathbf{P}\,.\,\boldsymbol{\nabla}_\sigma(\mathbf{P}\,.\,\mathbf{w}) + \boldsymbol{\xi}\,(\mathbf{B}\,.\,\mathbf{w}) + \boldsymbol{\xi}\boldsymbol{\nabla}_\sigma w_{(\boldsymbol{\xi})} - w_{(\xi)}\mathbf{B} \tag{A.56}$$

Surface divergence of $\mathbf{w}$ is

$$\mathrm{div}_\sigma \mathbf{w} = \mathrm{tr}(\boldsymbol{\nabla}_\sigma \mathbf{w})$$

It is useful to find the trace of the different components of Eq. (A.56).

$$\begin{aligned}
\mathrm{tr}(\boldsymbol{\xi}\,(\mathbf{B}\,.\,\mathbf{w}) + \boldsymbol{\xi}\boldsymbol{\nabla}_\sigma w_{(\xi)}) &= \mathrm{tr}(B_{\beta\alpha}w^\alpha \boldsymbol{\xi}\mathbf{a}^\beta + \frac{\partial w_{(\xi)}}{\partial y^\beta}\, \boldsymbol{\xi}\, \mathbf{a}^\beta) \\
&= (B_{\beta\alpha}w^\alpha + \frac{\partial w_{(\xi)}}{\partial y^\beta})\, \mathrm{tr}(\boldsymbol{\xi}\, \mathbf{a}^\beta) \\
&= (B_{\beta\alpha}w^\alpha + \frac{\partial w_{(\xi)}}{\partial y^\beta})\, (\boldsymbol{\xi}\,.\,\mathbf{a}^\beta) \\
&= 0
\end{aligned} \tag{A.57}$$

also from the definition of projection tensor, it can be written that

$$\text{tr}(\mathbf{P}\,.\,\boldsymbol{\nabla}_\sigma(\mathbf{P}\,.\,\mathbf{w})) = \text{div}_\sigma(\mathbf{P}\,.\,\mathbf{w}) \quad = w^\alpha_{,\alpha} \tag{A.58}$$

Thus, surface divergence of $\mathbf{w}$ is

$$\begin{aligned}
\text{div}_\sigma \mathbf{w} &= \text{div}_\sigma(\mathbf{P}\,.\,\mathbf{w}) - \text{tr}(w_{(\xi)}\mathbf{B}) \\
&= \text{div}_\sigma(\mathbf{P}\,.\,\mathbf{w}) - w_{(\xi)}\text{tr}(\mathbf{B}) \\
&= w^\alpha_{,\alpha} - w_{(\xi)}\text{tr}(\mathbf{B})
\end{aligned} \tag{A.59}$$

The mean curvature of the surface is defined as

$$\mathbf{H} = \frac{1}{2}\,\text{tr}(\mathbf{B}) \tag{A.60}$$

If $\mathbf{w}$ is a unit vector normal to the surface $\mathbf{w} = \boldsymbol{\xi}$ then, from Eq. (A.59), it can be written as

$$\mathbf{B} = -\boldsymbol{\nabla}_\sigma \boldsymbol{\xi} \tag{A.61}$$

### A.3.9   Surface divergence theorem

At any point on the surface $\Sigma$, the surface integral is

$$\int_\Sigma F\,dA = \int\int_\Sigma F(y^1, y^2)\sqrt{a}\,dy^1\,dy^2 \tag{A.62}$$

If $\mathbf{w}$ is any tangential vector field, $\mathbf{w} = w^\alpha\,\mathbf{a}_\alpha$, then from Eq. (A.59),

$$\text{div}_\sigma \mathbf{w} = w^\alpha_{,\alpha}$$

The above equation can be substituted in Eq. (A.62),

$$\begin{aligned}
\int_\Sigma \text{div}_\sigma \mathbf{w}\,dA &= \int\int_\Sigma w^\alpha_{,\alpha}\sqrt{a}\,dy^1\,dy^2 \\
&= \int\int_\Sigma \frac{\partial(\sqrt{a}w^\alpha)}{\partial y^\alpha}\,dy^1\,dy^2 \\
&= \int\int_\Sigma \left[\frac{\partial(\sqrt{a}w^1)}{\partial y^1} + \frac{\partial(\sqrt{a}w^2)}{\partial y^2}\right]\,dy^1\,dy^2
\end{aligned} \tag{A.63}$$

Green's theorem for a surface states that if $P(y^1, y^2)$ and $Q(y^1, y^2)$ are continuous function having continuous partial derivatives on the surface, then

$$\int\int_\Sigma \left[\frac{\partial P}{\partial y^1} + \frac{\partial Q}{\partial y^2}\right] dy^1\, dy^2 = \int_C \left[P\frac{dy^1}{ds} - Q\frac{dy^2}{ds}\right] ds \qquad (A.64)$$

Here, C is the piecewise smooth simple closed curve bounding $\Sigma$; $s$ indicate the arc length measured along the curve. From Eqs. (A.63) and (A.64), it can be written that

$$\int_\Sigma \mathrm{div}_\sigma \mathbf{w}\, dA = \int_C \sqrt{a}\, \left[w^1\frac{dy^1}{ds} - w^2\frac{dy^2}{ds}\right] ds$$
$$= \int_C \varepsilon_{\alpha\beta} w^\alpha \frac{dy^\beta}{ds}\, ds \qquad (A.65)$$

If $\boldsymbol{\lambda}$ is a unit tangent vector to the curve $C$ and $\boldsymbol{\mu}$ is a tangential vector field normal to the curve $C$, then

$$\boldsymbol{\lambda} \equiv \frac{d\mathbf{p}}{ds} = \frac{d\mathbf{p}}{dy^\beta}\frac{dy^\beta}{ds} = \frac{d\mathbf{p}}{dy^\beta}\mathbf{a}^\beta \qquad (A.66)$$

and

$$\boldsymbol{\mu} \equiv \boldsymbol{\varepsilon} \cdot \boldsymbol{\lambda} = \varepsilon_{\alpha\beta}\frac{dy^\beta}{ds}\mathbf{a}^\alpha \qquad (A.67)$$

From Eqs. (A.65) and (A.67),

$$\int_\Sigma \mathrm{div}_\sigma \mathbf{w}\, dA = \int_C (\mathbf{w} \cdot \boldsymbol{\mu})ds \qquad (A.68)$$

If $\mathbf{v}$ is any spatial vector field defined on the surface, it can be written that $\mathbf{P}.\mathbf{v} = \mathbf{w}$. From Eq. (A.59)

$$\int_\Sigma \mathrm{div}_\sigma \mathbf{v}\, dA = \int_\Sigma \mathrm{div}_\sigma(\mathbf{P} \cdot \mathbf{v})dA - \int_\Sigma 2H(\mathbf{v} \cdot \boldsymbol{\xi})dA$$
$$= \int_C (\mathbf{w} \cdot \boldsymbol{\mu})ds - \int_\Sigma 2H(\mathbf{v} \cdot \boldsymbol{\xi})dA \qquad (A.69)$$
$$= \int_C (\mathbf{v} \cdot \boldsymbol{\mu})ds - \int_\Sigma 2H(\mathbf{v} \cdot \boldsymbol{\xi})dA$$

Equation (A.69) uses the fact that

$$\int_C (\mathbf{w} \cdot \boldsymbol{\mu})ds = \int_C (\mathbf{v} \cdot \boldsymbol{\mu})ds \qquad (A.70)$$

because $(\mathbf{v}^{\xi} \cdot \boldsymbol{\mu}) = 0$. Equation (A.69) is referred as the surface divergence theorem.

## A.4  Kinematics of dividing surface

A dividing surface is the locus of a point whose position is a function of two para-
meters $y^1$ and $y^2$ on the surface.

$$\mathbf{z} = \mathbf{p}^{\sigma}(y^1, y^2) \tag{A.71}$$

The two surface coordinates $y^1$ and $y^2$ uniquely determine a point on the surface.
Each surface particle is a set of material particles occupying any particular point on
the surface. If the set of material particles is $\zeta^{\sigma}$ then

$$y^{\alpha} = X^{\alpha}(\zeta^{\sigma}) \qquad \alpha = 1, 2 \tag{A.72}$$

$\zeta^{\sigma}$ is also a surface particle. Surface particle has one to one mapping with sur-
face coordinates but the material particles has many to one mapping with surface
coordinates

$$\zeta^{\sigma} = X^{-1}(y^1, y^2) \tag{A.73}$$

and hence,

$$\mathbf{z} = \mathbf{p}^{\sigma}(X^1(\zeta^{\sigma}), X^2(\zeta^{\sigma})) \tag{A.74}$$

A moving and deforming dividing surface $\Sigma$ is the locus of a point whose position
is a function of two surface coordinates and time,

$$\mathbf{z} = \mathbf{p}^{\sigma}(y^1, y^2, t) \tag{A.75}$$

The intrinsic motion of surface particles on $\Sigma$ can be written as

$$
\begin{aligned}
y^{\alpha} &= X^{\alpha}(\zeta^{\sigma}, t) \qquad \alpha = 1, 2 \\
\zeta^{\sigma} &= X^{-1}(y^1, y^2, t)
\end{aligned}
\tag{A.76}
$$

Equation (A.76) tells how the surface particles move from point to point on the
surface independently of how the surface itself is moving. Thus, the motion of the

surface particles can be written as

$$\mathbf{z} = \mathbf{p}^\sigma(X^1(\zeta^\sigma), X^2(\zeta^\sigma), t) \tag{A.77}$$

If A is any scalar, vector, or tensor quantity and an explicit function of position on the surface and time, then

$$A = A(y^1, y^2, t) \tag{A.78}$$

The time derivative of the A following the motion of a surface particle is,

$$\frac{d_s A}{dt} \equiv \left(\frac{\partial A}{\partial t}\right)_{\zeta^\sigma} \tag{A.79}$$

The surface velocity $\mathbf{v}^\sigma$ is the time rate of change of position of a surface particle,

$$\mathbf{v}^\sigma = \frac{d_s \mathbf{z}}{dt} \tag{A.80}$$

Since all the materials particles are confined to the dividing surface, they must move at all times with a normal component of velocity equal to the normal component of velocity of surface.

At some reference time $t_\kappa$ the dividing surface A.75 takes the following form:

$$\mathbf{z}_\kappa = \kappa^\sigma(y_\kappa^1, y_{kappa}^2) \tag{A.81}$$

which can be called as the reference dividing surface. Thus, surface particles can be identified by there reference configuration or their position on the reference dividing surface. Also,

$$\begin{aligned} y_\kappa^\alpha &= X^\alpha(\zeta^\sigma, t_\kappa) \\ \zeta^\sigma &= X^{-1}(y_\kappa^1, y_\kappa^2, t_\kappa) \end{aligned} \tag{A.82}$$

From Eqs. (A.76) and (A.82), we can write that

$$y^\alpha = X_\kappa^\alpha(y_\kappa^1, y_\kappa^2, t_\kappa) \tag{A.83}$$

From Eq. (A.79), the surface material derivative of A can be written as,

$$
\begin{aligned}
\frac{d_s A}{dt} &\equiv \left(\frac{\partial A}{\partial t}\right)_{\zeta^\sigma} \equiv \left(\frac{\partial A}{\partial t}\right)_{(y^1_\kappa, y^2_\kappa)} \\
&= \left(\frac{\partial A}{\partial t}\right)_{(y^1, y^2)} + \left(\frac{\partial A}{\partial y^\alpha}\right)_t \frac{\partial X^\alpha_\kappa}{\partial t} \\
&= \left(\frac{\partial A}{\partial t}\right)_{(y^1, y^2)} + \nabla_\sigma A \cdot \dot{\mathbf{y}}
\end{aligned}
\tag{A.84}
$$

where $\dot{\mathbf{y}}$ is defined as the intrinsic surface velocity. From Eqs. (A.75), (A.80) and (A.84)

$$
\mathbf{v}^\sigma = \left(\frac{\partial \mathbf{p}^\sigma}{\partial t}\right)_{(y^1, y^2)} + \nabla_\sigma \mathbf{p}^\sigma \cdot \dot{\mathbf{y}}
\tag{A.85}
$$

If we defined $\mathbf{u}$ to be the time rate of change of spatial position following a surface point $(y^1, y^2)$,

$$
\mathbf{u} \equiv \left(\frac{\partial \mathbf{p}^\sigma}{\partial t}\right)_{(y^1, y^2)}
\tag{A.86}
$$

then Eqs. (A.85) and (A.86) can be combined to give

$$
\mathbf{v}^\sigma = \mathbf{u} + \dot{\mathbf{y}}
\tag{A.87}
$$

The definition of projection tensor and Eq. (A.26) have been used in writing the above equation.

## A.5   Conservation of mass

The conservation of mass states that if we follow a portion of material body through any number of translation, rotation, and deformation, the mass associate with it will not vary in time. Thus, mass $M$ of the body B can be written as,

$$
M = \int_B dm
\tag{A.88}
$$

because the mass is independent of time, it follows that

$$\frac{\partial M}{\partial t} = \frac{\partial}{\partial t} \int_B dm = 0 \qquad (A.89)$$

Let us consider a body consisting of two phases occupying regions $R^1$ and $R^2$ with mass density of each phase $i$ (i=1,2) is $\rho^i$ which is a continuous function of position in the phase $i$. There is no equation of state which describe the thermodynamic behaviour of of each phase accounting the mass distribution in the interfacial region. However, if we assign a mass density $\rho^{(\sigma:1,2)}$ having a units of mass per unit area on the Gibbs dividing surface $\Sigma^{1,2}$, the mass of the body can be written as,

$$M = \int_{R^1} \rho^1 \, dV + \int_{R^2} \rho^2 \, dV + \int_{\Sigma^{1,2}} \rho^{(\sigma:1,2)} \, dA \qquad (A.90)$$

Using Eq. (A.89), Eq. (A.90) can be written as

$$\frac{dM}{dt} = \frac{d}{dt} \int_{R^1} \rho^1 \, dV + \frac{d}{dt} \int_{R^2} \rho^2 \, dV + \frac{d}{dt} \int_{\Sigma^{1,2}} \rho^{(\sigma:1,2)} \, dA = 0 \qquad (A.91)$$

Eqs. (A.90) and (A.91) can, in principle, be generalized for a body consisting of $M$ phases. If $\Sigma^{i,j}$ be the dividing surface separating the phase $i$ and $j$ and the mass density assigned to this interface is $\rho^{(\sigma:i,j)}$, the conservation of mass can be written as

$$\frac{dM}{dt} = \frac{d}{dt} \sum_{i=1}^{M} \int_{R^i} \rho^i \, dV + \sum_{i=1}^{M-1} \sum_{j=i+1}^{M} \frac{d}{dt} \int_{\Sigma^{i,j}} \rho^{(\sigma:i,j)} \, dA = 0 \qquad (A.92)$$

If $\rho$ is a piecewise continuous function defined by $\rho^i$ in each phase $i$, then

$$\int_R \rho \, dV = \sum_{i=1}^{M} \int_{R^i} \rho^i \, dV \qquad (A.93)$$

where $R$ is the reason occupied by the body.

$$R = \sum_{i=1}^{M} R^i$$

Similarly, if the surface mass density $\rho^\sigma$ is a piecewise continuous function defined

by $\rho^{(\sigma:i,j)}$ on the dividing surface $\Sigma^{i,j}$, it can be written that

$$\int_{\Sigma} \rho^{\sigma} \, dA = \sum_{i=1}^{M-1} \sum_{j=i+1}^{M} \int_{\Sigma^{i,j}} \rho^{(\sigma:i,j)} \, dA \qquad (A.94)$$

Hence, the conservation of mass is

$$\frac{dM}{dt} = \frac{d}{dt} \left[ \int_{R} \rho \, dV + \int_{\Sigma} \rho^{\sigma} \, dA \right] = 0 \qquad (A.95)$$

## A.5.1 Surface transport theorem

The surface transport theorem is useful to evaluate the second integral on right side of Eq. (A.92). If $\psi^{\sigma}$ is any scalar, vector , or tensor valued function of time and position on the surface, then

$$\int_{\Sigma} \psi^{\sigma} \, dA = \int_{\Sigma} \left[ \frac{d_s \psi^{\sigma}}{dt} + \psi^{\sigma} \, \mathrm{div}_{\sigma} \mathbf{v}^{\sigma} \right] dA \qquad (A.96)$$

where $(d_s \psi^{\sigma}/dt)$ is surface material derivative defined in section A.5. Using the surface divergence theorem [Eq. (A.69)], Eqs.(A.87), and (A.84), an alternative form of the surface transport theorem can be written as

$$\int_{\Sigma} \psi^{\sigma} \, dA = \int_{\Sigma} \left( \frac{\partial \psi^{\sigma}}{\partial t} - \boldsymbol{\nabla}_{\sigma} \psi^{\sigma} \cdot \mathbf{u} - 2H \psi^{\sigma} (\mathbf{v} \cdot \boldsymbol{\xi}) \right) dA + \int_{C} \psi^{\sigma} (\mathbf{v}^{\sigma} \cdot \boldsymbol{\mu}) ds \quad (A.97)$$

## A.5.2 Transport theorem for a body containing dividing surface

For a body consisting of a single phase, the transport theorem says that

$$\frac{d}{dt} \int_{R} \psi \, dV = \int_{R} \frac{\partial \psi}{\partial t} \, dV + \int_{S} \psi (\mathbf{v} \cdot \mathbf{n}) \, dA \qquad (A.98)$$

where $\psi$ is a scalar, vector or tensor valued function of time and position in the region $R$ with a closed bounding surface $S$, $\mathbf{n}$ is the outward directed unit normal vector to the closed bounding surface.

If we consider a body $R$, bounded by a closed surface $S$, consisting of multiple

phases, we can define $S^i$ to be the portion of $S$ bounding phase $R^i$. The velocities of the boundaries of phase $i$ are

on $\qquad\qquad S^i \qquad : \quad \mathbf{v}^i$

on $\qquad\qquad \Sigma^{(i,j)} \quad : \quad \mathbf{u}^{(i,j)}$

Eq.(A.98) for the each phase is

$$\frac{d}{dt} \int_{R^i} \psi^i \, dV = \int_{R^i} \frac{\partial \psi^i}{\partial t} \, dV + \int_{S} \psi^i (\mathbf{v}^i \cdot \mathbf{n}) \, dA$$
$$- \sum_{\substack{j=1 \\ j \neq i}}^{M} \int_{\Sigma^{i,j}} \psi^i \left( \mathbf{u}^{(i,j)} \cdot \boldsymbol{\xi}^{(i,j)} \right) dA \qquad (A.99)$$

where $\boldsymbol{\xi}^{(i,j)}$ is the unit normal to $\Sigma^{(i,j)}$ pointing into $R^i$. If $\psi^i$ is continuous within $R^i$, then

$$\frac{d}{dt} \int_{R} \psi \, dV = \frac{d}{dt} \sum_{i=1}^{M} \int_{R^i} \psi^i \, dV \qquad (A.100)$$

It follows from the above equation that

$$\frac{d}{dt} \int_{R} \psi \, dV = \sum_{i=1}^{M} \int_{R^i} \frac{\partial \psi^i}{\partial t} \, dV + \sum_{i=1}^{M} \int_{S} \psi^i (\mathbf{v}^i \cdot \mathbf{n}) \, dA$$
$$- \sum_{\substack{j=1 \\ j \neq i}}^{M} \int_{\Sigma^{i,j}} \psi^i \left( \mathbf{u}^{(i,j)} \cdot \boldsymbol{\xi}^{(i,j)} \right) dA \qquad (A.101)$$

If $\psi$ and $\mathbf{v}$ denote piecewise continuous function defined by $\psi^i$ and $\mathbf{v}^i$ and that $\mathbf{u}$ is a piecewise continuous function defined by $\mathbf{u}^{(i,j)}$, Eq. (A.101) reduces to

$$\frac{d}{dt} \int_{R} \psi \, dV = \int_{R} \frac{\partial \psi}{\partial t} \, dV + \int_{S} \psi (\mathbf{v} \cdot \mathbf{n}) \, dA$$
$$- \int_{\Sigma} [\psi \, \mathbf{u} \cdot \boldsymbol{\xi}] \, dA \qquad (A.102)$$

where
$$[\psi \, \boldsymbol{\xi}] = \psi^i \, \xi^{(i,j)} + \psi^j \, \xi^{(j,i)}$$
$$= (\psi^i - \psi^j) \, \xi^{(i,j)} \qquad (A.103)$$

The divergence theorem for a single phase

$$\int_R \text{div}(\psi \mathbf{v}) \, dV = \int_S \psi(\mathbf{v} \cdot \mathbf{n}) \, dA \tag{A.104}$$

The divergence theorem for the body consisting of multiple phases can be written as

$$\int_R \text{div}(\psi \mathbf{v}) \, dV = \int_S \psi(\mathbf{v} \cdot \mathbf{n}) \, dA - \int_\Sigma [\psi \mathbf{v} \cdot \boldsymbol{\xi}] \, dA \tag{A.105}$$

From Eqs. (A.102), (A.104) and A.105, we can write that

$$\frac{d}{dt} \int_R \psi \, dV = \int_R \{\frac{\partial \psi}{\partial t} + \text{div}(\psi \mathbf{v})\} \, dV + \int_\Sigma [\psi(\mathbf{v} \cdot \boldsymbol{\xi} - \mathbf{u} \cdot \boldsymbol{\xi})] \, dA \tag{A.106}$$

Combining Eqs. (A.97) and (A.97)

$$\frac{d}{dt} \int_R \psi \, dV + \frac{d}{dt} \int_\Sigma \psi^\sigma \, dA = \int_R \{\frac{\partial \psi}{\partial t} + \text{div}(\psi \mathbf{v})\} \, dV$$
$$+ \int_\Sigma \left[\frac{d_s \psi^\sigma}{dt} + \psi^\sigma \, \text{div}_\sigma \mathbf{v}^\sigma + [\psi(\mathbf{v} \cdot \boldsymbol{\xi} - \mathbf{u} \cdot \boldsymbol{\xi})]\right] \, dA \tag{A.107}$$

Equation (A.107) is the transport theorem for a body containing a dividing surface.

## A.5.3  Jump mass balance

If $\psi = \rho$, then from Eq. (A.107)

$$\frac{d}{dt} \int_R \rho \, dV + \frac{d}{dt} \int_\Sigma \rho^\sigma \, dA = \int_R \{\frac{\partial \rho}{\partial t} + \text{div}(\rho \mathbf{v})\} \, dV$$
$$+ \int_\Sigma \left[\frac{d_s \rho^\sigma}{dt} + \rho^\sigma \, \text{div}_\sigma \mathbf{v}^\sigma + [\rho(\mathbf{v} \cdot \boldsymbol{\xi} - \mathbf{u} \cdot \boldsymbol{\xi})]\right] \, dA \tag{A.108}$$

From Eq. (A.95), we can write that

$$\int_R \{\frac{\partial \rho}{\partial t} + \text{div}(\rho \mathbf{v})\} \, dV + \int_\Sigma \left[\frac{d_s \rho^\sigma}{dt} + \rho^\sigma \, \text{div}_\sigma \mathbf{v}^\sigma + [\rho(\mathbf{v} \cdot \boldsymbol{\xi} - \mathbf{u} \cdot \boldsymbol{\xi})]\right] \, dA = 0 \tag{A.109}$$

For a body consisting of single phase, the integral over region R is zero (equation of continuity), which implies

$$\frac{\partial \rho}{\partial t} + \text{div}(\rho \mathbf{v}) = 0$$

Thus, Eq. (A.109) can be written as

$$\int_{\Sigma} \left[ \frac{d_s \rho^{\sigma}}{dt} + \rho^{\sigma} \, \text{div}_{\sigma} \mathbf{v}^{\sigma} + [\rho(\mathbf{v} \cdot \boldsymbol{\xi} - \mathbf{u} \cdot \boldsymbol{\xi})] \right] dA = 0 \qquad (A.110)$$

Equation (A.122) must be true for any portion of the dividing surface which implies that

$$\frac{d_s \rho^{\sigma}}{dt} + \rho^{\sigma} \, \text{div}_{\sigma} \mathbf{v}^{\sigma} + [\rho(\mathbf{v} \cdot \boldsymbol{\xi} - \mathbf{u} \cdot \boldsymbol{\xi})] \, dA = 0 \qquad (A.111)$$

This is called the jump mass balance equation. It expresses the requirement that mass should be conserved at every point on the dividing surface. Two special cases of the jump mass balance equations are

1. If there is no mass transfer from the interface,

$$\mathbf{v} \cdot \boldsymbol{\xi} = \mathbf{u} \cdot \boldsymbol{\xi} \qquad (A.112)$$

   If interface is stationary then

$$\mathbf{v} \cdot \boldsymbol{\xi} = 0 \qquad (A.113)$$

   Equation (A.113) is called as the kinematic boundary condition for steady free surface flows.

2. If there is no mass transfer from the interface and surface mass density is constant on the dividing surface, Eq. (A.123) simplified to

$$\text{div}_{\sigma} \mathbf{v}^{\sigma} = 0 \qquad (A.114)$$

   This means that there is no local dilation of phase interface.

## A.6  Conservation of momentum

Conservation of momentum states that time rate of change of the momentum of a body is equal to the applied force. Mathematically it can be written as

$$\frac{d}{dt} \int_B \mathbf{v} \, dm = \mathbf{F}^a \tag{A.115}$$

or it can be written as

$$\frac{d}{dt} \left[ \int_R \rho \mathbf{v} \, dV + \int_\Sigma \rho^\sigma \mathbf{v}^\sigma \, dA \right] = \mathbf{F}^a \tag{A.116}$$

The applied force on a body can be separated into two classes:

1. Body forces, $F_b^a$ : Body forces are assumed to be related to the mass of the bodies and are describe as though they are acting on each material particle.

$$F_b^a = \int_R \rho \, \mathbf{b} \, dV + \int_\Sigma \rho^\sigma \mathbf{b}^\sigma dA \tag{A.117}$$

   here $\mathbf{b}$ the body force per unit mass acting on the material within a phase, and $\mathbf{b}^\sigma$ the body force per unit mass exerted on the dividing surface.

2. Contact forces, $F_c^a$: Contact forces are those forces that appear to be exerted on one body or another through their common surface of contact. They are independent of the masses of the bodies on either side. If $C$ is the curve formed by the intersection of $\Sigma$ with $S$, we can write

$$F_c^a = \int_S \mathbf{t}(\mathbf{z}, S) \, dA + \int_C \mathbf{t}^\sigma(\mathbf{z}, S) ds \tag{A.118}$$

   Here, $\mathbf{t}(\mathbf{z}, S)$ is the stress vector, the contact force per unit area exerted upon a body by its bounding surface $S$: it is a function of position $\mathbf{z}$ on $S$. $\mathbf{t}^\sigma(\mathbf{z}, S)$ is the surface stress vector, the contact force per unit length at the curve $C$: it is a function of position $\mathbf{z}$ on $C$.

   There is a vector-valued function $\mathbf{t}(\mathbf{z}, \mathbf{n})$ defined for all the unit vectors $\mathbf{n}$ at

any point $\mathbf{z}$ within a single phase such that

$$\mathbf{t}(\mathbf{z}, S) = \mathbf{t}(\mathbf{z}, \mathbf{n}) \tag{A.119}$$

where $\mathbf{n}$ is the outwardly directed unit normal vector to $S$ at $\mathbf{z}$ with respected the body upon which the contact stress is applied.

There is a vector-valued function $\mathbf{t}^\sigma(\mathbf{z}, \boldsymbol{\mu})$ defined for all the unit tangent vectors $\boldsymbol{\mu}$ at any point $\mathbf{z}$ on a dividing surface $\Sigma$ such that

$$\mathbf{t}^\sigma(\mathbf{z}, C) = \mathbf{t}^\sigma(\mathbf{z}, \boldsymbol{\mu}) \tag{A.120}$$

Here, $\boldsymbol{\mu}$ is the unit tangent vector that is normal to $C$ at $\mathbf{z}$.

From the definition of applied forces, Eq. (A.116) can be written as

$$\frac{d}{dt}\left[\int_R \rho\mathbf{v}\, dV + \int_\Sigma \rho^\sigma\mathbf{v}^\sigma\, dA\right] = \int_S \mathbf{t}\, dA + \int_C \mathbf{t}^\sigma ds + \int_R \rho\mathbf{b}\, dV + \int_\Sigma \rho^\sigma\mathbf{b}^\sigma dA \tag{A.121}$$

If we put $\psi = \rho\mathbf{v}$ in surface transport theorem, Eq. (A.107), the left side of Eq. (A.121) is

$$\frac{d}{dt}\left(\int_R \rho\mathbf{v}\, dV + \int_\Sigma \rho^\sigma\mathbf{v}^\sigma\, dA\right) = \int_R \rho\{\frac{\partial\mathbf{v}}{\partial t} + \mathbf{v}\mathrm{div}(\mathbf{v})\}\, dV$$
$$+ \int_\Sigma \left(\rho^\sigma\frac{d_s\mathbf{v}^\sigma}{dt} + [\rho(\mathbf{v} - \mathbf{v}^\sigma)(\mathbf{v}\cdot\boldsymbol{\xi} - \mathbf{u}\cdot\boldsymbol{\xi})]\right) dA$$
$$\tag{A.122}$$

Thus, from Eqs. (A.121) and (A.122)

$$\int_R \rho\{\frac{\partial\mathbf{v}}{\partial t} + \mathbf{v}\mathrm{div}(\mathbf{v})\}\, dV + \int_\Sigma \left(\rho^\sigma\frac{d_s\mathbf{v}^\sigma}{dt} + [\rho(\mathbf{v} - \mathbf{v}^\sigma)(\mathbf{v}\cdot\boldsymbol{\xi} - \mathbf{u}\cdot\boldsymbol{\xi})]\right) dA$$
$$= \int_S \mathbf{t}\, dA + \int_C \mathbf{t}^\sigma ds + \int_R \rho\mathbf{b}\, dV + \int_\Sigma \rho^\sigma\mathbf{b}^\sigma dA \tag{A.123}$$

The stress vector $\mathbf{t}$ can be expressed in term of the stress tensor by

$$\mathbf{t} = \mathbf{T}\cdot\mathbf{n}$$

also the Green's transformation allows

$$
\begin{aligned}
\int_S \mathbf{t}\, dA &= \int_S (\mathbf{T} \cdot \mathbf{n})\, dA \\
&= \int_R \mathrm{div}\mathbf{T}\, dA + \int_\Sigma [\mathbf{T} \cdot \boldsymbol{\xi}]\, dA
\end{aligned}
\tag{A.124}
$$

The surface stress tensor can be expressed in terms of the surface stress tensor as

$$
\mathbf{t}^\sigma = \mathbf{T}^\sigma \cdot \boldsymbol{\mu}
\tag{A.125}
$$

Using the surface divergence theorem, we can write

$$
\begin{aligned}
\int_C \mathbf{t}^\sigma\, ds &= \int_C (\mathbf{T}^\sigma \cdot \boldsymbol{\mu})\, ds \\
&= \int_\Sigma \mathrm{div}_\sigma \mathbf{T}^\sigma\, dA
\end{aligned}
\tag{A.126}
$$

Using Eq. (A.124) and (A.126), Eq. (A.123) can be written as

$$
\int_R \rho\{\frac{\partial \mathbf{v}}{\partial t} + \mathbf{v}\,\mathrm{div}(\mathbf{v}) - \mathrm{div}\mathbf{T} - \rho\,\mathbf{b}\}\, dV
\tag{A.127}
$$

$$
+ \int_\Sigma \left( \rho^\sigma \frac{d_s \mathbf{v}^\sigma}{dt} - \mathrm{div}_\sigma \mathbf{T}^\sigma - \rho^\sigma \mathbf{b}^\sigma + [\rho(\mathbf{v} - \mathbf{v}^\sigma)(\mathbf{v} \cdot \boldsymbol{\xi} - \mathbf{u} \cdot \boldsymbol{\xi}) - \mathbf{T} \cdot \boldsymbol{\xi}] \right) dA = 0
$$

$$
\tag{A.128}
$$

For a body consisting of single phase, the integral over $R$ is zero, which implies

$$
\int_R \rho\{\frac{\partial \mathbf{v}}{\partial t} + \mathbf{v}\,\mathrm{div}(\mathbf{v}) - \mathrm{div}\mathbf{T} - \rho\,\mathbf{b}\}\, dV = 0
$$

and also integral over the dividing surface should be true for every portion of the dividing surface. Hence,

$$
\rho^\sigma \frac{d_s \mathbf{v}^\sigma}{dt} - \mathrm{div}_\sigma \mathbf{T}^\sigma - \rho^\sigma \mathbf{b}^\sigma + [\rho(\mathbf{v} - \mathbf{v}^\sigma)(\mathbf{v} \cdot \boldsymbol{\xi} - \mathbf{u} \cdot \boldsymbol{\xi}) - \mathbf{T} \cdot \boldsymbol{\xi}] = 0
\tag{A.129}
$$

Equation (A.129) is referred as the jump momentum balance. If there is no mass transfer through the interface and body force in small compared to other forces,

then for steady state, Eq. (A.129) is

$$\text{div}_\sigma \mathbf{T}^\sigma + [\mathbf{T} \cdot \boldsymbol{\xi}] = 0 \tag{A.130}$$

If the surface stress tensor is isotropic, then

$$\mathbf{T}^\sigma = \sigma \mathbf{P} \tag{A.131}$$

where $\sigma$ is the surface tension and $\mathbf{P}$ is projection tensor given by Eq. (A.26). Equation (A.130) can be written as

$$\text{div}_\sigma(\sigma \mathbf{P}) + [\mathbf{T} \cdot \boldsymbol{\xi}] = 0 \tag{A.132}$$

It can be prove by simple algebra that

$$\text{div}_\sigma(\sigma \mathbf{P}) = \boldsymbol{\nabla}_\sigma \sigma - \sigma \boldsymbol{\xi}(\boldsymbol{\nabla}_\sigma \cdot \boldsymbol{\xi}) \tag{A.133}$$

Hence, from Eqs. (A.132) and (A.133)

$$[\mathbf{T} \cdot \boldsymbol{\xi}] + \boldsymbol{\nabla}_\sigma \sigma - \sigma \boldsymbol{\xi}(\boldsymbol{\nabla}_\sigma \cdot \boldsymbol{\xi}) = 0 \tag{A.134}$$

If there is no spatial variation in surface tension then $\boldsymbol{\nabla}_\sigma \sigma$ can be neglected and

$$\begin{aligned} [\mathbf{T} \cdot \boldsymbol{\xi}] &= \sigma \boldsymbol{\xi}(\boldsymbol{\nabla}_\sigma \cdot \boldsymbol{\xi}) \\ (\mathbf{T}_2 - \mathbf{T}_1) \cdot \boldsymbol{\xi} &= \sigma \boldsymbol{\xi}(\boldsymbol{\nabla}_\sigma \cdot \boldsymbol{\xi}) \end{aligned} \tag{A.135}$$

Equation (A.135) is dynamic or stress boundary condition at the interface. It is same as the Eq. (2.27).

# Appendix B

# Derivation of the Jacobian Entries for Time Dependent Terms in the Momentum and Conformation Tensor Equations

Here, following the results of Pasquali [2000], derivatives of time dependent terms in Eqs. (2.22) and (2.24) with respect to the various fields variables are computed.

## B.1    Derivatives of Time Dependent Terms in the Momentum Equation

The modified time dependent term in Eq. (2.38) is

$$R_{t,i}^{\mathbf{m},\alpha} = \int_{\Omega_0} \psi_{\mathbf{m}}^{\alpha} \rho \left( \frac{\partial v_i}{\partial t} - \frac{\partial x_k}{\partial t} \nabla_k v_i \right) f d\Omega_0 \tag{B.1}$$

The subscript $t$ denotes the time dependent terms of the weighted residual integral.

- Derivatives with respect to the position basis function coefficients

$$\frac{\partial R_{t,i}^{\mathbf{m},\alpha}}{\partial x_j^\gamma} = \int_{\Omega_0} \psi_{\mathbf{m}}^\alpha \rho \left( \frac{\partial v_i}{\partial t} - \frac{\partial x_k}{\partial t} \nabla_k v_i \right) \nabla_j \varphi_{\mathbf{x}}^\gamma f d\Omega_0$$
$$+ \int_{\Omega_0} \psi_{\mathbf{m}}^\alpha \rho \left( \frac{\partial x_k}{\partial t} \nabla_j v_i \nabla_k \varphi_{\mathbf{x}}^\gamma - \frac{\varphi_{\mathbf{x}}^\gamma \nabla_j v_i}{\Delta t} \right) f d\Omega_0 \tag{B.2}$$

- Derivatives with respect to the velocity basis function coefficients

$$\frac{\partial R_{t,i}^{\mathbf{m},\alpha}}{\partial v_j^\gamma} = \int_{\Omega_0} \psi_{\mathbf{m}}^\alpha \rho \left( \frac{\varphi_{\mathbf{v}}^\gamma \delta_{ij}}{\Delta t} - \frac{\partial x_k}{\partial t} \nabla_k \varphi_{\mathbf{v}}^\gamma \, \delta_{ij} \right) f d\Omega_0 \tag{B.3}$$

Derivatives with respects to $p$, $\mathbf{L}$ and $\mathbf{M}$ are zero.

# B.2 Derivatives of Time Dependent Terms in the Conformation Tensor Equation

The modified time dependent term in Eq. (2.40) is

$$R_{t,ik}^{\mathbf{M},\alpha} = \int_{\Omega_0} \psi_{\mathbf{M}}^\alpha \rho \left( \frac{\partial M_{ik}}{\partial t} - \frac{\partial x_l}{\partial t} \nabla_l M_{ik} \right) f d\Omega_0 \tag{B.4}$$

- Derivatives with respect to the position basis function coefficients

$$\frac{\partial R_{t,ik}^{\mathbf{M},\alpha}}{\partial x_j^\gamma} = \int_{\Omega_0} \psi_{\mathbf{M}}^\alpha \left( \frac{\partial M_{ik}}{\partial t} - \frac{\partial x_l}{\partial t} \nabla_l M_{ik} \right) \nabla_j \varphi_{\mathbf{x}}^\gamma f d\Omega_0$$
$$+ \int_{\Omega_0} \psi_{\mathbf{M}}^\alpha \left( \frac{\partial x_l}{\partial t} \nabla_j M_{ik} \nabla_l \varphi_{\mathbf{x}}^\gamma - \frac{\varphi_{\mathbf{x}}^\gamma \nabla_j M_{ik}}{\Delta t} \right) f d\Omega_0 \tag{B.5}$$

- Derivatives with respect to the conformation basis function coefficients

$$\frac{\partial R_{t,ik}^{\mathbf{M},\alpha}}{\partial M_{jn}^\gamma} = \int_{\Omega_0} \psi_{\mathbf{M}}^\alpha \left( \frac{\varphi_{\mathbf{M}}^\gamma \delta_{ij} \delta_{kn}}{\Delta t} - \frac{\partial x_l}{\partial t} \nabla_l \varphi_{\mathbf{M}}^\gamma \, \delta_{ij} \delta_{kn} \right) f d\Omega_0 \tag{B.6}$$

Derivatives with respects to $p$, $\mathbf{v}$ and $\mathbf{L}$ are zero.

The following results from Pasquali [2000] are used to derive Eqs. (B.2), (B.3), (B.5), and (B.6).

- Derivatives of the determinant of mapping deformation gradient $f = \det \mathbf{F}$ with respect to position unknowns $x_j^\gamma$:

$$\frac{\partial f}{\partial x_j^\gamma} = f \nabla_j \varphi_x^\gamma \tag{B.7}$$

- Derivatives of the direct mapping deformation gradient $\mathbf{F}$ with respect to position unknowns $x_j^\gamma$:

$$\frac{\partial F_{ik}}{\partial x_j^\gamma} = \delta_{jk} \frac{\partial \varphi_x^\gamma}{\partial \xi_i} \tag{B.8}$$

- Derivatives of the inverse mapping deformation gradient $\mathbf{K}$ with respect to position unknowns $x_j^\gamma$:

$$\frac{\partial K_{ik}}{\partial x_j^\gamma} = -\nabla_i \varphi_x^\gamma K_{jk} \tag{B.9}$$

- Derivative of the gradient of a scalar, vector component, or tensor component $\Phi$ with respect to position basis function coefficient $x_j^\gamma$:

$$\frac{\partial \nabla_k \Phi}{\partial x_j^\gamma} = -\nabla_j \Phi \nabla_k \varphi_x^\gamma \tag{B.10}$$

The area and line integrals in the weighted residual and analytical Jacobian were evaluated with a 9-point and 3-point Gaussian integration scheme respectively.

# Appendix C

# Calculation of Characteristic Relaxation Times and Microscopic Parameters For Different Microscopic Constitutive Models

In this appendix, we discuss the systematic procedure adopted for determining the microscopic parameters H, $\zeta$, $h^*$, etc, such that identical values for $Wi$ (or equivalently, $\lambda_\eta$) are obtained in all the microscopic constitutive models used in micro-macro computations. The definition of $\lambda_\eta$ is

$$\lambda_\eta = \frac{[\eta]_0^\theta M \eta_s}{N_A k_B T} \tag{C.1}$$

where, $[\eta]_0^\theta$ is the intrinsic viscosity in a $\theta$-solution in the limit of zero shear rate, $M$ is the molecular weight and $N_A$ is the Avogadro number. In can be shown for dilute solutions [Bird et al., 1987a; Öttinger, 1996] that

$$\lambda_\eta = \lim_{n \to 0} \frac{\eta_{p,0}}{nkT} \tag{C.2}$$

The relationship of $\lambda_\eta$ to microscopic parameters in models with and without fluctuating hydrodynamic interactions (HI) is discussed separately in turn below. Before we do so, however, the following points are worth noting.

In all micro-macro simulations reported here, we set $R_{\mathrm{e}}^2/3 = 1$ and $k_{\mathrm{B}}T = 1$. $R_{\mathrm{e}}^2/3 = 1$ is maintained in order to be consistent with the length scale used in conformation tensor based models. Furthermore, for a given values of the viscosity ratio $\beta$ and $Wi$, the zero shear rate viscosity $\eta_{\mathrm{p},0}$ and the relaxation time $\lambda_\eta$ can be calculated form $\beta = \eta_{\mathrm{s}}/(\eta_{\mathrm{s}} + \eta_{\mathrm{p},0})$ and $Wi = \lambda_\eta v/L$, respectively. Note that $\eta_{\mathrm{s}}, v$ and $L$ are known. Once the values of $\eta_{\mathrm{p},0}$ and $\lambda_\eta$ are known, Eq. (C.2) can be used to find the polymer density $n$ in all cases.

1. **Dumbbells without HI:** For constitutive models without fluctuating HI, the relationship between $R_{\mathrm{e}}^2/3$ and $\lambda_\eta$, and the microscopic parameters H, $b$, and $\lambda_H = \zeta/4H$, can be obtained analytically [Bird et al., 1987a,b], and is given in Table C.1. For the fixed values of $R_{\mathrm{e}}^2/3$, $k_{\mathrm{B}}T$ and $b$ chosen here, the spring constant H can be evaluated from the expression for $R_{\mathrm{e}}^2/3$ (see Table C.1). For any particular value of $\lambda_\eta$, the calculated value of H, and the relationship between $\lambda_\eta$ and $\lambda_H$ (Table C.1), can then be used to determine the value of the drag coefficient $\zeta$ to be used in the microscopic model.

2. **Dumbbells with HI:** The presence of hydrodynamic interactions does not affect static properties, and as a result, expressions for $R_{\mathrm{e}}^2/3$, and the calculation of H, remains unaltered from the cases where HI is absent. However, since $\lambda_\eta$ for dumbbells with fluctuating HI cannot be derived analytically, a Green-Kubo formula [Diaz et al., 1990; Doi and Edwards, 1986] has been used to calculate the shear relaxation modulus $G_{\mathrm{p}}(t)$, from which the characteristic relaxation time can be obtained. Before discussing the Green-Kubo formula below, it is worth noting that in models with HI, rather than the drag coefficient $\zeta$, it is more common to use the non-dimensional parameter $h^*$. For these models, therefore, the parameter $h^*$ must be chosen such that the desired value of $\lambda_\eta$ can be obtained.

   The Green-Kubo formula relates $G_{\mathrm{p}}(t)$ to the equilibrium autocorrelation of the quantity $S_{xy} = Q_x \partial U/\partial Q_y$ by the expression

$$G_{\mathrm{p}} = \langle S_{xy}(t)\, S_{xy}(0) \rangle_{\mathrm{eq}} \tag{C.3}$$

Table C.1: End-to-end vector and characteristic relaxation time for different microscopic constitutive models [Bird et al., 1987b]

| Constitutive model | $R_e^2/3$ | $\lambda_\eta$ |
|---|---|---|
| Hookean | $k_{\mathrm{B}}T/H$ | $\lambda_H$ |
| FENE-P | $k_{\mathrm{B}}T(b-3)/Hb$ | $\lambda_H(b-3)/b$ |
| FENE | $k_{\mathrm{B}}T(b-5)/Hb$ | $\lambda_H(b-5)/b$ |

It can be shown that $\lambda_\eta$ is related to $G_{\mathrm{p}}$ by [Bird et al., 1987b]

$$\frac{\lambda_\eta}{\lambda_H} = \int_0^\infty G_{\mathrm{p}}(t)\,dt \qquad (C.4)$$

For Hookean dumbbells with HI, $\lambda_H$ is related to $h^*$ by

$$\lambda_H = \frac{3}{2}\left(\frac{\pi}{H}\right)^{3/2}\sqrt{k_{\mathrm{B}}T}\,\eta_{\mathrm{s}}h^* \qquad (C.5)$$

Equations (C.4) and (C.5) can be combined to give

$$\frac{2\lambda_\eta}{3\left(\pi/H\right)^{3/2}\sqrt{k_{\mathrm{B}}T}\,\eta_{\mathrm{s}}} = h^*\int_0^\infty G_{\mathrm{p}}(t)\,dt \qquad (C.6)$$

The right hand side of the equation above depends only on $h^*$, and can be determined once and for all, for any appropriate value of $h^*$.

Here, the right hand side is determined by carrying out equilibrium Brownian dynamics simulations. Basically, the product $S_{xy}(t)\,S_{xy}(0)$ is evaluated after each time step for every equilibrium trajectory, and the average of this product at any time over the ensemble of trajectories gives the autocorrelation function in Eq. (C.3). The values of $G_{\mathrm{p}}(t)$ obtained in this manner are then integrated with respect to $t$ using numerical quadrature. The dependence of the left hand side of Eq. (C.6) on $h^*$, determined in this manner, can be plotted as shown in Fig. C.1. For any given value of $\lambda_\eta$ and $\eta_{\mathrm{s}}$ and calculated value of H, the corresponding value of $h^*$ to be used in a microscopic model with fluctuating HI, can consequently be determined from the curve in Fig. C.1.
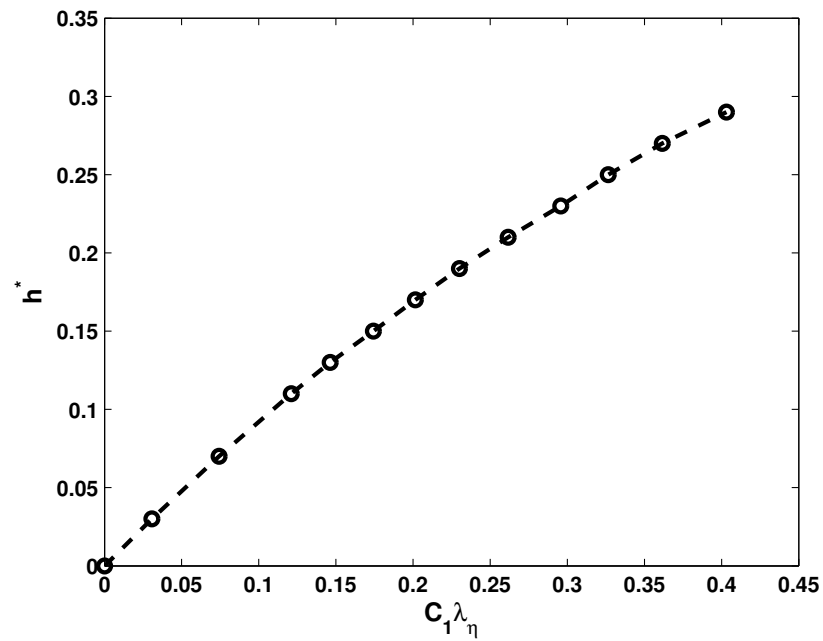
Figure C.1: Characteristic relaxation time of Hookean dumbbells with hydrodynamic interaction. $C_1 = \dfrac{2}{3\left(\pi/H\right)^{3/2}\sqrt{k_\mathrm{B}T}\,\eta_\mathrm{s}}$. The line drawn is for guiding the eye. The error bars in the Brownian dynamics simulations are much smaller than the size of the symbols.

# Appendix D

# Derivation of the Jacobian Matrix For the Configuration Fields Equation

Here, analytical Jacobian entries of the configuration field equation for FENE force are computed. From Eq. (3.39)

$$
\begin{aligned}
\mathbf{G} &= \mathbf{Q}_{\mathrm{n}+1}\left(1 - \frac{Q_{\mathrm{n}+1}^2}{b} + \frac{H\,\Delta t}{\zeta}\right) - \mathbf{\Gamma}\left(1 - \frac{Q_{\mathrm{n}+1}^2}{b}\right) \\
G_i &= Q_{i,\,\mathrm{n}+1}\left(1 - \frac{Q_{\mathrm{n}+1}^2}{b} + \frac{H\,\Delta t}{\zeta}\right) - \Gamma_i\left(1 - \frac{Q_{\mathrm{n}+1}^2}{b}\right) \\
G_i^{\alpha} &= \int_{\Omega_e}\left[Q_{i,\,\mathrm{n}+1}\left(1 - \frac{Q_{\mathrm{n}+1}^2}{b} + \frac{H\,\Delta t}{\zeta}\right) - \Gamma_i\left(1 - \frac{Q_{\mathrm{n}+1}^2}{b}\right)\right]\psi^{\alpha}d\Omega_e
\end{aligned}
\tag{D.1}
$$

The Jacobian entries are obtained by differentiating Eq.(D.1) with the respect to $Q_{j,\,\mathrm{n}+1}^{\beta}$. With $Q_{i,\,\mathrm{n}+1} = Q_{i,\,\mathrm{n}+1}^{\gamma}\,\varphi_{\mathbf{Q}}^{\gamma}$ and $\mathbf{J}_{ij}^{\alpha\beta} = \dfrac{\partial G_i^{\alpha}}{\partial Q_{j,\,\mathrm{n}+1}^{\beta}}$

$$
\mathbf{J}_{ij}^{\alpha\beta} = \int_{\Omega_e}\left[\left(1 - \frac{Q_{\mathrm{n}+1}^2}{b} + \frac{H\,\Delta t}{\zeta}\right)\frac{\partial Q_{i,\,\mathrm{n}+1}}{\partial Q_{j,\,\mathrm{n}+1}^{\beta}} - \frac{Q_{i,\,\mathrm{n}+1}}{b}\frac{\partial Q_{\mathrm{n}+1}^2}{\partial Q_{j,\,\mathrm{n}+1}^{\beta}} + \frac{\Gamma_i}{b}\frac{\partial Q_{\mathrm{n}+1}^2}{\partial Q_{j,\,\mathrm{n}+1}^{\beta}}\right]\psi^{\alpha}d\Omega_e
\tag{D.2}
$$

The first derivative on the RHS of Eq. (D.2) is:

$$\frac{\partial Q_{i,\,\text{n}+1}}{\partial Q_{j,\,\text{n}+1}^{\beta}} = \varphi_{\mathbf{Q}}^{\gamma}\, \frac{\partial Q_{i,\,\text{n}+1}^{\gamma}}{\partial Q_{j,\,\text{n}+1}^{\beta}} = \varphi_{\mathbf{Q}}^{\gamma} \delta_{ij}^{\gamma\beta} = \varphi_{\mathbf{Q}}^{\beta} \delta_{ij} \tag{D.3}$$

The derivative appearing in second and third term on the RHS of Eq. (D.2) is:

$$\begin{aligned}
\frac{\partial Q_{\text{n}+1}^2}{\partial Q_{j,\,\text{n}+1}^{\beta}} &= \frac{\partial (\mathbf{Q}_{\text{n}+1} \cdot \mathbf{Q}_{\text{n}+1})}{\partial Q_{j,\,\text{n}+1}^{\beta}} = 2\,\mathbf{Q}_{\text{n}+1} \cdot \frac{\partial \mathbf{Q}_{\text{n}+1}}{\partial Q_{j,\,\text{n}+1}^{\beta}} \\
&= 2\, Q_{k,\,\text{n}+1} \frac{\partial Q_{k,\,\text{n}+1}}{\partial Q_{j,\,\text{n}+1}^{\beta}} = 2\, Q_{k,\,\text{n}+1} \varphi_{\mathbf{Q}}^{\gamma} \frac{\partial Q_{k,\,\text{n}+1}^{\gamma}}{\partial Q_{j,\,\text{n}+1}^{\beta}} \\
&= 2\, Q_{k,\,\text{n}+1} \varphi_{\mathbf{Q}}^{\gamma}\, \delta_{kj}^{\gamma\beta} = 2\, Q_{k,\,\text{n}+1}\, \varphi_{\mathbf{Q}}^{\beta} \delta_{kj} \\
&= 2\, Q_{j,\,\text{n}+1}\, \varphi_{\mathbf{Q}}^{\beta}
\end{aligned} \tag{D.4}$$

Combining equations (D.2), (D.3) and (D.4), we get

$$\mathbf{J}_{ij}^{e,\alpha\beta} = \int_{\Omega_e} \left[ \left( 1 - \frac{Q_{\text{n}+1}^2}{b} + \frac{H\,\Delta t}{\zeta} \right) \delta_{ij} - \frac{2}{b} Q_{i,\,\text{n}+1} Q_{j,\,\text{n}+1} + \frac{2}{b} \Gamma_i\, Q_{j,\,\text{n}+1} \right] \psi_{\mathbf{Q}}^{\alpha} \varphi_{\mathbf{Q}}^{\beta}\, d\Omega_e \tag{D.5}$$

# Appendix E

# Equivalence of Newton's Method and LSC Method for a Linear Dumbbell Model

Here, we show analytically that for linear dumbbell models both the Newton's method and the LSC method are identical.

For a linear dumbbell model Eq. (3.38) is

$$\mathbf{Q}_{n+1} = \frac{\boldsymbol{\Gamma}}{1 + (\Lambda \, \Delta t / \zeta)} \tag{E.1}$$

Equation (E.1) is a linear equation in $\mathbf{Q}_{n+1}$. The finite element discretization of Eq. (E.1) results in a set of linear equations for each configuration field which can then be solved with Newton's method. Thus, for each configuration field:

$$\sum_{\beta} \mathbf{J}^{e,\,\alpha\beta} \, \Delta \boldsymbol{\Upsilon}^{e,\,\beta}_{n+1} = -\mathbf{R}^{e,\,\alpha}_{\mathbf{Q}} \tag{E.2}$$

$\mathbf{R}^{e,\,\alpha}_{\mathbf{Q}}$ is the elemental residual vector given by

$$\mathbf{R}^{e,\,\alpha}_{\mathbf{Q}} = \int_{\Omega_e} \left[ \mathbf{Q}_{n+1} - \frac{\boldsymbol{\Gamma}}{1 + (\Lambda \, \Delta t / \zeta)} \right] \psi^{\alpha}_{\mathbf{Q}} \, d\Omega_e \tag{E.3}$$

evaluated using the configuration fields at the previous Newton iteration. With

$\mathbf{Q} = \sum_{\beta} \mathbf{Q}^{\beta} \varphi_{\mathbf{Q}}^{\beta}$ and $\mathbf{\Upsilon}_{n+1}^{e,\beta} = \left( \mathbf{Q}_{n+1}^{\beta} \right)$, the above equation can also be written as

$$
\begin{aligned}
\mathbf{R}_{\mathbf{Q}}^{e,\alpha} &= \sum_{\beta} \mathbf{Q}^{\beta} \int_{\Omega_e} \psi_{\mathbf{Q}}^{\alpha} \varphi_{\mathbf{Q}}^{\beta} \, d\Omega_e - \int_{\Omega_e} \frac{\mathbf{\Gamma}}{1 + (\Lambda \, \Delta t/\zeta)} \, \psi_{\mathbf{Q}}^{\alpha} \, d\Omega_e \\
&= \sum_{\beta} \mathbf{\Upsilon}_{n+1}^{\beta} \int_{\Omega_e} \psi_{\mathbf{Q}}^{\alpha} \varphi_{\mathbf{Q}}^{\beta} \, d\Omega_e - \int_{\Omega_e} \frac{\mathbf{\Gamma}}{1 + (\Lambda \, \Delta t/\zeta)} \, \psi_{\mathbf{Q}}^{\alpha} \, d\Omega_e
\end{aligned}
\tag{E.4}
$$

$\mathbf{J}^{e,\alpha\beta}$ is the elemental Jacobian matrix obtained by differentiating Eq. (3.39) with respect to $\mathbf{Q}_{n+1}^{\beta}$. The components of the $\mathbf{J}^{e,\alpha\beta}$ are

$$
\mathbf{J}^{e,\alpha\beta} = \int_{\Omega_e} \boldsymbol{\delta} \, \psi_{\mathbf{Q}}^{\alpha} \varphi_{\mathbf{Q}}^{\beta} \, d\Omega_e
\tag{E.5}
$$

independent of the configuration fields.

It can be seen from Eq. (E.5) that the Jacobian matrix is a diagonal matrix. Eq. E.2 can be rewritten as:

$$
\begin{aligned}
&\sum_{\beta} \left( \int_{\Omega_e} \boldsymbol{\delta} \, \psi_{\mathbf{Q}}^{\alpha} \varphi_{\mathbf{Q}}^{\beta} \, d\Omega_e \right) \left( \mathbf{\Upsilon}_{n+1}^{e,\beta} - \mathbf{\Upsilon}_{0,n+1}^{e,\beta} \right) \\
&= -\sum_{\beta} \mathbf{\Upsilon}_{0,n+1}^{\beta} \int_{\Omega_e} \psi_{\mathbf{Q}}^{\alpha} \varphi_{\mathbf{Q}}^{\beta} \, d\Omega_e + \int_{\Omega_e} \frac{\mathbf{\Gamma}}{1 + (\Lambda \, \Delta t/\zeta)} \, \psi_{\mathbf{Q}}^{\alpha} \, d\Omega_e
\end{aligned}
\tag{E.6}
$$

which can be further simplified as:

$$
\sum_{\beta} \int_{\Omega_e} \mathbf{\Upsilon}_{n+1}^{e,\beta} \boldsymbol{\delta} \, \psi_{\mathbf{Q}}^{\alpha} \varphi_{\mathbf{Q}}^{\beta} \, d\Omega_e = \int_{\Omega_e} \frac{\mathbf{\Gamma}}{1 + (\Lambda \, \Delta t/\zeta)} \, \psi_{\mathbf{Q}}^{\alpha} \, d\Omega_e
\tag{E.7}
$$

$$
\int_{\Omega_e} \mathbf{Q}_{n+1} \psi_{\mathbf{Q}}^{\alpha} \, d\Omega_e = \int_{\Omega_e} \frac{\mathbf{\Gamma}}{1 + (\Lambda \, \Delta t/\zeta)} \, \psi_{\mathbf{Q}}^{\alpha} \, d\Omega_e
\tag{E.8}
$$

Equation (E.8) is same as the Eq. (3.47) with $\tilde{\mathbf{Q}}_{n+1}$ as

$$
\tilde{\mathbf{Q}}_{n+1} = \frac{\mathbf{\Gamma}}{1 + (\Lambda \, \Delta t/\zeta)}
\tag{E.9}
$$

# Bibliography

Baaijens, F. P. T. (1998). Mixed finite element methods for viscoelastic flow analysis: a review. *J. Non-Newtonian Fluid Mech.*, 79:361–385.

Babuska, I. (1971). Error-bounds for finite element method. *Numerical Mathematics*, 16:322–333.

Bajaj, M., Bhat, P. P., Prakash, J. R., and Pasquali, M. (2004). Micro-macro simulation of viscoelastic free surface flows using the Brownian configuration fields method. In *Fourteenth International Congress on Rheology*, Seoul, South Korea. 22 Aug. - 27 Aug.

Bajaj, M., Bhat, P. P., Prakash, J. R., and Pasquali, M. (2005). Multiscale simulation of viscoelastic free surface flows. *J. Non-Newtonian Fluid Mech.* Accepted.

Bauman, T., Sullivan, T., and Middleman, S. (1982). Ribbing instability in coating flowseffect of polymer additives. *Chem. Eng. Comm.*, 14:35–46.

Behr, M., Franca, L. P., and Tezduyar, T. E. (1993). Stabilized finite element methods for the velocity-pressure-stress formulation of incompressible flows. *Comp. Methods Appl. Mech. Eng.*, 104:31–48.

Benjamin, D. F. (1994). *Roll Coating Flows and Multiple Roll Systems.* PhD thesis, University of Minnesota, Minneapolis, MN. Available from UMI, Ann Arbor, MI, order number 9512679.

Beris, A. N. and Edwards, B. J. (1994). *Thermodynamics of Flowing Systems with Internal Microstructure.* Oxford University Press, Oxford, 1st edition.

Bhat, P. P., Basaran, O. A., and Pasquali, M. (2005). Dynamics of viscoelastic liquid filaments: Low Capillary number flows. *J. Non-Newtonian Fluid Mech.* In preparation.

Bhatara, G., Shaqfeh, E. S. G., and Khomami, B. (2004). Influence of viscoelasticity on the interfacial dynamics of air displacing fluid flows–a computational study. *J. Non-Newtonian Fluid Mech.*, 122:313–332.

Bhatara, G., Shaqfeh, E. S. G., and Khomami, B. (2005). The influence of polymer concentration and chain architecture on free surface displacement flows of polymeric fluids. *J. Rheol.*, 49:929–962.

Bird, R. A., Armstrong, R. C., and Hassager, O. (1987a). *Dynamics of Polymeric Liquids*, volume 1. John Wiley & Sons, New York, 2nd edition.

Bird, R. A., Curtiss, C. F., Armstrong, R. C., and Hassager, O. (1987b). *Dynamics of Polymeric Liquids*, volume 2. John Wiley & Sons, New York, 2nd edition.

Brezzi, F. (1974). On the existence, uniqueness and approximation of saddle-point problems arising from lagrangian multipliers. *RAIRO, Modelisation Math. Anal. Numer.*, 8:129–151.

Brooks, A. N. and Hughes, T. J. R. (1982). Streamline Upwind-Petrov-Galerkin formulation for convection dominated flows with particular emphasis on the incompressible Navier-Stokes equations. *Comp. Meth. Appl. Mech. Eng.*, 32:199–259.

Carvalho, M. S. and Kheshgi, H. S. (2000). Low-flow limit in slot coating: Theory and experiments. *AIChE J.*, 46:1907–1917.

Carvalho, M. S. and Scriven, L. E. (1997a). Deformable roll coating flows: Steady state and linear perturbation analysis. *J. Fluid Mech.*, 339:143–172.

Carvalho, M. S. and Scriven, L. E. (1997b). Flows in forward deformable roll coating gaps: Comparison between spring and plane strain model of roll cover. *J. Comp. Phys.*, 138:449–479.

Carvalho, M. S. and Scriven, L. E. (1999). Three-dimensional stability analysis of free surface flows: Application to forward deformable roll coating. *J. Comp. Phys.*, 151:534–562.

Christodoulou, K. N. and Scriven, L. E. (1992). Discretization of free surface flows and other moving boundary problems. *J. Comp. Phys.*, 99:39–55.

Cifre, J. G. H. and De la Torre, J. G. (1999). Steady-state behaviour of dilute polymers in elongational flow. dependence of the critical elongational rate on chain length, hydrodynamic interaction, and excluded volume. *J. Rheology*, 43:339–358.

Cormenz, J., Ledda, A., and Laso, M. (2002). Calculation of free surface using CONNFFESSIT. *J. Rheol.*, 45:237–258.

Coyle, D. J., Macosko, C. W., and Scriven, L. E. (1990). Stability of symmetrical film splitting between conter-rotating rollers. *J. Fluid Mech.*, 216:437–458.

DE Almeida, V. F. (1995). *Gas-Liquid Counterflow Through Constricted Passages.* PhD thesis, University of Minnesota, Minneapolis, MN. (Available from UMI, Ann Arbor, MI, order number 9615160).

DE Almeida, V. F. (1999). Domain deformation mapping: Application to variational mesh generation. *SIAM J. Sci. Comput.*, 20:1252–1275.

DE Gennes, P. G. (1979). *Scaling Concepts in Polymer Physics.* Cornell University Press, Ithaca, 1st edition.

DE Santos, J. M. (1991). *Two-phase Cocurrent Downflow through Constricted Passages.* PhD thesis, University of Minnesota, Minneapolis, MN. (Available from UMI, Ann Arbor, MI, order number 9119386).

Diaz, F. G., De la Torre, J. G., and Freire, J. J. (1990). Viscoelastic properties of simple flexible and semirigid models from Brownian dynamics simulations. *Macromolecules*, 23:3144–3149.

Doi, M. and Edwards, S. F. (1986). *The Theory of Polymer Dynamics.* Oxford University Press, Oxford, 1st edition.

Dontula, P. (1999). *Polymer Solutions in Coating Flows.* PhD thesis, University of Minnesota, Minneapolis, MN. Available from UMI, Ann Arbor, MI, order number 9937847.

Doyle, P. S. and Shaqfeh, E. S. G. (1998). Brownian dynamic simulations of freely draining, flexible bead-rod chains: start-up of extensional and shear flow. *J. Non-Newtonian Fluid Mech.*, 76:43–78.

Duff, I. S., Erisman, A. M., and Reid, J. K. (1989). *Direct Methods for Sparse Matrices.* Oxford University Press, Oxford, 1st edition.

Fan, Y., Phan-Thien, N., and Zheng, R. (1999a). Simulation of fibre suspension flows by the brownian configuration field method. *J. Non-Newtonian Fluid*, 84:257–274.

Fan, Y., Tanner, R. I., and Phan-Thien, N. (1999b). Galerkin/least-square finite–element methods for steady viscoelastic flows. *J. Non-Newtonian Fluid*, 84:233–256.

Fattal, R. and Kupferman, R. (2004). Constitutive laws for the matrix-logarithm of the conformation tensor. *J. Non-Newtonian Fluid Mech*, 124:281–285.

Fattal, R. and Kupferman, R. (2005). Time-dependent simulation of viscoelastic flows at high weissenberg number using the log-conformation representation. *J. Non-Newtonian Fluid Mech*, 124:23–37.

Feigl, K., Laso, M., and Öttinger, H. C. (1995). CONNFFESSIT approach for solving a two-dimensional viscoelastic fluid problem. *Macromolecules*, 28:3261–3274.

Gates, I. D. (1999). *Slot coating flows: Feasibility, quality.* PhD thesis, University of Minnesota, Minneapolis, MN. (Available from UMI, Ann Arbor, MI, order number 9946975).

Glass, J. E. (1978a). Dynamics of roll spatter and tracking. 1. commercial latex trade paints. *J. Coat. Technol.*, 50:53–60.

Glass, J. E. (1978b). Dynamics of roll spatter and tracking. 2. formulation effects in experimental paints. *J. Coat. Technol.*, 50:61–68.

Glass, J. E. (1978c). Dynamics of roll spatter and tracking. 3. importance of extensional viscosities. *J. Coat. Technol.*, 50:56–71.

Graham, M. D. (2003). Interfacial hoop stress and instability of viscoelastic free surface flows. *Phys. Fluids*, 15:1702–1710.

Grande, E., Laso, M., and Picasso, M. (2003). Calculation of variable-topology free surface flows using CONNFFESSIT. *J. Non Newtonian Fluid Mech.*, 1113:127–145.

Greener, J., Sullivan, T., Turner, B., and Middleman, S. (1980). Ribbing instabilities of a two-roller coater:Newtonian fluids. *Chem. Eng. Comm.*, 5:73–83.

Gresho, P. M., Lee., R. L., and Sani, R. C. (1979). Computer simulation of polymer chain relaxation via Brownian motion. In *Recent Advances in Numerical Methods in Fluids, Swansea, U. K.*, volume 27.

Grillet, A. M., Lee, A. G., and Shaqfeh, E. S. G. (1999). Observations of ribbing instabilities in elastic fluid flows with gravity stabilization. *J. Fluid Mech.*, 399:49–83.

Grmela, M. and Carreau, P. J. (1987). Conformation tensor rheological models. *J. Non-Newtonian Fluid Mech.*, 23:271–294.

Grmela, M. and Öttinger, H. C. (1997). Dynamics and thermodynamics of complex fluids. I. Development of a general formalism. *Phys. Rev. A*, 56:6620–6632.

Guénette, R., Abdelmalek, Z., Fortin, A., Carreau, P., and Grmela, M. (1992). Simulation of viscoelastic flows using a conformation tensor model. *J. Non-Newtonian Fluid Mech.*, 45:187–208.

Guénette, R. and Fortin, M. (1995). A new finite element method for computing viscoelastic flows. *J. Non-Newtonian Fluid Mech.*, 60:27–52.

Gupta, S. (2000). Interfecial flow. Class Notes.

Halin, P., Lielens, R., Keunings, R., and Legat, V. (1998). The Lagrangian partical method for macroscopic and micro-macro viscoelastic flow computations. *J. Non-Newtonian Fluid Mech.*, 79:387–403.

Harlow, F. H. and Welch, J. E. (1965). Numerical calculation of time-dependent viscous incompressible flow. *Phys. Fluids*, 8:2182–2189.

Herrchen, M. and Ottinger, H. (1997). A detailed comparison of various fene dumbbell models. *J. Non Newtonian Fluid Mech.*, 68:17–42.

Higgins, B. G. and Scriven, L. E. (1980). Ribbing instabilities of a two-roller coater:Newtonian fluids. *Chem. Eng. Sci.*, 35:459–466.

Hirt, C. W. and Nichols, B. D. (1981). Volume of fluid (vof) method for the dynamics of free boundaries. *J. Comput. Phys.*, 39:201–225.

Hsieh, C. C., Li, L., and Larson, R. G. (2003). Modeling hydrodynamic interaction in Brownian dynamics: simulations of extensional flows of dilute solutions of DNA and polystyrene. *J. Non-Newtonian Fluid Mech.*, 114:147–191.

Hu, X., Ding, Z., and Lee, L. J. (2005). Simulation of 2D transient viscoelastic flow using the CONNFFESSIT approach. *J. Non-Newtonian Fluid Mech.*, 127:107–122.

Huerta, A. and Liu, W. K. (1988). Viscous flow with large free surface motion. *Comp. Methods Appl. Mech. Eng.*, 69:277–324.

Hulsen, M. A., Fattal, R., and Kupferman, R. (2005). Flow of viscoelastic fuids past a cylinder at high weissenberg number: Stabilized simulations using matrix logarithms. *J. Non-Newtonian Fluid Mech*, 127:27–39.

Hulsen, M. A., van Heel, A. P. G., and van den Brule, B. H. A. A. (1997). Simulation of viscoelastic flow using Brownian configuration fields. *J. Non-Newtonian Fluid Mech.*, 70:79–101.

Jongschaap, R. J. J., de Haas, K. H., and Damen, C. A. J. (1994). A generic matrix representation of configuration tensor rheological models. *J. Rheol.*, 38:769–796.

Keunings, R. (2001). Advances in the computer modeling of the flow of polymeric liquids. *Comp. Fluid Dyn. J.*, 9:449–458.

Kistler, S. F. and Schweizer, P. M. (1997). *Liquid Film Coating*. Chapman and Hall, New York.

Kistler, S. F. and Scriven, L. E. (1984). Coating flow theory by finite element and asymptotic analysis of the Navier-Stokes system. *Int. J. Numer. Methods Fluid.*, 4:207–229.

Knudsen, K. D., De la Torre, J. G., and Elgsaeter, A. (1996). Gaussian chains with excluded volume and hydrodynamic interaction: shear rate dependence of radius of gyration, intrinsic viscosity and flow birefringence. *Polymer*, 37:1317–1322.

Kumar, K. S. and Prakash, J. R. (2003). Equilibrium swelling and universal ratios in dilute polymer solutions: exact Brownian dynamics simulations for a delta function excluded volume potential. *Macromolecules*, 36:78427856.

Landau, L. and Levich, B. (1942). Dragging of a liquid by a moving plate. *Acta Physicochim*, 17:42.

Larson, R. G., Hu, H., Smith, D. E., and Chu, S. (1999). Brownian dynamics simulations of a DNA molecule in an extensional flow field. *J. Rheol.*, 43:267–304.

Larson, R. G., Perkins, T. T., Smith, D. E., and Chu, S. (1997). Hydrodynamics of a DNA molecule in a flow field. *Phys. Rev. A*, 55:1794–1797.

Laso, M. and Ottinger, H. (1993). Calculation of viscoelastic flow using moleculat models: the CONNFFESSIT approach. *J. Non Newtonian Fluid Mech.*, 47:1–20.

Laso, M., Picasso, M., and Öttinger, H. C. (1997). 2-D time-dependent viscoelastic flow calculations using CONNFFESSIT. *AIChE J.*, 43:877–892.

Laso, M., Ramirez, J., and Picasso, M. (2004). Implicit micromacro methods. *J. Non Newtonian Fluid Mech.*, 122:215–226.

Lee, A. G., Shaqfeh, E. S. G., and Khomami, B. (2002). A study of viscoelastic free surface flows by finite element method: Hele-Shaw and slot coating flows. *J. Non-Newtonian Fluid Mech.*, 108:327–362.

Lewis, R. W., Navti, S. E., and Taylor, C. (1997). A mixed Lagrangian-Eulerian approach to modelling fluid flow during mould filling. *Int. J. Numer. Methods Fluids*, 25:931–952.

Luskin, M. and Rannacher, R. (1982). On the smoothing property of the Crank-Nicolson scheme. *Applicable Anal.*, 14:117–135.

Magda, J. J., Larson, R. G., and Mackay, M. E. (1988). Deformation-dependent hydrodynamic interaction in flows of dilute polymer solutions. *J. Chem. Phys.*, 89:25042513.

Maronnier, V., Picasso, M., and Rappaz, J. (2003). Numerical simulation of three-dimensional free surface flows. *Int. J. Numer. Meth. Fluids*, 42:697–716.

Masud, A. and Hughes, T. (1997). A space-time Galerkin/least-squares finite element formulation of the Navier-Stokes equations for moving domains problems. *Comp. Methods Appl. Mech. Eng.*, 146:91–126.

Mill, C. C. and South, G. R. (1967). Formation of ribs on rotating rollers. *J. Fluid Mech.*, 28:523–529.

Musson, L. C. (2001). *Two-layer slot coating*. PhD thesis, University of Minnesota, Minneapolis, MN. (Available from UMI, Ann Arbor, MI, order number 3008715).

Ning, C. Y., Tsai, C. C., and Liu, T. J. (1996). The effect of polymer additives on extrusion slot coating. *Chem. Eng. Sci.*, 51:3289–3297.

Oscar, M. C., Arora, D., Behr, M., and Pasquali, M. (2004). Four-field galerkin/least-squares formulation for viscoelastic fluids. *J. Non-Newtonian Fluid Mech.* Accepted.

Öttinger, H. C. (1987). Translational diffusivity from the zimm model. *J. Chem. Phys.*, 87:31563165.

Öttinger, H. C. (1989). Renormalization-group calculation of excluded-volume effects on the viscometric functions of dilute polymer solutions. *Phys. Rev. A*, 40:2664–2671.

Öttinger, H. C. (1996). *Stochastic Processes in Polymeric Fluids*. Springer Verlag, Berlin, 1st edition.

Pasquali, M. (2000). *Polymer Molecules in Free Surface Coating Flows*. PhD thesis, University of Minnesota, Minneapolis, MN. Available from UMI, Ann Arbor, MI, order number 9963019.

Pasquali, M. and Scriven, L. E. (2002). Free surface flows of polymer solutions with models based on the conformation tensor: Computational method and benchmark problems. *J. Non-Newtonian Fluid Mech.*, 108:363–409.

Pasquali, M. and Scriven, L. E. (2004). Theoretical modelling of microstructured liquids: A simple thermodynamic approach. *J. Non-Newtonian Fluid Mech.*, 120:101–135.

Pearson, J. R. A. (1960). The stability of viscous flows under rollers and spreaders. *J. Fluid Mech.*, 7:481–500.

Pitts, E. and Greiller, J. (1961). The flow of thin liquid films between rollers. *J. Fluid Mech.*, 11:33–50.

Prabhakar, R. (2005). *Predicting the Rheological Properties of Dilute Polymer Solutions using Bead-Spring Models: Brownian Dynamics Simulations and Closure Approximations*. PhD thesis, Monash University, VIC, Australia.

Prabhakar, R. and Prakash, J. R. (2002). Viscometric function for Hookean dumbbells with excluded volume and hydrodynamic interaction. *Journal of Rheology*, 46:1191–1220.

Prabhakar, R. and Prakash, J. R. (2004). Multiplicative separation of the influences of excluded volume, hydrodynamic interactions and finite extensibility on the rheological properties of dilute polymer solutions. *J. Non-Newtonian Fluid Mech.*, 116:163–182.

Prakash, J. R. (2002). Rouse chains with excluded volume interactions in steady simple shear flow. *J. Rheol.*, 46:1353–1380.

Rajagopalan, D., Armstrong, R. C., and Brown, R. A. (1990). Finite element methods for calculation of steady, viscoelastic flows using constitutive equations with a newtonian viscosity. *J. Non-Newtonian Fluid Mech.*, 36:159–192.

Ramaswamy, B. (1990). Numerical simulation of unsteady viscous free surface flow. *J. Comp. Phys.*, 90:396–430.

Romero, O. J., Suszynski, W. J., Scriven, L. E., and Carvalho, M. S. (2004). Low-flow limit in slot coating of dilute solutions of high molecular weight polymer. *J. Non-Newtonian Fluid Mech.*, 118:137–156.

Ruschak, K. J. (1976). Limiting flows in pre–metered coating device. *Chem. Eng. Sci.*, 31:1057–1060.

Ruschak, K. J. (1980). A method for incorporating free boundaries with surface tension in finite element fluid-flow simulators. *Int. J. Numer. Methods Eng.*, 15:639–648.

Ruschak, K. J. (1985). Coating flows. *J. Fluid Mech.*, 17:65–89.

Sackinger, P. A., Schunk, P. R., and Rao, R. R. (1996). A Newton-Raphson pseudo-solid domain mapping technique for free and moving boundary problems: a finite element implementation. *J. Comp. Phys.*, 125:83–103.

Saito, H. and Scriven, L. E. (1981). Study of coating flow by the finite element method. *J. Comp. Phys.*, 42:53–76.

Salamon, T. R., Bornside, D. E., Armstrong, R. C., and Brown, R. A. (1995). The role of surface tension in the dominant balance in the die swell singularity. *Phys. Fluids*, 7:2328–2344.

Salamon, T. R., Bornside, D. E., Armstrong, R. C., and Brown, R. A. (1997a). Local similarity solutions for the stress field of an Oldroyd-B fluid in the partial-slip/slip flow. *Phys. Fluids*, 9:2191–2209.

Salamon, T. R., Bornside, D. E., Armstrong, R. C., and Brown, R. A. (1997b). Local similarity solutions in the presence of a slip boundary condition. *Phys. Fluids*, 9:1235–1247.

Sartor, L. (1990). *Slot coating: Fluid mechanics and die design.* PhD thesis, University of Minnesota, Minneapolis, MN. (Available from UMI, Ann Arbor, MI, order number 9109372).

Savage, M. (1984). Mathematical model for the onset of ribbing. *J. AIChE*, 30:999–1002.

Schäfer, L. (1999). *Excluded Volume Effects in Polymer Solutions.* Springer-Verlag, Berlin.

Schroeder, C. M., Babcock, H. P., Shaqfeh, E. S. G., and Chu, S. (2003). Observation of polymer conformation hysteresis in extensional flow. *Science*, 301:15151519.

Schroeder, C. M., Shaqfeh, E. S. G., and Chu, S. (2004). Effect of hydrodynamic interactions on DNA dynamics in extensional flow: Simulation and single molecule experiments. *Macromolecules*, 37:9242–9256.

Siginer, D. A., Kee, D. D., and Chabra, R. P. (1999). *Advances in the Flow and Rheology of Non–Newtonian Fluids*. Elsevier Science.

Silliman, W. J. and Scriven, L. E. (1980). Separating flow near a static contact line - slip at a wall and shape of a free-surface. *J. Comp. Phys.*, 34:287–313.

Slattery, J. C. (1990). *Interfacial Transport Phenomena*. Springer-Verlag.

Somasi, M. and Khomami, B. (2000). Linear stability and dynamics of viscoelastic flows using time-dependent stochastic simulation technique. *J. Non-Newtonian Fluid Mech.*, 93:339–362.

Somasi, M. and Khomami, B. (2001). A new approach for studying the hydrodynamic stability of fluids with microstructure. *Phys. of Fluids*, 13:1811–1814.

Somasi, M., Khomami, B., Woo, N. J., Hur, J. S., and Shaqfeh, E. S. G. (2002). Brownian dynamics simulation of bead-rod and bead-spring chains: numerical algorithm and coarse-graining issues. *J. Non-Newtonian Fluid Mech.*, 108:227–255.

Sun, J., Smith, M. D., Armstrong, R. C., and Brown, R. A. (1999). Finite element method for viscoelastic flows based on the discrete adaptive viscoelastic stress splitting and the discontinuous galerkin method: DAVSS-G/DG. *J. Non-Newtonian Fluid Mech.*, 86:281–307.

Sunthar, P. and Prakash, J. R. (2005). Parameter free prediction of DNA conformations in elongational flow by successive fine graining. *Macromolecules*, 38:617–640.

Szady, M. J., Salamon, T. R., Liu, A. W., Armstrong, R. C., and Brown, R. A. (1995). A new mixed finite element method for viscoelastic flows governed by differential constitutive equations. *J. Non-Newtonian Fluid Mech.*, 59:215–243.

Tomea, M. F., Mangiavacchi, N., Cuminato, J. A., Castelo, A., and McKee, S. (2002). A finite difference technique for simulating unsteady viscoelastic free surface flows. *J. Non-Newtonian Fluid Mech.*, 106:61–106.

Van Heel, A. P. G., Hulsen, M. A., and van den Brule, B. H. A. A. (1990). On the selection of parameters in the fene-p model. *J. Non-Newtonian Fluid Mech.*, 75:253–271.

Xie, X. (2005). *Modeling Viscoelastic Free Surface and Interfacial Flows, with Applications to the Deformation of Droplets and Blood Cells.* PhD thesis, Rice University, Houston, TX.

Xie, X. and Pasquali, M. (2004). A new, convenient way of imposing open-flow boundary conditions in two- and three-dimensinoal viscoelastic flows. *J. Non-Newtonian Fluid Mech.*, 122:159–176.

Zevallos, G. A., Carvalho, M. S., and M., P. (2005). Forward roll coating flows of viscoelastic liquids. *J. Non-Newtonian Fluid Mech.*, 130:96–109.

Zylka, W. and Öttinger, H. C. (1989). A comparison between simulations and various approximations for Hookean dumbbells with hydrodynamic interactions. *J. Chem. Phys.*, 94:4628–4636.

Zylka, W. and Öttinger, H. C. (1991). Calculation of various universal properties for dilute polymer solutions undergoing shear flow. *Macromolecules*, 24:484–494.